Polymerization Kinetics of Cyclic Esters by Metal Alkoxide Complexes and Catalytic Decarbonylation of Bio-Derived Carboxylic Acids to Commodity Alkenes

A Dissertation
SUBMITTED TO THE FACULTY OF THE
UNIVERSITY OF MINNESOTA
BY

Maria Olivia Miranda

IN PARTIAL FULFILLMENT OF THE REQUIREMENTS
FOR THE DEGREE OF
DOCTOR OF PHILOSOPHY

William B. Tolman, Marc A. Hillmyer, Advisors

May 2014

Acknowledgements

First, I would like to thank the collaborators and coworkers that I worked closely with on all my projects, specifically Dr. Agostino Pietrangelo and Dr. Keying Ding. Their guidance, patience, and kindness shaped me into the scientist I am today. My remaining collaborators, Dr. Beth Moscato-Goodpaster, Prof. Chris Schaller, Dr. Anne LaPointe, Prof. Geoff Coates, Dr. Alex John, Dr. Hugo Vasquez-Lima, Josh Marell, Prof. Chris Cramer, Anna Dunn, and Prof. Clark Landis are not only extremely talented individuals, but also great people to work with. It is an understatement to say that the sum of the whole is much greater than the parts.

My advisors, Profs. Bill Tolman and Marc Hillmyer, have been outstanding mentors, examples, and advocates. I especially thank them for holding higher standards than seem achievable or reasonable, and then asking their students to exceed them.

I'd also like to acknowledge past and present members of the Tolman and Hillmyer groups. The graduates and members of these groups are exceptional scientists and people and I am so grateful to call them friends, mentors, peers, and collaborators.

My family is amazing. My brothers, Joe Miranda and Danny Miranda, are rock stars. They are constant sources of support and are best at reminding me to aim higher and to find humor in every situation, no matter how dire. My parents, Jeanne Miranda and Rick Miranda, are the sole reason(s) I wanted to become a scientist. They are both incredible scientists and people, and I could not have asked for better role models. They never told me that I couldn't or shouldn't, and words cannot express my gratitude for their unwavering belief in me. Finally, I'd like to thank my partner in crime, Marcus Pobloske, for listening to and humoring me, reminding me what is important, and always being there. You deserve a medal.

To my family.

Abstract

Plastic materials are an integral part of modern life; however, nearly every plastic, or polymer, is derived from petroleum resources, which are non-sustainable, non-degradable, and can be toxic to humans and the environment. Developing methodologies to synthesize and characterize alternative materials that are degradable, safe, and sustainable has therefore been a vibrant research area. This thesis describes two approaches towards the development of sustainable polymers and monomers (the building blocks from which polymers are made). The first aims to understand the fundamental mechanistic details of metal-catalyzed ring-opening polymerization of renewable cyclic ester monomers to degradable polyesters. The second targets the catalytic synthesis of common petroleum-based monomers from sustainable and biomass-derived carboxylic acids.

Table of Contents

LIST OF TABLES ..... **VII**

LIST OF FIGURES ..... **IX**

LIST OF SCHEMES ..... **XVI**

LIST OF EQUATIONS ..... **XVII**

LIST OF ABBREVIATIONS ..... **XVIII**

1 TWO APPROACHES TOWARDS THE DEVELOPMENT OF SUSTAINABLE POLYMERS **1**

1.1 OVERVIEW 2

1.2 CYCLIC ESTER POLYMERIZATION 7

1.2.1 Introduction *7*

1.2.2 Metal-Catalyzed Ring-Opening Polymerization *8*

1.3 DECARBONYLATION OF BIO-DERIVED CARBOXYLIC ACIDS 20

1.3.1 Introduction *20*

1.3.2 Decarbonylation of Carboxylic Acids *21*

2 THE ROLES OF MONOMER BINDING AND ALKOXIDE NUCLEOPHILICITY IN ALUMINUM-CATALYZED POLYMERIZATION OF E-CAPROLACTONE **29**

2.1 OVERVIEW 30

2.2 INTRODUCTION 31

2.3 RESULTS AND DISCUSSION 34

2.3.1 Synthesis and Characterization of Complexes *34*

2.3.2 Mechanistic Proposal and Methodology for Determining Rate Constants *35*

2.3.3 Isolation of a Complex After Polymerization *46*

2.3.4 Rate Constants and Mechanistic Interpretations *47*

2.3.5 Theoretical Calculations *57*

2.4 SUMMARY AND CONCLUSIONS 62

2.5 EXPERIMENTAL SECTION 64

2.5.1 General Considerations *64*

2.5.2 Synthetic Procedures *64*

2.5.3 ^{1}H NMR Spectroscopy Kinetic Analyses *65*

2.5.4 Derivation of Equation 2.7 ..... *67*

2.5.5 Data and Error Analysis *68*

2.5.6 Experimental Details for X-ray Crystal Structure of 4 ..... *69*

2.5.7 Theoretical methods *71*

2.6 ACKNOWLEDGEMENTS 73

3 UNDERSTANDING THE MECHANISM OF POLYMERIZATION OF E-CAPROLACTONE CATALYZED BY ALUMINUM SALEN COMPLEXES **74**

3.1 OVERVIEW 75

3.2 INTRODUCTION 76

3.3 RESULTS AND DISCUSSION 79

3.3.1 Synthesis and Characterization of Ligands and Catalysts 79
3.3.2 Polymerization Kinetics 80
3.3.3 Interpretation of Kinetic Parameters 93
3.3.4 Density Functional Modeling 96
3.4 SUMMARY AND CONCLUSIONS 110
3.5 EXPERIMENTAL SECTION 112
3.5.1 General Considerations 112
3.5.2 Synthetic Procedures 112
3.5.3 ^{1}H NMR Kinetics 115
3.5.4 Density Functional Calculations 117
3.5.5 Derivation of Equation 3.1 Using Substrate Inhibition Mechanism 119
3.5.6 Experimental Details for X-ray Structure of 2 (R = OMe) 119
3.6 ACKNOWLEDGMENTS 121

4 CATALYTIC DECARBONYLATION OF BIOMASS-DERIVED CARBOXYLIC ACIDS AS AN EFFICIENT ROUTE TO COMMODITY MONOMERS 122
4.1 OVERVIEW 123
4.2 INTRODUCTION 124
4.3 RESULTS AND DISCUSSION 127
4.3.1 Mono-Alkyl Succinates 127
4.3.2 Hydrocinnamic Acid 130
4.3.3 3-Cyanopropanoic Acid 135
4.4 SUMMARY AND CONCLUSIONS 137
4.5 EXPERIMENTAL SECTION 138
4.5.1 General Considerations 138
4.5.2 Synthetic Procedures 139
4.5.3 Large Scale Decarbonylation Reactions 142
4.5.4 ASTM-D6866-12 Standard Test Results 145
4.6 ACKNOWLEDGMENTS 153

5 EARTH-ABUNDANT METAL CATALYSTS FOR THE DECARBONYLATION OF HYDROCINNAMIC ACID TO STYRENE 154
5.1 OVERVIEW 155
5.2 INTRODUCTION 156
5.3 RESULTS AND DISCUSSION 159
5.3.1 Primary High-Throughput Experimentation Screen 159
5.3.2 Secondary High-Throughput Experimentation Screen 161
5.3.3 Conventional Experimentation 164
5.3.4 Mechanistic Implications 167
5.4 SUMMARY AND CONCLUSIONS 170
5.5 EXPERIMENTAL SECTION 171
5.5.1 General Considerations 171
5.5.2 High-throughput Screening 172
5.5.3 Large Scale Decarbonylation Reactions 186
5.6 ACKNOWLEDGMENTS 191

6 BIBLIOGRAPHY 192

A KINETICS OF CYCLIC ESTER POLYMERIZATION INITIATORS USING STOPPED-FLOW 1H NMR SPECTROSCOPY 209

A.1 OVERVIEW 210

A.2 BACKGROUND 211

A.3 STOPPED-FLOW ^{1}H NMR SPECTROSCOPY EXPERIMENTS 213

A.3.1 [(BDI)MgOi-Pr]$_2$ Initiator 214

A.3.2 (NNO)ZnOEt Initiator 217

A.4 EXPERIMENTAL SECTION 221

A.4.1 General Considerations 221

A.4.2 Updated Synthesis of (NNO)ZnOEt 221

A.4.3 Stopped-Flow Stacked ^{1}H NMR Spectra 224

List of Tables

Table 1.1. k_p values for various initiators for ROP of LA. 17

Table 2.1. Summary of kinetic parameters V_{max} and K_{eq} determined using RPKA method.[a] 43

Table 2.2. Average values of kinetic parameters determined from COPASI fits and RPKA and NMR peak analyses. 45

Table 2.3. Activation parameters associated with k_2. 49

Table 2.4. Thermodynamic parameters associated with K_{eq} as determined by COPASI and NMR peak analysis methods. 50

Table 2.5. Relative 333 K enthalpies (kcal/mol) of different catalyst structures with and without bound CL.[a] 58

Table 3.1. Average values of kinetic parameters determined from COPASI fits and ^{1}H NMR peak analysis. 83

Table 3.2. Comparison of saturation kinetic parameters obtained from COPASI, RPKA and NMR Δδ analysis for polymerization of CL by 2 (R = Br) at 333 K. 85

Table 3.3. Comparison of kinetic parameters determined from experiments performed in an NMR tube and in stirring experiment (highlighted in gray). 91

Table 3.4. Thermodynamic parameters associated with K_{eq} for catalysts 2 determined by COPASI and ^{1}H NMR peak analysis. 94

Table 3.5. Activation parameters for k_2 95

Table 3.6. Free energies (kcal/mol) relative to separated reactants for reaction paths involving O_{ester}-Al coordination in the truncated r and more elaborate s models.[a] 101

Table 3.7. Free energies (kcal/mol) relative to separated reactants for reaction paths involving $O_{carbonyl}$-Al coordination in truncated r and more elaborate s models (see also Figure 3.20).[a] 101

Table 3.8. Free energies (kcal/mol) relative to separated reactants for reaction paths involving O_{ester}-Al coordination in full *para*-substituted models.[a] 104

Table 3.9. Free energies (kcal/mol) relative to separated reactants for reaction paths involving $O_{carbonyl}$-Al coordination in full *para*-substituted models.[a] 105

Table 4.1. Yields (%) for the catalytic decarbonylation of mono-alkyl succinates.[a] 128

Table 4.2. Yields (%) of decarbonylation using hydrocinnamic acid.[a] 131

Table 5.1. Representative results of HTE primary screen reactions of hydrocinnamic acid to yield styrene.[a] 160

Table 5.2. Effect of CO, CO_2, and N_2 on decarbonylation of hydrocinnamic acid.[a] 164

Table 5.3. Effect of nickel precursor, KI and PPh_3/Ni ratio on decarbonylation of hydrocinnamic acid.[a] 165

Table 5.4. Optimiziation of Ni-catalyzed decarbonylation of hydrocinnamic acid.[a] 166

Table 5.5. HTE primary screen, plate 1. Reaction temperature: 180 °C. Reaction time: 30 min. Metal loading: 1 mol%. Ligand loading: 10 mol%. 174

Table 5.6. HTE primary screen, plate 2. Reaction temperature 100 °C. Reaction time: 60 min. Metal loading: 1 mol%. Ligand loading: 10 mol%. 174

Table 5.7. HTE primary screen, plate 3. Reaction temperature 180 °C. Reaction time: 40 min. Metal loading: 1 mol%. Ligand loading: 10 mol%, except pyridine (20 mol%). Ligands on left-hand side of bolded line were loaded with the first six metal precursors, and ligands on the right-hand side of the bolded line were loaded with the final six precursors. 175

Table 5.8. HTE primary screen, plate 4. Reaction temperature: 180 °C. Reaction time: 30 min. Metal loading: 1 mol% (first six columns), 2 mol% (final six columns). Ligand loading: 10 mol%, except pyridine (20 mol%). Green denotes strong signal for styrene when visualized under UV light, orange denotes a weaker signal (qualitative). 176

Table 5.9. HTE secondary screen to determine styrene yields based on metal precursor and L/M ratio. Reaction temperature: 180 °C. Reaction time: 1 hr. Under N_2 atmosphere (ambient pressure). 177

Table 5.10. HTE secondary screen to determine styrene yields based on metal precursor and L/M ratio. Reaction temperature: 180 °C. Reaction time: 2 hr. Under N_2 atmosphere (ambient pressure). 178

Table 5.11. HTE primary screen to determine styrene yields with zero valent and divalent Ni and Fe precursors and phosphine ligands. Reaction temperature: 180 °C. Reaction time: 2 hr. Under N_2 atmosphere (ambient pressure). 180

Table 5.12. HTE primary screen to determine styrene yields with zero-valent and divalent Ni and Fe precursors and phosphine ligands. Reaction temperature: 180 °C. Reaction time: 2 hr. Under CO atmosphere (100 psi). 183

Table A.1 Summary of the kinetic parameters obtained from stopped-flow ^{1}H NMR spectroscopy. 219

List of Figures

Figure 1.1. Monomers LA and CL and their respective polymers, PLA and PCL, from ROP. 7

Figure 1.2. Aluminum binaphthyl-salen alkoxide initiator for the ROP of LA. 11

Figure 1.3. β-Diiminate initiators for the ROP of LA. 12

Figure 1.4. Kinetic schemes typically assumed in the ROP of cyclic ester by single site metal complexes. Top: second order reaction; bottom: pseudo-first order reaction. 14

Figure 1.5. Representative example of the kinetic treatment typically applied to study the ROP of cyclic ester. $[LA]_0$ = 0.84 M, $[BnOH]_0$ = 25 mM, $[NEt_3]$ = 50 mM, 21 °C, CD_2Cl_2. Left: illustrative kinetic data for polymerization of LA using various concentration of $InCl_3$ with fits to the first order decay equation $[LA]_t = [LA]_0\exp(-k_{obs}t)$. $[InCl_3]_0$ = 4.7 mM (black), 8.5 mM (light green), 16.1 mM (dark green), 23.7 mM (blue). Right: kinetic plot of k_{obs} vs. $[InCl_3]_0$ for the polymerization of LA (same data as in right plot). Closed circles denote constant values for $[BnOH]_0$ and $[NEt_3]_0$ as above, open circles represent a constant ratio of NEt_3:BnOH:$InCl_3$ = 2:1:1. 15

Figure 1.6. Structures of initiators mentioned in Table 1.1 17

Figure 1.7. A representative group of the chemicals derived from either the fermentation or chemical transformation of glucose. 21

Figure 1.8. Proposed mechanism for the decarbonylation of carboxylic acids using rhodium and palladium. 24

Figure 1.9. Phosphine ligands and palladium sources used for the decarbonylation of carboxylic acids. 25

Figure 2.1. Coordination-insertion mechanism for cyclic ester ring-opening polymerizations. 31

Figure 2.2. [CL] and [PCL] *vs*. time data (•,▲) and fit (–) to Equation 2.1 for polymerization of CL catalyzed by 3 at 333 K. Fit parameters: K_M = 1.046(9) M, k_2 = 0.0328(2) s^{-1}. 38

Figure 2.3. Alternative rate law fits by COPASI to data for the polymerization of CL by 2 at 323 K. Top, left: first-order fit to Equation 2.3. Top, right: linearized first-order fit to Equation 2.4. Bottom, left: second-order fit to Equation 2.5. Bottom, right: linearized second-order fit to Equation 2.6. 39

Figure 2.4. Left: [CL] *vs*. time data (•) fit to 7^{th} order polynomial (–). Right: Rate *vs*. [CL] data obtained from derivative of 7^{th} order polynomial on left (•) and fit to Equation 2.1 (–) for the polymerization of CL by 3 at 333 K. 40

Figure 2.5. Fits of n^{th} (n = 2–9) order polynomial functions to a representative data set for the polymerization of CL by 3. $[3]_0$ = 6.88(2) mM, $[CL]_0$ = 2.6 M, 333 K, toluene-d_8. Points represent the derivative of polynomial order indicated; red line is fit to Equation 2.1. For n = 5, fit to Equation 2.1 would not converge. 42

Figure 2.6. A portion of the ^{1}H NMR spectra acquired during the polymerization of CL by 3 at 333 K showing how the aryl resonances for the complex in solution change as a function of reaction time, as measured by the indicated peak separation Δδ..... 44

Figure 2.7. Plot of Δδ *vs*. [CL] during the polymerization of CL for 2 and 3 at 333 K, with the fit to Equation 2.7. 45

Figure 2.8. Line drawing of complex 4 (top), and representation of the X-ray crystal structure of 4, showing 50% thermal ellipsoids with all hydrogen atoms (except those on the bridging hydroxo groups) and *t*-butyl and -NO_2 substituents omitted for clarity (bottom). Selected interatomic distances (Å) and angles (deg) are as follows: Al1−O1, 1.7859(14), Al1−O1', 1.8626(14), Al1−O2, 1.7702(14), Al1−O3, 1.7733(14), Al1−N1, 2.1253(16), Al1−Al1', 2.8007(11), O1−H, 0.80(2), N2−H, 1.865, O1−N2, 2.658; O1−Al1−O2, 125.69(7), O1−Al1−O3, 119.25(7), O1−Al1−N1, 92.46(6), O1-Al1-O1', 77.96(7), O2−Al1−O3, 114.99(7), O2−Al1−N1, 90.90(6), O2−Al1−O1', 97.50(6), O3−Al1−N1, 89.13(6), O3−Al1−O1', 92.52(6), N1−Al1−O1', 169.81(6), Al1−O1−Al1', 100.26(7), Al1−O1−H, 126.2(15), Al1−O1'−H', 133.5(15), O1−H−N2, 170.13. 47

Figure 2.9. Hammett plot for k_2 (black) and K_{eq} (red). The rate constants presented that were not determined directly from the data were extrapolated from the thermodynamic parameters obtained from the Eyring (k_2) and van't Hoff (K_{eq}) plots (Table 2.3 and Table 2.4). 48

Figure 2.10. Erying plot for k_2 for catalysts 1 (red triangle), 2 (black circle), 3 (blue diamond)..... 49

Figure 2.11. Van't Hoff plot for K_{eq} for catalsts 1 (red triangles), 2 (black circles), 3 (blue diamonds). The designation NMR or COPASI indicates which analysis method (vida supra) was used to obtain the data. NMR: NMR peak analysis method. COPASI: kinetic analysis using COPASI. 51

Figure 2.12. Full stacked VT-^{1}H NMR spectra (500 MHz, toluene-d_8) of 1 from 193 K to 292 K. 54

Figure 2.13. Left: portion of VT-^{1}H NMR spectra (–) and fit (--) to determine rate constant, *k*, for fluxional process in 1. Right: Erying analysis of determined rate constants, $R^2 = 0.9815$. See text for thermodynamic parameters. 54

Figure 2.14. Full stacked VT-^{1}H NMR spectra (500 MHz, toluene-d_8) of 1 with 50 equiv. pyridine from 193 K to 292 K 55

Figure 2.15. Full stacked VT-^{1}H NMR spectra (500 MHz, toluene-d_8) of 1 with 1 equiv. of pyridine from 193 K to 292 K. 55

Figure 2.16. Portions of the VT ^{1}H NMR spectra in Figure 2.12 of complex 1 in toluene-d_8 with no added reagents. 56

Figure 2.17. Portions of the VT ^{1}H NMR spectra in Figure 2.14 of complex 1 in toluene-d_8 in the presence of 50 equiv pyridine (pyr). The spectrum of the free (uncoordinate, protonated version) of the ligand is shown for reference at the top of the stacked plot. Asteriks denote spinning side-bands associate with free pyr resonance. 56

Figure 2.18. Ball-and-stick stereostructures of representative $L^{H}AlOR$ (R = $(CH_2)_5CO_2Me$) complexes with L^{H} coordinate in tetradentate (a, c) and tridentate (b, d) fashion, with (a, b) and without (c, d) coordinated ε-caprolactone. All structures were fully optimized at the DFT level of theory (see Methods section). Hydrogen atoms are not shown for clarity, carbon atoms are gray, nitrogen atoms are blue, oxygen atoms are red, and aluminum atoms are purple. The illustrated structures are designated Mono-RO in Table 2.5. Structures in which the terminal ester of the alkoxide ligand also coordinate Al, designated Bi-RO in Table 2.5, are higher in enthalpy than those shown here..... 59

Figure 3.1. Coordination-insertion mechanism for the polymerization of cyclic esters.. 76

Figure 3.2. Complexes studied in Chapter 2 (1) and this chapter (2). 77

Figure 3.3. Representation of the X-ray crystal structure of 2 (R = OMe), showing nonhydrogen atoms as 50% thermal ellipsoids. Selected interatomic distances (Å) and angles (deg): Al1−O1, 1.8107(13); Al1−O2, 1.7899(12); Al1−O3, 1.7292(13); Al1−N1, 2.0042(14); Al1−N2, 2.0445(15); O3−Al1−O2, 115.98(6); O3−Al1−O1, 100.22(6); O2−Al1−O1, 97.57(6); O3−Al1−N1, 113.60(6); O2−Al1−N1, 129.72(6); O1−Al1−N1, 87,59(6); O3−Al1−N2, 96.96(6); O2−Al1−N2, 88.00(6); O1−Al1−N2, 161.05(6); N1−Al1−N2, 78.22(6). 80

Figure 3.4. Illustrative conversion *vs.* time profile for decay of CL (■) and growth of PCL (◆) resonances during ROP catalyzed by R = OMe at 333 K, determined from ^{1}H NMR spectra, along with fits (−) determined by COPASI. 82

Figure 3.5. Plots of rate *vs*. [CL] for polymerizations of CL by R = OMe, R = Br, and R = NO_2. Plots were generated using COPASI fit parameters (V_{max} and K_M), measured CL concentrations and Equation 3.1. 82

Figure 3.6. Portion of the ^{1}H NMR spectra acquired during polymerization of CL by 2 (R = Br) at 333 K illustrating how the aryl resonances of the complex in solution change as a function of reaction time. The indicated peak separation was used to independently evaluate K_{eq} (see Equation 3.2). Note the conversion of the catalyst during early reaction times (t = 0-1 hr) that is modeled in Figure 3.13. 84

Figure 3.7. Representative plots of Δδ as a function of [CL] determined from the difference between the imine catalyst residues of catalyst 2 (R = OMe, left; R = Br, middle; R = NO_2, right) at 333 or 323 K. Data points (•) were fit (−) to Equation 3.2, yielding the K_{eq} shown. 84

Figure 3.8. Left: [CL] *vs*. time data (black) and fit to fourth order polynomial ($y = a + bx + cx^2 + dx^3 + ex^4$ red) for catalyst 2 (R = Br) at 333 K. Right: derivative of obtained polynomial ($y' = b + 2cx + 3dx^2 + 4ex^3$) *vs*. [CL] (black), with a non-linear fit to Equation 3.1 (red; $R^2 = 0.9982$) and obtained COPASI fit parameters (as in Figure 3.5)..... 85

Figure 3.9. Results from COPASI fits to the kinetic data for the polymerization of CL by 2 (R = Br) at 333 K. Data are shown in black and fits to first-order (left), second-order (middle), and Michaelis-Menten (right) rate equations are shown in red, with errors shown in green. 86

Figure 3.10. Linearized data (black) for first- (left) and second-order (right) rate equations with calculated linear fits (red). 87

Figure 3.11. Top: data (black) and fits to first-order (blue) and Michaelis-Menten (red) kinetics rate equations obtained from COPASI for catalyst 2 (R = Br) at 333 K for (a) $[CL]_0$ = 2 M and (b) $[CL]_0$ = 1 M. Middle: errors associated with the fits are shown in (c) $[CL]_0$ = 2 M and (d) $[CL]_0$ = 1 M. Fits were obtained using contributions from [CL] only. Bottom: (e) linearized data (black) for first-order rate equations along with calculated linear fits fits (red) for $[CL]_0$ = 1 M. Compare to the plot shown in Figure 3.10, left, for which $[CL]_0$ = 2 M. 89

Figure 3.12. Left: concentration *vs*. time profile for decay of CL resonances during the stirred polymerization reaction catalyzed by R = NO_2 at 298 K along with fit (–) determined by COPASI to Equation 3.1. Right: Erying plot for 2 (R = NO_2) with values obtained from ^{1}H NMR method in black and the value obtained from the stirred polymerization in red. 90

Figure 3.13. Left: growth of ultimate catalyst species present in polymerization (black circles), decay of initial catalytic species present in polymerizations (red squares) and fits (–,–) to first-order decay equation $[cat]_t = [cat]_0 \exp(-k_{obs}t)$ for 2 (R = Br) at 333 K and $[CL]_0$ = 2 M. Right: observed pseudo-first order rate constant k_{obs} *vs*. [CL]. 92

Figure 3.14. Hammett plot for k_2 (black) and K_{eq} (red). Values for the rate constants k_2 and K_{eq} at temperatures that were not experimentally measured but presented were obtained by extrapolating the thermodynamic parameters from the Eyring (k_2, Table 3.5) and Van't Hoff (K_{eq}, Table 3.4) plots. 93

Figure 3.15. Van't Hoff plot for K_{eq} (R = OMe, red triangles; R = Br, black circles; R = NO_2, blue diamonds). Closed points denote equilibrium constant values determined by COPASI; open points denote values determined by ^{1}H NMR peak analysis method. 94

Figure 3.16. Erying plot for k_2 values. 95

Figure 3.17. Truncated model r for catalysts 2. 96

Figure 3.18. Eight distinct CL r complex structures from which alkoxide insertion may proceed. [a] Orientation of the CL is given relative to the nitrogen ligands. [b] Orientation of the ester or carbonyl oxygen is given relative to the nitrogen donors. 98

Figure 3.19. Reaction path for *v* (same as *i*, *iii*, and *vii*); this path is computed to have higher activation free energy relative to that shown in Figure 3.20. 99

Figure 3.20. Reaction path for r-*vi*; this path is computed to have the lowest activation free energy of eight distinct stereochemical possibilities shown in Figure 3.18. 99

Figure 3.21. Lowest-energy pathway corresponding to s-*vi* pathway 103

Figure 3.22. Proposed ROP mechanisms that yield the rate law described by M = [(salen)Al] moiety. 107

Figure 3.23. Unproductive complex of CL with *p*-NO_2-catalyst. 108

Figure 4.1. Decarbonylation of long-chain fatty acids using Pd or Rh catalysts first demonstrated by Miller. 124
Figure 4.2. Ligands used in this chapter to study catalytic decarbonylation of carboxylic acids. 127
Figure 4.3. Preparation of mono-alkyl succinates from succinic acid and alcohols. 127
Figure 4.4. Decarbonylation of mono-alkyl succinates to alkyl acrylates. 127
Figure 4.5. Representative GC-MS traces of distillate mixtures from decarbonylation of the mono-alkyl succinates 1, 2, and 3, and PPh_3 as the ligand for 1 and DPEphos as the ligand for 2 and 3. 129
Figure 4.6. GC-MS traces of the sealed reaction between 1 (left) and 3 (right) and pivalic anhydride at 190 °C for 2 hours. 130
Figure 4.7. Competitive reaction with decarbonylation that produces alkyl pivalates. 130
Figure 4.8. Decarbonylation of hydrocinnamic acid to styrene. 131
Figure 4.9. Representative GC-MS trace of distillate mixture using hydrocinnamic acid (7) as the substrate and DPEphos as the ligand. 133
Figure 4.10. Representative GC-MS trace of distillate mixture using 3-cyanopropanoic acid as the substrate and PPh_3 as the ligand. 136
Figure 5.1. Ligands and metal precursors used in primary high-throughput screening reactions. 159
Figure 5.2. Heat map illustrating the effect of L/M ratio on styrene yield and [styrene]/[ethylbenzene] ratio. M = 5 mol%, L = PPh_3, KI = 10 mol%, 2 hr, 180 °C. Data adapted from Table 5.10. The size of the circle is proportional to the styrene yield in that well. Colors correspond to [styrene]/[ethylbenzene] ratio: 0.8–1 green; 1–1.8 yellow-green; 1.8–2.5 yellow; 2.5–5 orange; 5–7 red orange, >7 red. 162
Figure 5.3. Ligands and metal precursors used in the second set of high-throughput screening reactions. 163
Figure 5.4. Heat map illustrating styrene yields from the HTE screen of reactions with Ni(0), Ni(II), Fe(0), and Fe(II) precursors and phosphine ligands. M = 2 mol%, L = 10 mol%, KI =10 mol%, 2 hr, 180 °C. Data adapted from Table 5.11. The size of a circle is proportional to the styrene yield in that well. Colors correspond to [styrene]/[ethylbeznene] ratio: 1–2 green; 2–4 yellow-green; 4–8 yellow; 8–27 orange; 27–74 red orange, >74 red. 163
Figure 5.5. Styrene dimers isolated from reaction mixture. 167
Figure 5.6. Potential side reactions to produce styrene dimers and ethylbenzene. 169
Figure 5.7. Representative GC-MS chromatograms of distillate isolated from reaction in Table 5.4, Entry 7 (left) and Table 5.4, Entry 8 (right). 187
Figure 5.8. GC-MS chromatogram (full, left; zoom of region from 16 to 18 min, right) of reaction flask after reaction had been terminated, diluted with hexanes, and filtered. The solvent was removed *in vacuo* and reside was taken up in a small amount of hexanes for GC-MS analysis. 189

Figure 5.9. Mass spectrum of peaks with retention times 16.73 min (top left), 17.26 min (top right), and 17.41 min (bottom) from chromatograms in Figure 5.8. 189

Figure 5.10. GC-MS chromatogram (full, left; zoom of region from 16 to 18 min, right) of solid residue left in the reaction flask after reaction had been terminated, diluted with hexanes, and filtered to obtain the insoluble products. The insoluble products were then dissolved in $CHCl_3$, stirred with deionized water, and then washed with NaOH and HCl. The $CHCl_3$ was removed *in vacuo* and this is the GC-MS of the resulting solid. 190

Figure 5.11. Mass spectrum of peaks with retention times 16.73 min (top left), 17.26 min (top right), and 17.41 min (bottom) from chromatograms in Figure 5.10. 190

Figure A.1. Initiators studied using stopped-flow ^{1}H NMR spectroscopy for the ROP of CL. 212

Figure A.2. Concentration *vs*. time profile for ROP of CL initiated by [(BDI)MgO*i*-Pr]$_2$. 214

Figure A.3. Fits of concentration *vs*. time for ROP of CL initiated by [(BDI)MgO*i*-Pr]$_2$ for first order rate equation (left) and Michaelis-Menten rate equation (right). Fit parameters for first order fit: $k_1 = 0.0101(1)$ s^{-1}. Fit parameters for Michaelis-Menten fit: $V_{max} = 0.024(8)$ M/s, $k_2 = 9.6(3)$ s^{-1}, $K_M = 1.09(8)$ M, $K_{eq} = 0.92(7)$ M^{-1}. 215

Figure A.4. Potential monomer-dimer catalyst equilibrium to explain observed saturation kinetics for the ROP of CL by [(BDI)MgO*i*-Pr]$_2$. 216

Figure A.5. Fits of concentration *vs*. time for ROP of CL initiated by (NNO)ZnOEt for first order rate equation (top, left), Michaelis-Menten rate equation (top, right) and overlay of fits from both rate equations (bottom). Fit parameters for first order fit: $k_1 = 0.00970(6)$ s^{-1}. Fit parameters for Michaelis-Menten fit: $V_{max} = 0.12(4)$ M/s, $k_2 = 48 \pm 16$ s^{-1}, $K_M = 11 \pm 4$ M, $K_{eq} = 0.09(3)$ M^{-1}. [(NNO)ZnOEt] = 2.5 mM. 217

Figure A.6. Fits of concentration *vs*. time for ROP of CL initiated by (NNO)ZnOEt for first order rate equation (top, left), Michaelis-Menten rate equation (top, right) and overlay of fits from both rate equations (bottom). Fit parameters for first order fit: $k_1 = 0.0307(2)$ s^{-1}. Fit parameters for Michaelis-Menten fit: $V_{max} = 0.25(7)$ M/s, $k_2 = 36 \pm 10$ s^{-1}, $K_M = 7 \pm 2$ M, $K_{eq} = 0.14(4)$ M^{-1}. $[(NNO)ZnOEt]_{tot} = 7$ mM. 218

Figure A.7. (a) Reported synthetic route to (NNO)ZnOEt. (b) Altered and succcessful synthetic route to same product. 221

Figure A.8. Overlay of the ^{1}H NMR spectra of the clean reaction product between (NNO)ZnEt and excess EtOH (top, red), (NNO)ZnEt alone (middle, light blue), and the crude reaction product between (NNO)ZnEt and 1 equiv. EtOH (bottom, dark blue). 222

Figure A.9. ^{1}H NMR spectrum of the isolated (NNO)ZnOEt after reaction with excess EtOH and heating in THF. 224

Figure A.10. Stacked ^{1}H NMR spectra obtained from stopped-flow experiment using $[[(BDI)MgO\textit{i}\text{-}Pr]_2]_0$ = 2.5 mM. First spectrum (bottom) was obtained 3 seconds after mechanical stop, and every subsequent spectra was obtained every 7 seconds. 225

Figure A.11. Stacked ^{1}H NMR spectra obtained from stopped-flow experiment using $[(NNO)ZnOEt]_0$ = 2.5 mM. First spectrum (bottom) obtained 1 second after mechanical stop, and every subsequent spectra was obtained every 5 seconds. 226

Figure A.12. Stacked ^{1}H NMR spectra obtained from stopped-flow experiment using [(NNO)ZnOEt] = 7 mM. First spectrum (bottom) obtained 1 second after mechanical stop, and every subsequent spectra obtained every 5 seconds. 227

List of Schemes

Scheme 1.1. Coordination-insertion mechanism by metal-alkoxide initiators for the ROP of cyclic esters (e.g., ε-caprolactone, shown). 10

Scheme 1.2. Proposed mechanism for ROP of LA by $InCl_3$, BnOH, and NEt_3 initiating system generated in situ. 16

Scheme 1.3. Coordination insertion mechanism for ROP of cyclic esters by metal alkoxide initiators, expanded to describe coordination and insertion events, and their respective rate constants, K_{eq} and k_2. 18

Scheme 1.4. General decarbonylation reaction. 22

Scheme 2.1. Synthesis of ligands and complexes examined in this chapter. 34

Scheme 2.2. Proposed mechanism for CL polymerization by Al complexes. 37

Scheme 2.3. Proposed mechanisms for binding of CL to catalysts 1-3. 52

Scheme 2.4. Proposed binding of pyridine to complex 1 57

Scheme 4.1. Proposed decarbonylation mechanism. 125

Scheme 5.1. Catalytic decarbonylation of carboxylic acids to alkenes. 156

Scheme 5.2. Catalytic decarbonylation of hydrocinnamic acid to styrene using pivalic anhydride as an additive. 156

Scheme 5.3. Proposed mechanism of Ni-catalyzed decarbonylation. 169

List of Equations

Equation 1.1 8
Equation 1.2 9
Equation 1.3 14
Equation 1.4 14
Equation 1.5 18
Equation 1.6 19
Equation 2.1 37
Equation 2.2 37
Equation 2.3 39
Equation 2.4 39
Equation 2.5 39
Equation 2.6 39
Equation 2.7 45
Equation 2.8 68
Equation 2.9 68
Equation 2.10 69
Equation 2.11 69
Equation 3.1 78
Equation 3.2 81
Equation 3.3 86
Equation 3.4 86
Equation 3.5 86
Equation 3.6 86

List of Abbreviations

PLA	Polylactide
LA	Lactide
ROP	Ring-opening polymerization
$Đ$	Molecular weight distribution or dispersity
$Sn(Oct)_2$	Tin(II) bis(2-ethylhexanoate)
PCL	Polycaprolactone
CL	ε-Caprolactone
M_n	Number average molecular weight
p	Percent monomer conversion
$\bar{v}$	Kinetic chain length
M_w	Weight average molecular weight
N_n	Number average degree of polymerization
$[M]_0$	Initial monomer concentration
$[M]_t$	Monomer concentration at time = t
$L_nM–OR$	Single site metal alkoxide initiator
OMe	Methoxide/methoxy
^1H NMR	Proton nuclear magnetic resonance
T_m	Melting temperature
Me	Methyl
i-Pr	*iso*-Propyl
O*i*-Pr	*iso*-Propoxide
$N(SiMe_3)_2$	Bis(trimethylsilyl)amide
CH_2Cl_2	Methylene chloride or dichloromethane
k_p	Second order rate constant for polymerization
k_{obs}	Pseudo-first order rate constant for ROP
BnOH	Benzyl alcohol
NEt_3	Triethylamine
CD_2Cl_2	Deuterated dichloromethane
K_{eq}	Equilibrium constant
k_2	Rate constatnt for alkoxide insertion
ATRP	Atom-transfer radical polymerization
RAFT	Reversible addition-fragmentation chain-transfer polymerization
TON	Turnover number
PPh_3	Triphenylphosphine
DMPU	1,3-Dimethyltetrahydro-2(1*H*)-pyrimidinone
NO_2	Nitro
NMe_2	Dimethylamino
NH_2	Amino
PGSE	Pulsed gradient spin echo
t-Bu	*tert*-Butyl
K_M	Michaelis constant
V_{max}	Maximum reaction velocity

RPKA	Reaction progress kinetic analysis
δ	Chemical shift
Δδ	Chemical shift difference
Å	Angstroms
σ_p	Hammett *para* parameter
$\Delta H^{\ddagger}$	Enthalpy of activation
$\Delta S^{\ddagger}$	Entropy of activation
$\Delta G^{\ddagger}$	Gibbs free energy of activation
ρ	Reaction constant, sensitivity constant, slope of line in Hammett plot
ΔH^{o}	Standard enthalpy
ΔS^{o}	Standard entropy
ΔG^{o}	Standard Gibbs free energy
VT	Variable temperature
T_c	Coalescence temperature
pyr	Pyridine
d	Doublet
s	Singlet
m	Multiplet
t	Triplet
dq	Doublet of quartets
app d	Apparent doublet
DFT	Density functional theory
EWG	Electron withdrawing group
K	Kelvin
°C	Degrees Celsius
M	Molarity, moles per liter
MeOH	Methanol
sec/s	Second
h	Hour
PES	Potential energy surface
TS	Transition state
kcal	Kilocalories
mol	Mole
Ac_2O	Acetic anhydride
n-Bu	*normal*-Butanol
Piv_2O	Pivalic anhydride
GC-MS	Gas chromatography-mass spectrometry
DPEphos	Bis[(2-diphenylphosphino)phenyl] ether
DPPE	1,2-Bis(diphenylphosphino)ethane
DPPP	1,3-Bis(diphenylphosphino)propane
Xantphos	4,5-Bis(diphenylphosphino)-9,9-dimethylxanthene
g	grams
mol%	Mole percent
p-TsOH	*para*-Toluenesulfonic acid

PivOH	Pivalic acid
TLC	Thin-layer chromatography
BIMP	Bis(aminomethyl)phenol
POI	Phenoxyimine
PhBI	Phenyl bis(imine)
PyrBI	Pyridyl bis(imine)
ADI	α-Diimine
bipy	Bipyridine
TMEDA	Tetramethylethylenediamine
N-MI	*N*-Methylimidazole
DME	Dimethoxyethane
MeCN	Acetonitrile
OTf	Triflate
OAc	Acetate
acac	Acetylacetonate
$P(Cy)_3$	Tricyclohexylphosphine
$P(OPh)_3$	Triphenylphosphite
IMes	Bis(2,4,6-trimethylphenyl)-imidazol-2-ylidene
IPr	Bis(2,6-di-*iso*-propylphenyl)-imidazol-2-ylidene
DPPB	1,4-Bis(diphenylphosphino)butane
Phen	Phenanthroline
DPPF	1,1′-Bis(diphenylphosphino)ferrocene
Davephos	2-Dicyclohexylphosphino-2′-(*N*,*N*-dimethylamino)biphenyl
COD	1,4-Cyclooctadiene
THF	Tetrahydrofuran
mL	Milliliters
μL	Microliters
GC	Gas chromatography
$CHCl_3$	Chloroform

1 Two Approaches Towards the Development of Sustainable Polymers

1.1 Overview

"Everything's plastic, we're all going to die sooner or later, so what does it matter."

– Elizabeth Wurtzel, *Prozac Nation*, 1994

Elizabeth Wurtzel's quote stands out in her autobiographical novel *Prozac Nation*, portraying her quite dim outlook toward her future and the future of her peers. That she ties the notion of "everything" being plastic into this depressed worldview highlights general negative attitudes to the pervasiveness of plastics in our daily lives. Certainly, Wurtzel is correct that plastics are a critical part of modern, daily life. Additionally, one could argue that she has a negative reaction to plastics for good reason - plastic materials permeate society, filling landfills (only approximately 9% of plastic waste was recycled in 2012[1]) and oceans where they do not degrade and can affect various ecosystems. The majority of these materials are derived from oil, which is diminishing in availability and subject to volatile price fluctuations, and it is often damaging to the environment to transform chemicals into plastics.[2]

However, even though "we're all going to die", "it" does indeed "matter". This is inherently the core of the concept of sustainability: meeting the needs of the present without compromising the ability of future generations to meet their own needs.[3] The current state of the way we produce and dispose of plastic materials is unequivocally unsustainable. Upending the status quo is a growing and continued challenge in polymer science; societies' dependence on inexpensive, high-performance, and convenient plastic products demands development of sustainable alternatives.

Plastics exhibit a wide range of material properties, from hard to tacky, tough to elastic, and soft to extremely strong. The characteristics of products like adhesives,

protective eyewear, and bicycle tires are due to the development of polymers from petrochemical monomers over the past century. Many monomers have been developed from petrochemicals, and their corresponding polymers (and many types of copolymers) have been creatively developed to produce desirable properties for nearly every application. As a result, it is impossible to imagine that a single monomer derived from renewable resources could supplant the wide variety of polymers in use today, requiring the need for development of new monomers and polymers.

A variety of approaches have already been taken to develop renewable polymers. For example, significant research has gone into manipulating the properties of biopolymers like cellulose and starch for use in commodity materials, which have a history of use ranging back to celluloid and cellulose acetate in the late 19th and early 20th centuries.[4] Additionally, using microbes or genetically altered plants to make polymers directly (like polyhydroxyalkanoates) has found some commercial interest, as well as using amino acids as monomers. However the most common approach involves either chemical or enzymatic transformation of the raw materials derived from plants (like glucose, terpenes, or vegetable oils) into monomers and their respective polymers.[5] Common to all of these approaches is the aim to develop bio-derived (and potentially biodegradable) materials that will replace petroleum-based plastics.

Development of bio-based plastics can be generally put into two categories: (1) synthesis of brand new monomers (or polymers) from renewable resources and (2) new preparations of already known petrochemical monomers (or polymers) from renewable resources. Progress in both strategic directions is necessary to address the dependence on petroleum-based plastics. New monomers are critical to create degradable and safe materials, since current monomers often lack these properties. However, ignoring current monomers also ignores the decades of research carried out to optimize their polymer

properties – instead, tapping into this knowledge by redeveloping these monomers from a renewable resource allows for continued use of these monomers, polymers, and their properties in the future.

A prominent class of new renewable monomers is cyclic esters, or lactones. These monomers have gained particular interest for a variety of reasons. They are obtained often from fermentation of the sugars in biomass, they are degradable, and their polymers exhibit a wide range of physical and mechanical properties depending on the size of and substituents on the lactone ring. The most successful commercial example is poly(lactide) (PLA); it is made from lactide (LA), the cyclic ester dimer of lactic acid. PLA is compatible in biological tissue, biodegradable, and compostable.

PLA and other polyesters made from lactones are typically synthesized through ring-opening polymerization (ROP) – a process that involves use of an initiator, which is often metal-containing. Many metal catalysts have been developed, and they typically contain a Lewis-acidic metal (e.g., Zn, Al, Y, Sn, and Ti), an ancillary, supporting ligand, and an initiating group (often alkoxides, but others have been studied). ROP by metal initiators is considered "living", affording control over the polymer molecular weight to yield polymers of narrow molecular weight range ($Đ < 1.1$). Despite many years of studying a wide variety of initiators, it is typically not well understood why different initiators yield different rates of polymerization. Understanding why initiators operate at different rates will enable development of sound design rules for new initiators useful for improving polymerization methods of already known monomers, or facilitating polymerization of currently undeveloped monomers. Chapters 2 and 3 in this thesis describe our efforts to develop such understanding through detailed kinetics studies.

Development of new monomers requires significant basic research into many aspects of polymer science. Not only does the chemistry to synthesize the monomer and

polymer have to be optimized, but also the polymer's material properties must be fundamentally understood in order to appropriately develop it for commercial application. This iterative process can be quite time intensive, and often requires implementation of entirely new markets for these brand new polymers, potentially presenting an economic barrier to commercial development.[6] A parallel track of developing current petrochemical monomers (olefins) is quite attractive from a commercial perspective; the monomers are identical to those currently used, allowing the same polymerization methods to be used to generate polymers with identical material properties to their petrochemical-based counterparts. Additionally, having alternative routes from biomass to these monomers will be critical when production of these monomers from oil becomes prohibitively expensive due to dwindling worldwide oil supplies.

In order to obtain renewable olefins, biomass needs to be catalytically deoxygenated, since biomass has a much higher oxygen content compared to oil. Obviously, developing strategies to deoxygenate biomass or biomass-derived chemicals is critical to obtaining olefin monomers. Ideally, these strategies would be catalytic and selective, affording targeted olefin products with low catalyst loadings, low temperatures, functional group tolerance, high yields, and high selectivity. Using catalytic methods to synthesize these monomers is also in keeping with the principles of Green Chemistry, which is becoming a more and more important set of rules to judge old and design new processes. Expanding the current suite of catalytic methods for synthesis of "old" monomers from renewable resources will enable the continued use of these monomers in the future. Chapters 4 and 5 of this thesis describe our work toward this goal.

In summary, this thesis describes dual efforts to (a) understand the mechanism of cyclic ester polymerizations by metal-alkoxide catalysts, and (b) to develop new routes to

useful olefin monomers from biomass-derived feedstocks. Through both approaches, inroads in replacing petrochemical plastics with renewable alternatives are made.

1.2 Cyclic Ester Polymerization

1.2.1 Introduction

As described in the previous section, cyclic esters are becoming a common class of bio-based monomers, especially with the commercialization of PLA in recent years.[7] In the United States, LA is derived from the biological fermentation of glucose found in corn.[8] After purification, LA is polymerized to PLA using an initiator (tin(II) bis(2-ethylhexanoate, $Sn(Oct)_2$, is commercially used) via ROP.[7] PLA is used in a variety of products, ranging from disposable packaging, silverware, cups, and fibers, and these products are both recyclable and compostable.[9–11] Another unique feature of PLA is that it is biocompatible, and it is used in surgical applications and time-released drug delivery systems.[12–14]

While LA has garnered much attention, it is not the only cyclic ester able to undergo ROP. Polycaprolactone (PCL, Figure 1.1) is also a degradable polyester, and while the monomer, ε-caprolactone (CL), is not made on the industrial scale from biomass, it has been demonstrated that it can be bio-derived.[15–17] Nonetheless it has desirable properties for commercial applications like oil and water resistance, and easy

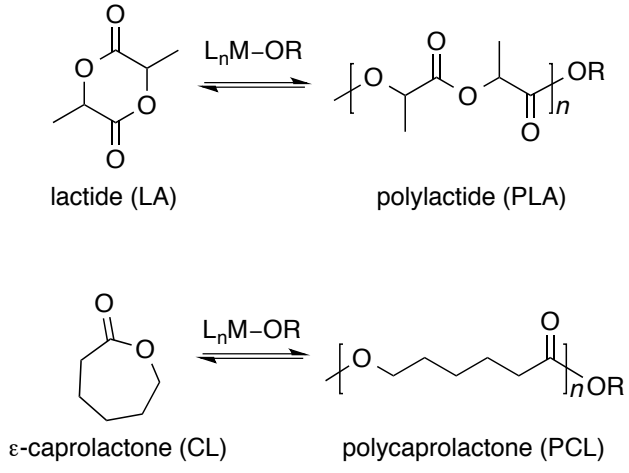

Figure 1.1. Monomers LA and CL and their respective polymers, PLA and PCL, from ROP.

thermal processing.[5] Other renewable and/or degradable lactone monomers like menthide, [18 – 20] carvomenthide, [21 , 22] glycolide, [23] β-butyrolactone, [24 , 25] and δ-valerolactone[15,16] have been developed and successfully polymerized and co-polymerized using ROP to polymers with a wide variety of material properties.

1.2.2 Metal-Catalyzed Ring-Opening Polymerization

The ROP of cyclic esters can be carried out by many types of initiator/catalyst combinations, i.e., anionic,[26–29] cationic,[30–32] nucleophilic/organocatalysts,[33–37] and metal-based systems. This introduction and Chapters 2 and 3 focus entirely on metal-based initiators, and readers interested in other initiators not presented here are directed to useful review articles.[15,16,23,38–41]

No matter which initiator is used to carry out the ROP of cyclic esters, ROP is characterized by being a controlled, or living, polymerization.[23] A living polymerization is defined as "a chain-growth process for which there are no irreversible termination or transfer reactions".[42] Living polymerization processes typically exhibit a low dispersity ($Đ$), and a linear relationship between number average molecular weight (M_n) and both percent monomer conversion, p (Equation 1.1) and kinetic chain length, $\bar{\nu}$ (Equation 1.2). The dispersity is a measure of the width of the molecular weight distribution, equal to the weight average molecular weight divided by the number average molecular weight (M_w/M_n). Kinetic chain length is defined as the ratio between the number of monomers consumed ($[M]_0 - [M]_t$) to the number of polymer chains (i.e., number average degree of polymerization, N_n). Without termination or transfer reactions, the total number of polymer chains is equal to the initial concentration of the monofunctional initiating species, $[I]_0$.

Equation 1.1

$$p = \frac{[M]_0 - [M]_t}{[M]_0}$$

Equation 1.2

$$\bar{v} = N_n = \frac{[M]_0 - [M]_t}{[I]_0}$$

If a linear relationship exists by either holding $[M]_0/[I]_0$ constant and measuring M_n as a function of p, or by varying $[M]_0/[I]_0$ and measuring M_n has a function of N_n, combined with low dispersities, then the polymerization is likely living.[42] By varying the monomer to initiator ratio, polymers with a variety of molecular weights can be accurately targeted and acquired with a narrow molecular weight distribution ($Đ \leq 1.2$). Ensuring that initiator and catalyst systems operate in a controlled manner is crucial for targeting a specific molecular weight for an application, successful synthesis of block polymers, and facile study of the mechanistic details of ROP (for a given initiator).

Typical metal initiators are well controlled, and numerous metals, ranging across the periodic table, have been studied for the ROP. Some of the simplest and most effective metal-containing initiators are metal alkoxides. Typically, metal alkoxides derived from Lewis acidic metals like aluminum,[43] zinc,[23,44,45] lanthanum,[46] samarium,[46] yttrium,[46, 47] calcium,[48] germanium,[49] tin(II),[50] tin(IV),[51, 52] and iron[53] are employed. However, while these simple metal alkoxides are able to polymerize cyclic esters, they often suffer from poor control over the polymerization by facilitating transesterification reactions, aggregation of metal sites, and enhanced sensitivity to hydrolysis, which can introduce new initiating sites, eroding the dispersity and control.

In an effort to exert more control over the polymerization, discrete, single-site catalysts for the ROP of cyclic esters have been developed. Generally, these complexes consist of an ancillary ligand (L_n) and a single initiating group (often an alkoxide, OR) both bound to a metal center (M). The ancillary ligand prevents aggregation of metal sites, and tunes the electronics of, or sterics around, the metal center to optimize the polymerization. A general formula for a single-site metal initiator is $L_nM–OR$.

Whether the metal-based initiator is single-site or not, they all are thought to follow a similar coordination-insertion mechanism for the ROP of cyclic esters (Scheme 1.1). The coordination-insertion mechanism involves coordination of the carbonyl oxygen on the monomer to an open coordination site on the metal, followed by insertion

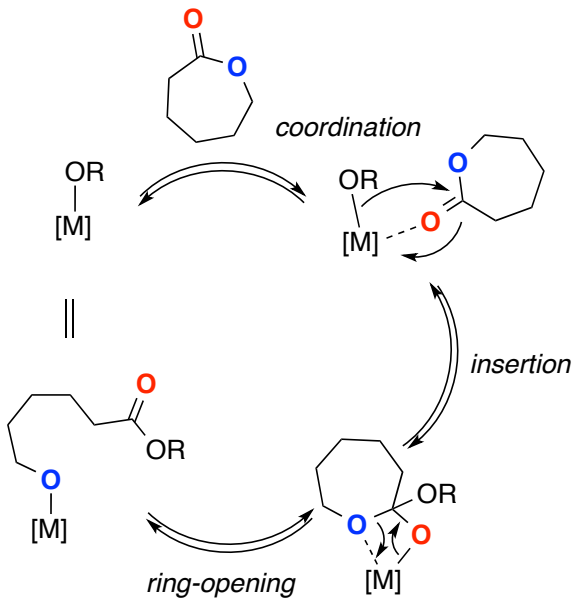

Scheme 1.1. Coordination-insertion mechanism by metal-alkoxide initiators for the ROP of cyclic esters (e.g., ε-caprolactone, shown).

of the metal-bound alkoxide into the carbonyl carbon of the monomer. This generates a tetrahedral ortho-alkoxide intermediate, which collapses to break the acyl-oxygen bond and open the lactone ring. The newly opened ring is now a new metal alkoxide species, and additional monomers can be incorporated in a similar fashion, elongating the polymer chain.

As in the case for clustered metal alkoxides, many different metals have been used for the ROP of cyclic esters by single-site initiators; however, some of the best studied are those containing aluminum, zinc, and magnesium, with other metals like tin, titanium, indium, calcium, sodium, yttrium, and scandium also having been used.[23,25]

For example, one of the most thoroughly studied initiators for the ROP of LA is an aluminum alkoxide complex bearing a chiral binaphthyl-salen ligand (Figure 1.2,

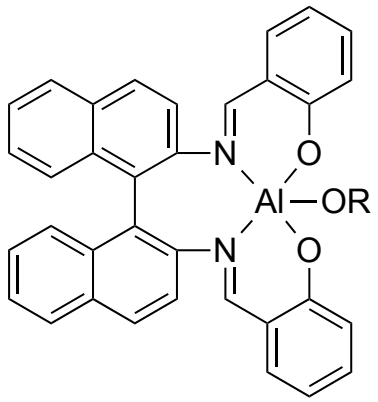

[(SalBINAP)AlOR]
R = Me, *i*-Pr

Figure 1.2. Aluminum binaphthyl-salen alkoxide initiator for the ROP of LA.

shown as racemate). Studied in both the enantiopure (*R*) and racemic forms, this initiator ([(SalBINAP)AlOR]) is thought to polymerize LA through the coordination-insertion mechanism presented in Scheme 1.1. By examining the end group of low molecular weight polymer samples obtained from the polymerization of LA by [(SalBINAP)AlOMe], it was confirmed that ring-opening occurs through the acyl-oxygen by the presence of –OMe resonances in the proton nuclear magnetic resonance (^{1}H NMR) spectrum of the polymer.[54] Additionally, the molecular weight of the polymer increases linearly with conversion and the obtained polymers have low $Đ$ (1.05–1.1), as expected for a living polymerization without transesterification. Most interesting are the thermal properties of the resulting PLA isolated from the racemic initiator and racemic LA – the T_m ranged from 179 °C to 191 °C – nearly 10 to 20 °C higher than for enantiopure PLA.[54–57] The high melting point implies a stereoblock structure along the polymer chain. Indeed, these initiators have been shown to preferentially polymerize one enantiomer of

LA over the other (the ratio of rate constants for polymerization of D- and L-LA is approximately 20[54]), but polymer chains can exchange between enantiomers of the initiator, resulting in a stereoblock structure rather than two discrete stereopure chains.[57] Kinetic analysis indicates that the rate of polymerization is first-order in both monomer and initiator.

Another family of initiators that have been studied for the ROP of LA are based on a β-diiminate ligand with various metals (Figure 1.3, zinc,[58–60] magnesium,[59,60,61] tin,[62] and calcium[63]). All are thought to proceed through the coordination-insertion mechanism,

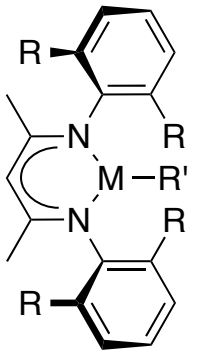

M = Zn, Mg, Sn, Ca
R = *i*-Pr
R' = O*i*-Pr, $N(SiMe_3)_2$

Figure 1.3. β-Diiminate initiators for the ROP of LA.

due to the observation of the R′ initiating fragment at the polymer chain ends, indicative of acyl-oxygen cleavage. All except Mg exhibit narrow molecular weight distributions ($Đ$ < 1.2), and have linear relationships between molecular weight and conversion characteristic of living polymerizations, with experimental molecular weights in line with the theoretical molecular weights expected for a single-site initiator. The Mg initiator is the most rapid and least well controlled ($Đ$ = 1.59), but addition of *iso*-propanol to the polymerization results in a much more controlled (1.20 < $Đ$ < 1.35) process.[59] The rates of polymerization roughly follow the electropositivity of the metal center, Mg > Zn > Ca

> Sn, which is postulated to be due to enhancement of the coordination step of the mechanism. For the Zn-containing analogue, in contrast to the [(SalBINAP)AlOR] system, the rate of polymerization was determined to be first order in monomer and fractional order in Zn (1.56). While the origin of the fractional order is unknown, it is thought to be due to aggregation of metal species during the polymerization.[59]

1.2.2.1 Kinetics to Study Mechanism

As alluded to in the previous section, in addition to end group analysis and molecular weight control studies, one of the major ways that catalysts are characterized is through kinetic analysis of the polymerization. Kinetic analyses are most useful in those cases where the initiator is "well-behaved" – meaning it is involved in minimal transesterification reactions and termination reactions, ensuring a living polymerization. Thus, kinetic analyses tend to go hand in hand with other methods of studying ROP, but are often the last point of investigation. However, studying reaction kinetics provides insight into mechanism that can often not be obtained otherwise. Therefore, it can be a powerful tool in understanding reaction mechanism and reaction pathways.[64,65]

In a typical analysis of ROP kinetics by single-site metal alkoxide catalysts, a solution polymerization (e.g., in CH_2Cl_2 or toluene) is carried out at relatively low concentrations of monomer ($[M]_0$ < 1.0 M), and usually a fixed, low, monomer to initiator ratio (e.g., 50:1). The simplest mechanism one can imagine to describe an ideal living polymerization such as the ROP of cyclic esters is a second-order reaction (each substrate is first order, Figure 1.4, top) between monomer and initiator to generate polymer in a single step, with a single second order rate constant, k_p, with a rate equation as in Equation 1.3. In the absence of transfer or termination reactions, this is generally a reasonable assumption.

Equation 1.3

$$-\frac{d[M]}{dt} = k_p[I][M]$$

Equation 1.4

$$-\frac{d[M]}{dt} = k_{obs}[M]$$

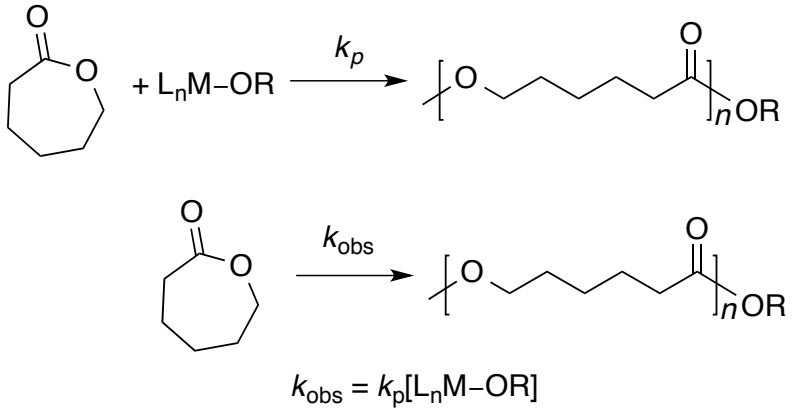

Figure 1.4. Kinetic schemes typically assumed in the ROP of cyclic ester by single site metal complexes. Top: second order reaction; bottom: pseudo-first order reaction.

Finally, because the concentration of initiator is small and unchanging compared to the concentration of monomer (often $50 < [M]_0/[I]_0 < 500$ for kinetic studies), a kinetic flooding situation can be assumed. This assumption simplifies the rate expression to pseudo-first order (Figure 1.4, bottom, Equation 1.4), with a new pseudo-first order rate constant k_{obs}. This rate constant may be expressed as the product of the second order rate constant, k_p, and the concentration of initiator. Simplification of the rate expression in this manner greatly streamlines collection and analysis of kinetic data. In order to obtain k_p, many polymerizations can be run, varying the initial concentration of metal initiator, and plotting k_{obs} vs. [L_nM–OR]. A linear fit with a zero intercept signifies adherence to the

proposed second order rate law, and the slope of the linear fit is a measure of k_p (Figure 1.5).[66]

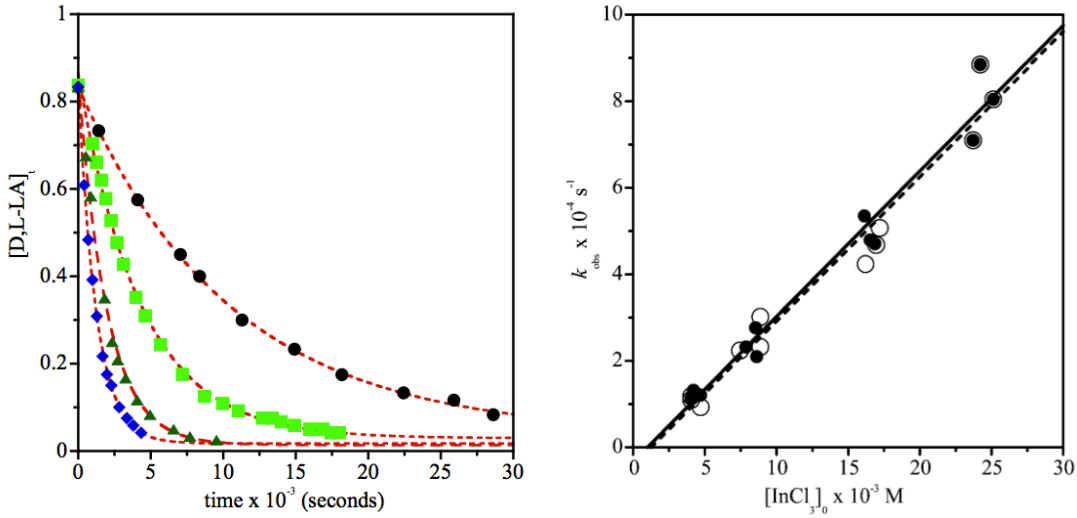

Figure 1.5. Representative example of the kinetic treatment typically applied to study the ROP of cyclic ester. $[LA]_0$ = 0.84 M, $[BnOH]_0$ = 25 mM, $[NEt_3]$ = 50 mM, 21 °C, CD_2Cl_2. Left: illustrative kinetic data for polymerization of LA using various concentration of $InCl_3$ with fits to the first order decay equation $[LA]_t = [LA]_0\exp(-k_{obs}t)$. $[InCl_3]_0$ = 4.7 mM (black), 8.5 mM (light green), 16.1 mM (dark green), 23.7 mM (blue). Right: kinetic plot of k_{obs} vs. $[InCl_3]_0$ for the polymerization of LA (same data as in right plot). Closed circles denote constant values for $[BnOH]_0$ and $[NEt_3]_0$ as above, open circles represent a constant ratio of NEt_3:BnOH:$InCl_3$ = 2:1:1.

A representative example is presented in Figure 1.5 (data taken from reference 66). In this case, a simple initiator system comprised of indium trichloride, benzyl alcohol (BnOH), and triethylamine (NEt_3), was studied for the ROP of LA. In Figure 1.5, left, the first order decay of the monomer LA was monitored by ^{1}H NMR spectroscopy to at least four half lives, and the subsequent decay profile was fit to a first order decay equation to extract a value for k_{obs}, the pseudo-first order rate constant. This was done for four different concentrations of $[InCl_3]_0$, and the obtained k_{obs} values were plotted against their $[InCl_3]_0$ concentrations to obtain a linear fit with a slope of k_p. In addition to obtaining values for k_p, the authors were able to determine the orders in the reagents using this plot;

a linear, positively correlated relationship between k_{obs} and $[InCl_3]_0$ also indicates that the reaction is first-order in $InCl_3$. Similar processes can be carried out for BnOH and NEt_3 to

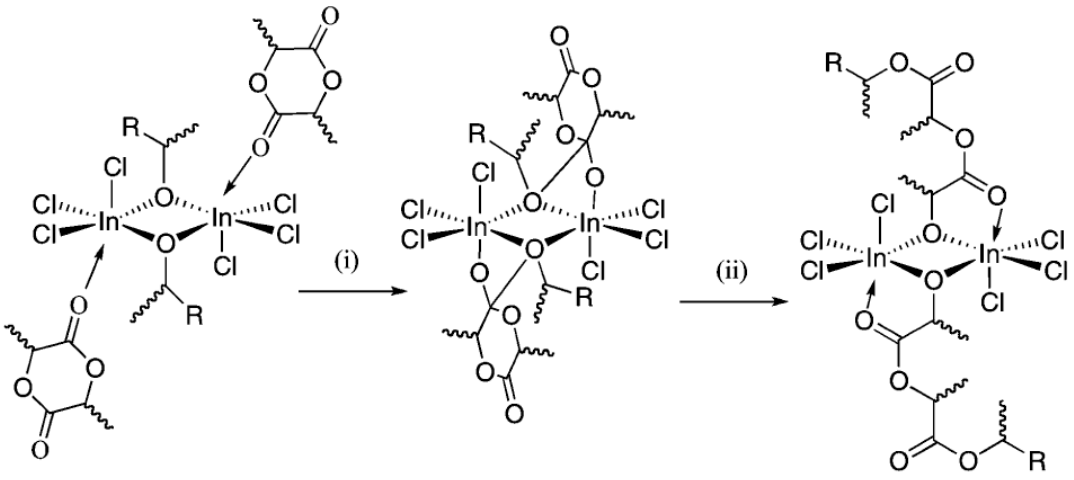

Scheme 1.2. Proposed mechanism for ROP of LA by $InCl_3$, BnOH, and NEt_3 initiating system generated in situ.

determine their orders – in this case, both plots of k_{obs} vs. $[BnOH]_0$ and $[NEt_3]_0$ showed no correlation between concentration and the pseudo-first order rate constant (i.e., they are flat, horizontal lines), indicating a rate law of the form: $-d[LA]/dt = k_p[InCl_3][LA]$ for this system. Using this form of the rate law, and other experimental evidence, the authors were able to formulate a supposed mechanism for polymerization where in situ generation of the initiator complex is rapid, and a dimeric form of the initiator is responsible for ROP (Scheme 1.2).

This type of kinetic analysis is quite useful. Not only is it relatively simple, but also it enables quantitative comparison of initiator efficiencies for the ROP of a particular monomer. For example, Table 1.1 contains a range of k_p values determined for various catalysts for the ROP of LA (structures in Figure 1.6).[67–70]

Table 1.1. k_p values for various initiators for ROP of LA.

Initiator	k_p ($M^{-1}s^{-1}$)	Temp. (°C)	Reference
$InCl_3$/BnOH/NEt_3	0.3	21	66
[{(NNO)InCl}$_2$(μ-OEt)(μ-Cl)]	0.56	25	67
[L_1ZnOEt]	2.2	25	68
[CysalenAlO*i*-Pr]	0.00015	70	69
Al(O*i*-Pr)$_3$	0.01	70	70

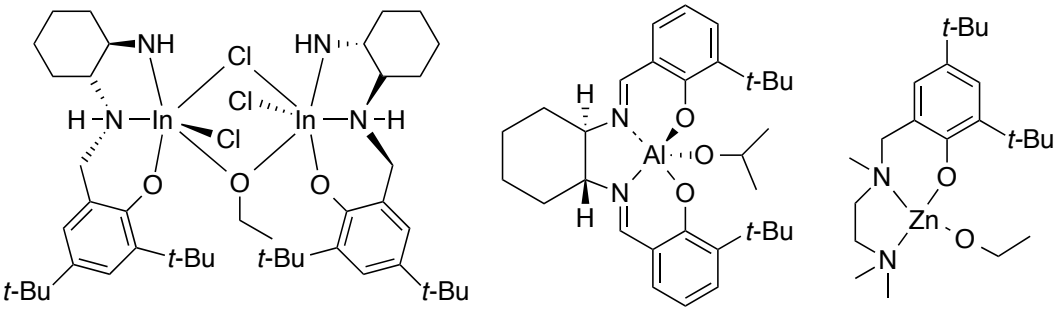

Figure 1.6. Structures of initiators mentioned in **Table 1.1**.

From the values in Table 1.1, it is clear that there is a wide disparity between initiators and the value for k_p. The initiator with the highest rate (largest k_p), is the monomeric [L_1ZnOEt] initiator, while the lowest rate clearly belongs to the cyclohexyl-bridged aluminum salen initiator. The others fall in between these in terms of rate, as do many polymerization initiators developed. It is useful to note that the pseudo-first order rate constant k_{obs} is also a useful parameter to compare initiators, but only at the same $[I]_0$, which is often done when studying many initiators in a similar manner and under identical conditions.

However, while k_p allows initiators to be compared to one another in terms of rate, it provides little insight into why these differences exist from a mechanistic perspective. This arises because the second order rate constant k_p is a composite rate constant describing all the elementary steps of the polymerization mechanism. As a

result, kinetic information about the individual steps, like coordination of monomer and alkoxide insertion, cannot be obtained from this single rate constant. Clearly, metal identity and ligand structure both play roles in affecting the polymerization rate, but the key questions are which mechanistic steps do these parameters influence – coordination of the monomer to the metal center, alkoxide insertion into the bound monomer, or both? By understanding how the initiator structure influences polymerization rate, novel initiators can be designed rationally to optimize for activity and selectivity.

In Chapters 2 and 3, attempts to answer this question using detailed kinetic analysis are made by expanding the traditional rate equation from a single rate constant k_p to a description of the polymerization that includes reversible coordination of monomer (M) to the metal alkoxide initiator (I), described by K_{eq}, and irreversible alkoxide insertion, described by k_2 (Scheme 1.3). The rate equation to describe this expanded mechanism is the traditional Michaelis-Menten equation often used for enzyme kinetics (Equation 1.5).

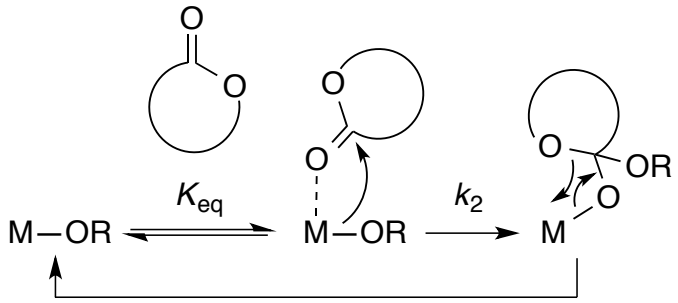

Scheme 1.3. Coordination insertion mechanism for ROP of cyclic esters by metal alkoxide initiators, expanded to describe coordination and insertion events, and their respective rate constants, K_{eq} and k_2.

Equation 1.5

$$-\frac{d[M]}{dt} = \frac{k_2[I][M]}{1/K_{eq} + [M]}$$

In order for Equation 1.5 to apply to the mechanistic scheme, [*M*] must be greater than $1/K_{eq}$, otherwise, Equation 1.5 simplifies to Equation 1.6 – a variation of Equation 1.3, where $k_p = k_2K_{eq}$.

Equation 1.6

$$-\frac{d[M]}{dt} = k_2K_{eq}[I][M]$$

Thus, the key requirement for observing Michaelis-Menten saturation behavior is to study the kinetics of ROP at sufficiently high initial concentrations of monomer. As mentioned previously, studying the kinetics of ROP of cyclic esters typically is carried out with $[M]_0 < 1$ M, which apparently is not a high enough $[M]_0$ to observe rate saturation (as simple first order fits to the data suffice). While this mechanistic scheme (Scheme 1.3) and new rate law (Equation 1.5) are a straightforward expansion of the usual rate law (Equation 1.3), measuring the kinetics of ROP at high enough initial concentrations of monomer to see saturation behavior is a new endeavor. Chapters 2 and 3 describe whether these experimental conditions of high $[M]_0$ and kinetic analyses can be applied to the ROP of cyclic esters, and if they can, what mechanistic insights, coupled with theoretical calculations performed by researchers in Prof. Christopher C. Cramer's group at the University of Minnesota, Twin Cities, they can provide about how monomer coordination and alkoxide insertion are affected by ligand architecture and electronic environment.

By having a clearer understanding of the variables that affect initiator performance for the ROP of cyclic esters, the development of new initiators will be expedited. Instead of designing initiators with limited knowledge of how variables like metal identity and ligand architecture influence polymerization efficiency, initiators can be designed rationally *and* rationally chosen by synthetic polymer chemists to polymerize monomers, which either have already been developed or have yet to be developed.

1.3 Decarbonylation of Bio-Derived Carboxylic Acids

1.3.1 Introduction

While PLA has become an important sustainable plastic and much research is devoted to extending the applications of PLA, it is unfeasible to envision PLA as a replacement for every petrochemically derived plastic due to the wide variety of properties that commercial plastics have. It is of utmost importance to develop biorenewable plastics with a broad range of physical attributes. In order to achieve this end, we need access to a versatile array of building blocks from which to construct polymers.

Nature produces approximately 170 million metric tons of biomass a year, consisting of terpenes, vegetable oils, lignins and sugars.[71] Terpenes and vegetable oils provide a large number of valuable chemicals, and much research has been focused on transforming lignin into useful fine chemicals, but they comprise the smallest proportion of biomass. Sugars, or carbohydrates, make up approximately 75% of biomass, and only approximately 3−4% is actually utilized for food or non-food applications.[72] The majority of carbohydrates that come from biomass are five- or six-carbon sugars, and can be transformed into other useful compounds by either fermentative or chemical methods.

If one looks at the compounds that can be derived from glucose alone, both by fermentation and chemical methods (Figure 1.7), carboxylic acids are a common functional group among these chemicals. Many of them are also identified by the U.S. Department Of Energy as among the Top 12 Value Added Chemicals from Biomass.[73] While there is much interest in the chemical transformations of these relevant molecules, methodologies for turning a carboxylic acid moiety into a terminal alkene are relatively unexplored. Not only do alkenes provide another point of functionalization, allowing

complexity to be grown from these molecules, terminal alkenes are commonly used for polymerization, and nearly all commercial polymers today are some type of polyolefin.

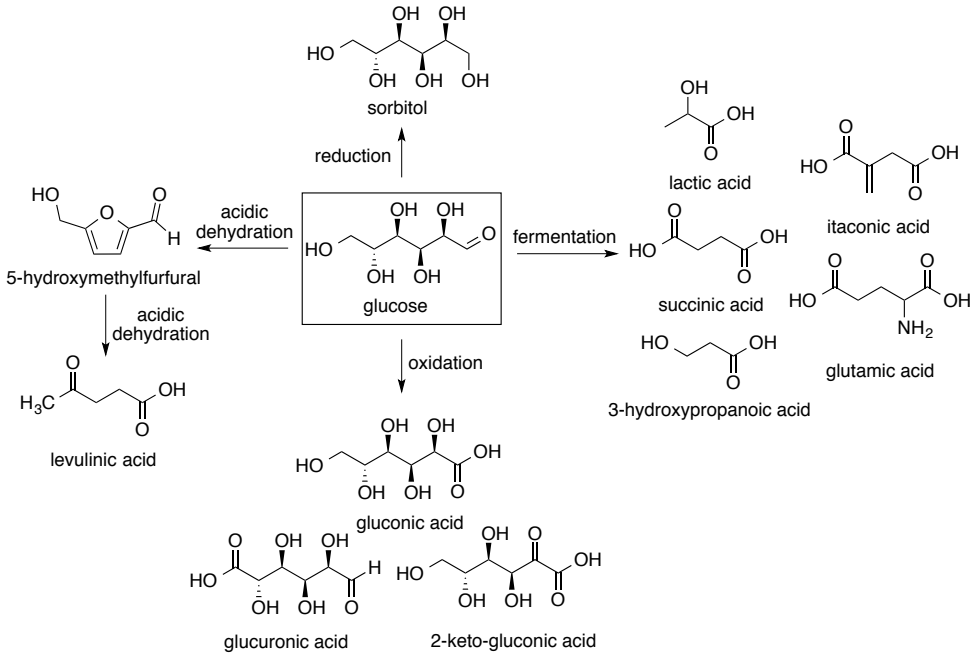

Figure 1.7. A representative group of the chemicals derived from either the fermentation or chemical transformation of glucose.

Synthesis of current petroleum-derived olefinic monomers from biomass would be quite useful for the reasons enumerated above. Utilizing similar polymerization methods like free-radical polymerization, anionic, cationic and other controlled polymerization techniques like atom-transfer radical polymerization (ATRP) and reversible addition-fragmentation chain-transfer polymerization (RAFT)[74] would allow for immediate penetration of these "new" bio-derived monomers into the marketplace.

1.3.2 Decarbonylation of Carboxylic Acids

Decarbonylation is the extrusion of a carbon monoxide from a molecule, which can be carried out with or without the removal of a β-hydrogen from the alkyl portion of the substrate, often in the form of water or acid (Scheme 1.4). Of particular interest are

those decarbonylation reactions that are coupled to β-hydrogen elimination, as those produce terminal alkenes, rather than alkane products. Aldehydes,[75,76] acyl halides,[77] and carboxylic acids have all been shown to undergo decarbonylation and elimination. In order to achieve decarbonylation and elimination, it is crucial that the alkyl chain consist of at least three carbons (including the carboxylic acid carbon) and that a hydrogen atom be present on the carbon chain β to the carboxylic acid, as this is the proton removed during the elimination step.[78]

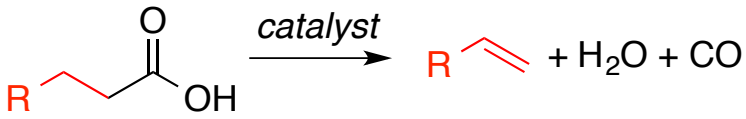

Scheme 1.4. General decarbonylation reaction.

Transition metal compounds are used to carry out the dehydrative decarbonylation (now referred to solely as "decarbonylation" for the remainder of this chapter and Chapters 4 and 5) of these carbonyl-containing compounds, and can be used either stoichiometrically or catalytically, but catalytic decarbonylation is most often studied and most desirable. Metals studied for this process are usually third-row transition metals like rhodium,[79–81] ruthenium,[77–79] and palladium,[80,82] but platinum, osmium, iridium,[78] nickel-tin pairs,[83] but more recently iron[84] and nickel[85,86] have also been used.

The decarbonylation of long chain fatty acids or short chain carboxylic acids has been explored to use the alkene products as fuels.[77–81,83] A first report for the decarbonylation of carboxylic acids (specifically stearic acid) uses tris-(diethyl-phenylphosphine)rhodium(III) chloride ($(Et)_2PhPRhCl_3$) as the catalyst.[80] The reaction is heated to 280 °C for 3 hours in neat stearic acid and low yields of the alkene heptadecene were reported. Moreover, under similar conditions, catalysts that are efficient for the decarbonylation of aldehydes and acyl halides, tris-(triphenylphosphine)rhodium(I) chloride ($(Ph_3P)_3RhCl$), rhodium trichloride and palladium(II) chloride were unsuccessful

for the decarbonylation of stearic acid. However, when bis-(triphenylphosphine)palladium(II) chloride ($(Ph_3P)_2PdCl_2$) or exogenous triphenylphosphine (PPh_3) was added to reactions with $RhCl_3$ or $PdCl_2$ (10:1:5 ratio acid to catalyst to phosphine) the yield of heptadecene increased to 26%, 25%, and 10%, respectively. The reaction can be pushed to completion by conducting the reaction with the $RhCl_3/PPh_3$ catalyst combination under a stream of nitrogen. Presumably, the nitrogen helps to drive the reaction to completion by removing volatile byproducts like carbon monoxide. Both the hydrated and anhydrous versions of $RhCl_3$ were used, and the hydrated catalyst yielded more heptadecene than the anhydrous version. Anhydrous $RhCl_3$ is likely polymeric, resulting in a less accessible metal for reaction. The highest turnover number (TON, moles of product formed per mole of catalyst used) observed was 250 for $RhCl_3$. However, a number of isomers of heptadecene were generated from the reaction. Ozonolysis studies showed that 1-heptadecene was produced, but 2- and 3-heptadecene were also present in the product mixture.

The active catalyst species is likely a carbonyl adduct of the rhodium-chloride-phosphine complex, as chlorocarbonyl[bis-triphenylphosphine]rhodium(I) ($(Ph_3P)_2Rh(CO)Cl$) was isolated from the reaction mixture and is also active for decarbonylation. The postulated mechanism for the reaction requires (1) the formation of a stearic anhydride, followed by (2) oxidative addition of the anhydride to four-coordinate rhodium(I), yielding an acyl-rhodium(III) bond and six-coordinate rhodium, then (3) loss of a ligand (either carbon monoxide or PPh_3) followed by (4) rearrangement to the six-coordinate rhodium(III) alkyl then (5) reductive elimination of stearic acid and the heptadecene, returning the rhodium(I) starting catalyst (Figure 1.8).[80] A similar mechanism can be envisioned for the Pd(II)/Pd(0) catalysts.

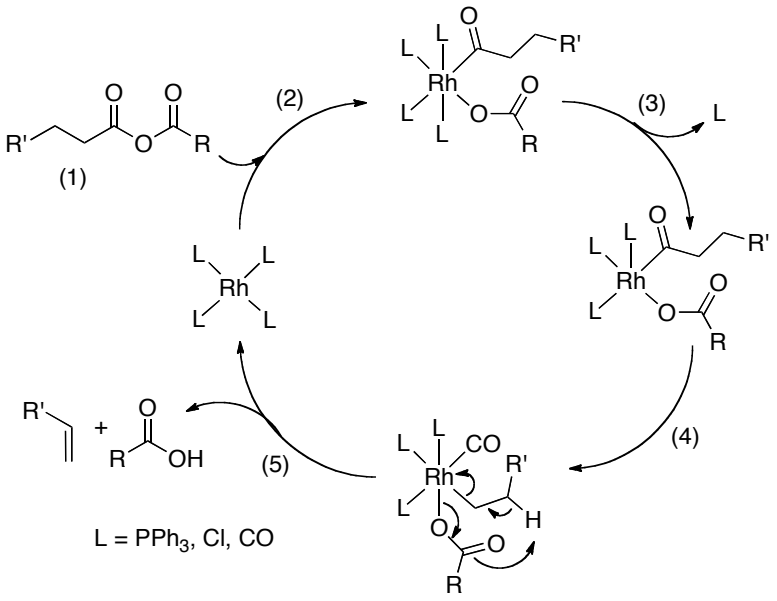

Figure 1.8. Proposed mechanism for the decarbonylation of carboxylic acids using rhodium and palladium.

Because the proposed mechanism for decarbonylation requires the formation of a symmetrical anhydride of the carboxylic acid, presumably to activate the carboxylic acid for oxidative addition, addition of an external anhydride would form a mixed anhydride system, which would likely undergo more facile decarbonylation. In fact, reaction with equimolar amounts of acetic anhydride and decanoic acid, $(Ph_3P)_2PdCl_2$ (0.01 mol% based on carboxylic acid) and PPh_3 (0.50 mol%, based on carboxylic acid) resulted in decarbonylation at a lower temperature (180 °C), shorter reaction time (45 min), 97% of 1-nonene as the product and TON of 12,370.[81] However, in order to ensure selectivity for the terminal olefin, the product must be distilled from the reaction mixture as it is made. Isomerization to internal olefins is likely due to interaction with the catalytic species. As a result, in order to obtain higher boiling point 1-alkenes, reactions must be carried out under reduced pressure in addition to high temperature.

Pivalic anhydride has also been shown to be successful in generating a mixed anhydride system with carboxylic acids capable of decarbonylation using Pd(II) catalysts.[87] Using phenylbutanoic acid as the substrate, as isomerization to the internal alkenes would be facile due to the formation of a stable benzylic alkene, a variety of Pd(II) sources and phosphine ligands were screened for their selectivity and activity of the decarbonylation to the terminal alkene 3-phenylpropene. Reactions were carried out at 110 °C, using a 2 equivalent excess of pivalic anhydride, 3 mol% Pd source and 9 mol% of the phosphine (based on carboxylic acid) for 16 hours.

Using $PdCl_2$ and PPh_3 in toluene, no alkene product was observed.[87] However, under the same conditions in the highly polar solvent 1,3-dimethyltetrahydro-2(1*H*)-pyrimidinone (DMPU), 27% of the target terminal alkene was observed. Reactions using different combinations of phosphine ligands and palladium sources (Figure 1.9) were

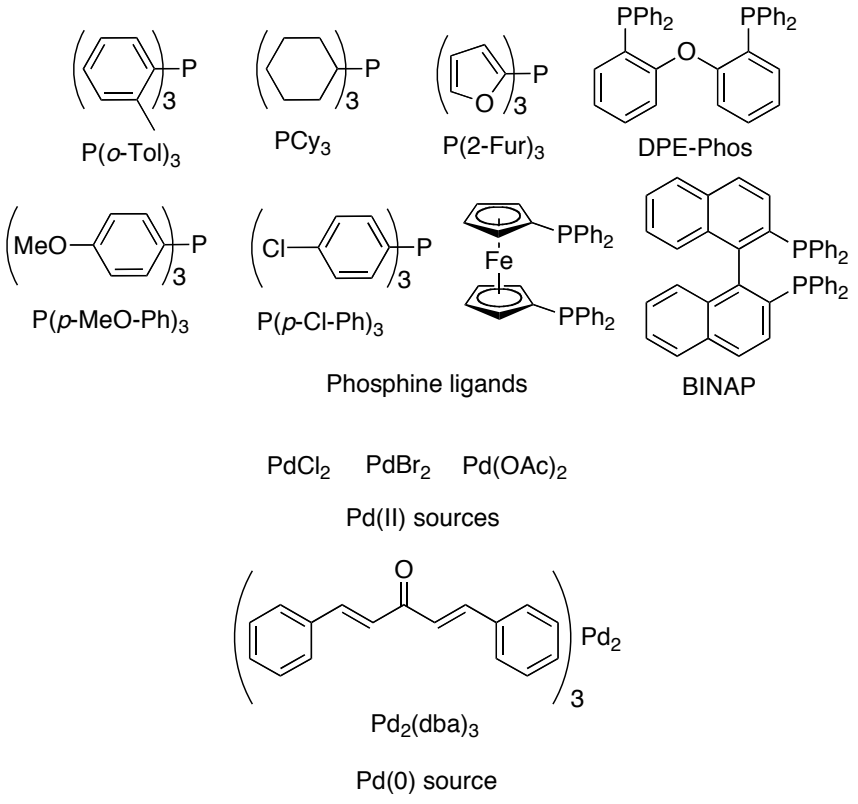

Figure 1.9. Phosphine ligands and palladium sources used for the decarbonylation of carboxylic acids.

conducted under similar conditions, and the results were quite variable. Using P(*o*-Tol)$_3$, P(Cy)$_3$, P(*p*-OMe-Ph)$_3$, P(2-Fur)$_3$ and BINAP as phosphines and $PdCl_2$ as the Pd source, little or no product was observed. However, with DPPF and P(*p*-Cl-Ph)$_3$ and $PdCl_2$ the terminal alkene was generated in moderate yield (52% and 28%, respectively). DPE-Phos and $PdCl_2$ generated the highest yield (83%) of the desired alkene, with less than 2% impurity of the internal alkene. Reactions with DPE-Phos and $PdBr_2$, $Pd(OAc)_2$ and $Pd_2(dba)_3$ were also attempted, but either the selectivity was reversed in the case of $PdBr_2$ (98% generation of the internal alkene), or less terminal alkene was produced (67% with $Pd(OAc)_2$ and 60% with $Pd_2(dba)_3$). Attempts to add bases like potassium carbonate or pyridine were unsuccessful in increasing the yield of the terminal alkene. Also, the most polar solvents, DMPU, *N*-methyl-2-pyrrolidone and diglyme, were the most successful (83%, 70%, 62%, respectively) for generation of the terminal alkene. Dichlorobenzene, toluene and dimethylsulfoxide were unsuccessful in generating any alkene product.

More complex carboxylic acids were shown to decarbonylated effectively using the above system.[87] Longer alkyl chain and fatty acids, and substrates with ester, phenyl, and ether functional groups all underwent successful decarbonylation. An appealing aspect of this method is that reactions are conducted at more moderate temperatures and distillation of the terminal alkene is not required in order to prevent isomerization to the internal alkene. However, large amounts of both the palladium catalyst and phosphine ligand are required, as well as an excess of anhydride. Additionally, the reaction must be stopped before completion in order to preserve selectivity of the terminal alkene. If full conversion is reached, the selectivity drops from 97:3 (terminal:internal) to 85:15.

Addition of an amine base like NEt_3 allows the reaction to run to completion and maintain selectivity.[88,89] Using the same conditions (3 mol% $PdCl_2$, 9 mol% DPE-Phos, 2 equivalents anhydride, DMPU, 110 °C, 16 hours) with the addition of 1 equivalent of

NEt_3 and using acetic anhydride in place of pivalic anhydride, selectivity for the terminal alkene remained 97:3 even when full conversion of the acid was achieved. The amount of NEt_3 could be reduced to 9 mol% with retention of selectivity. Additionally, the reactions maintained selectivity when carried out at temperatures as low as 70 °C, but conversion of substrate dropped to 20%.[90] It is likely that the NEt_3 helps stabilize the catalytic species, which helps prevent isomerization of the terminal alkene.[88,89] Additionally, alkylamines have been shown to facilitate the reduction of Pd(II) to the catalytically active Pd(0) species.

We aimed to extend the palladium-catalyzed decarbonylation reaction to bio-derived carboxylic acids like hydrocinnamic acid, mono-alkyl succinates, and 3-cyanopropanic acid, and optimize reaction conditions to be highly selective and high yielding, with low catalyst loadings and in the absence of solvent. The results of these efforts are described in Chapter 4.

Despite some reports using first-row transition metals for the decarbonylation of carboxylic acids, extension of this process to use first-row transition metals is largely unexplored but of great interest because of the high cost and low abundance of metals like palladium, iridium, and rhodium compared to their first-row counterparts. In one notable and recent example, iron(II) chloride (10 mol%) was used to catalytically decarbonylate a variety of carboxylic acids substrates with the addition of acetic anhydride, phosphine ligands (e.g. 1,5-bis(diphenylphosphino)pentane, 20 mol%), and an additive potassium iodide at 240 °C.[84] Yields were moderate (between 58% to 88% depending on substrate), but the selectivity for terminal olefins was rather high, ranging from 91:9 to 98:2, terminal:internal under optimized conditions. Most interestingly, the authors observe a marked increase in selectivity when the reactions were run under a pressure of CO (as high as 20 atm). They postulate that the isomerization to internal

olefins is facilitated by an iron-hydride species that persists after the β-hydrogen has been eliminated, before the reductive elimination of acetic acid. No comment on why CO has a positive effect on the selectivity for the terminal olefin was made. Excess CO could prevent olefin isomerization either by occupying coordination sites and preventing reinsertion of the terminal alkene onto the catalyst, or by facilitating reductive elimination of acetic acid.

In order to address the dearth of literature on first-row transition metals for decarbonylation of carboxylic acids, we aimed to discover examples using a high-throughput method. Chapter 5 describes the results of a high-throughput experimental approach to screen many metal and ligand combinations for decarbonylation activity in collaboration with Prof. Geoffrey W. Coates and Dr. Anne M. LaPointe of Cornell University. We combined these studies with conventional experimentation and optimization to develop new decarbonylation catalysts with first-row transition metals.

2 The Roles of Monomer Binding and Alkoxide Nucleophilicity in Aluminum-Catalyzed Polymerization of ε-Caprolactone

In part from:

Keying Ding, Maria O. Miranda, Beth Moscato-Goodpaster, Noureddine Ajellal, Laurie E. Breyfogle, Eric D. Hermes, Chris P. Schaller, Stephanie E. Roe, Christopher J. Cramer, Marc A. Hillmyer, and William B. Tolman. *Macromolecules*, **2012**, *45*, 5387-5396.

2.1 Overview

The kinetics of polymerization of ε-caprolactone (CL) initiated by aluminum-alkoxide complexes supported by the dianionic forms of *N*,*N*-bis[methyl-(2-hydroxy-3-*tert*-butyl-5-R-phenyl)]-*N*,*N*-dimethylethylenediamines, (L^R)Al(O*i*-Pr) (R = OMe, Br, NO_2) were studied. The ligands are sterically similar but have variable electron donating characteristics due to the differing remote (*para*) ligand substituents R. Saturation kinetics was observed using $[CL]_0$ = 2-2.6 M and $[complex]_0$ = 7 mM, enabling independent determination of the substrate coordination (K_{eq}) and insertion (k_2) events in the ring-opening polymerization process. Analysis of the effects of the substituent R as a function of temperature on both K_{eq} and k_2 yielded thermodynamic parameters for these steps. The rate constant k_2, related to alkoxide nucleophilicity, was strongly enhanced by electron-donating R substituents, but the binding parameter K_{eq} is invariant as a function of ligand electronic properties. Density functional calculations provide atomic-level detail for the structures of key reaction intermediates and their associated thermochemistries.

2.2 Introduction

As described in Chapter 1, the ring-opening polymerization (ROP) of cyclic esters is a key method for the synthesis of renewably derived and biodegradable materials, which are of interest for supplanting petroleum-derived plastics in a multitude of applications.[23,38,91,92] Metal-alkoxide complexes are effective catalysts for ROP of a variety of cyclic esters,[15,23,38,91,92] of which ε-caprolactone (CL) and lactide (LA) are particularly well-studied examples. Improving the performance and versatility of metal-alkoxide catalysts is an important research goal that may be achieved through understanding the mechanism(s) of the ROP process and applying that knowledge to catalyst design and development. Metal-alkoxide complexes are thought to operate by a 'coordination-insertion' mechanism, whereby a Lewis acidic metal center binds and activates the monomer, rendering it susceptible to nucleophilic attack by a bound growing alkoxide chain (Figure 2.1). While a useful paradigm, this oft-cited picture is simplistic, and although some aspects of the bond making and breaking events have been discerned from theory,[93, 94] detailed insights from experiment[95] are scant and sometimes contradictory.

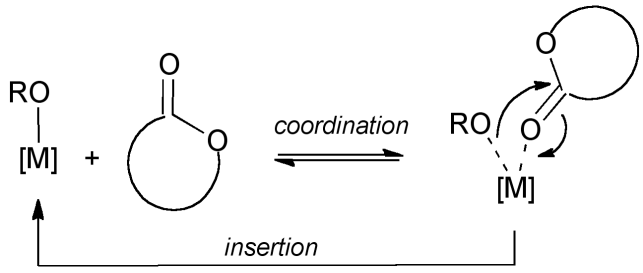

Figure 2.1. Coordination-insertion mechanism for cyclic ester ring-opening polymerizations.

For example, a number of workers have sought to address the role of metal ion Lewis acidity in ROP reactions.[96 – 104] Comparative studies of both bis(morpholinomethyl)phenoxy and tris(pyrazolyl)hydroborate complexes have indicated

that LA polymerization rates are enhanced in the presence of more electropositive metals (Ca > Mg > Zn).[102, 103] Increasing electrophilicity of Zn(II) ions in complexes of neutral N-donor ligands has been correlated with higher activity in LA polymerizations.[104] The practice of modifying ancillary ligands has allowed for additional investigations in which electron donating and withdrawing groups are used to tune catalyst reactivity. Thus, studies of aluminum complexes of tetradentate salen- and salan-type ligands have shown enhanced LA polymerization rates with ligands that incorporate electron-withdrawing substituents such as chlorine.[96, 98, 99]

In contrast, we previously reported the catalytic polymerization of CL by aluminum alkoxide complexes and found that an electronegative bromine substituent on the supporting ligand retards the overall reaction rate.[105] Similarly, in LA polymerizations using a related aluminum system, slightly slower polymerization rates were reported for a complex supported by a ligand having chlorine instead of methyl substituents.[97] For LA polymerizations using a titanium salen catalyst the order of reactivity decreases as the ligand substituent becomes more electron withdrawing (MeO > alkyl > I > Cl).[100] Furthermore, in magnesium complexes employing phenolic benzenesulfonate ligands, increasing electronegativity of halogen substituents in the ligand also results in reduced reaction rates.[101]

The apparently variable effects of changing the Lewis acidity of the metal center on ROP reaction rates suggest that the sensitivity of the coordination and insertion steps to Lewis acidity may differ. A pronounced electronic effect on monomer binding is typically assumed, wherein factors that render the metal center more positively charged are postulated to result in stronger monomer binding and activation to give higher polymerization rates. However, increased Lewis acidity of the metal center may also induce stronger binding of the growing alkoxide chain to the metal, retarding transfer of

the alkoxide to the carbonyl of the monomer. A clear understanding of how the coordination and insertion steps respond to perturbations of the electron density at the metal center through delineation of kinetic parameters for each step is needed. Yet metal-alkoxide promoted ROP reaction rates have only yielded composite propagation rate constants that include contributions from both coordination and insertion processes, complicating interpretation of kinetic and thermodynamic parameters.

In this chapter, the kinetics studies of CL polymerization by a series of well-characterized, monomeric Al complexes supported by ligands with virtually identical steric profiles but with different remote substituents having variable electron-donating characteristics are described. Under conditions of high initial concentrations of CL we observed saturation behavior, and this has enabled the determination of binding and catalytic turnover rate constants and associated thermodynamic parameters as a function of ligand substituent. These data, in conjunction with DFT calculations, provide mechanistic knowledge and insights of general significance for metal-alkoxide catalyzed ROP reactions critical for sustainable polymer synthesis.

2.3 Results and Discussion

2.3.1 Synthesis and Characterization of Complexes

Three Al alkoxide complexes **1-3** supported by ligands $(L^R)^{2-}$ (R = OMe, Br, NO_2 in the *para* position of the phenolate moiety) were prepared as outlined in Scheme 2.1. The syntheses of **1**[105] and **2**[105,106] (R = OMe, Br) were reported previously (including X-ray crystal structures of **1** and **2**). New derivative **3**[107] (R = NO_2) was characterized by ^1H NMR spectroscopy and elemental analysis. The ligand with R = NO_2 was reported[105], but subsequent work indicated that it was not appropriately identified; the synthesis and characterization reported here supersedes that work. The ligand syntheses employed a double Mannich condensation of the corresponding substituted phenols. Yields of the ligand precursors L^R were sensitive to the nature of the variable substituent, ranging from 20% for R = NO_2 to 80% for R = OMe. Unfortunately, the strongly electron donating *p*-

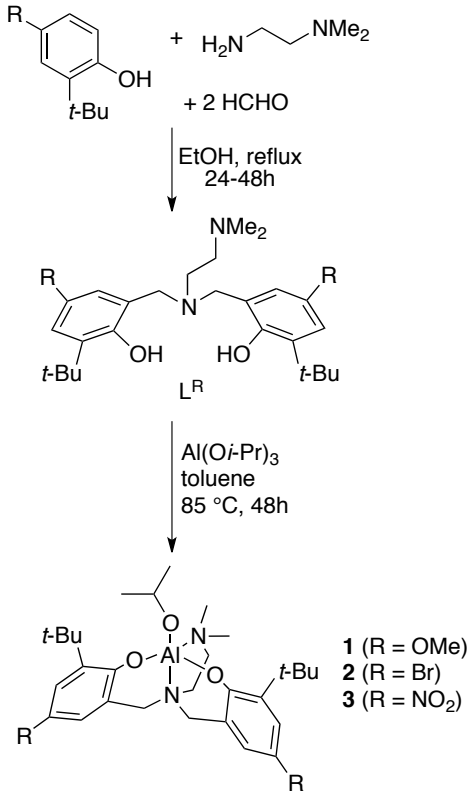

Scheme 2.1. Synthesis of ligands and complexes examined in this chapter.

amino derivatives, R = NMe_2 or NH_2, proved unattainable either through coupling with L^{Br} or reduction of L^{NO2}.

Coordination of the respective ligands to aluminum was effected through thermolysis of Al(O*i*-Pr)$_3$ with equimolar amounts of the ligand in toluene (Scheme 2.1). Yields of complexes **1**–**3** were between 70 and 76%. The products were readily isolated as white (**1** and **2**) and pale yellow (**3**) solids by filtration, evaporation of volatiles and washing of the residues with cold pentane. The compounds are air- and moisture-sensitive, and soluble in aromatic hydrocarbons (toluene, benzene). In general, ^{1}H NMR spectra for **1**–**3** are quite similar; the only variations are the resonances associated with the *para*-substituent and chemical shift differences for the two aromatic protons adjacent to the *para*-substituent. All of the data support monomeric, 5-coordinate structures for the complexes as drawn in Scheme 2.1, with no evidence for aggregation or fluxionality in solution. Previously reported Pulsed Gradient Spin Echo (PGSE) measurements for an analogous *tert*-butyl substituted ligand (R = *t*-Bu) in CD_2Cl_2 were consistent with this conclusion.[68]

2.3.2 Mechanistic Proposal and Methodology for Determining Rate Constants

In previously published work, all catalysts were shown to promote controlled polymerizations of CL to yield narrow molecular weight distribution ($Đ$ < 1.15) polycaprolactone (PCL) of prescribed molecular weights (M_n) that were linear functions of conversion and monomer-to-catalyst ratio.[105, 107] Since all catalysts are similarly well-behaved, they are well-suited for kinetics studies.

The mechanism of the polymerization reaction proposed in Scheme 2.2 provides a framework for interpretation of experimental kinetics data. With the caveat that assumptions about substrate binding and subsequent steps can be difficult to verify, we suggest that ROP involves reversible binding of a cyclic ester to the metal (k_1/k_{-1}),

followed by transfer of an attached alkoxide to the activated carbonyl (k_2), and collapse of the resulting tetrahedral intermediate to re-form the carbonyl and generate a new propagating alkoxide (k_3). The latter two steps are conceivably reversible. However, the considerably negative free energy change of ring-opening[108] suggests that the barrier for the ring-opening (k_3) would be lower compared to both ring-closing (k_{-3}) and alkoxide deinsertion (k_{-2}). Based on the general precedent for rapid collapse of the tetrahedral intermediate in the reactions of carboxylic acid derivatives, k_3 is probably post-rate determining. Thus, we simplify the mechanistic description to include only k_1, k_{-1} and k_2. Accordingly, we anticipated that saturation kinetics could be observed at sufficiently high [CL] and that the Michaelis-Menten equation (Equation 2.1) (Al = complex **1**–**3**) would fit the data, ultimately enabling the determination of K_M and k_2 values. In addition, if binding is rapidly reversible, so that $k_{-1} >> k_2$, K_M simplifies to the inverse of the binding constant (K_{eq}) between CL and the aluminum complex.

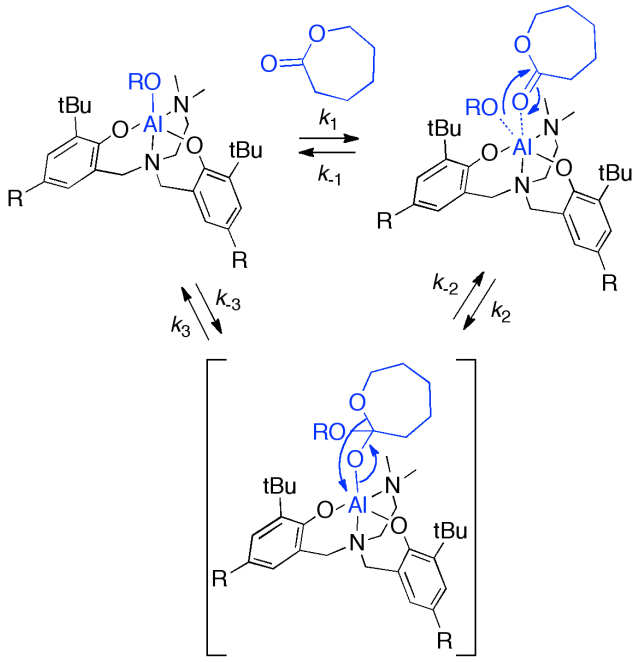

Scheme 2.2. Proposed mechanism for CL polymerization by Al complexes.

Equation 2.1

$$-\frac{d[CL]}{dt} = \frac{d[PCL]}{dt} = \frac{k_2[Al][CL]}{K_M + [CL]}$$

$$V_{\max} = k_2[Al]$$

Equation 2.2

$$K_M = \frac{k_{-1}}{k_1} = \frac{1}{K_{eq}}$$

2.3.2.1 Reaction Conditions and COPASI Methodology

To test the above model, the progress of CL polymerizations catalyzed by **1-3** was evaluated by ^{1}H NMR spectroscopy. Reactions were performed in triplicate with a fixed initial concentration of monomer ($[CL]_0$ = 2.0–2.6 M) and catalyst ($[Al]_0$ = 7.0 mM) in

toluene over a range of temperatures (18.5–80 °C). These conditions differ from those used in previous kinetics studies of **1-3**, where $[CL]_0$ = 1.0 M was used at 25 °C.[105,107] Concomitant decay and growth of the resonances associated with the monomer and polymer were assessed and the concentrations of both as a function of time were modeled according to Equation 2.1 (where $V_{max} = k_2[Al]$) by using COPASI (version 4.7.34),[109] a software package used for simulation and analysis of complex multi-step equilibria in systems biology and for analysis of complex kinetics.[110] We also evaluated one data set using a reaction progress kinetic analysis (RPKA) approach (described in more detail in section 2.3.2.2),[111,112] but chose to use COPASI for the complete study because (a) results using RPKA varied with the order of the polynomial used to fit the data (see section 2.3.2.2), and (b) with COPASI we were able to accurately and conveniently fit multiple species at once to solve for K_M and k_2. As an example, data for CL polymerization by **3** at 333 K with COPASI fits to Equation 2.1 are shown in Figure 2.2. The quality of the fits supports saturation behavior described by Equation 2.1, and this conclusion is further corroborated by the inability to account for the concentration data using simpler first- or second-order rate laws (Figure 2.3).[64] Additionally, we were able to corroborate the

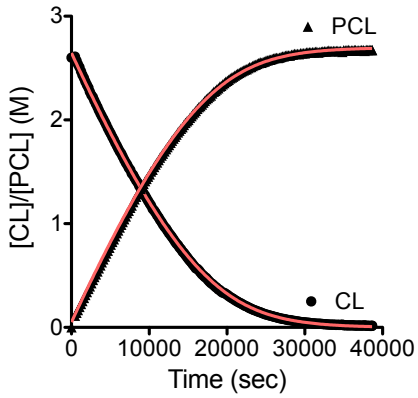

Figure 2.2. [CL] and [PCL] *vs*. time data (•,▲) and fit (–) to **Equation 2.1** for polymerization of CL catalyzed by **3** at 333 K. Fit parameters: K_M = 1.046(9) M, k_2 = 0.0328(2) s^{-1}.

presence of a rapid pre-equilibrium using an independent ^{1}H NMR peak analysis method (described in section 2.3.2.3).

Equation 2.3

$$-\frac{d[CL]}{dt} = k_1[CL]$$

Equation 2.4

$$\ln\left(\frac{[CL]_0}{[CL]_t}\right) = k_1 t$$

Equation 2.5

$$-\frac{d[CL]}{dt} = k_{2'}[CL]^2$$

Equation 2.6

$$\frac{1}{[CL]_t} - \frac{1}{[CL]_0} = k_{2'}t$$

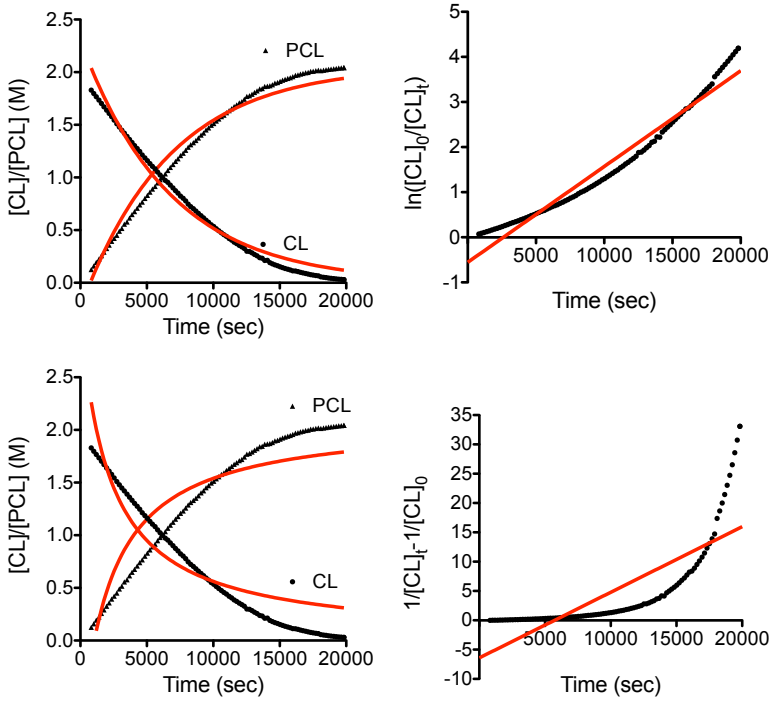

Figure 2.3. Alternative rate law fits by COPASI to data for the polymerization of CL by **2** at 323 K. Top, left: first-order fit to **Equation 2.3**. Top, right: linearized first-order fit to **Equation 2.4**. Bottom, left: second-order fit to **Equation 2.5**. Bottom, right: linearized second-order fit to **Equation 2.6**.

2.3.2.2 Reaction Progress Kinetic Analysis (RPKA)

A selected subset of data for the polymerization of **3** at 333 K was chosen for evaluation of an alternative data analysis method to COPASI, reaction progress kinetic analysis (RPKA). The instantaneous rates as a function of [CL] were extracted from the time-dependent concentration data by first fitting the [CL] *vs.* time data to an arbitrary n^{th}-order polynomial function ($9 \leq n \leq 2$) (representative plot with fit to the 7th order polynomial in Figure 2.4, left). Differentiation of the polynomials with respect to time yielded the instantaneous reaction rates, and these were plotted vs. [CL] (Figure 2.4, right and Figure 2.5). Using a non-linear regression, the rate *vs.* [CL] curves were fit to the Michaelis-Menten equation, and K_M and V_{max} were directly determined from these fits. In general these fits were of good quality ($R^2 > 0.9$). The determined K_M and V_{max} values are listed in Table 2.1. The data was best fit using approximately a seventh-order polynomial (Table 2.1, Entry 3). RKPA could thus be used to obtain kinetic parameters, however, the exact results obtained depend somewhat upon the order of the polynomial employed during the fitting. Often, higher order polynomials can overfit the data, as observed by

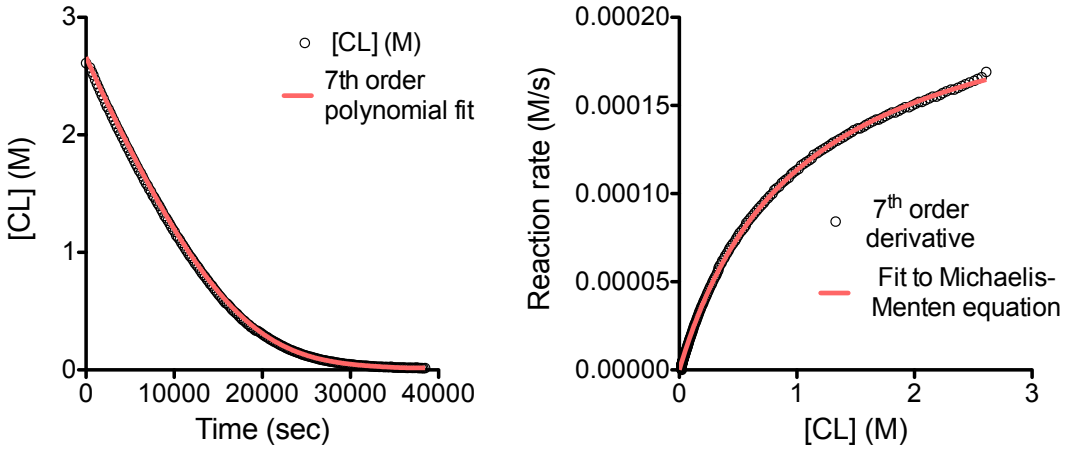

Figure 2.4. Left: [CL] *vs.* time data (•) fit to 7th order polynomial (–). Right: Rate *vs.* [CL] data obtained from derivative of 7th order polynomial on left (•) and fit to **Equation 2.1** (–) for the polymerization of CL by **3** at 333 K.

the change in curvature of derivative of the polynomial, especially at high [CL]. Also, the fifth order polynomial would not converge to a solution when fit to Equation 2.1. Despite obvious variations in the appearance of the fits based on polynomial order, the actual differences between the determined kinetic parameters are quite small. While the similarity and goodness-of-fits reinforces that this is an effective method to analyze the data and we are indeed observing saturation kinetics, we chose not to use RPKA to analyze the entirety of the data because of these differences between polynomial orders. Additionally, COPASI is quite convenient and also yields high quality fits, so we chose to use COPASI instead of RPKA to analyze the remainder of the data.

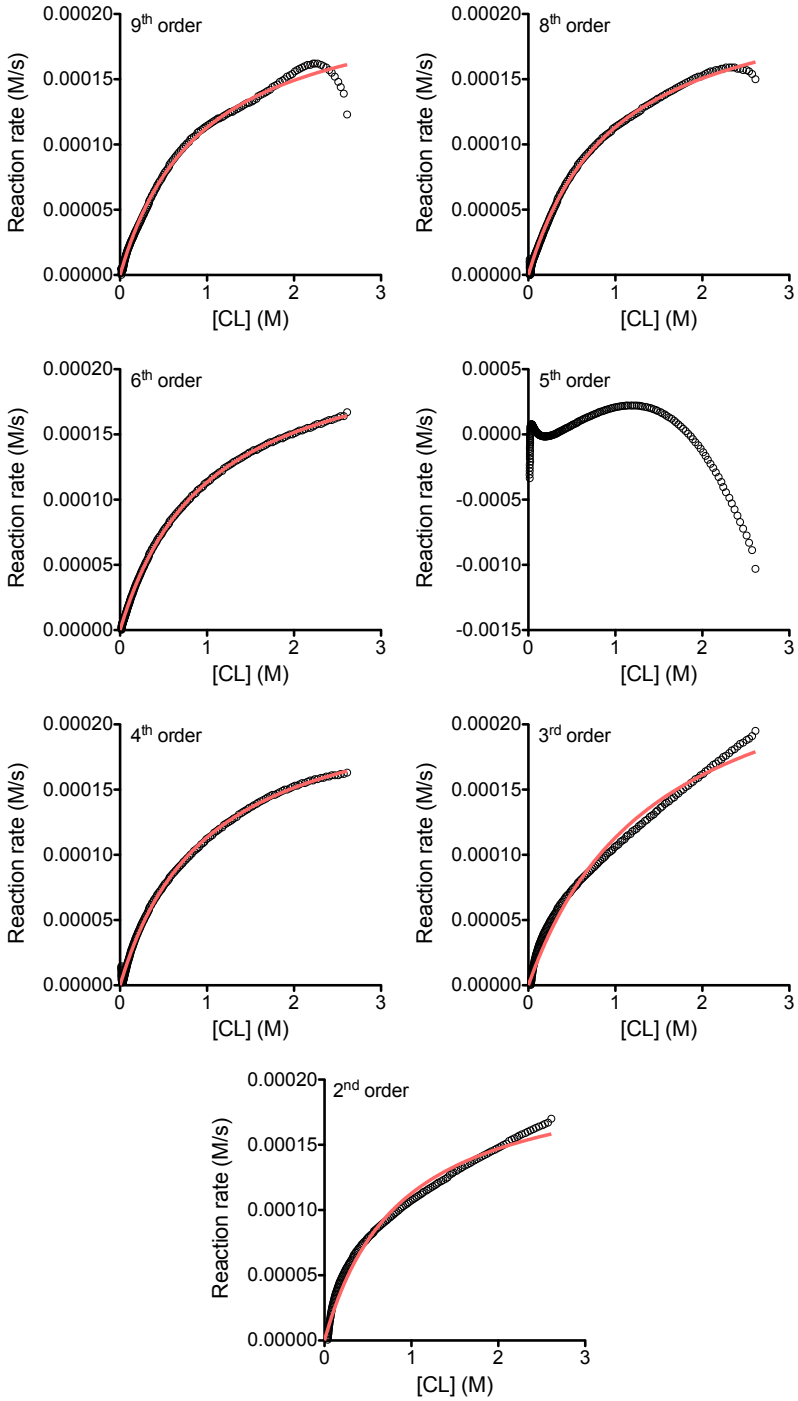

Figure 2.5. Fits of n^{th} (n = 2–9) order polynomial functions to a representative data set for the polymerization of CL by **3**. $[\mathbf{3}]_0$ = 6.88(2) mM, $[CL]_0$ = 2.6 M, 333 K, toluene-d_8. Points represent the derivative of polynomial order indicated; red line is fit to **Equation 2.1**. For n = 5, fit to **Equation 2.1** would not converge.

Table 2.1. Summary of kinetic parameters V_{max} and K_{eq} determined using RPKA method.[a]

Entry	Order *n* polynomial	V_{max} (M/s) (x10^4)	K_M (M)	R^2
1	9	2.19(2)	0.94(2)	0.9941
2	8	2.25(1)	0.99(1)	0.9984
3	7	2.291(8)	1.021(8)	0.9995
4	6	2.284(9)	1.016(9)	0.9993
5	5	d.n.c.[b]	d.n.c.[b]	d.n.c.[b]
6	4	2.28(2)	1.01(1)	0.9980
7	3	2.80(7)	1.48(7)	0.9845
8	2	2.11(7)	0.87(7)	0.9544

[a] Conditions: catalyst **3** at 333 K. [b] D.n.c. indicates that fit did not converge to a solution.

2.3.2.3 ^{1}H NMR Peak Analysis to Determine K_{eq}

In addition to observing changes in [CL] and [PCL] by ^{1}H NMR spectroscopy during the course of the polymerization, we also noted changes in the aryl resonances of the catalyst as polymerization proceeded (Figure 2.6). The two resonances separate from each other during the polymerization, such that the difference in chemical shift between the two peaks increases as [CL] decreases (moving from bottom to top of the stacked plot in Figure 2.6). To explain this phenomenon, we hypothesize that there is a rapid equilibrium between two complexes in solution that involves CL, such that a single set of resonances are seen at each point in time but their relative peak positions shift as a function of [CL]. The simplest such equilibrium would be that involving CL binding to the catalyst, described by K_{eq}. Thus, by appropriate fitting of the aryl peak position separation ($\Delta\delta$) as a function of [CL], K_{eq} (or K_M, assuming $k_{-1} >> k_2$) may be measured independently of the polymerization rate measurements, allowing the kinetic model for the polymerization to be tested. In this approach, we ignore the possibility of esters in the backbone of PCL binding to the catalyst and assume that at the end of the reaction, the

catalyst is in an unbound state. This is consistent with the general inability of Al-based alkoxides to effect polymer transesterification.

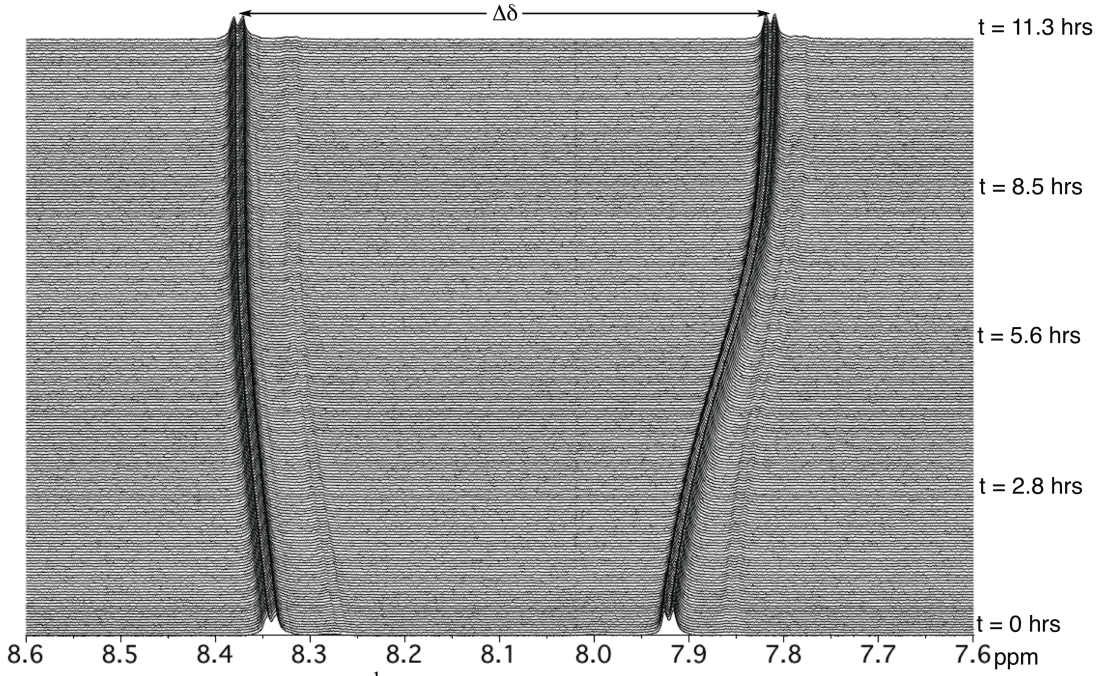

Figure 2.6. A portion of the ^{1}H NMR spectra acquired during the polymerization of CL by **3** at 333 K showing how the aryl resonances for the complex in solution change as a function of reaction time, as measured by the indicated peak separation Δδ.

Plots of Δδ versus [CL] were fit using a non-linear regression to Equation 2.7 and K_{eq} values were determined, as illustrated in Figure 2.7 for one experiment using **2** and **3** at 333 K. Due to spectral overlap issues this analysis was not possible for **1**. For the case of **3**, the K_{eq} values determined from the separate NMR and kinetic analyses were in close agreement (cf. at 323K, K_{eq} (NMR) = 0.87 ± 0.03 M, K_{eq} (COPASI avg) = 1.04 ± 0.05 M), while for **2** they were within a factor of 4 (at 323K, K_{eq} (NMR) = 0.60 ± 0.08 M, K_{eq} (COPASI avg) = 1.82 ± 0.07 M, Table 2.2). Note, however, that this latter difference corresponds to a $\Delta\Delta G° < 1$ kcal/mol, on the order of experimental error (see discussion of thermodynamics below). Importantly, the agreement between the K_{eq} values determined

by the two independent methods provides further support for the mechanistic picture shown in Scheme 2.2 and the validity of Equation 2.1.

Equation 2.7

$$\Delta\delta = \Delta\delta_{uncoord} + \frac{(\Delta\delta_{uncoord} - \Delta\delta_{coord})[CL]}{K_M + [CL]}$$

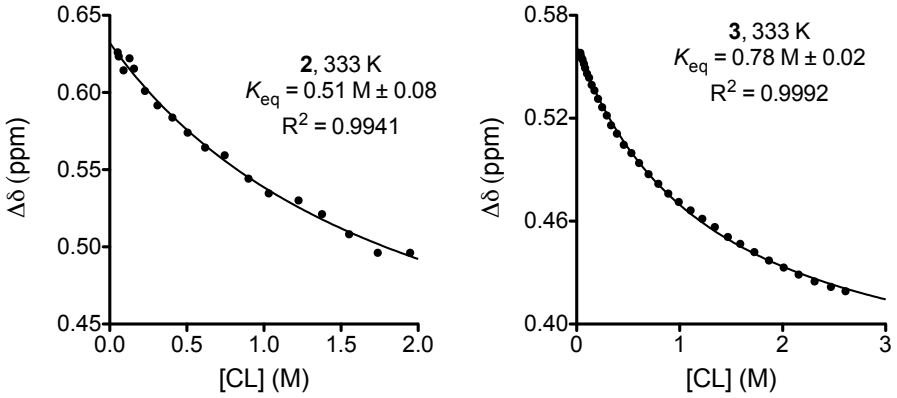

Figure 2.7. Plot of Δδ *vs*. [CL] during the polymerization of CL for **2** and **3** at 333 K, with the fit to **Equation 2.7**.

Table 2.2. Average values of kinetic parameters determined from COPASI fits and RPKA and NMR peak analyses.

Entry	Temp (K)	Catalyst	R	K_{eq} COPASI/RPKA (M^{-1})	K_{eq} NMR (M^{-1})	k_2 (s^{-1}) (x10^2)
1	291.5	**1**	OMe	0.72(7)	[a]	1.52(6)
2	303	**1**	OMe	1.12(6)	[a]	3.6(2)
3	313	**1**	OMe	1.28(5)	[a]	7.1(3)
4	323	**1**	OMe	1.25(6)	[a]	18.84(5)
5	313	**2**	Br	1.5(1)	0.53(4)	1.53(4)
6	323	**2**	Br	1.82(7)	0.60(8)	3.61(9)
7	333	**2**	Br	1.92(3)	0.49(1)	8.3(2)
8	343	**2**	Br	1.44(7)	0.51(9)	18(2)
9	323	**3**	NO_2	1.04(5)	0.87(3)	1.40(5)
10	333	**3**	NO_2	0.98(3)	0.78(5)	3.1(2)

11[b]	333	**3**	NO_2	0.979(8)	-	3.33(1)
12	343	**3**	NO_2	1.1(1)	0.78(9)	6.0(4)
13	353	**3**	NO_2	1.05(7)	0.77(3)	11.1(2)

[a] Value could not be determined due to spectral overlap. [b] RPKA analysis results from 7th order polynomial (vide supra).

2.3.3 Isolation of a Complex After Polymerization

After polymerization experiments using **3** were completed and the NMR tubes were allowed to stand in air at room temperature for several days, crystals were observed within the polymer solution in the tubes. An X-ray crystal structure determination was performed that showed the crystals to comprise the dinuclear complex **4** (Figure 2.8). The complex contains two symmetry-related Al centers, each ligated in tridentate fashion by $(L^{NO2})^{2-}$. The dimethylamino arms of the ligand are not complexed to the metal, and instead are hydrogen-bonded to hydroxides that bridge the Al sites. These sites adopt slightly distorted trigonal bipyramidal geometries (τ = 0.74),[113] with the trigonal plane including three oxygen atoms, two from the phenoxides on the ligand (O2, O3) and one from a bridging hydroxide (O1). The nitrogen (N1) and the other bridging hydroxide moiety (O1') are the axial donors (N1−Al1−O1' = 169.80°). The Al-O and Al-N interatomic distances are similar to those reported previously for complexes **1**, **2**, and an analog featuring $(L^{tBu})^{2-}$.[105,106] We surmise that the hydroxide ligands derive from water impurities introduced during or after the polymerization, although we have not explored this issue in detail. Importantly, the identification of **4** provides unequivocal precedence for the notion that the dimethylamino arm of $(L^{R})^{2-}$ can dissociate from an Al(III) center, which may occur during polymerization catalysis (see below).

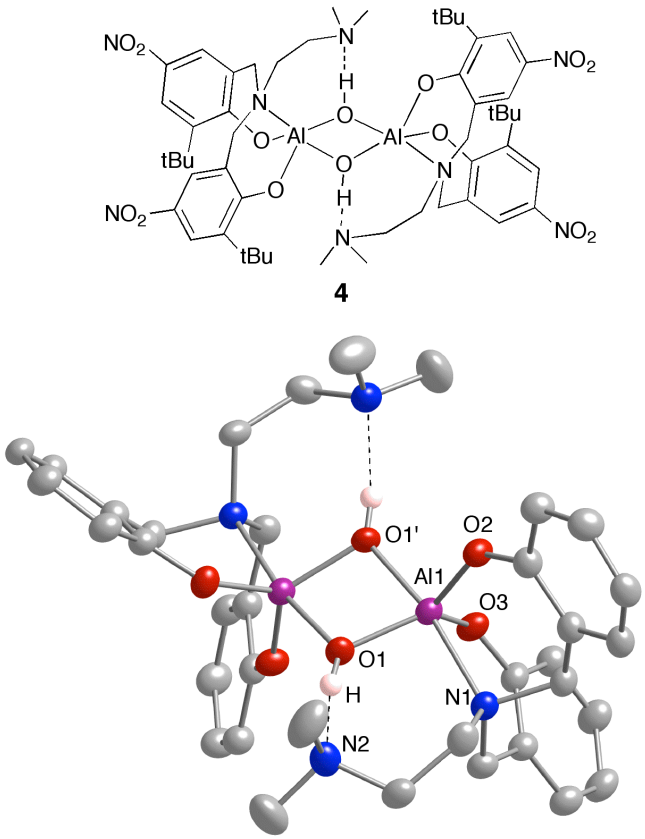

Figure 2.8. Line drawing of complex **4** (top), and representation of the X-ray crystal structure of **4**, showing 50% thermal ellipsoids with all hydrogen atoms (except those on the bridging hydroxo groups) and *t*-butyl and -NO_2 substituents omitted for clarity (bottom). Selected interatomic distances (Å) and angles (deg) are as follows: Al1−O1, 1.7859(14), Al1−O1', 1.8626(14), Al1−O2, 1.7702(14), Al1−O3, 1.7733(14), Al1−N1, 2.1253(16), Al1−Al1', 2.8007(11), O1−H, 0.80(2), N2−H, 1.865, O1−N2, 2.658; O1−Al1−O2, 125.69(7), O1−Al1−O3, 119.25(7), O1−Al1−N1, 92.46(6), O1-Al1-O1', 77.96(7), O2−Al1−O3, 114.99(7), O2−Al1−N1, 90.90(6), O2−Al1−O1', 97.50(6), O3−Al1−N1, 89.13(6), O3−Al1−O1', 92.52(6), N1−Al1−O1', 169.81(6), Al1−O1−Al1', 100.26(7), Al1−O1−H, 126.2(15), Al1−O1'−H', 133.5(15), O1−H−N2, 170.13.

2.3.4 Rate Constants and Mechanistic Interpretations

Turning first to analysis of k_2 (Table 2.2), its dependencies on ligand substituent R and temperature are revealed in plots of log(k_2) vs. σ_ρ[114] (Figure 2.9) and ln(k_2/T) vs. 1/T (Figure 2.10). Linear correlations between substituent electronic parameters and k_2 were

observed at all temperatures and essentially invariant negative ρ values (slopes) were found (average ρ = -1.1(1)). Clearly, increasing the electron-donating capability of the *para*-substituent significantly enhances the insertion step, and the linear correlation supports an invariant mechanism across the series. The trend may be rationalized by invoking a prominent role played by binding of the alkoxide nucleophile in this system: more electron-donating ligands render the alkoxide more labile and more reactive, presumably through decreasing the Lewis acidity of the metal and thus the strength of the Al-OR interaction.

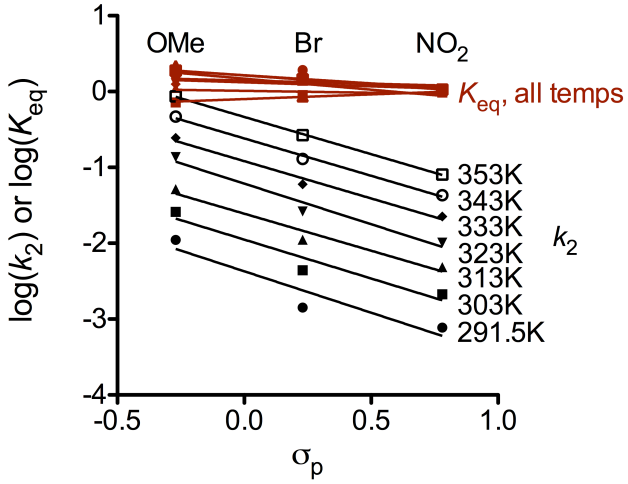

Figure 2.9. Hammett plot for k_2 (black) and K_{eq} (red). The rate constants presented that were not determined directly from the data were extrapolated from the thermodynamic parameters obtained from the Eyring (k_2) and van't Hoff (K_{eq}) plots (**Table 2.3** and **Table 2.4**).

Further insights into the insertion process are provided by the activation parameters determined from the Eyring plots for k_2 (Figure 2.10; Table 2.3). In general, modest activation enthalpies accompany negative activation entropies. The parameters imply a moderate degree of bond breaking and ordering in going to the transition state,

consistent with a concerted transfer of the metal-bound alkoxide to the coordinated carbonyl with cleavage of the carbonyl π bond.

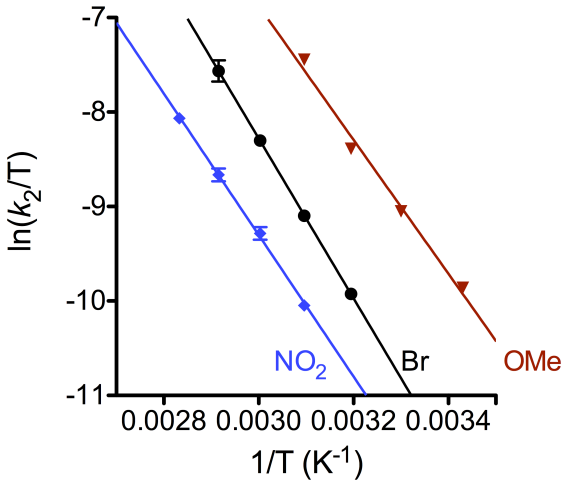

Figure 2.10. Erying plot for k_2 for catalysts **1** (red triangle), **2** (black circle), **3** (blue diamond).

Table 2.3. Activation parameters associated with k_2.

Complex	R	$\Delta H^{\ddagger}$ (kcal/mol)	$\Delta S^{\ddagger}$ (cal/molK)	$\Delta G^{\ddagger}$ (kcal/mol, 323K)
1	OMe	14.1 ± 0.5	-19 ± 1	20.1 ± 0.6
2	Br	16.8 ± 0.3	-13.3 ± 0.4	21.1 ± 0.3
3	NO_2	14.9 ± 0.5	-21.0 ± 0.7	21.7 ± 0.4

Considering next K_{eq} (assuming $K_M^{-1} = K_{eq}$, Equation 2.2), one encounters a different situation (Table 2.2). At all temperatures and for all catalysts, plots of log(K_{eq}) vs. σ_p (Figure 2.9) give slightly negative average ρ values of -0.1(2) that are effectively close to zero, indicating that the equilibrium is insensitive to substituents. Surprisingly, it appears as though monomer binding is unaffected by the electronic nature of the ligand, and therefore the electrophilicity at the metal center. This observation is further supported

by the thermodynamic data, which for ease of interpretation are plotted in Figure 2.11 as ln(K_{eq}) vs. 1/T; thermodynamic parameters derived from K_{eq} are listed in Table 2.4. Excellent agreement between the parameters determined independently from the kinetic analysis and the analysis of the NMR resonances for the Al complex during polymerization supports the validity of the overall mechanistic model and a rapid pre-equilibrium before monomer insertion. Again, these plots all have slopes of essentially zero, and have standard Gibbs free energies of nearly zero. In the case of **1**, the small, positive enthalpy change and positive entropy change support a dissociative interchange process,[115] indicating a possible ligand rearrangement occurring simultaneously with monomer binding.

Table 2.4. Thermodynamic parameters associated with K_{eq} as determined by COPASI and NMR peak analysis methods.

Complex	Method	R	$\Delta H°$ (kcal/mol)	$\Delta S°$ (cal/molK)	$\Delta G°$ (kcal/mol, 323K)
1	COPASI	OMe	3.3 ± 0.5	11 ± 2	-0.2 ± 0.8
2	COPASI	Br	-0.1 ± 0.8	0.6 ± 2	-0.3 ± 1
2	NMR	Br	-0.6 ± 1	-3 ± 3	0.4 ± 1
3	COPASI	NO_2	0.3 ± 0.4	0.9 ± 1	-0.01 ± 0.8
3	NMR	NO_2	-0.9 ± 0.3	-3 ± 1	0.1 ± 0.5

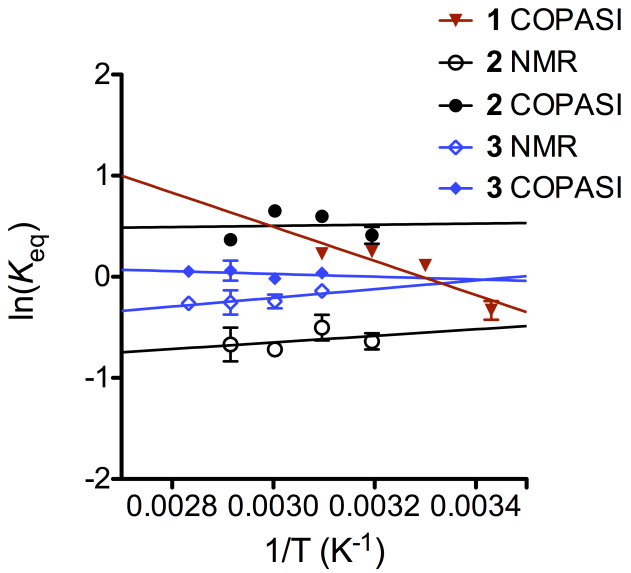

Figure 2.11. Van't Hoff plot for K_{eq} for catalsts **1** (red triangles), **2** (black circles), **3** (blue diamonds). The designation NMR or COPASI indicates which analysis method (vida supra) was used to obtain the data. NMR: NMR peak analysis method. COPASI: kinetic analysis using COPASI.

To rationalize the monomer binding thermodynamics for the complexes supported by electron donating and withdrawing ligands, we propose different pathways for each type of system, which may operate in parallel (Scheme 2.3). In one pathway (**A**), an amine arm of the ligand dissociates, opening up a vacant coordination site. Monomer then approaches the resulting four-coordinate aluminum complex, which is less sterically crowded than its precursor, and binds to form a pentacoordinate intermediate. This route would be favored in complexes with electron-donating substituents (i.e., **1**) that can stabilize a lower-coordinate aluminum intermediate. Increasing temperature would promote dissociation of the ligand arm, as reflected in the positive $\Delta S°$ associated with K_{eq}, and facilitate monomer binding and reaction. In a second pathway (**B**), monomer coordinates to the aluminum complex directly to form an octahedral intermediate. This pathway would be favored for the complexes with electron withdrawing ligands (i.e., **2**

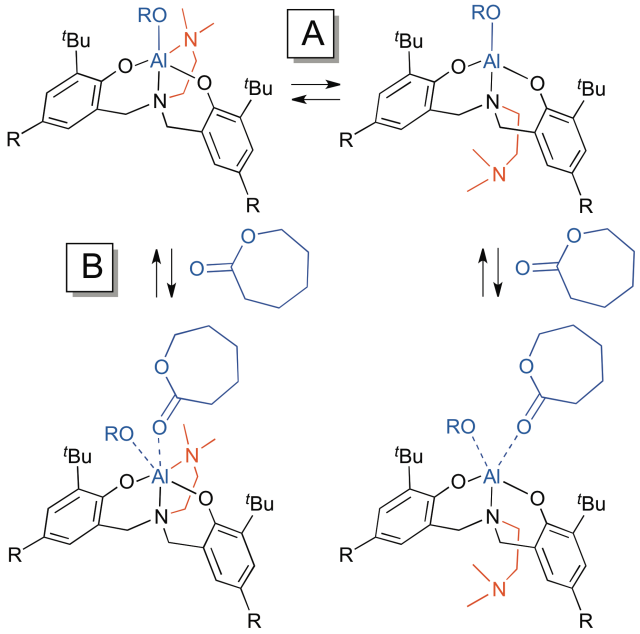

Scheme 2.3. Proposed mechanisms for binding of CL to catalysts **1**-**3**.

and **3**), for which dissociation of the ligand arm is retarded by the enhanced Lewis acidity of the metal. In these complexes, increasing temperature has little effect on binding of the monomer.

The amine arm dissociation central to the above hypothesized mechanistic scheme is supported by several lines of evidence. Precedence comes from a report describing this phenomenon for a vanadium complex of $(L^{tBu})^{2-}$,[116] proposed involvement of amine arm dissociation in ROP catalysis by zinc catalysts,[117] and the X-ray structure of **4**. In addition, we performed variable temperature (VT) NMR studies on **1** (toluene-d_8, 500 MHz) with and without exogenous pyridine, the binding of which would mimic coordination of CL during polymerization. In the absence of added pyridine, several peaks in the ^{1}H NMR spectrum measured at room temperature reversibly decoalesced to separate signals upon cooling (Figure 2.12). For example (Figure 2.16), single peaks in the room temperature spectrum for the amine-arm methyl groups (NMe_2) and the

methoxy aryl substituents convert to two separate resonances at 193 K (T_c ~ 230-235 K). The low temperature spectrum is consistent with a static C_s symmetric geometry for the complex as found in its X-ray crystal structure.[105] The methoxy resonances (3.63 ppm) in Figure 2.12 were analyzed using the Topspin 3.1 DNMR module to model the dynamics of this process. The resonances were modeled using simplex iterations, and each peak was treated as an isolated spin system with two singlets at the low temperature limit that coalesced into a single peak at higher temperatures (Figure 2.13, left). Rate constants were determined at each temperature, and Erying analysis revealed activation parameters $\Delta H^{\ddagger}$ = 7.9(3) kcal/mol and $\Delta S^{\ddagger}$ = -14.6(7) cal/molK ($\Delta G^{\ddagger}$ (298 K) = 12.3(4) kcal/mol, Figure 2.13, right), consistent with a fast intramolecular exchange process that averages the chemical environment of the ligand hydrogen atoms at room temperature, presumably via interconversion of degenerate square-pyramidal geometries potentially through a Berry-pseudorotation or a turnstile mechanism.[118]

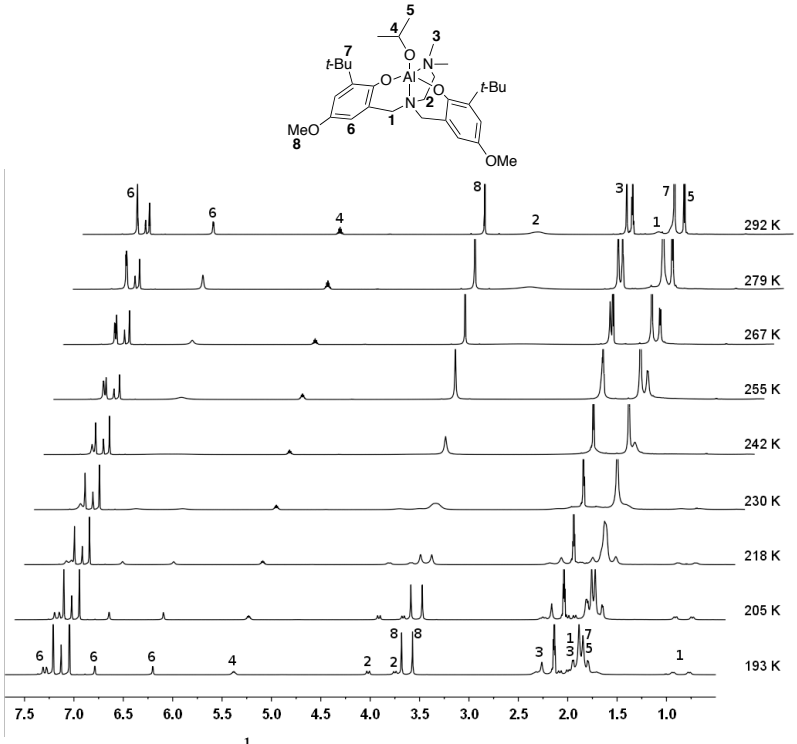

Figure 2.12. Full stacked VT-^{1}H NMR spectra (500 MHz, toluene-d_8) of **1** from 193 K to 292 K.

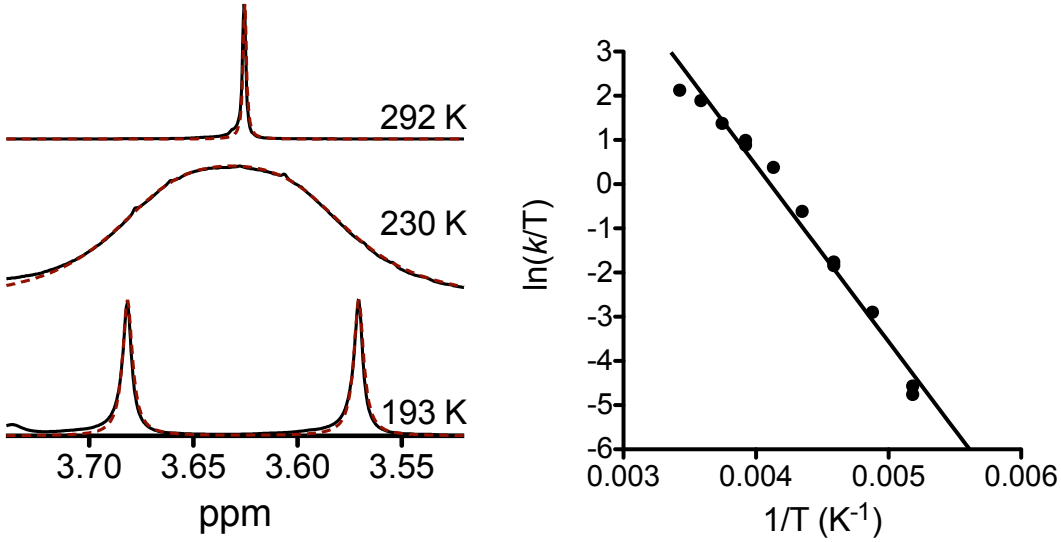

Figure 2.13. Left: portion of VT-^{1}H NMR spectra (–) and fit (--) to determine rate constant, *k*, for fluxional process in **1**. Right: Erying analysis of determined rate constants, $R^2 = 0.9815$. See text for thermodynamic parameters.

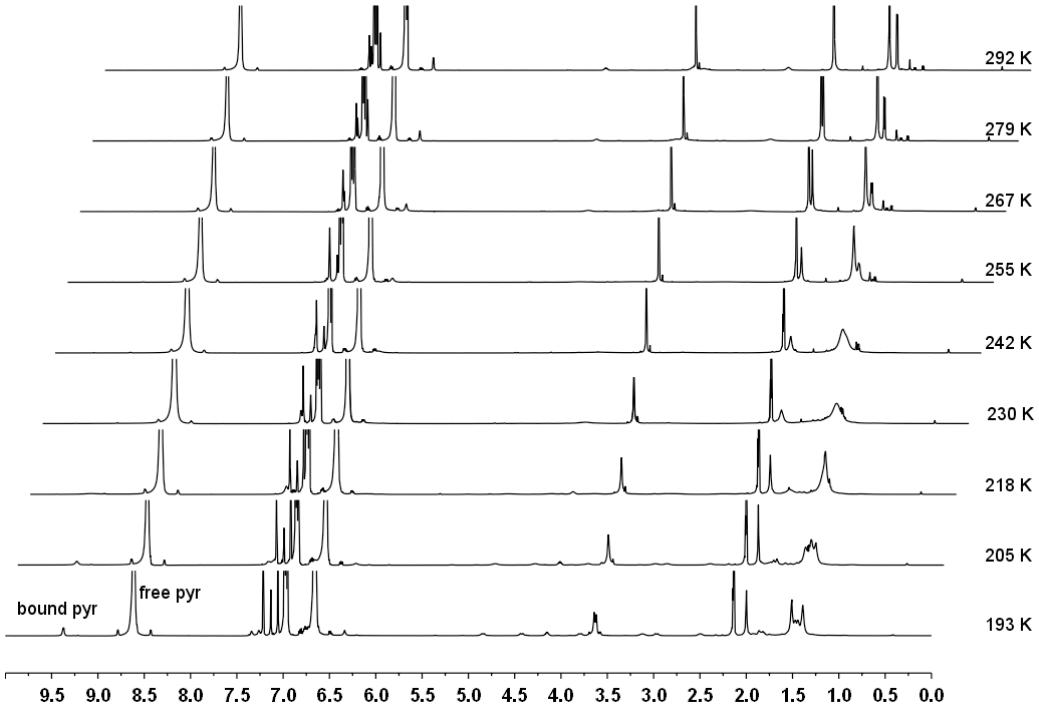

Figure 2.14. Full stacked VT-^{1}H NMR spectra (500 MHz, toluene-d_8) of **1** with 50 equiv. pyridine from 193 K to 292 K

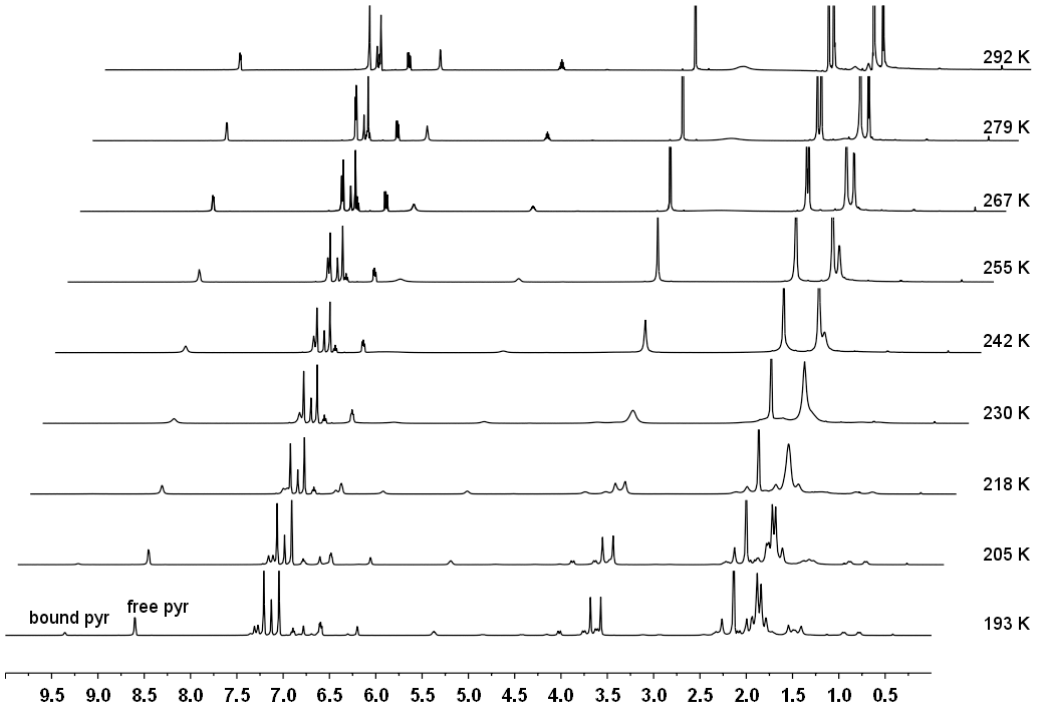

Figure 2.15. Full stacked VT-^{1}H NMR spectra (500 MHz, toluene-d_8) of **1** with 1 equiv. of pyridine from 193 K to 292 K.

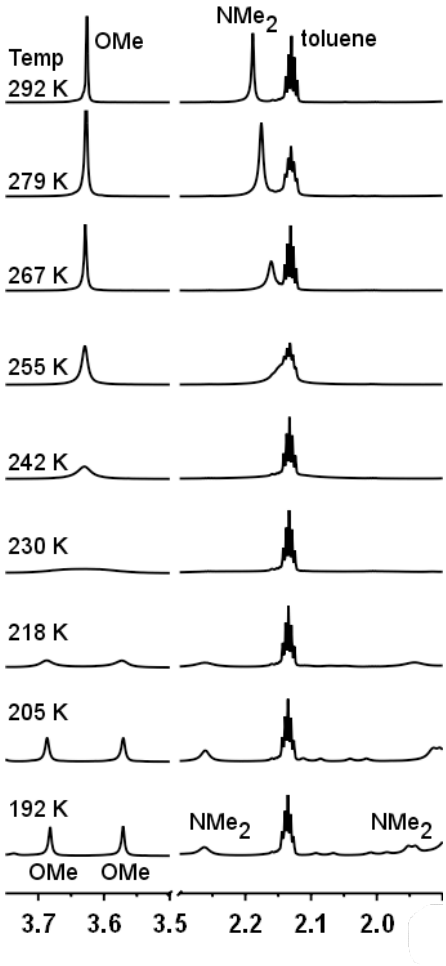

Figure 2.16. Portions of the VT ^{1}H NMR spectra in **Figure 2.12** of complex **1** in toluene-d_8 with no added reagents.

Figure 2.17. Portions of the VT ^{1}H NMR spectra in **Figure 2.14** of complex **1** in toluene-d_8 in the presence of 50 equiv pyridine (pyr). The spectrum of the free (uncoordinate, protonated version) of the ligand is shown for reference at the top of the stacked plot. Asteriks denote spinning side-bands associate with free pyr resonance.

In the presence of excess pyridine (50 eq), only free pyridine and an averaged set of peaks for **1** are apparent in the NMR spectrum measured at 292 K (Figure 2.14). Upon cooling, however, changes in the spectrum occur that support binding of pyridine and

displacement of the amine-arm of the supporting ligand (Scheme 2.4). Notably, at 193 K a peak for coordinated pyridine appears at δ 9.4 ppm, ~0.8 ppm downfield from free pyridine, and a singlet for the NMe_2 group appears at δ 2.0 pm, at the same position as in the free (uncoordinated, protonated) ligand (Figure 2.17). With 1 eq. of pyridine, the identical set of peaks assigned to the pyridine adduct are seen at 193 K, in conjunction with those associated with **1** alone (Figure 2.15). In sum, the VT NMR data in the presence pyridine support lability of the dimethylamino arm, as proposed in Scheme 2.3.

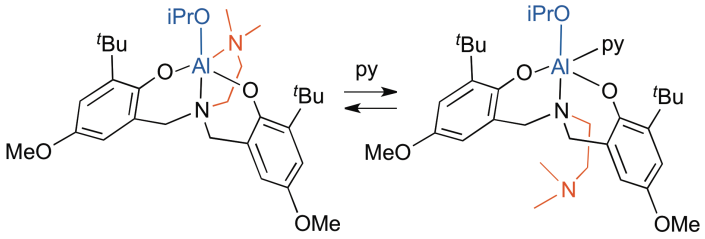

Scheme 2.4. Proposed binding of pyridine to complex **1**.

2.3.5 Theoretical Calculations

(Performed by Eric D. Hermes and Christopher J. Cramer)

To further evaluate the mechanism shown in Scheme 2.3, we carried out density functional calculations on the complexes with and without coordination of the amine arm and with and without bound CL. The nature of the catalyst, the alkoxide, and CL is such that substantial conformational diversity is possible, but representative structures are presented in Figure 2.18 for L^{H} for simplicity (calculations were done for complexes **1**–**3**). In the absence of CL binding, the coordination geometry about Al is roughly tetrahedral when the amine arm is decoordinated (Figure 2.18d) and roughly trigonal bipyramidal when the amine arm is coordinated (Figure 2.18c). The enthalpy cost to decoordinate the amine arm is predicted to range from 16.4 kcal/mol for L^{OMe} to 19.2 kcal/mol for L^{NO2} (Table 2.5; compare Mono-RO Arm-off column to Mono-RO Arm-on column). Considering the *free energies* of arm decoordination at 333 K (not tabulated),

values for all three ligands are predicted to be about 3 kcal/mol less positive than the enthalpies of decoordination. However, the magnitude of the entropic contribution favoring decoordination is likely underestimated. Identification of all of the relevant arm-off and arm-on conformational isomers is not practical due to their sizes, but the decreased steric congestion around aluminum in the arm-off case would be expected to permit a substantially larger number of conformers to exist at low energy compared to the arm-on alternative. This would contribute to even more entropic lowering of the population free energy in the arm-off case.

Table 2.5. Relative 333 K enthalpies (kcal/mol) of different catalyst structures with and without bound CL.[a]

	Arm-off			Arm-on		
p-Subst	Bi-RO[b]	Mono-RO[c]	Mono-RO/CL[d]	Bi-RO[b]	Mono-RO[c]	Mono-RO/CL[d]
OMe	21.6	16.4	7.7	6.8	0.0	-3.1
Br	20.9	17.8	7.5	5.0	0.0	-4.9
NO_2	20.0	19.2	6.8	2.2	0.0	-8.5

[a] Monocoordinated alkoxide and infinitely separated CL. [b] Enthalpies computed as sum of M06-L/6-31G(d) thermal contributions (see Methods) and SMD(toluene)/M06-2X/6-311+G(d)//M06-L/6-31G(d) electronic energies for structures analogous to those shown in Figure 2.18, i.e., not accounting for potentially large populations of conformational isomers within each structural class. [c] Bidentate alkoxide/ester and infinitely separated CL. [d] Monocoordinated alkoxide with bound CL.

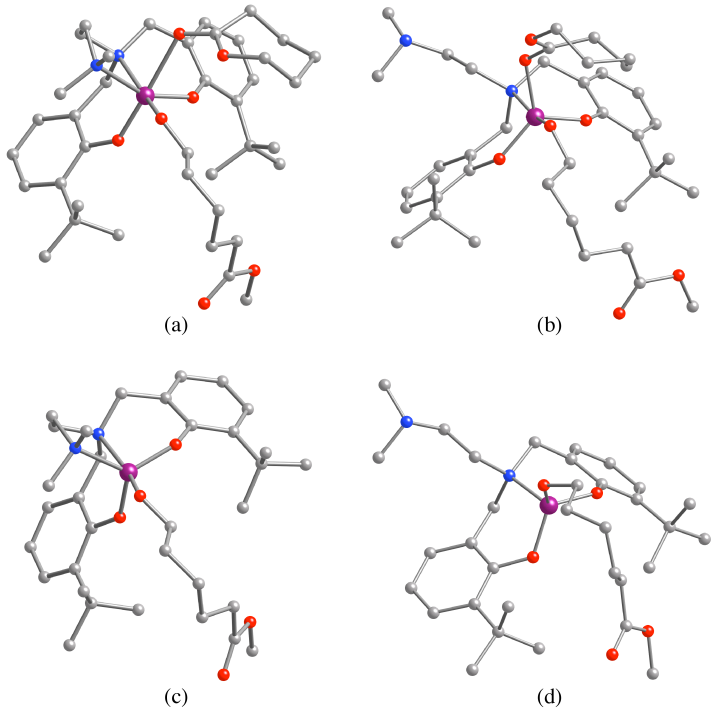

Figure 2.18. Ball-and-stick stereostructures of representative L^{H}AlOR (R = $(CH_2)_5CO_2Me$) complexes with L^{H} coordinate in tetradentate (a, c) and tridentate (b, d) fashion, with (a, b) and without (c, d) coordinated ε-caprolactone. All structures were fully optimized at the DFT level of theory (see Methods section). Hydrogen atoms are not shown for clarity, carbon atoms are gray, nitrogen atoms are blue, oxygen atoms are red, and aluminum atoms are purple. The illustrated structures are designated Mono-RO in **Table 2.5**. Structures in which the terminal ester of the alkoxide ligand also coordinate Al, designated Bi-RO in **Table 2.5**, are higher in enthalpy than those shown here.

We evaluated the tendency for the propagating alkoxide itself to act as a bidentate ligand, through the coordination of its ester carbonyl to Al. We have located such structures (not shown) and in the arm-off case, they are enthalpically less stable than their monocoordinated alkoxide antecedents by from 5.2 (L^{OMe}) to 0.8 (L^{NO2}) kcal/mol. In the arm-on case, the enthalpic preference for monocoordination increases in every case by about 2 kcal/mol; the direction of this change is as expected given the decreased Al electrophilicity that results from coordination of the amine functionality. Entropic

considerations for individual 333 K structures like those shown in Figure 2.18 further destabilize the bidentate structures by 3 to 4 kcal/mol in free energy (not tabulated). As noted above, such an estimate is likely somewhat too low given the flexibility of the alkoxide chain when it is monocoordinated compared to bound in a bidentate fashion. In any case, there appears to be no strong bias for a growing polymer chain to block the approach of new monomer to the catalytic center.

The arm-on and arm-off structures with bound CL have roughly octahedral and trigonal bipyramidal coordination about the aluminum atom, respectively (Figure 2.18a and Figure 2.18b). If we consider the enthalpies of complexation of CL to the catalyst, in the arm-off case the complexation is exothermic by –12.4 kcal/mol for L^{NO2} and –8.7 kcal/mol for L^{OMe} (of course, it is predicted to be *endo*thermic to decoordinate the amine, but comparing data columns two and three of Table 2.5 permits us to quantify the enthalpy of CL coordination subsequent to arm *de*coordination). The same complexation enthalpies range from –8.5 to –3.1 kcal/mol when the amine arm remains coordinated (final two data columns of Table 2.5). As expected, the exothermicities are smaller, and the range of variation is smaller, when the coordinated amine decreases the Al Lewis acidity. We may also compare the enthalpic cost to decoordinate the amine arm *after* CL complexation: it ranges from 15.3 kcal/mol for L^{NO2} to 10.8 kcal/mol for L^{OMe}. We note that these are clearly upper bounds as coordination of a toluene solvent molecule to a vacant Al site may reduce these enthalpic costs, and this effect is not included in the calculations.

While it is tempting to compare the *measured* enthalpies of complexation in Table 2.4 with the computed enthalpies of complexation in Table 2.5, the complexity of the experimental situation does not permit such a straightforward comparison. Over the temperature range studied experimentally, the apparent complexation enthalpies (and

entropies) reflect averages over populations of arm-on and arm-off conformers that are themselves varying with temperature. In so far as none of the experimental ligands has an enthalpy of binding sufficiently negative to suggest that it exists solely as a population of arm-on conformers over the whole temperature range, it is not possible to use the theoretical data to make predictions about the apparent van't Hoff parameters in the absence of much more reliable estimates for entropy changes than can be obtained from the usual ideal-gas, rigid-rotator, harmonic-oscillator approximations that are typically combined with electronic structure calculations to estimate solute partition functions. Taken as a whole, however, the density functional predictions provide good support for the experimental interpretation of arm-on and arm-off isomers contributing differentially to the equilibrium populations of many of the studied catalyst-CL complexes, and in particular suggest that arm decoordination will be much more facile for the L^{OMe} ligand whether before or after CL complexation.

2.4 Summary and Conclusions

Through the use of ^{1}H NMR spectroscopy, saturation kinetics in the polymerization of CL by a series of Al catalysts was measured, thus enabling dissection of the typically observed composite propagation constant into separate insertion (k_2) and monomer binding (K_{eq}) parameters. By analysis of the trends in these parameters as a function of the electronic characteristics of remote supporting ligand substituents and temperature, thermodynamic information on the separate insertion and monomer binding steps was obtained. The overall slower rates observed for complexes with electron withdrawing substituents is seen to derive entirely from k_2, as reflected by an average ρ = -1.02(8) in log(k_2) vs. σ_p plots over a range of temperatures. Analysis of activation parameters for k_2 show that entropic effects are predominant determinants of the trends in the rate constants. The trends in K_{eq} as a function of substituent and temperature are more complicated, with changes in thermodynamic parameters that we interpret as deriving from populations of species both pre- and post-complexation that consist of structures having either a bound or unbound dimethylamino arm (Scheme 2.3). Variable temperature NMR data acquired for complex **1** both with and without added pyridine, the binding of which models CL coordination during catalysis, are consistent with lability of the dimethylamino arm. Results from theory support the hypothesis that amino decoordination is less enthalpically unfavorable with ligands substituted by electron-donating groups, and such decoordination is evidently more important to binding over the temperature range examined here based on the more positive apparent entropy of complexation determined from van't Hoff analysis.

While the mechanistic insights provided herein are unique to the particular catalyst system studied and for polymerization of one lactone, CL, they nonetheless have important broader implications for how other catalysts might operate and for the design

of new ones, particularly in view of the general significance of catalytic syntheses of sustainable materials.[15,23,38,91,92] Electronic variation of supporting ligand substituents clearly can have multiple influences during a polymerization process, and it would appear that differences in the relative importance of these influences (i.e., on insertion and substrate coordination) likely underlie the contradictory rate trends that have been observed in the literature. These factors can be understood through dissection of what are usually composite propagation rate constants, an approach that has much promise for future studies of catalysts other than those studied herein. The applicability of this methodology is demonstrated in Chapter 3, where these same general principles are applied to a more rigid aluminum-based catalyst system with both opposite electronic trends to the complexes in this chapter and less propensity for a ligand arm to decoordinate, potentially allowing for a clearer picture of how electronic variation affects binding and insertion of monomer to the catalyst.

2.5 Experimental Section

2.5.1 General Considerations

All reactions were carried out under an inert atmosphere using standard Schlenk and drybox techniques, unless otherwise indicated. Reagents were obtained from commercial suppliers and used as received unless otherwise indicated. CL was purified by distillation from CaH_2 and stored under N_2. Deuterated solvents were dried over CaH_2 or sodium, distilled under vacuum and stored under N_2. Protiated solvents were degassed and passed through a solvent purification system (Glass Contour, Laguna CA) prior to use. The ligands[105,119,120] and complexes with R = OMe and Br, as well as 2-*tert*-butyl-4-nitrophenol[121] were prepared by published methods. ^{1}H NMR spectra were recorded on a Varian VI-300 NMR spectrometer and their chemical shifts (δ) for ^{1}H spectra are referenced to residual protium in the deuterated solvent. The temperature of the probe was calibrated using an ethylene glycol standard for kinetics experiments. Variable low-temperature NMR studies were performed on a Bruker Avance III 500 MHz spectrometer equipped with a BBFO SmartProbe. The temperature of the probe was calibrated using a methanol standard. The two methoxy resonances in the VT-^{1}H NMR spectra of **1** were fit using Topspin 3.1 DNMR program as independent spin systems using simplex iterations and fit on chemical shift (δ), intensity, and rate constant (k).

2.5.2 Synthetic Procedures

***N*,*N*-Bis[methyl-(2-hydroxy-3-*tert*-butyl-5-nitrophenyl)]-*N*,*N*-dimethylethylenediamine (L^{NO2}).** 2-*tert*-Butyl-4-nitrophenol (3.1245 g, 16 mmol), *N*,*N*-dimethylethylenediamine (0.88 mL, 8.1 mmol), paraformaldehyde (0.6349, 21.1 mmol), and 50 mL of absolute ethanol were added to a 350 mL screw cap bomb flask. The flask was sealed and heated to 125 °C and allowed to react for 24 hours. After allowed the flask to come to room temperature, the flask was opened in air and cooled to -20 °C. A

precipitate formed and was filtered over a glass frit and washed with ice-cooled methanol (50 mL). The product was dissolved in minimum CH_2Cl_2 and recrystallized from ethanol at 0 °C to give an off white powder (0.7840 g, 20%). ^{1}H NMR (300 MHz, CD_2Cl_2): δ 8.11 (d, 2H, J = 2.7 Hz), 7.90 (d, 2H, J = 2.7 Hz), 3.71 (s, 4H), 2.69 (s, 4H), 2.37 (s, 6H), 1.38 (s, 18H). Anal. Calcd for $C_{26}H_{38}N_4O_6$: C 62.13, H 7.62, N 11.15. Found: C 62.23, H 7.78, N 11.13.

(L^R)Al(O*i*Pr) (3, R = NO_2). In a nitrogen-filled glove box, an oven-dried 15 mL screw cap bomb flask was charged with aluminum *iso*-propoxide (125.1 mg, 0.61 mmol), *N*,*N*-bis[methyl-(2-hydroxy-3-tert-butyl-5-nitrophenyl)]-*N*',*N*'-dimethylethylenediamine (309.3 mg, 0.62 mmol), and 3 mL of toluene. The flask was sealed, removed from the glove box, heated to 85 °C and allowed to stir for 2 days. After the reaction time had completed, the flask was cooled and returned to the glove box. A precipitate had formed upon cooling. The toluene was removed *in vacuo*, and the remaining off-white powder was triturated three times with 5 mL of pentane. The product was recrystallized from CH_2Cl_2 and pentane (243.4 mg, 70%). ^{1}H NMR (300 MHz, CD_2Cl_2): δ 8.15 (d, 2H, J = 3.0 Hz), 7.86 (d, 2H, J = 3.0 Hz), 4.63 (septet, 1H, J = 5.7 Hz), 3.76 (app d, 2H, J = 13.2 Hz), 3.56 (app d, 2H, J = 13.2 Hz), 2.79 (m, 4H), 2.67 (s, 6H), 1.43 (s, 18H), 1.20 (d, 6H, J = 6 Hz). Anal. Calcd for $C_{29}H_{43}AlN_4O_7$: C 59.37, H 7.39, N 9.55. Found: C 58.60, H 7.10, N 9.28.

2.5.3 ^{1}H NMR Spectroscopy Kinetic Analyses

A representative procedure for the kinetic studies is described. To an oven-dried NMR tube in a nitrogen filled glove box, 500 μL of a stock solution of catalyst in toluene-d_8 (0.0092 M) and 10 μL of the internal standard bis(*para*-trimethylsilyl)benzene in toluene-d_8 (0.28 M) were added. The NMR tube was capped with a septum and wrapped with parafilm. A gas tight syringe was loaded with 190 μL of ε-caprolactone

(CL) stock solution (7.4 M), also in toluene-d_8. The target final concentrations of catalyst, internal standard and CL were 0.007 M, 0.004 M, and 2 M, respectively. The gas tight syringe containing CL was inserted into a rubber septum to prevent air contamination during the experiment setup. The NMR tube and syringe were removed from the glove box and brought to the spectrometer. The temperature on the NMR spectrometer (300 MHz Varian Inova) was calibrated using an ethylene glycol standard. The catalyst and internal standard mixture was calibrated to a 30° pulse width, and a ^{1}H NMR spectrum was taken with the calibrated 30° pulse width, spin rate of 16 Hz, and delay time of 10 seconds to obtain accurate catalyst integrations. Next, the tube was ejected from the spectrometer and CL was injected through the septum into the NMR tube. The contents of the tube were well mixed before reinserting the NMR tube into the spectrometer. Using the previously calibrated 30° pulse width, an arrayed set of spectra were taken at 96, 192, or 384 seconds with 8, 16, or 32 scans, respectively, spin rate of 16 Hz, acquisition time 2 seconds, and a delay time of 10 seconds to complete relaxation of spins and accurate integrations. The gain was adjusted such that it was as high as possible. The arrayed experiment was allowed to proceed until polymerization had completed (monitored by the disappearance of the CL residues). For each catalyst, four temperatures were carefully chosen, and three reactions were repeated at that temperature. The obtained arrayed NMR data were phased and baseline corrected before being integrated by Mestrenova (a chemistry software for NMR analysis, http://mestrelab.com/). The integrations were recorded and entered into an Excel spreadsheet. Absolute concentrations of all species as a function of time were computed relative to the concentration of internal standard. Reaction time was calculated in seconds from the known length of time per spectrum. For the RPKA analysis, the kinetic parameters were extracted from the time-dependent concentration data by fitting to an arbitrary *n*th order

polynomial function (e.g., a 9th order polynomial, $[CL] = a_0 + a_1t + \ldots + a_9t^9$) and differentiating this function with respect to time ($d[CL]/dt = a_1 + 2a_2t \ldots + 9a_9t^8$) to obtain instantaneous rate data. Kinetic parameters were determined by best fit to the Michaelis-Menten equation, (Equation 2.1); representative fits are shown in Figure 2.5. For the COPASI analysis, the concentration *vs.* time data obtained from the ^{1}H NMR data were input into COPASI program and fitted with Michaelis-Menten model (Equation 2.1) to obtain K_M and k_2 values. The reaction rates were calculated by Equation 2.1 and plotted as a function of concentration. Kinetic parameters determined by COPASI (average over 3 trials) are listed in Table 2.2. All linear and non-linear curve fits were performed using Graphpad Prism or Origin software. In general for all COPASI fits, concentrations of both CL and PCL *vs*. time data were input into the program. Initial values for the respective kinetic parameters of k_1/k_2, = 0.0001, k_2 = 0.0001, V_{max} = 0.001, and/or K_M = 1 were used (depending on the equation used for fitting; $K_M = 1/K_{eq}$). In addition, the program was allowed to fit both the initial concentrations of CL and PCL, with $[CL]_0$ bound from $-\infty$ to $+\infty$ and given an initial starting value of 2 M and $[PCL]_0$ bound from 0 to $+\infty$ and given an initial starting value of 0 M. The Levenberg-Marquardt method of fitting was used with an iteration limit of 20000 and a tolerance of $1x10^{-10}$. Both [PCL] and [CL] were fit simultaneously by the program and the fits were run repeatedly with updated parameters until the fit stopped changing. For the linearized forms of the first- (Equation 2.4) and second- (Equation 2.6) order fits, the same data was linearized, plotted and fit to a straight line ($y = mx + b$).

2.5.4 Derivation of Equation 2.7

$$\delta = \frac{\sum c_i \delta_i}{\sum c_i};$$

$$f(coord) = catalyst\ fraction\ coordinated = 1 - f(uncoord);$$

$$\Delta\delta = observed\ chemical\ shift\ difference$$

$$[Al]_{tot} = [Al] + [Al \cdot CL]$$

$$\Delta\delta = \left(1 - \frac{[Al \cdot CL]}{[Al]_{tot}}\right)\Delta\delta_{uncoord} + \left(\frac{[Al \cdot CL]}{[Al]_{tot}}\right)\Delta\delta_{coord};$$

$$Michaelis\text{-}Menten\ relation\text{:}\ [Al \cdot CL] = \frac{[Al]_{tot}[CL]}{K_M + [CL]};$$

$$\frac{[Al \cdot CL]}{[Al]_{tot}} = \frac{[CL]}{K_M + [CL]};$$

$$\Delta\delta = \left(1 - \frac{[CL]}{K_M + [CL]}\right)\Delta\delta_{uncoord} + \left(\frac{[CL]}{K_M + [CL]}\right)\Delta\delta_{coord};$$

$$\Delta\delta = \Delta\delta_{uncoord} + \frac{(\Delta\delta_{uncoord} - \Delta\delta_{coord})[CL]}{K_M + [CL]}$$

2.5.5 Data and Error Analysis

The rate constants k_2 and the associated standard deviations were calculated using Equation 2.8 and Equation 2.9. Equation 2.9 is derived from standard indeterminate error analysis rules.[122]

Equation 2.8

$$k_2 = \frac{V_{\max}}{[Al]}$$

Equation 2.9

$$\sigma_{k_2} = \frac{V_{\max}}{[Al]}\left(\sqrt{\left(\frac{\sigma_{V_{\max}}}{V_{\max}}\right)^2 + \left(\frac{\sigma_{[Al]}}{[Al]}\right)^2}\right)$$

Error bars in the Erying and van't Hoff plots were determined by carrying the standard deviation in k_2 or K_{eq} throughout the calculations using standard indeterminate error analysis rules.[1] We assumed no error in the temperature for these calculations. For the Erying plots, all of the ln(k_2/T) data was plotted *vs.* 1/T and was fit to a standard

linear regression (y = mx + b) using GraphPad Prism version 5.0a for Mac OSX (GraphPad Software, San Diego California USA, www.graphpad.com). A similar procedure was followed for the van't Hoff plots, except ln(K_{eq}) was plotted *vs.* 1/T. The linear regressions and errors were used to determine the thermodynamic parameters from the linearized Erying (Equation 2.10) and van't Hoff (Equation 2.11) equations.[64] Indeterminate error analysis methods were used to propagate the error from the error in the regression to the error in the thermodynamic parameters.

Equation 2.10

$$\ln\frac{k_2}{T} = -\frac{\Delta H^{\ddagger}}{RT} + \ln\frac{k_B}{T} + \frac{\Delta S^{\ddagger}}{R}$$

Equation 2.11

$$\ln K_{eq} = -\frac{\Delta H^{\circ}}{RT} + \frac{\Delta S^{\circ}}{R}$$

The rate constants used in the Hammett plots of log(k_2) or log(K_{eq}) *vs.*σ_p that were not determined directly from the data were extrapolated from the thermodynamic parameters obtained from the Erying plot (k_2) and van't Hoff plot (K_{eq}). The Hammett plots were fit to a standard linear regression (y = mx+b) using GraphPad Prism version 5.0a for Mac OSX (GraphPad Software, San Diego California USA, www.graphpad.com) to determine ρ values.

2.5.6 Experimental Details for X-ray Crystal Structure of 4

After a typical kinetics run was completed, the NMR tube was allowed to sit at room temperature and X-ray quality crystals were grown in the NMR tube. To extract the crystals, the NMR tube was broken on a glass slide, and a crystal was removed before the polymer was allowed to solidify. A crystal (approximate dimensions 0.3 x 0.25 x 0.2 mm) was placed onto the tip of a 0.1 mm diameter glass capillary and mounted on a

Bruker APEX II, CCD area detector diffractometer for a data collection at 173(2) K.[123] A preliminary set of cell constants was calculated from reflections harvested from three sets of 20 frames. These initial sets of frames were oriented such that orthogonal wedges of reciprocal space were surveyed. This produced initial orientation matrices determined from 287 reflections. The data collection was carried out using MoKα radiation (graphite monochromator) with a frame time of 60 seconds and a detector distance of 6 cm. A randomly oriented region of reciprocal space was surveyed to the extent of one sphere and to a resolution of 0.77 Å. Four major sections of frames were collected with 0.30º steps in ω at four different φ settings and a detector position of -28º in 2θ. The intensity data were corrected for absorption and decay (SADABS).[124] Final cell constants were calculated from the xyz centroids of 8419 strong reflections from the actual data collection after integration (SAINT).[125] The structure was solved using SHELXS-97 (Sheldrick, 2000)[5] and refined using SHELXL-97 (Sheldrick, 2000).[126] The space group C2/c was determined based on systematic absences and intensity statistics. A direct-methods solution was calculated which provided most non-hydrogen atoms from the E-map. Full-matrix least squares / difference Fourier cycles were performed which located the remaining non-hydrogen atoms. All non-hydrogen atoms were refined with anisotropic displacement parameters. All hydrogen atoms were placed in ideal positions and refined as riding atoms with relative isotropic displacement parameters, except the hydrogens on the bridging OH moieties. These were placed from the difference map. The final full matrix least squares refinement converged to $R1 = 0.0490$ and $wR2 = 0.1331$ (F^2, all data).

There is some positional disorder in the toluene-d_8 molecule, where the toluene occupies two positions (80% majority, 20% minority). Additionally, the toluene-d_8 molecules were initially refined with hydrogen atoms until convergence, and then were

replaced with deuterium atoms. The toluene molecules were then modeled as rigid groups to prevent the refinement from becoming unstable. It is a known problem that the AFIX commands in SHELX, which place constraints on atoms, cannot be used on both H and D atoms. Modeling each entire toluene-d_8 molecule as a rigid group is a solution to this problem, and allowed the refinement to converge with fully deuterated toluene molecules. Further refinement was carried out on the deuterated molecules and no shifting occurred after the atom change. There is also some positional disorder in one of the NO_2 groups that are part of the ligand. The disordered NO_2 group was modeled with four oxygen atoms (88% major, 12% minor), and constraints were applied to ensure anisotropic displacement parameters were equivalent for each pair of oxygens. There is also some disorder in the *tert*-butyl groups on the ligand, but this disorder was not modeled, as it is minor and would not drastically improve the quality of the structural solution.

2.5.7 Theoretical methods

(Performed by Eric D. Hermes and Christopher J. Cramer)

Gas-phase geometries were fully optimized at the density functional level of theory making use of the M06-L functional,[127] the 6-31G(d) basis set,[128] and an additional automatically generated density fitting basis set employed to speed integral evaluation. All structures were characterized as local minima from computation of analytic vibrational frequencies, which were also used to construct 333 K molecular partition functions using the ideal-gas, rigid-rotator, harmonic-oscillator approximation.[129] In the vibrational partition function, all frequencies below 50 cm^{-1} were replaced with a value of 50 cm^{-1} to correct for the inadequacy of the harmonic-oscillator approximation for such normal modes, and thermochemical contributions to enthalpies and entropies were computed from the resulting M06-L partition functions.[129]

The thermochemical contributions were added to single-point energies computed with the M06-2X functional[130] and the 6-311+G(d,p) basis set.[128] The M06-2X functional is particularly appropriate for these large, primarily organic architectures, where dispersion interactions between bulky groups may play a key role in stabilizing particular geometries and complexes.[131, 132] The single point M06-2X calculations also included the effects of toluene solvation with the SMD continuum solvation model.[133] All thermochemistries are reported for a standard state of 1 M (consistent with the usual experimental convention).[129] We assume that the computed free energies of solvation are dominated by enthalpic effects, and thus include them in full in both reported enthalpies and free energies in discussion.

All calculations were accomplished with the Gaussian 09 electronic structure program suite.[134]

2.6 Acknowledgements

This work was funded by the National Science Foundation (CHE-0610183 and -0952054 to C. J. C, -0842654 to W. B. T. and M. A. H. and a Graduate Research Fellowship under Grant No. 00006595 to M. O. M.) and the Center for Sustainable Polymers, a National Science Foundation supported Center for Chemical Innovation (CHE-1136607) for financial support of this research.

3 Understanding the Mechanism of Polymerization of ε-Caprolactone Catalyzed by Aluminum Salen Complexes

In part from:

Maria O. Miranda, Yvonne DePorre, Hugo Vazquez-Lima, Michelle A. Johnson, Daniel J. Marell, Christopher J. Cramer, and William B. Tolman. *Inorganic Chemistry*, **2013**, *52*, 13692-13701.

3.1 Overview

Studies of the kinetics of polymerization of ε-caprolactone (CL) by salen-aluminum catalysts comprising ligands with similar steric profiles but different electron donating characteristics (R = OMe, Br, or NO_2) were performed using high initial monomer concentrations (2 M < $[CL]_0$ < 2.6 M) in toluene-d_8 at temperatures ranging from 20 °C to 90 °C. Saturation behavior was observed, enabling determination of monomer equilibrium constants (K_{eq}) and catalytic rate constants (k_2) as a function of R and temperature. While K_{eq} varied only slightly with the electron donating properties of R (Hammett ρ = + 0.16(8)), k_2 showed a more significant dependence reflected by ρ = +1.4(1). Thermodynamic parameters $\Delta G°$ (associated with K_{eq}) and $\Delta G^{‡}$ (associated with k_2) were determined, with the former being ~0 kcal/mol for all catalysts and the latter exhibiting the trend R = OMe > Br > NO_2. DFT calculations were performed to characterize mechanistic pathways at a microscopic level of detail. Lowest energy transition-state structures feature incipient bonding of the nucleophile to the lactone carbonyl that is approaching the metal ion, but a distinct CL adduct is *not* an energy minimum on the reaction pathway, arguing against K_{eq} being associated with coordination of monomer according to the typical coordination-insertion mechanism. An alternative hypothesis is presented associating K_{eq} with 'nonproductive' coordination of substrate in a manner that *inhibits* the polymerization reaction at high substrate concentrations.

3.2 Introduction

Chapter 1 enumerates the importance of ring-opening polymerization (ROP) of cyclic esters as an important method for converting renewable resources to aliphatic polyesters, sustainable materials useful for myriad applications and as potential alternatives to petrochemical polymers.[135,136] Polymerization of monomers like lactide (LA) and ε-caprolactone (CL) have been particularly well studied using a variety of polymerization methods.[9,15,16,23,91] Metal-alkoxide catalysts are often employed as ROP catalysts in both academic and industrial settings, and are especially attractive because of their ability to generate high molecular weight polymers in controlled fashion, with low polydispersities, and with maintenance of end-group fidelity.[9,15,23,91]

The mechanistic paradigm for ROP by single-site metal alkoxide catalysts is the so-called 'coordination-insertion' pathway (Figure 3.1). According to this mechanism, monomer coordinates through the carbonyl oxygen to a vacant site on the Lewis acidic metal (K_{eq}), followed by alkoxide insertion into the activated carbonyl carbon (k_2) and ring-opening to generate a new propagating alkoxide. While widely accepted, significant gaps in our understanding of this mechanism remain. For example, variable electronic and steric effects of supporting ligands on rates of ROP catalyzed by metal alkoxide complexes raise questions about the relative importance of monomer binding, alkoxide nucleophilicity, or both in controlling polymerization reactivity. Thus, for various salen aluminum catalysts, the groups of Gibson and Nomura both observed increased rates for

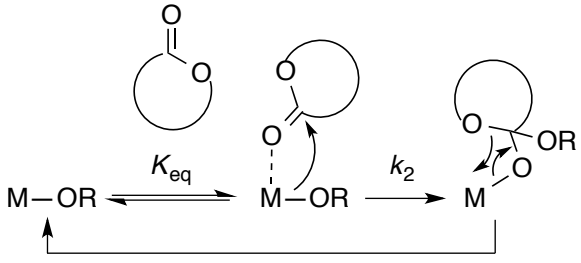

Figure 3.1. Coordination-insertion mechanism for the polymerization of cyclic esters.

the polymerization of LA when the ligands were substituted with electron-withdrawing groups (EWGs).[99,137] They postulated the enhancement is due to increased Lewis acidity of the aluminum, which boosts monomer binding and activation. Another study using a dinuclear salan aluminum complex found contradictory rate trends between monomers; in the case of LA polymerization, EWGs increased the rate, whereas in the case of CL polymerization, the opposite effect was observed.[138] Rate attenuation by EWGs has also been observed for titanium salen complexes,[100] magnesium complexes bearing benzenesulfonate phenol ligands,[101] and some aluminum alkoxide complexes supported by bis(phenolate)diamine ligands (**1**).[105]

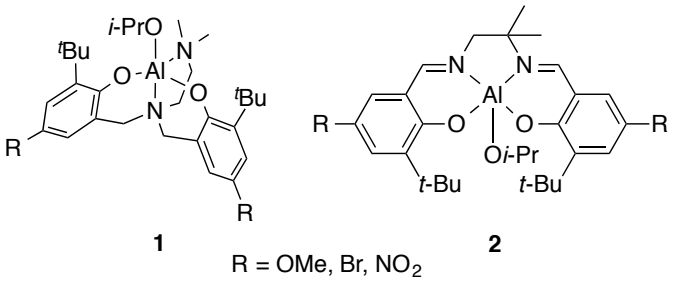

Figure 3.2. Complexes studied in Chapter 2 (**1**) and this chapter (**2**).

In Chapter 2 we examined the kinetics of CL polymerization catalyzed by the latter aluminum alkoxide complexes (Figure 3.2, **1**) in detail.[139] We found that by studying the reactions using high concentrations of monomer, saturation kinetics were observed, enabling determination of a monomer binding equilibrium constant, K_{eq}, and a catalytic rate constant, k_2, that we attributed to the coordination and insertion steps, respectively, by fitting to Equation 3.1. The data showed that the origin of the rate differences across the series of catalysts is entirely due to differences in k_2, and on the basis of both experiment and theory we argued that the nucleophilicity of the alkoxide is the determining factor (increasing nucleophilicity with increasing electron-donation). However, analysis of the catalytic activity of **1** was complicated by the potential for decoordination of the dimethylalkylamino arm of the polydentate ligand.

Equation 3.1

$$-\frac{d[CL]}{dt} = \frac{d[PCL]}{dt} = \frac{k_2[\mathbf{2}][CL]}{1/K_{eq} + [CL]}$$

$$V_{\max} = k_2[\mathbf{2}]$$

With the aim of further understanding the diverse electronic and steric effects of ligand substituents on the ROP efficiencies of metal alkoxide complexes, we turned our attention to aluminum complexes supported by salen-type ligands (Figure 3.2, **2**), where decoordination of the ligand from the metal ion is unlikely. Such Schiff base complexes have been used extensively in catalysis,[140,141] and (with variable substituents and linkers between the imino nitrogen atoms) are notably effective for ROP of a variety of lactones.[54–57,69,95,99,137,142–149] Published kinetic/mechanistic studies of ROP catalyzed by Schiff base Al compounds have provided important information, such as ligand structural effects on ROP rates for a variety of lactones[148] (cf. the aforementioned rate enhancement of LA polymerization by electron withdrawing ligand substituents),[99,137] ^{1}H NMR spectroscopic evidence for reversible LA coordination to the catalyst,[95] and the basis for observed poly(lactide) (PLA) tacticity in stereospecific polymerizations.[55–57,95,142,143,146]

In this chapter the results of detailed kinetic studies of CL polymerization by well-characterized, monomeric aluminum salen complexes with identical steric profiles but variable remote substituents with differing electron donating characteristics (**2**) are reported. Using our previously described methodology involving ^{1}H NMR spectroscopic analysis of ROP kinetics performed with high initial monomer concentrations,[139] we again observed saturation behavior that enabled determination of K_{eq} and k_2 values for the catalyst series **2**, but with trends opposite to that seen for **1**. Density functional theory (DFT) calculations were performed in order to rationalize the kinetic data, and provided key mechanistic insights, including a new rationale for the experimental rate law that has significant, broader implications for evaluating metal-alkoxide catalyzed ROP kinetics.

3.3 Results and Discussion

3.3.1 Synthesis and Characterization of Ligands and Catalysts

The ligands required to synthesize complexes **2** (R = OMe, Br, NO_2) were prepared using a traditional imine condensation between the three differently substituted salicylaldehydes and 2-methylpropane-1,2-diamine in yields ranging from 35% (R = Br) to 98% (R = OMe). Complexes **2** were synthesized in high yields (84-97%) via thermolysis of equimolar amounts of ligand and aluminum tris(*iso*-propoxide) in toluene. Complexes **2** (R = Br, NO_2) were isolated as analytically pure yellow and light brown solids, respectively, directly from the reaction mixture, whereas **2** (R = OMe) required recrystallization from toluene and pentane to isolate pure, bright yellow, material. The compounds are air- and moisture-sensitive and soluble in chlorinated (dichloromethane) and aromatic hydrocarbon (toluene) solvents. As in the case of their ligands, the catalysts have similar features in their ^{1}H NMR spectra, with the most significant differences being in the aryl region; the aryl residues shift downfield as the electron-withdrawing nature of the catalyst increases. In solution the complexes appear monomeric, as expected because of the presence of the *t*-butyl substituents[150] and as indicated by a single set of resonances in their ^{1}H NMR spectra and a single resonance in their ^{27}Al NMR spectra at 35, 34 and 33 ppm (R = OMe, Br, or NO_2, respectively). This ^{27}Al NMR chemical shift region is indicative of a five-coordinate aluminum center, and matches that reported previously for a pentacoordinate salen-type aluminum alkoxide (35 ppm).[69,143,151,152]

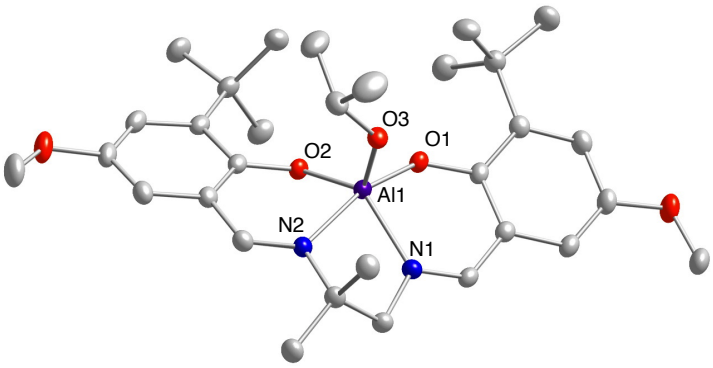

Figure 3.3. Representation of the X-ray crystal structure of 2 (R = OMe), showing nonhydrogen atoms as 50% thermal ellipsoids. Selected interatomic distances (Å) and angles (deg): Al1−O1, 1.8107(13); Al1−O2, 1.7899(12); Al1−O3, 1.7292(13); Al1−N1, 2.0042(14); Al1−N2, 2.0445(15); O3−Al1−O2, 115.98(6); O3−Al1−O1, 100.22(6); O2−Al1−O1, 97.57(6); O3−Al1−N1, 113.60(6); O2−Al1−N1, 129.72(6); O1−Al1−N1, 87,59(6); O3−Al1−N2, 96.96(6); O2−Al1−N2, 88.00(6); O1−Al1−N2, 161.05(6); N1−Al1−N2, 78.22(6).

In addition, a crystal of **2** (R = OMe) suitable for X-ray diffraction was obtained from a toluene/hexane mixture at −40 °C. The structure (Figure 3.3) features a monomeric complex with a 5-coordinate aluminum ion in a geometry between square pyramidal and trigonal bipyramidal ($\tau = 0.52$).[95] Other structures of complexes with the 2-methylpropane-1,2-diamine backbone display similarly intermediate τ parameters ($0.48 < \tau < 0.56$); bond distances and angles are consistent with other aluminum salen-type structures.[99,137,146,150,152,153]

3.3.2 Polymerization Kinetics

Polymerizations of CL using catalysts **2** were performed in triplicate with a fixed initial concentrations of CL ($2\ M < [CL]_0 < 2.6\ M$) and catalyst ($5.5\ mM < [\mathbf{2}]_0 < 7\ mM$) in toluene-$d_8$ at temperatures ranging from 20 °C to 90 °C. As in a previous study[139] and Chapter 2, features due to the growth of polymer and decay of monomer were monitored by ^{1}H NMR spectroscopy to polymerization completion (conversions > 99%) and their concentrations as a function of time were fit to the Michaelis-Menten expression

(Equation 2.1) using the global kinetics fitting program COPASI (version 4.8).[109] Good agreement between the fit and the data was obtained (representative plot in Figure 3.4). These fits, and curved rate *vs*. [CL] plots derived from both the COPASI analysis (Figure 3.5) and a reaction progress kinetic analysis[111] (presented in section 3.3.2.1) support saturation behavior; significantly poorer fits were obtained using simpler first- or second-order rate equations (presented in section 3.3.2.2). Average values from replicate runs for K_{eq} and k_2 are listed in Table 3.1. In addition, independent measurements of K_{eq} were obtained by analyzing observed changes in the chemical shift of the aryl and imine catalyst residues (Figure 3.6) as a function of time and [CL], using Equation 3.2, as in Chapter 2 (fits shown in Figure 3.7).[139] Comparison of these K_{eq} values with those obtained from the averaged COPASI fits shows reasonable agreement between the independently calculated parameters (Table 3.1), providing further evidence for the validity of Equation 3.1. The data are thus consistent with the typical kinetic model associated with eq. 1 involving pre-equlibrium monomer binding followed by insertion, but other kinetic models described by Equation 3.1 are also possible (vide infra).

Equation 3.2

$$\Delta\delta = \Delta\delta_{uncoord} + \frac{(\Delta\delta_{uncoord} - \Delta\delta_{coord})[CL]}{K_M + [CL]}$$

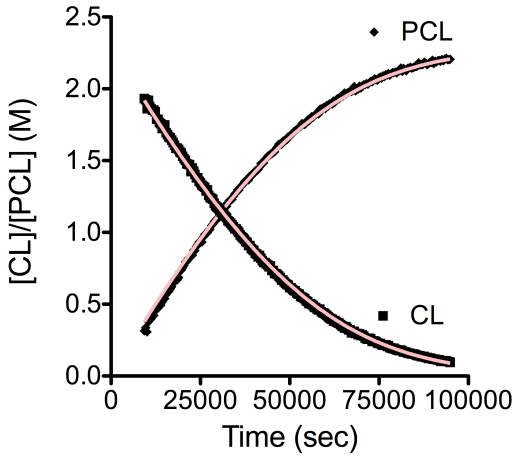

Figure 3.4. Illustrative conversion *vs.* time profile for decay of CL (■) and growth of PCL (◆) resonances during ROP catalyzed by R = OMe at 333 K, determined from ^{1}H NMR spectra, along with fits (–) determined by COPASI.

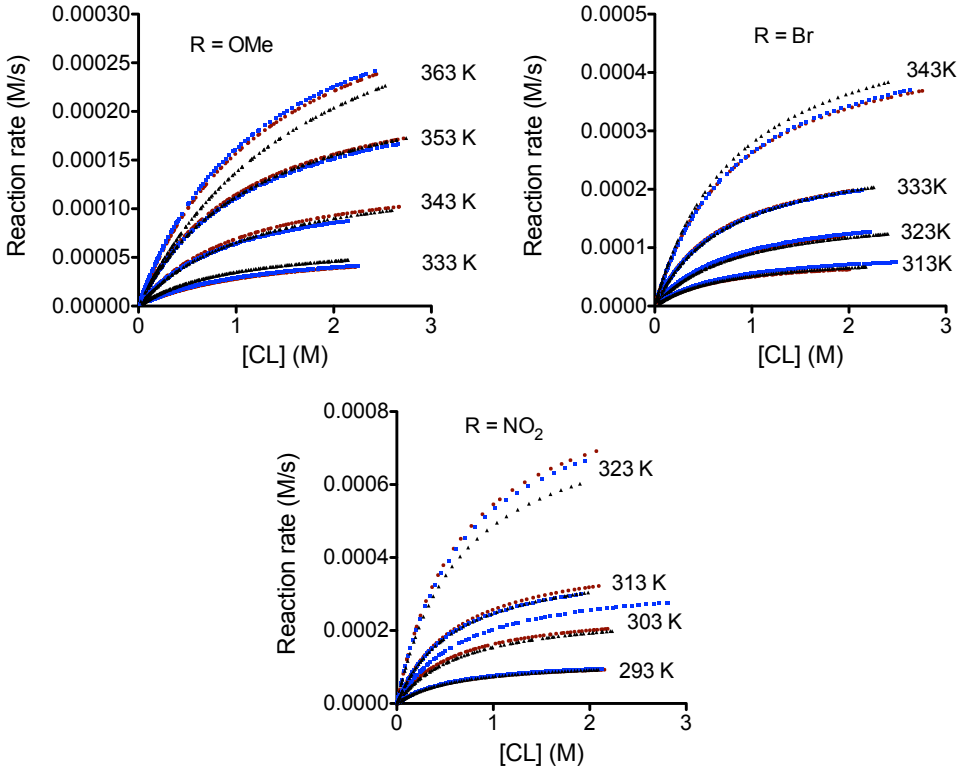

Figure 3.5. Plots of rate *vs*. [CL] for polymerizations of CL by R = OMe, R = Br, and R = NO_2. Plots were generated using COPASI fit parameters (V_{max} and K_M), measured CL concentrations and **Equation 3.1**.

Table 3.1. Average values of kinetic parameters determined from COPASI fits and ^{1}H NMR peak analysis.

Entry	Temp (K)	R	K_{eq} COPASI (M^{-1}) [a]	K_{eq} NMR (M^{-1}) [b]	k_2 (s^{-1}) ($x10^2$)
1	333	OMe	0.9(1)	0.70(5)	1.00(3)
2	343	OMe	0.92(9)	0.54(7)	2.1(1)
3	353	OMe	0.86(3)	0.56(5)	3.8(1)
4	363	OMe	0.7(1)	0.50(7)	5.9(1)
5	313	Br	1.38(8)	0.83(6)	1.39(8)
6	323	Br	1.19(5)	0.8(1)	2.7(1)
7	333	Br	1.37(6)	0.76(4)	4.3(2)
8	343	Br	1.16(2)	0.64(5)	7.9(6)
9	293	NO_2	1.64(5)	2.2(3)	2.34(6)
10	303	NO_2	1.5(1)	1.7(2)	5.2(5)
11	313	NO_2	1.66(7)	1.7(3)	8.0(4)
12	323	NO_2	1.45(4)	1.5(1)	15.4(8)

[a] Detemined from COPASI analysis of kinetic data. [b] Average of all K_{eq} values determined from the $\Delta\delta$ (NMR) analysis for triplicate runs at each temperature.

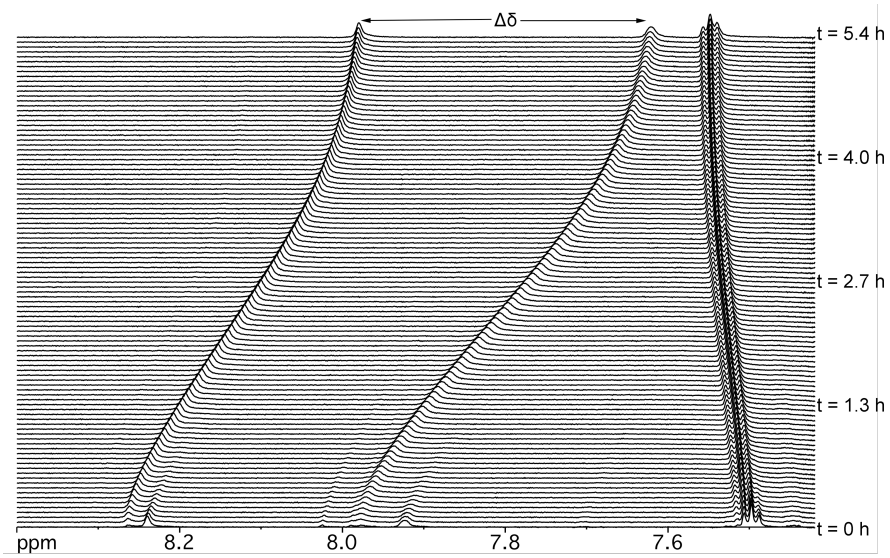

Figure 3.6. Portion of the ^{1}H NMR spectra acquired during polymerization of CL by 2 (R = Br) at 333 K illustrating how the aryl resonances of the complex in solution change as a function of reaction time. The indicated peak separation was used to independently evaluate K_{eq} (see **Equation 3.2**). Note the conversion of the catalyst during early reaction times (t = 0-1 hr) that is modeled in **Figure 3.13**.

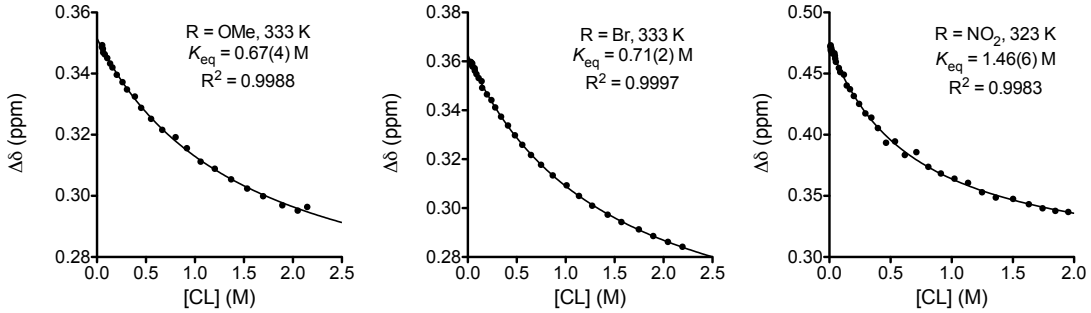

Figure 3.7. Representative plots of Δδ as a function of [CL] determined from the difference between the imine catalyst residues of catalyst 2 (R = OMe, left; R = Br, middle; R = NO_2, right) at 333 or 323 K. Data points (•) were fit (−) to **Equation 3.2**, yielding the K_{eq} shown.

3.3.2.1 Reaction Progress Kinetic Analysis

An independent evaluation by a reaction progress kinetic analysis (RPKA)[111] further supports the conclusion that saturation kinetics is appropriate. When the [CL] *vs*. time profile is fit to a polynomial of order n ($2 \leq n \leq 9$) and the derivative of that polynomial is taken, a rate *vs*. [CL] profile may be obtained to which the saturation

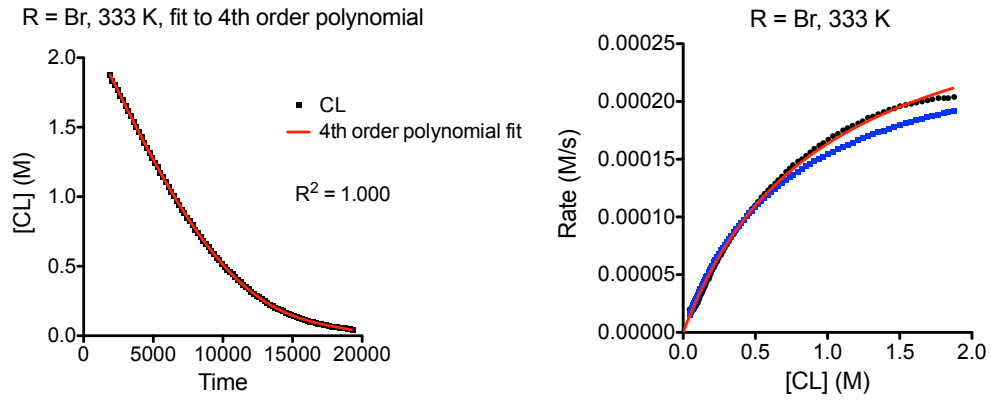

Figure 3.8. Left: [CL] *vs*. time data (black) and fit to fourth order polynomial ($y = a + bx + cx^2 + dx^3 + ex^4$ red) for catalyst **2** (R = Br) at 333 K. Right: derivative of obtained polynomial ($y' = b + 2cx + 3dx^2 + 4ex^3$) *vs*. [CL] (black), with a non-linear fit to **Equation 3.1** (red; R^2 = 0.9982) and obtained COPASI fit parameters (as in **Figure 3.5**).

kinetics Equation 3.1 can be fit. Chapter 2 demonstrated how the order *n* of the polynomial affects the fit, and after applying this analysis, it was determined that a polynomial of order 4 was sufficient to fit the data without magnifying the natural noise – a phenomenon that occurs with higher order polynomial fits.[139] The polynomial and derivative data (black) and fits (red) are shown in Figure 3.8, along with an overlay of the calculated rate *vs*. [CL] as described in the caption of Figure 3.5 (blue). Clear saturation is observed in the rate *vs*. [CL] profile obtained from the RPKA, with good agreement between the COPASI analysis and the RPKA, notably when K_M and V_{max} are compared (Table 3.2).

Table 3.2. Comparison of saturation kinetic parameters obtained from COPASI, RPKA and NMR Δδ analysis for polymerization of CL by **2** (R = Br) at 333 K.

Analysis type	K_{eq} (M^{-1})	V_{max} (M/s) (x10^5)
COPASI	1.38(2)	26.6(2)
RPKA	1.05(2)	32.0(3)
NMR Δδ analysis	0.76(4)	-

3.3.2.2 Fits to First- and Second-Order Rate Equations

In order to test the assignment of the observed polymerization rate data to saturation kinetics, we attempted to fit the data to first-order and second-order rate equations (Equation 3.3 or Equation 3.5) using both COPASI and linearized forms of the rate equations (Equation 3.4 or Equation 3.6). For the linearized forms of the first- (Equation 3.4) and second- (Equation 3.6) order fits, the same data was linearized, plotted and fit to a straight line (y = mx + b).

Equation 3.3

$$-\frac{d[CL]}{dt} = k_1[CL]$$

Equation 3.4

$$\ln\left(\frac{[CL]_0}{[CL]_t}\right) = k_1 t$$

Equation 3.5

$$-\frac{d[CL]}{dt} = k_{2'}[CL]^2$$

Equation 3.6

$$\frac{1}{[CL]_t} - \frac{1}{[CL]_0} = k_{2'}t$$

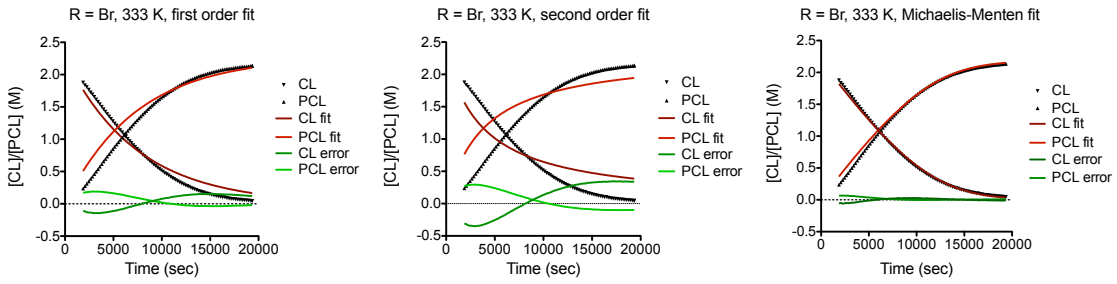

Figure 3.9. Results from COPASI fits to the kinetic data for the polymerization of CL by **2** (R = Br) at 333 K. Data are shown in black and fits to first-order (left), second-order (middle), and Michaelis-Menten (right) rate equations are shown in red, with errors shown in green.

The COPASI fits to first- and second-order equations (Equation 3.3 and Equation 3.6) using the entire concentration range studied ($[CL]_0$ = 2 M) are compared to the fit to Equation 3.1 in the text (saturation kinetics) for catalyst **2** (R = Br) at 333 K in Figure 3.9. Fits of the [CL] data to the linearized Equation 3.4 and Equation 3.6 are shown in Figure 3.10. These plots are illustrative; similar analyses of data for other catalysts at other temperatures were obtained, but are not shown. It is clear from these plots that the fits to the first- and second-order rate equations are inappropriate, and inferior to the fit to the saturation kinetics equation (Equation 3.1).

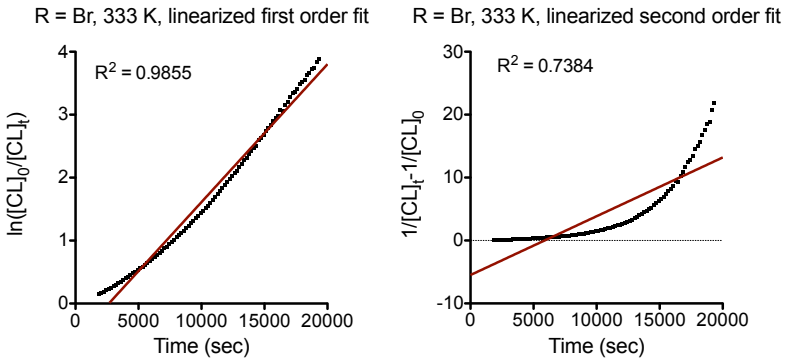

Figure 3.10. Linearized data (black) for first- (left) and second-order (right) rate equations with calculated linear fits (red).

It is informative to compare the results of first-order and saturation kinetics fits to the data over two different concentration ranges, starting from $[CL]_0$ = 1 M or $[CL]_0$ = 2 M. In this analysis, no data for the concentration of PCL was used, and the fits were generated as described above using COPASI, except with $[CL]_0$ = 1 M or $[CL]_0$ = 2 M. As shown in Figure 3.11, the fits for $[CL]_0$ = 2 M obtained from COPASI for both the saturation kinetics case (Equation 3.1) and first-order case (Equation 3.3) are visibly different from one another in the concentration *vs*. time profile, and this difference is highlighted in the error plot, where the first-order fit has significantly more associated

error than the saturation kinetics fit. Interestingly, with $[CL]_0 = 1$ M, the fits are nearly indistinguishable, as reflected by comparable errors for both. Similarly, if the data are truncated such that $[CL]_0 = 1$ M and the linearized form of the first-order rate equation is applied (Figure 3.11e), the fit is improved compared to when the entire data set ($[CL]_0 = 2$ M) is used. Taken together, these plots indicate that at $[CL]_0 \leq 1$ M, the first-order and saturation kinetics fits are indistinguishable, and that only by raising $[CL]_0$ can clear evidence for saturation behavior be obtained. This conclusion is relevant to the recent analysis performed by Pepels *et al*,[148] where saturation kinetics were not observed under conditions where $[\text{monomer}]_0 \leq 1$ M.

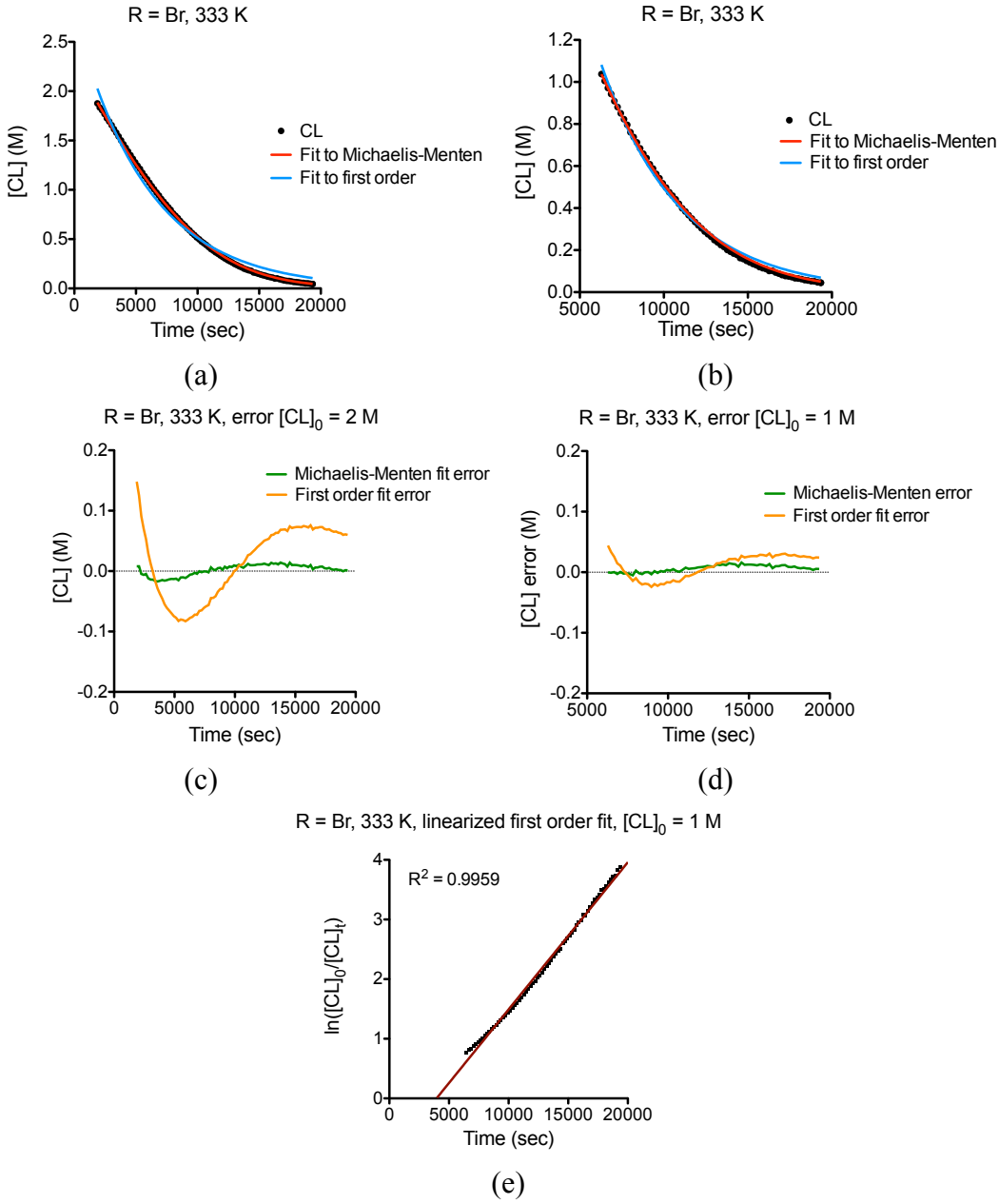

Figure 3.11. Top: data (black) and fits to first-order (blue) and Michaelis-Menten (red) kinetics rate equations obtained from COPASI for catalyst 2 (R = Br) at 333 K for (a) $[CL]_0$ = 2 M and (b) $[CL]_0$ = 1 M. Middle: errors associated with the fits are shown in (c) $[CL]_0$ = 2 M and (d) $[CL]_0$ = 1 M. Fits were obtained using contributions from [CL] only. Bottom: (e) linearized data (black) for first-order rate equations along with calculated linear fits fits (red) for $[CL]_0$ = 1 M. Compare to the plot shown in **Figure 3.10**, left, for which $[CL]_0$ = 2 M.

3.3.2.3 Test of Effect of Stirring on the Kinetics

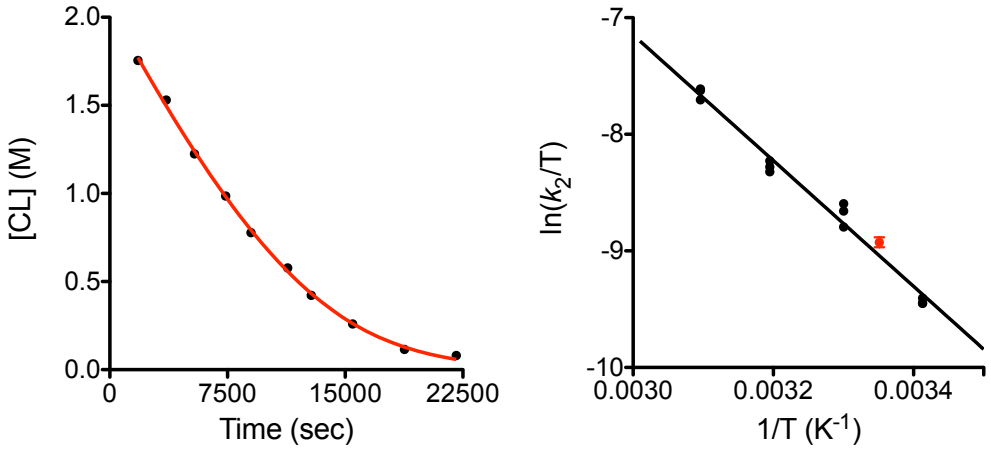

Figure 3.12. Left: concentration *vs*. time profile for decay of CL resonances during the stirred polymerization reaction catalyzed by R = NO_2 at 298 K along with fit (–) determined by COPASI to **Equation 3.1**. Right: Erying plot for 2 (R = NO_2) with values obtained from ^{1}H NMR method in black and the value obtained from the stirred polymerization in red.

Using **2** (R = NO_2) at 298 K (average temperature inside nitrogen-filled glove box over the course of the reaction) with [**2** (R = NO_2)]$_{tot}$ = 5.8 mM and [CL]$_0$ = 2 M (total volume 5 mL) a stirred polymerization was carried out in toluene to test whether viscosity effects were significant enough to affect the polymerization kinetics carried out in an NMR tube. Aliquots (100 µL) of the reaction were removed at the indicated time points, quenched with a small amount (approx. 0.5 mL) of MeOH and the solvent removed *in vacuo*. The resulting material was taken up in deuterated chloroform for conversion determination, and [CL]$_t$ was calculated based on conversion. A plot of [CL] *vs*. time is shown in Figure 3.12, left, along with the fit determined from COPASI. A comparison of fit parameters obtained at 293 K and 303 K are presented in Table 3.3, with the data from the stirred experiment highlighted. As seen in Figure 3.12, left, the fit to the Michaelis-Menten equation is excellent, and the fit parameters (Table 3.3) are in line with expectations based on the temperature at which the stirred reaction was carried

out. A further confirmation of this fact is found in Figure 3.12, right, where the data for the stirred reaction is added to the Erying plot for **2** (R = NO_2). Based on this analysis, we believe that viscosity has little affect on our observed changes in concentration.

Table 3.3. Comparison of kinetic parameters determined from experiments performed in an NMR tube and in stirring experiment (highlighted in gray).

Entry	Temp (K)	K_{eq} COPASI (M^{-1})	V_{max} (M/s) (x10^5)	k_2 (s^{-1}) (x10^2)
1	293[a]	1.62(4)	12.3(1)	2.13(3)
2	293[a]	1.70(4)	11.79(9)	2.30(2)
3	293[a]	1.61(5)	12.0(1)	2.41(3)
4	298[b]	1.1(2)	24(2)	4.0(2)
5	303[a]	1.66(5)	26.1(2)	4.6(6)
6	303[a]	1.42(5)	34.6(4)	5.6(8)
7	303[a]	1.49(3)	25.9(2)	5.26(6)

[a] Reaction done using NMR method. [b] Reaction done in vial with stirring (described above).

3.3.2.4 Induction Period Kinetics

An induction period was seen in the kinetic runs, as had been noted previously for ROP by related aluminum systems, and close inspection of ^{1}H NMR spectra revealed transformations of the catalyst during these early reaction times (cf. t = 0 to 1.3 h in Figure 3.6). The initial ^{1}H NMR spectrum obtained soon after mixing of the catalyst with CL contained imine peaks different from those of the catalyst in the absence of CL, suggesting some rapid change of the catalyst structure in the presence of substrate. In addition, these peaks smoothly converted to a second set of peaks as polymerization began. This conversion follows first order kinetics, with a rate that is similar to the rate of polymerization (Figure 3.13, left). A plot of k_{obs} *vs*. $[CL]_0$ over the range 0.1 M < $[CL]_0$ < 2.0 M (Figure 3.13, right) showed only slight variation of k_{obs} (2-fold), indicating that the observed conversion rate is essentially independent of [CL] over the concentration range

studied. The NMR data suggest structural changes to the catalyst and/or pre-catalyst, possibly including binding of monomer, initiation via *iso*-propoxide insertion, or some other geometric change, but definitive conclusions cannot be drawn with the information currently available. It is possible that this induction period also displays saturation behavior, and that we are monitoring this process in the saturation regime, thus giving the apparent zero-order relationship with [CL]. Unfortunately, attempts to monitor the rearrangement at lower concentrations of CL were unsuccessful due to overlapping peaks at lower [CL]. Additional experiments were performed where complex **2** (R = Br) and CL (1 equiv. to 70 equiv.) were mixed and monitored by both ^{27}Al and ^{1}H NMR spectroscopy. No change in the ^{27}Al spectrum was observed upon addition and heating of 1 equiv. of CL or even through 35% conversion of CL ($[CL]_0$ = 0.5 M) into PCL. The peak associated with our 5-coordinate catalyst did not shift from free catalyst, indicating that if binding is occurring, it is very rapid compared to the NMR timescale.

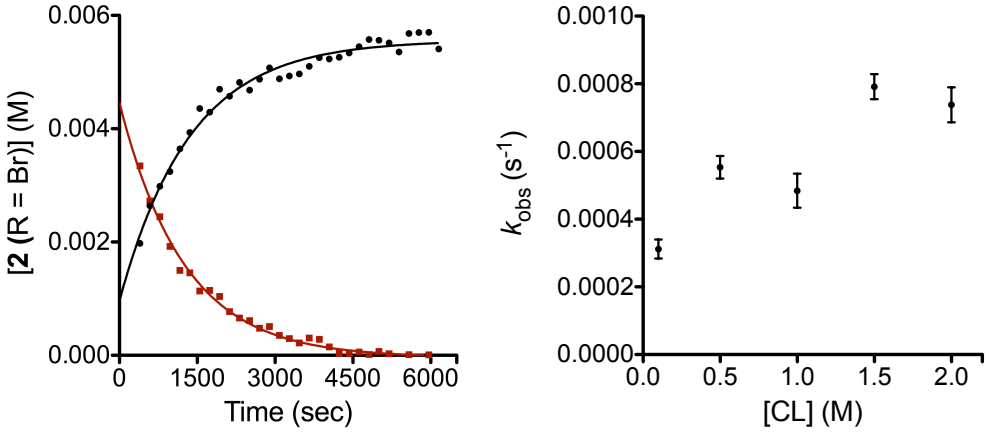

Figure 3.13. Left: growth of ultimate catalyst species present in polymerization (black circles), decay of initial catalytic species present in polymerizations (red squares) and fits (−,−) to first-order decay equation $[cat]_t = [cat]_0 exp(-k_{obs}t)$ for **2** (R = Br) at 333 K and $[CL]_0$ = 2 M. Right: observed pseudo-first order rate constant k_{obs} *vs*. [CL].

3.3.3 Interpretation of Kinetic Parameters

We evaluated the dependencies of K_{eq} and k_2 on the catalyst R group and temperature through Hammett, Eyring, and Van't Hoff plots, with the aim of discerning electronic effects and obtaining thermodynamic parameters. Turning first to K_{eq}, we find only very weak dependencies on substituent and temperature from plots of log(K_{eq}) *vs.* σ_p (Figure 3.14, red)[114] and ln(K_{eq}) *vs.* 1/T (Figure 3.15), respectively. A linear relationship between log(K_{eq}) and σ_p with a small positive slope ρ (average = + 0.16(8)) indicates that the equilibrium constant for monomer binding is slightly enhanced by EWGs, in line with previous explanations for the reactivity of aluminum salen complexes.[99] However, this effect is small, which is highlighted by the small differences in the $\Delta G°$ values (Table 3.4) calculated from Figure 3.15 (e.g., the $\Delta\Delta G°$ between **2** with R = OMe and R = Br at 333K is less than 0.4 kcal/mol). For all catalysts studied, $\Delta G°$ values are zero within

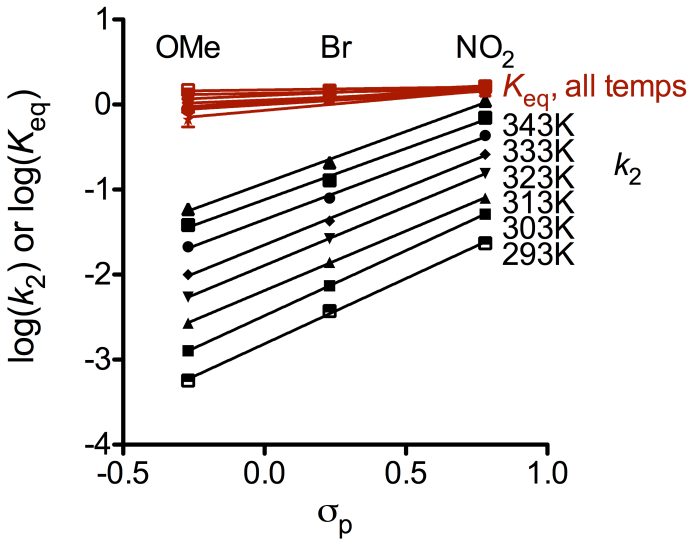

Figure 3.14. Hammett plot for k_2 (black) and K_{eq} (red). Values for the rate constants k_2 and K_{eq} at temperatures that were not experimentally measured but presented were obtained by extrapolating the thermodynamic parameters from the Eyring (k_2, **Table 3.5**) and Van't Hoff (K_{eq}, **Table 3.4**) plots.

experimental error. Importantly, the small differences in K_{eq} and $\Delta G°$ as a function of substituents cannot fully explain the differences in the observed overall rates for this set of catalysts.

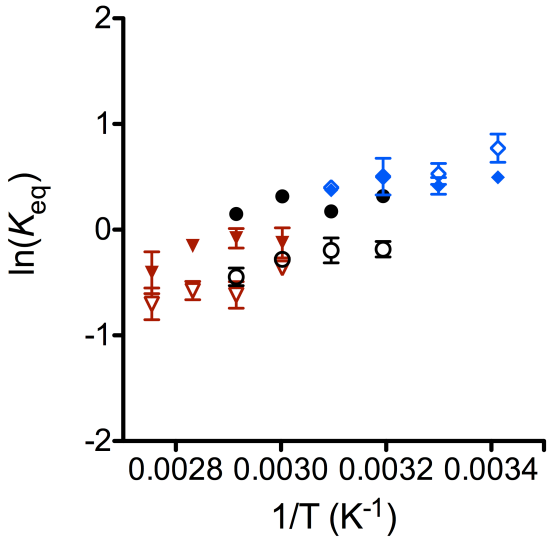

Figure 3.15. Van't Hoff plot for K_{eq} (R = OMe, red triangles; R = Br, black circles; R = NO_2, blue diamonds). Closed points denote equilibrium constant values determined by COPASI; open points denote values determined by ^{1}H NMR peak analysis method.

Table 3.4. Thermodynamic parameters associated with K_{eq} for catalysts **2** determined by COPASI and ^{1}H NMR peak analysis.

Entry	R	Method	$\Delta H°$ (kcal/mol)	$\Delta S°$ (cal/molK)	$\Delta G°$ (kcal/mol, 323 K)
1	OMe	COPASI	-2.1 ± 0.9	-7 ± 3	-0.03 ± 1
2	OMe	NMR	-2.3 ± 0.5	-8 ± 2	0.2 ± 0.7
3	Br	COPASI	-0.8 ± 0.5	-2 ± 1	-0.2 ± 0.6
4	Br	NMR	-1.8 ± 0.3	-6 ± 1	0.2 ± 0.5
5	NO_2	COPASI	-0.5 ± 0.3	-0.8 ± 1	-0.2 ± 0.5
6	NO_2	NMR	-2.2 ± 0.4	-6 ± 1	-0.2 ± 0.6

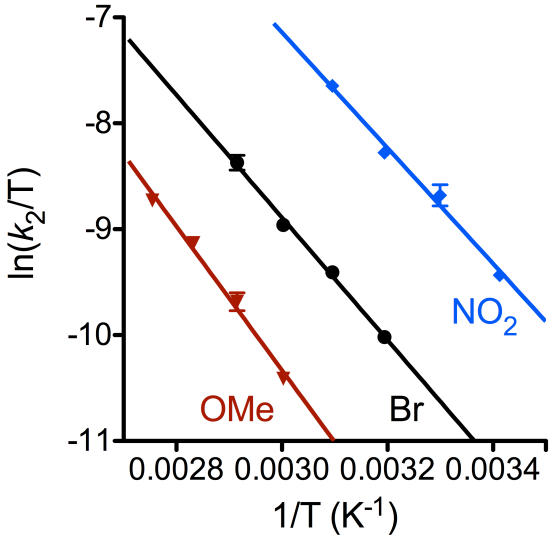

Figure 3.16. Erying plot for k_2 values.

Table 3.5. Activation parameters for k_2.

R	$\Delta H^{\ddagger}$ (kcal/mol)	$\Delta S^{\ddagger}$ (cal/molK)	$\Delta G^{\ddagger}$ (kcal/mol, 323 K)
OMe	13.5 ± 0.5	-27 ± 2	22.3 ± 0.8
Br	11.5 ± 0.3	-30 ± 2	21.3 ± 0.7
NO_2	10.8 ± 0.4	-29 ± 2	20.2 ± 0.8

The dependencies of k_2 on substituent R and temperature are more striking (Figure 3.14, black; Figure 3.16), and show that the overall rate differences between the ROP polymerizations by catalysts **2** arise from this kinetic parameter. Linear relationships between log(k_2) and the σ_p values at all temperatures have similar positive slopes (ρ) with an average value of +1.4(1). The linear correlations support a similar mechanism(s) across the series of catalysts, and the positive ρ values reflect enhancement of k_2 with increasing substituent electron withdrawing power. This trend is notably opposite from that reported previously for catalysts **1** ($\rho = -1.1(1)$).[139] Further insight is provided by the

activation parameters calculated using the Eyring equation from Figure 3.16 (Table 3.5). A clear trend in both the activation enthalpy and Gibb's free energy of activation that mimics the overall rate order is observed, albeit with no discernable trend in the activation entropies (within error). The modest positive activation enthalpies accompanied by negative activation entropies imply a degree of bond breaking and ordering in the transition state consistent with the insertion process, with further understanding made available from DFT calculations (see below).

3.3.4 Density Functional Modeling

(Performed by Hugo Vazquez-Lima, Michelle A. Johnson, Daniel J. Marell, Christopher J. Cramer)

3.3.4.1 Pathway Analysis on Models Lacking *para* Substituents

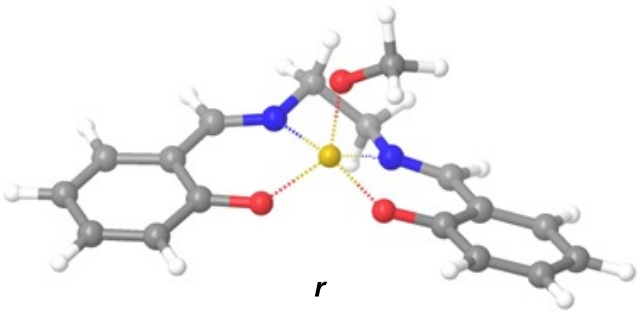

Figure 3.17. Truncated model **r** for catalysts **2**.

In order to characterize in microscopic detail the various elementary steps associated with the ROP mechanism, we began by applying a density functional theory model that has been extensively validated for organic and main-group inorganic systems (M06-2X/6-311+G(d,p)//M06-L/6-31+G(d,p) including toluene solvation effects using a quantum chemical continuum model; see section 3.5.4 for full details) to a truncated model catalyst from which bulky alkyl substituents were removed (and isopropoxide truncated to methoxide) to facilitate initial identification of important stationary-point structures (denoted **r**, Figure 3.17).[154] Many complexes of **r** with CL can be found and identified as minima on the potential energy surface (PES). These include van der Waals

complexes, with CL "stacking" above or below an aromatic ring, and various structures coordinating either of the two ester oxygen atoms of CL to the aluminum atom. However, while all of these structures are minima on the potential energy surface, they are all predicted to have positive free energies relative to separated reactants, such that product distributions would be expected to follow the Curtin-Hammett principle. As a result, we will therefore begin with a focus primarily on transition-state (TS) structures and their energies. Later, however, we will return to the myriad of catalyst•CL complexes to rationalize what we believe to be substrate-inhibition effects in the observed kinetics.

As noted above, the calculations indicate that monomer coordination to aluminum does *not* generate a significantly stable intermediate that precedes a separate insertion step, (as is often assumed, cf. Figure 3.1). Nonetheless, the alkoxide and CL must indeed be brought into proximity in order to accomplish the alkoxide insertion step. Consideration of this step leads to eight stereochemically distinct and mechanistically productive insertion orientations of the alkoxide and CL relative to the catalyst structure. These eight orientations (Figure 3.18) differ in the orientation of the CL monomer and the orientation of the non-coordinated oxygen (carbonyl or ester) relative to the nitrogen ligands (*trans*/*trans*, *trans*/*cis*, *cis*/*trans*, and *cis*/*cis*) as well as whether coordination occurs through the monomer carbonyl or ester oxygen atom ($O_{carbonyl}$ and O_{ester}, respectively).

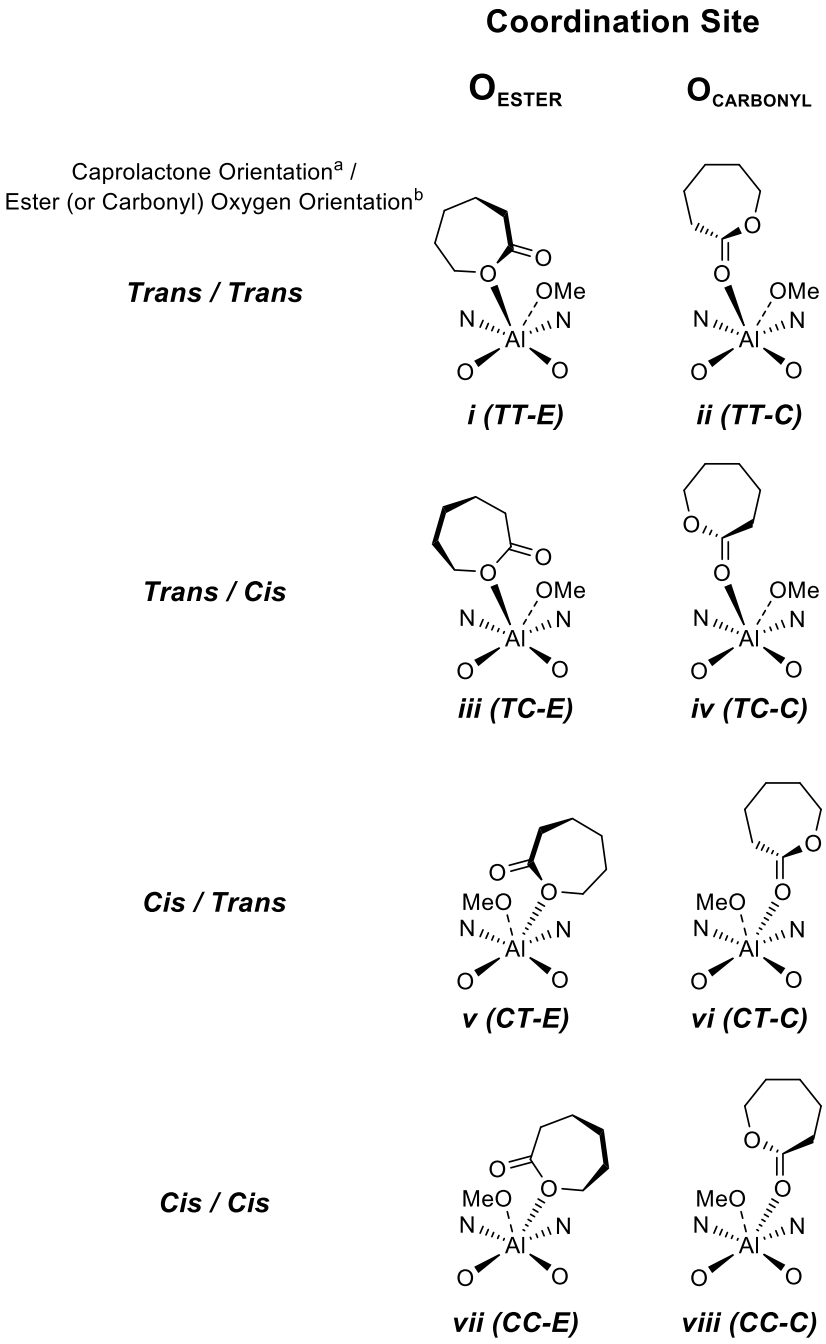

Figure 3.18. Eight distinct CL **r** complex structures from which alkoxide insertion may proceed. [a] Orientation of the CL is given relative to the nitrogen ligands. [b] Orientation of the ester or carbonyl oxygen is given relative to the nitrogen donors.

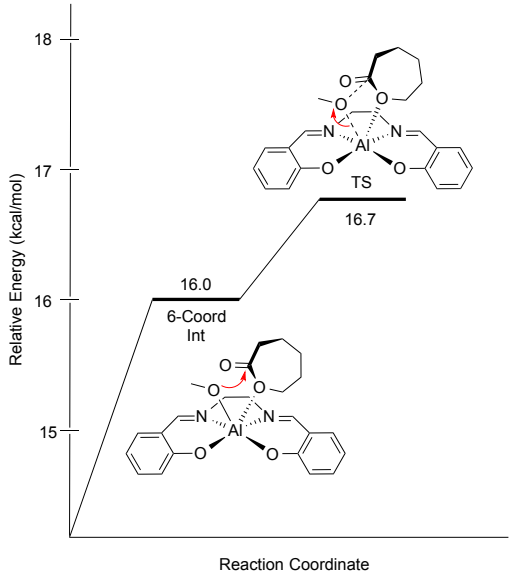

Figure 3.19. Reaction path for ***v*** (same as ***i***, ***iii***, and ***vii***); this path is computed to have higher activation free energy relative to that shown in **Figure 3.20**.

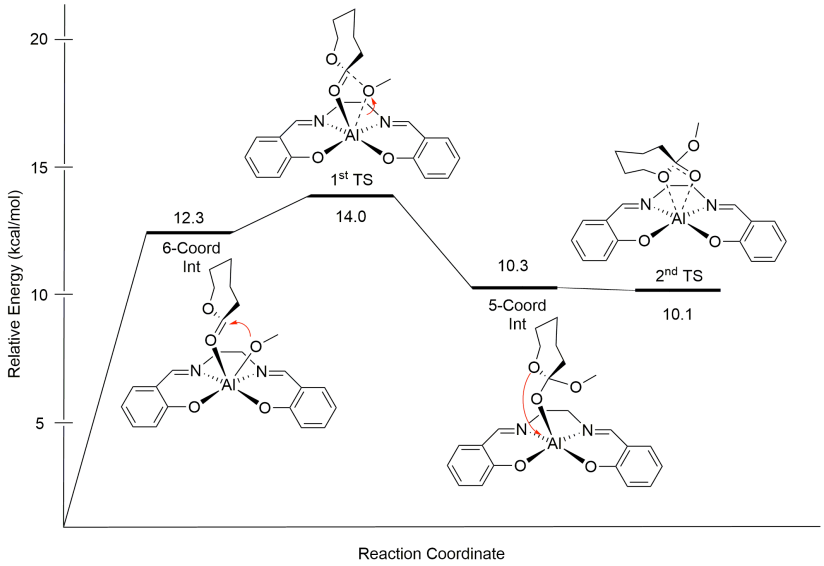

Figure 3.20. Reaction path for **r-*vi***; this path is computed to have the lowest activation free energy of eight distinct stereochemical possibilities shown in **Figure 3.18**.

The ring-opening polymerization proceeds via two distinct mechanistic routes depending on how CL coordinates to the Al center along the insertion pathway. Initial approach involving the ester oxygen (***i***, ***iii***, ***v***, ***vii***) provides access to an alkoxide-insertion TS structure from which ring-opened product is directly obtained (Figure 3.19). By

contrast, initial approach involving the carbonyl oxygen (***ii***, ***iv***, ***vi***, ***viii***) leads to an alkoxide-insertion TS structure that generates a reactive orthoalkoxide intermediate (Figure 3.20, 1st TS). Subsequent exchange of the newly generated alkoxide oxygen and the original ester oxygen, with concomitant ring opening, then proceeds via a second TS structure that leads to ring-opened product.

The relative free energies for the key stationary points on all pathways for the truncated model **r** are listed in Table 3.6 and Table 3.7 for O_{ester} and $O_{carbonyl}$ coordination, respectively (these Tables also include data for a more elaborate model **s** including all experimental alkyl substituents described below). The ring-opening pathway associated with ***vi*** (***CT-C***) was found to have the *lowest* activation free energy of all eight possible pathways, 14.0 kcal/mol, with the rate limiting step being the initial alkoxide insertion. Note that the initial 6-coordinate intermediate is 12.3 kcal/mol above separated reactants in free energy, even though it is predicted to be a minimum on the potential energy surface. Also, the orthoalkoxide intermediate is predicted to be a very shallow minimum on the potential energy surface, such that adding thermal contributions to arrive at a free energy leads to the intermediate being effectively degenerate with the 2nd TS structure for ring-opening that generates product alkoxide. As such, the orthoalkoxide is kinetically irrelevant. Cases **r-*i***, **r-*ii***, **r-*v***, and **r-*viii*** have rate-limiting free energies of activation of 15-17 kcal/mol, i.e., only slightly above that for **r-*vi***. In the remaining cases, **r-*iii***, **r-*iv***, and **r-*vii***, steric clashes between the phenyl rings of the Al-Salen complex and the CL ring destabilize the rate-determining TS structures leading to activation free energies above 19 kcal/mol.

Table 3.6. Free energies (kcal/mol) relative to separated reactants for reaction paths involving O_{ester}-Al coordination in the truncated **r** and more elaborate **s** models.[a]

Orientation	6-Coordinate Intermediate	TS Structure
r-*i*	12.9	16.8
s-*i*	16.7	17.7
r-*iii*	11.8	19.5
s-*iii*	17.6	22.2
r-*v*	16.0	16.7
s-*v*	17.9	17.6
r-*vii*	[b]	19.6
s-*vii*	[b]	20.2

[a] See computational methods section for theoretical details. [b] No stationary point preceding the TS structure could be located.

Table 3.7. Free energies (kcal/mol) relative to separated reactants for reaction paths involving $O_{carbonyl}$-Al coordination in truncated **r** and more elaborate **s** models (see also **Figure 3.20**).[a]

Orientation	6-Coordinate Intermediate	1st Transition State	5-Coordinate Intermediate	2nd Transition State
r-*ii*	11.4	17.2	9.2	14.8
s-*ii*	[b]	16.5	7.0	15.3
r-*iv*	11.3	19.3	6.9	7.4
s-*iv*	[b]	18.0	6.2	11.3
r-*vi*[c]	**12.3**	**14.0**	**10.3**	**10.1**
s-*vi*[c]	[b]	**14.9**	**10.6**	**12.2**
r-*viii*	8.1	17.3	10.4	15.6
s-*viii*	[b]	17.6	8.7	13.9

[a] See computational methods section for theoretical details. [b] Stationary points were not computed for these structures. [c] This pathway has the lowest rate-limiting activation free energy of the eight stereochemically distinct possibilities.

With results in hand for the eight pathways associated with model **r**, we next examined the influence of the two *t*-butyl and two methyl groups that are present in the experimental salen ligand by introducing them into the computational model, hereafter referred to as model **s**. The mean unsigned difference between the relative free energies for corresponding stationary points of model **r** *vs.* model **s** (Table 3.6 and Table 3.7) is only 1.8 kcal/mol, indicating that most of the relative energies are not especially perturbed by the additional steric bulk in model **s**. However, all of the structures involving coordination to the *ester* oxygen are *de*stabilized, because these structures bring the CL ring into closer proximity to the steric bulk of the full catalyst model. Indeed, the 6-coordinate intermediate **s-*iii*** is destabilized by 5.8 kcal/mol relative to the truncated ***r*** model owing to unfavorable interactions with the methyl groups on the salen bridge. The looser complexes associated with carbonyl oxygen coordination are by contrast in some cases *stabilized* by favorable dispersion interactions (i.e., attractive London forces at van der Waals contact), e.g., the 5-coordinate intermediate **s-*ii*** whose relative energy is 2.2 kcal/mol more stable than that of **r-*ii***. As might be expected given the small mean unsigned difference between models **r** and **s**, we find that again the lowest energy pathway upon inclusion of the alkyl substitution is pathway ***vi*** (Figure 3.21), with a rate-limiting free energy of activation of 14.9 kcal/mol, which is slightly increased from the 14.0 kcal/mol value obtained with model **r**.

3.3.4.2 Influence of *para* Substituents on the Reaction Pathways

Having assessed the effect of additional steric bulk in the salen ligand, we examine next the electronic effects observed with *para* substitution. The same eight pathways (***i*** – ***viii***) were investigated for the **s** model substituted with *p*-MeO, *p*-Br, and *p*-NO_2, corresponding to the experimental systems **2**. In addition, we chose to use ethoxide in place of methoxide to mimic more accurately a growing polymer chain.

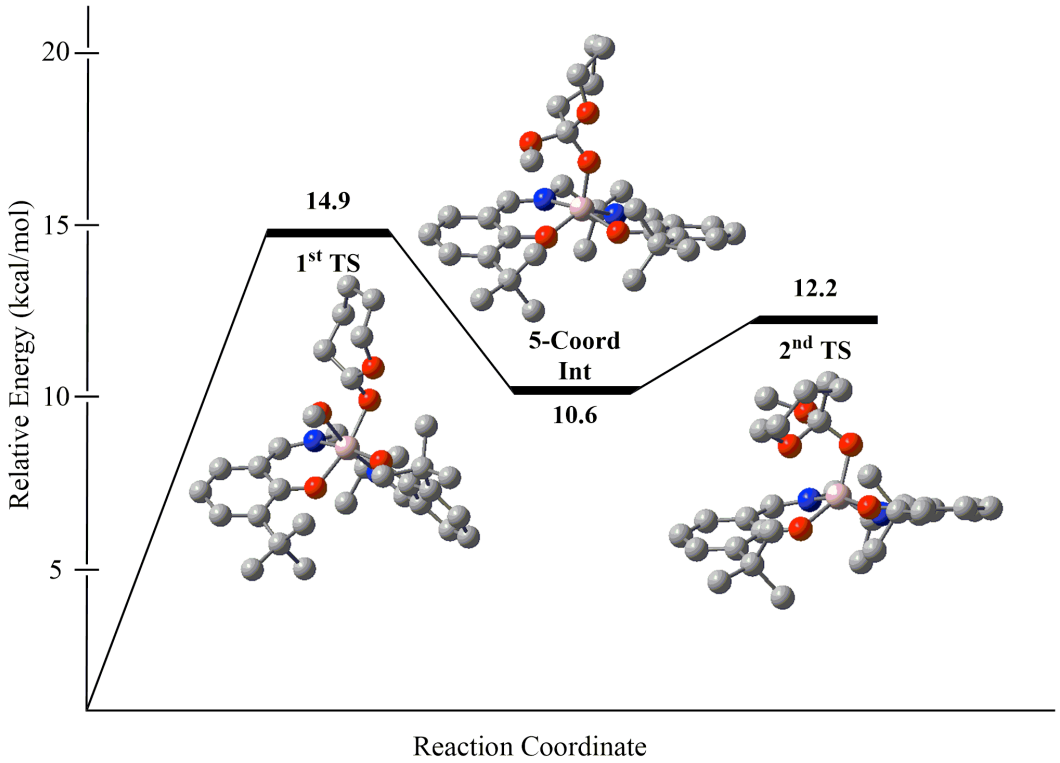

Figure 3.21. Lowest-energy pathway corresponding to **s-*vi*** pathway.

There are some general trends to be observed for the ester coordination pathway (Table 3.8). The lactone-coordinated intermediate is stabilized by substitution at the *para* position for all pathways and substitutions. With increasing electron-withdrawing power of the substituent (OMe < Br < NO_2), the intermediate is further stabilized (mean unsigned difference between the model **s** and each substituent is 1.3, 2.9, and 3.7 kcal/mol respectively), consistent with the increased Lewis acidity of the Al atom that is expected with aryl rings substituted by more EWGs. That increased Lewis acidity may be assessed through the evaluation of the CM5 partial atomic charge[155] of the Al atom, which increases smoothly from 0.535 to 0.538 to 0.544 with the substituent going from MeO to Br to NO_2.

For the subsequent TS structures, the *para*-methoxy substituted compounds show mixed results with some pathways being stabilized and some destabilized, over a range of

–0.3 to +1.9 kcal/mol relative to unsubstituted **s** results above (cf. Table 3.7). In the case of *p*-Br, the range is –2.0 to +0.1, and in the case of *p*-NO_2, it is –1.7 to +0.4. The variability in the *para* substitution effect in these systems may be associated with varying degrees of dissociative character in the separation of the nucleophile alkoxide *from* the aluminum atom (which would be expected to be *disfavored* by EWGs) and associative character of the newly formed alkoxide *to* the aluminum atom (which would be *favored* by the same EWGs). The differing geometries associated with each path permit such differentiation. However, as the free energies of activation in Table 3.8 considerably exceed those associated with carbonyl coordination (vide infra) we will not explore these trends further.

Table 3.8. Free energies (kcal/mol) relative to separated reactants for reaction paths involving O_{ester}-Al coordination in full *para*-substituted models.[a]

Orientation	6-Coordinate Intermediate	Transition State
i-OMe	14.3	17.4
i-Br	12.4	16.7
i-NO₂	11.6	16.0
iii-OMe	17.7	23.8
iii-Br	15.6	22.0
iii-NO₂	15.8	21.7
v-OMe	16.6	18.3
v-Br	15.6	15.6
v-NO₂	13.6	16.3
vii-OMe	[b]	22.1
vii-Br	[b]	20.3
vii-NO₂	[b]	20.6

[a] See computational methods section for theoretical details. [b] No stationary points preceding the TS structure could be located.

Consistent with the results for the **r** and **s** models above, pathway ***vi*** in the carbonyl coordination pathway case was found to have the lowest rate-limiting free energy of activation, and to show a trend in relative activation free energies relative to *p*-MeO of –1.2 for *p*-Br, and –2.8 for *p*-NO_2 (Table 3.9). These free energy differences are in reasonable agreement with those measured (–1.0 ± 1.1 and –2.1 ± 1.1, respectively; derived from Table 3.5). Analysis of the geometries along pathway ***vi*** indicates that substitution with increasingly electron-withdrawing groups in the salen ligand leads to an increasingly more compact coordination of the reactants in the rate-determining TS structure. Thus, the Al-O bond distances to the carbonyl group of the incoming cyclic ester are 1.929, 1.912, and 1.892 Å, respectively, for the complexes with *p*-MeO, Br, and NO_2 substituents. Concomitantly, the C-O distances for the forming bond between the carbonyl carbon and the ethoxide nucleophile are 1.784, 1.769, and 1.744 Å, respectively (the Al-O bond distance to the methoxide varies by less than 0.005 Å over the different substitutions). Thus, it appears that the more electrophilic Al center best stabilizes the incipient tetrahedral intermediate character in the TS structure, thereby effecting the observed rate acceleration.

Table 3.9. Free energies (kcal/mol) relative to separated reactants for reaction paths involving $O_{carbonyl}$-Al coordination in full *para*-substituted models.[a]

Orientation	1st Transition State	5-Coordinate Intermediate	2nd Transition State
ii-OMe	21.7	8.9	17.1
ii-Br	21.9	8.3	13.5
ii-NO₂	18.4	9.0	15.1
iv-OMe	19.2	6.3	11.1
iv-Br	20.2	6.2	14.5
iv-NO₂	19.0	5.3	9.2
vi-OMe[b]	**14.3**	**11.5**	**12.3**

vi-Br[b]	**13.1**	**10.8**	**10.4**
vi-NO$_2$[b]	**11.5**	**11.5**	**10.6**
viii-OMe	20.0	9.0	15.2
viii-Br	18.4	7.8	15.2
viii-NO$_2$	17.9	8.2	10.9

[a] See computational methods section for theoretical details.
[b] These pathways have the lowest rate-limiting activation free energies of the eight stereochemically distinct possibilities.

While the predicted free energies of activation show a trend with respect to substitution that agrees well with experiment, they are considerably smaller in magnitude than those measured experimentally. Comparison of the enthalpic and entropic contributions to the theoretical free energies, compared to the experimental values, indicates that theory predicts much smaller *enthalpies* of activation, but much larger *entropies* of activation. Such behavior might be associated with either or both of two phenomena. First, in the actual polymerization process, the growing polymer chain may associate with the catalyst, either through non-covalent interactions or through coordination of oxygen functionality to aluminum, and the requirement that the chain be displaced by CL would be expected to increase the enthalpy of activation and decrease the entropy of activation. Similarly, solvent toluene could enjoy particularly favorable π-stacking interactions with the aromatic rings of the salen ligand, for example, again introducing a larger enthalpy of activation and a less unfavorable entropy of activation (owing to solvent release) associated with reaction CL. In the absence of detailed (and impractical) simulations including solvent and an actual polymer chain, however, it is difficult to do more than speculate about these possibilities.

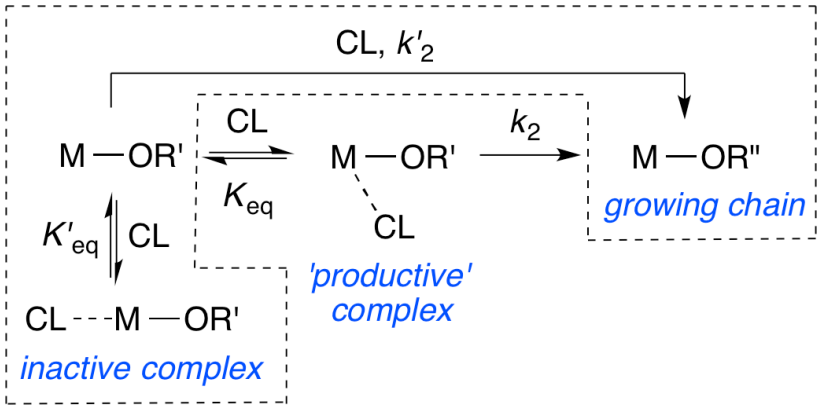

Figure 3.22. Proposed ROP mechanisms that yield the rate law described by M = [(salen)Al] moiety.

Also, as noted above, a key finding from the DFT calculations was *unfavorable* free energies for pre-reactive complexes that are implicated by the usual interpretation of the Michaelis-Menten equation (Equation 3.1), wherein a pre-equilibrium substrate binding step (K_{eq}) is followed by a catalytic turnover step (k_2; Figure 3.22). In order to reconcile the experimentally observed rate law (Equation 3.1) with the absence of such a binding step from the calculated reaction trajectories, we propose a different mechanism involving *substrate inhibition* (steps enclosed by dashed line in Figure 3.22, characterized by K'_{eq} and k'_2) that yields an experimental rate law indistinguishable from Equation 3.1 (see section 3.5.5 for derivation). According to this mechanism, reversible substrate binding can be *non*productive, owing to formation of an *inactive* species. This species would be expected to be favored at high CL concentrations, resulting in rate retardation under these conditions (saturation kinetics). One such complex that can be imagined involves coordination of CL to Al *trans* to the alkoxide ligand, generating a complex that could not lead to intramolecular nucleophilic attack. Many such 6-coordinate Al(salen) complexes are known (a search of the Cambridge Crystallographic Database, v. 5.34, revealed >20 such structures).[156–158] To specifically explore this possibility in our system,

we computed the structure of the relevant complex for the *p*-NO_2 substituted salen case (Figure 3.23). It has a free energy that is 8.4 kcal/mol lower than any of the productively coordinated species presented in Table 3.6 and Table 3.7. In addition, while not shown, we also located various van der Waals complexes of CL with the aromatic portions of the salen ligand that were also predicted to have lower free energies than productively coordinated complexes (adjacent to the alkoxide ligand). A quantitative measure of the inhibitory effect would require a statistical average over all non-productive complexes, which is not practical in the absence of detailed molecular simulations. Nevertheless, the substrate inhibition mechanism (steps K'_{eq} and k'_2) is consistent with the experimental kinetics, and provides an alternative to the assumption in the pre-equilibrium mechanism that K_{eq} refers to productive coordination of substrate as a separate step prior to alkoxide insertion. Indeed, the substrate inhibition model represents a potentially important general phenomenon in ROP with catalysts for which both productive and unproductive coordination geometries of substrate and catalyst are available.

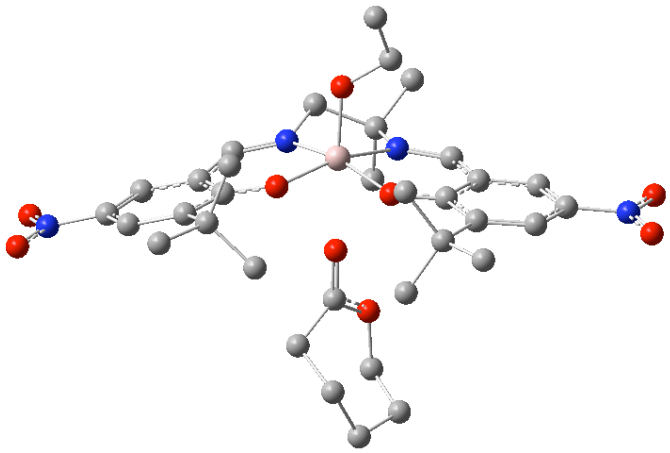

Figure 3.23. Unproductive complex of CL with *p*-NO_2-catalyst.

As a final, technical point related to the modeling, we note that use of the M06-L functional, with its well established ability to account for attractive medium-range electron correlation effects (sometimes informally referred to as "dispersion", although that term really should only be used for longer-range attractive effects varying as r^{-6} with distance), is critical for the determination of accurate catalyst-CL complex geometries. When the 6-coordinate precursor structure corresponding to ***r-vi*** is reoptimized with the B3LYP functional, for example, which does *not* account for medium-range correlation effects, the bond distance between the carbonyl oxygen and the aluminum atom changes from the M06-L value of 2.18 Å to a value of 4.89 Å, i.e., the CL fully decoordinates.

3.4 Summary and Conclusions

Detailed kinetic studies of the polymerization of CL by salen-aluminum catalysts **2** (R = OMe, Br, or NO_2) supported by ligands with similar steric profiles but different electron donating characteristics revealed saturation behavior that fits to Equation 3.1. While K_{eq} varied only slightly with the electron donating properties of R (Hammett ρ = + 0.16(8)), k_2 showed a more significant dependence reflected by ρ = +1.4(1). These conclusions were buttressed by the dependencies of K_{eq} and k_2 with temperature that led to essentially invariant $\Delta G°$ values of ~ 0 kcal/mol for all catalysts (Table 3.4) and a discernable trend in $\Delta H^{‡}$ of R = OMe > Br > NO_2 (Table 3.5). The observation of faster rates with EWGs on the supporting ligand agrees with the results of previous studies of ROP reactions catalyzed by related salen-aluminum complexes.[99,137]

The lowest energy reaction trajectories calculated by DFT (**r** and **s-*vi***) have similarities to those proposed for ROP of lactide stereoisomers by (β-diketiminate)Zn and -Sn catalysts,[93,94] in particular with respect to the first transition state structure that features incipient attack of the nucleophile to the lactone carbonyl that is bound to the metal ion. With respect to the effects of the remote ligand substituents, both the trend and the free energy of activation differences observed experimentally are reproduced in pathway *vi*. The greater Lewis acidity of the electron-deficient metal ion accelerates the reaction via transition state stabilization that involves increased bonding between the Al ion and the lactone carbonyl and between the nucleophilic alkoxide and the lactone carbonyl carbon.

Interestingly, DFT calculations indicated that a distinct CL adduct is not a free energy minimum on the reaction pathway, arguing against K_{eq} being associated with productive coordination of monomer according to the typical coordination-insertion mechanism (Figure 3.1 and Figure 3.22). Instead, we propose that K_{eq} corresponds to

'nonproductive' coordination of substrate that inhibits the reaction at high substrate concentrations, with k_2 thus encompassing both 'productive' coordination and insertion steps that occur smoothly along the reaction trajectory. This attribution of saturation behavior to monomer inhibition has potentially significant implications for interpretation of mechanistic studies of ROP catalysis and for the design of new catalysts. For example, we predict that catalysts for which nonproductive monomer coordination is prevented may be particularly efficient, particularly when high monomer concentrations are used (e.g., neat or in the melt). Additionally, the current mechanistic paradigm of monomer coordination as distinct a separate step from alkoxide insertion may not in fact be true for many catalysts in the literature, implying that more detailed study of catalyst kinetics is necessary to understand how general this phenomenon is.

3.5 Experimental Section

3.5.1 General Considerations

All reactions were carried out under an inert atmosphere using standard Schlenk and drybox techniques, unless otherwise indicated. Reagents were obtained from commercial suppliers and used as received unless otherwise indicated. CL was purified by distillation from CaH_2 and stored under N_2. Deuterated solvents were dried over CaH_2 or sodium, distilled under vacuum and stored under N_2. Protiated solvents were degassed and passed through a solvent purification system (Glass Contour, Laguna CA) prior to use. ^{1}H and ^{13}C NMR spectra were recorded on a Varian VI-300 NMR spectrometer or a Bruker Avance III 500 MHz spectrometer equipped with a BBFO SmartProbe and their chemical shifts (δ) for ^{1}H and ^{13}C spectra are referenced to residual protium in the deuterated solvent (for ^{1}H) and deuterated solvent itself (for ^{13}C). Chemical shifts for ^{27}Al NMR were externally referenced to aluminum *tris*(acetylacetonate) in toluene-d_8. 2-Hydroxy-3-(*tert*-butyl)-5-methoxybenzaldehyde, [159] 2-hydroxy-3-(*tert*-butyl)-5-bromobenzaldehyde, [160] and 2-hydroxy-3-(*tert*-butyl)-5-nitrobenzaldehyde [161] were synthesized according to literature procedures. Elemental analyses were performed by Complete Analysis Laboratories, Inc., Parsippany, NJ.

3.5.2 Synthetic Procedures

Ligand Syntheses. The benzaldehyde (H_2L^{OMe}: 7.7 g, 83% pure, 31 mmol; H_2L^{Br}: 1.40 g, 5.44 mmol; H_2L^{NO2}: 1.61 g, 88% pure, 6.35 mmol) was added to a round bottom flask with the appropriate amount of absolute ethanol to give 0.63 M benzaldehyde. 2-Methylpropane-1,2-diamine (0.5 equivalents) was added in one portion to the flask with stirring. A reflux condenser was added and the mixture was refluxed at 100 °C for 2 h, then allowed to cool to room temperature. The crude solution was placed in a −30 °C freezer overnight to induce precipitation of the protonated form of the ligand.

After recovery by filtration washing with 40 mL of hexanes and in the case of H_2L^{Br}, recrystallization from dichloromethane and hexanes at −30 °C overnight, the solid product was placed in a vacuum oven overnight before bringing into the glovebox for metallation. Yield: H_2L^{OMe}: 5.62 g, 98%; H_2L^{Br}: 1.08 g, 35%; H_2L^{NO2}: 1.38 g, 87%). H_2L^{OMe}: ^{1}H NMR (500 MHz, $CDCl_3$) δ 13.95 (s, 1H, O*H*), 13.42 (s, 1H, O*H*), 8.35 (s, 1H, C*H*=N), 8.31 (s, 1H, C*H*=N), 6.96 (app t, *J* = 3.37 Hz, 2H, Ar*H*,), 6.60 (d, *J* = 3 Hz, 1H, Ar*H*), 6.58 (d, *J* = 3 Hz, 1H, Ar*H*), 3.76 (s, 3H, ArO*Me*), 3.75 (s, 3H, ArO*Me*), 3.72 (s, 2H, NC*H*$_2$C(CH$_3$)$_2$N), 1.44 (s, 6H, NCH$_2$C(C*H*$_3$)$_2$N), 1.42 (s, 9H, Ar*t-Bu*), 1.41 (s, 9H, Ar*t-Bu*); ^{13}C NMR (125 MHz, $CDCl_3$) δ 167.26, 162.37, 155.32, 155.13, 151.31, 151.24, 139.15, 139.14, 118.61, 118.42, 118.09, 117.99, 111.72, 111.62, 70.57, 60.28, 55.91, 35.14, 35.12, 29.41, 29.39, 25.69. Anal. Calcd for $C_{28}H_{40}N_2O_2$: C, 71.76; H, 8.60; N, 5.98. Found: C, 71.73; H, 8.57; N, 5.98.

H_2L^{Br}: ^{1}H NMR (500 MHz, $CDCl_3$) δ 14.39 (s, 1H, O*H*), 13.83 (s, 1H, O*H*), 8.29 (s, 1H, C*H*=N), 8.25 (s, 1H, C*H*=N), 7.37 (d, *J* = 2.5 Hz, 1H, Ar*H*), 7.36 (d, *J* = 2 Hz, 1H, Ar*H*), 7.23 (d, *J* = 2.5 Hz, 1H, Ar*H*), 7.20 (d, *J* = 2.5 Hz, 1H, Ar*H*), 3.72 (s, 2H, NC*H*$_2$C(CH$_3$)$_2$N), 1.43 (s, 6H, NCH$_2$C(C*H*$_3$)$_2$N), 1.40 (s, 18H, Ar*t-Bu*); ^{13}C NMR (125 MHz, $CDCl_3$) δ 166.37, 161.45, 159.97, 159.69, 140.32, 140.29, 132.63, 132.39, 131.98, 131.84, 119.98, 119.91, 109.90, 109.70, 70.35, 60.45, 35.25, 35.23, 29.25, 25.55. Anal. Calcd for $C_{26}H_{34}Br_2N_2O_2$: C, 55.14; H, 6.05; N, 4.95. Found: C, 55.08; H, 6.09; N, 4.90.

H_2L^{NO2}: ^{1}H NMR (500 MHz, $CDCl_3$) δ 15.68 (s, 1H, O*H*), 14.94 (s, 1H, O*H*), 8.43 (app s, 2H, C*H*=N), 8.23 (d, *J* = 2.5 Hz, 1H, Ar*H*), 8.20 (d, *J* = 2.5 Hz, 1H, Ar*H*), 8.13 (d, *J* = 2.5 Hz, 1H, Ar*H*), 8.12 (d, *J* = 3 Hz, 1H, Ar*H*), 3.82 (s, 2H, NC*H*$_2$C(CH$_3$)$_2$N), 1.54 (s, 2H, NC*H*$_2$C(CH$_3$)$_2$N), 1.52 (s, 6H, NCH$_2$C(C*H*$_3$)$_2$N), 1.43 (s, 9H, Ar*t-Bu*), 1.42 (s, 9H, Ar*t-Bu*); ^{13}C NMR (125 MHz, $CDCl_3$) δ 168.59, 167.12, 166.73, 161.83, 140.26, 139.93, 139.02, 126.90, 126.44, 125.39, 117.19, 116.78, 69.47,

60.47, 70.35, 60.45, 35.45, 35.41, 29.07, 25.45. Anal. Calcd for $C_{26}H_{34}N_4O_6$: C, 62.63; H, 6.87; N, 11.24. Found: C, 62.54; H, 6.67; N, 11.15.

Aluminum complexes (2). In a nitrogen-filled glove box, equimolar amounts of the pro-ligand (H_2L^{OMe}: 0.596 g, 1.27 mmol; H_2L^{Br}: 0.719 g, 1.27 mmol; H_2L^{NO2}: 0.778 g, 1.56 mmol) and aluminum tris(*iso*-propoxide) were added to an oven-dried 15 mL screw cap glass vessel. Toluene (3 mL) was added and the vessel was equipped with a stir bar, sealed, and removed from the glove box. The sealed vessel was heated to 90 °C for 3 days, after which time it was cooled to room temperature and returned to the glove box. Toluene was removed *in vacuo* from the homogeneous solutions to yield the products as a colored powders (R = OMe: bright yellow; R = Br: yellow; R = NO_2: light brown). The powder was triturated with pentane and collected by filtration through a glass frit. In the cases of R = Br and NO_2, the solid was dried on a vacuum line overnight and used without further purification. The resulting solid in the case of R = OMe was recrystallized from toluene/pentane at −40 °C and the crystals were dried overnight on a vacuum line before use. Yields: R = OMe: 0.591 g (84%); R = Br: 0.712 g (86%); R = NO_2: 0.879 g (97%).

R = OMe: ^{1}H NMR (500 MHz, toluene-d_8) δ 7.93 (s, 1H, C*H*=N), 7.45 (s, 1H, C*H*=N), 7.38 (d, *J* = 3 Hz, 1H, Ar*H*), 7.36 (d, *J* = 3 Hz, 1H, Ar*H*), 6.38 (d, *J* = 3 Hz, 1H, Ar*H*), 6.27 (d, *J* = 2.6 Hz, 1H, Ar*H*), 4.15 (q, *J* = 6 Hz, 1H, OC*H*$(CH_3)_2$), 3.75 (d, *J* = 12 Hz, 1H, NC*H*$_2$C$(CH_3)_2$N), 3.52 (s, 3H, ArO*Me*), 3.49 (s, 3H, ArO*Me*), 2.47 (d, *J* = 12 Hz, 1H, NC*H*$_2$C$(CH_3)_2$N), 1.76 (s, 9H, Ar*t-Bu*), 1.74 (s, 9H, Ar*t-Bu*), 1.17 (d, *J* = 6.0 Hz, 3H, OCH(C*H*$_3)_2$), 1.11 (s, 3H, NCH$_2$C(C*H*$_3)_2$N), 1.10 (d, *J* = 6.3 Hz, 3H, OCH(C*H*$_3)_2$), 0.62 (s, 3H, NCH$_2$C(C*H*$_3)_2$N); ^{27}Al NMR (130 MHz, toluene-d_8) δ 35.23. Anal. Calcd for $C_{31}H_{45}AlN_2O_5$: C, 67.37; H, 8.21; N, 5.07. Found: C, 67.43; H, 8.23; N, 4.98.

R = Br: ^{1}H NMR (500 MHz, toluene-d_8) δ 7.70 (d, J = 2.7 Hz, 1H, Ar*H*), 7.69 (d, J = 2.8 Hz, 1H, Ar*H*), 7.64 (s, 1H, C*H*=N), 7.18 (s, 1H C*H*=N), 6.97 (d, J = 2.6 Hz, 1H, Ar*H*), 6.91 (d, J = 2.6 Hz, 1H, Ar*H*), 4.05 (q, J = 5.9 Hz, 1H, OC*H*$(CH_3)_2$), 3.65 (d, J = 12.3 Hz, 1H, NC*H*$_2$C$(CH_3)_2$N), 2.39 (d, J = 12.2 Hz, 1H, NC*H*$_2$C$(CH_3)_2$N), 1.65 (s, 9H, Ar*t-Bu*), 1.63 (s, 9H, Ar*t-Bu*), 1.15 (d, J = 6.0 Hz, 3H, OCH(C*H*$_3)_2$), 1.06 (d, J = 6.3 Hz, 3H, OCH(C*H*$_3)_2$), 1.06 (s, 3H, NCH$_2$C(C*H*$_3)_2$N), 0.57 (s, 3H, NCH$_2$C(C*H*$_3)_2$N); ^{27}Al NMR (130 MHz, toluene-d_8) δ 34.11. Anal. Calcd for $C_{29}H_{39}AlBr_2N_2O_3$: C, 53.55; H, 6.04; N, 4.31. Found: C, 53.60; H, 6.08; N, 4.31.

R = NO_2: ^{1}H NMR (500 MHz, toluene-d_8) δ 8.49 (d, J = 2.1 Hz, 1H, Ar*H*), 8.48 (d, J = 2.3 Hz, 1H, Ar*H*), 7.92 (d, J = 2.4 Hz, 1H, Ar*H*), 7.76 (d, J = 2.3 Hz, 1H, Ar*H*), 7.66 (s, 1H, C*H*=N), 7.10 (s, 1H, C*H*=N), 3.96 (q, J = 5.7 Hz, 1H, OC*H*$(CH_3)_2$), 3.59 (d, J = 12.4 Hz, 1H, NC*H*$_2$C$(CH_3)_2$N), 2.43 (d, J = 12.3 Hz, 1H, NC*H*$_2$C$(CH_3)_2$N), 1.62 (s, 9H, Ar*t-Bu*), 1.60 (s, 9H, Ar*t-Bu*), 1.10 (d, J = 5.8 Hz, 3H, OCH(C*H*$_3)_2$), 1.04 (s, 3H, NCH$_2$C(C*H*$_3)_2$N), 1.03 (d, J = 6.3 Hz, 3H, OCH(C*H*$_3)_2$), 0.58 (s, 3H, NCH$_2$C(C*H*$_3)_2$N); ^{27}Al NMR (130 MHz, toluene-d_8) δ 33.07. Anal. Calcd for $C_{29}H_{39}AlN_4O_7$: C, 59.78; H, 6.75; N, 9.62. Found: C, 59.78; H, 6.78; N, 9.62.

3.5.3 ^{1}H NMR Kinetics

A representative procedure for the kinetic studies is described. To an oven-dried NMR tube in a nitrogen-filled glove box, 500 μL of a stock solution of catalyst in toluene-d_8 (0.0092 M) and 10 μL of the internal standard bis(*para*-trimethylsilyl)benzene in toluene-d_8 (0.28 M) were added. The NMR tube was capped with a septum and wrapped with parafilm. A gas tight syringe was loaded with 190 μL of ε-caprolactone (CL) stock solution (7.4 M), also in toluene-d_8. The target final concentrations of catalyst, internal standard and CL were 0.0062 M, 0.004 M, and 2 M, respectively. The gas tight syringe containing CL was inserted into a rubber septum to prevent air contamination

during the experiment setup. The NMR tube and syringe were removed from the glove box and brought to the spectrometer. The temperature on the NMR spectrometer (300 MHz Varian Inova) was calibrated using an ethylene glycol standard. A ^{1}H NMR spectrum was taken of the initial catalyst and internal standard solution before addition of CL with a relaxation time of 10 seconds and a 30° pulse width to ensure complete relaxation for quantitative integrations to determine catalyst concentration. Next, the tube was ejected from the spectrometer and CL was injected through the septum into the NMR tube, and the time between CL injection and start of the ^{1}H NMR data acquisition was recorded in minutes. The contents of the tube were well mixed before reinserting the NMR tube into the spectrometer. Again, a relaxation time of 10 seconds and a 30° pulse width were used for quantitative purposes, and an arrayed set of spectra were taken every 96, 192, or 384 s with 8, 16, or 32 scans, respectively, spin rate of 16 Hz, acquisition time 2 s, and maximum gain. The arrayed experiment was allowed to proceed until polymerization had completed, as indicated by the disappearance of the CL peaks. For each catalyst, four temperatures were carefully chosen, and three reactions were repeated at each temperature. The obtained arrayed NMR data were phased and baseline corrected in Mestrenova (http://mestrelab.com/) before being integrated by the same program. The integrations were recorded and entered into an Excel spreadsheet. Absolute concentrations of all species as a function of time were computed relative to the concentration of internal standard. Reaction time was calculated in seconds from the known length of time per spectrum and the time between CL injection and the start of the ^{1}H NMR data acquisition. The concentration *vs.* time data obtained from the ^{1}H NMR data were input into the COPASI program and fit to Equation 3.1 to obtain K_M and k_2 values. In general for all COPASI fits, concentrations of both CL and PCL *vs*. time data were input into the program with the first 10% of the concentration data omitted to avoid

the induction period and ensure proper temperature equilibration. Initial values for the respective kinetic parameters of k_1 = 0.0001, $k_{2'}$ = 0.0001, V_{max} = 0.001, and/or K_M = 1 were used (depending on the specific fit; $K_M = 1/K_{eq}$). In addition, the program was allowed to fit both the initial concentrations of CL and PCL, with $[CL]_0$ bound from −∞ to +∞ and given an initial starting value of either 2 or 1 M, depending on the analysis (vide infra), and $[PCL]_0$ bound from 0 to +∞ and given an initial starting value of 0 M. The Levenberg-Marquardt method of fitting was used with an iteration limit of 20000 and a tolerance of $1x10^{-10}$. Both [PCL] and [CL] were fit simultaneously by the program and the fits were run repeatedly with updated parameters until the fit stopped changing. The reaction rates were calculated by Equation 3.1 and plotted as a function of concentration, as shown in Figure 3.5. All linear and non-linear curve fits were performed using Graphpad Prism software. In a test of the significance of possible viscosity effects on the kinetics performed in the NMR tubes, a stirred polymerization using **2** (R = NO_2) at 298 K (average temperature inside nitrogen-filled glove box over the course of the reaction) with $[\mathbf{2}\ (R = NO_2)]_{tot}$ = 5.8 mM and $[CL]_0$ = 2 M (total volume 5 mL). Aliquots were removed at selected time points for NMR analysis, which revealed rate parameters similar to those seen in the NMR tube experiments. Error propagation and fittings to Erying and van't Hoff equations were performed as described in Chapter 2, section 2.5.5.

3.5.4 Density Functional Calculations

All stationary molecular geometries were fully optimized in the gas phase at the M06-L level of density functional theory[127] employing the 6-31+G(d,p) basis set[128] in the *Gaussian09* electronic structure program suite.[134] The nature of individual stationary points, i.e., their characterization as either minima or transition-state structures, was verified by the computation of analytical vibrational frequencies. These same calculations, within the conventional ideal-gas, rigid-rotator, quantum-mechanical

harmonic-oscillator (QMHO) approximation,[129] permitted the computation of thermal contributions to 323.15 K free energies. To compensate for errors in the QMHO approximation when applied to very low-frequency normal modes, vibrational frequencies below 50 cm^{-1} were replaced by values of 50 cm^{-1} (the quasi-harmonic approximation[162]). When the local minima associated with intervening TS structures were not obvious, their connections to individual TS structures were established by manually displacing TS structure geometries slightly in either direction along the computed reaction coordinates and allowing the subsequent structures to fully minimize to the relevant equilibrium structure. Higher than default integral accuracies (keyword int=(acc2e=11)) were required to converge frequency calculations; computed electronic energies were insensitive to this change. The effects of toluene as solvent were included through calculations at the same level of theory using the SMD quantum-mechanical continuum solvation model for the gas-phase optimized structures. In select instances, we explored the influence of reoptimization of the geometries including solvation and determined that the effects were small, and in so far as geometric convergence was considerably slower with the solvation model included, we restricted our consideration to gas-phase structures. Final, best-estimate composite free energies in solution were computed by replacing the M06-L/6-31+G(d,p) gas-phase electronic energies with single-point electronic energies computed using the M06-2X density functional[130] and the 6-311+G(d,p) basis set.[128] The M06-2X functional is particularly appropriate for these large, primarily organic architectures, where dispersion interactions between bulky groups may play a key role in stabilizing particular geometries and complexes.[131,132] Minima connected through individual TS structures were determined by displacing the geometries of TS structures by small amounts in both directions along their corresponding reaction coordinates and permitting the resulting structures to optimize to

their associated minima. All thermochemistries are reported for a standard state of 1 M (consistent with the usual experimental convention).[129] We assume that the computed free energies of solvation are dominated by enthalpic effects, and include them in both reported enthalpies and free energies in discussion.

3.5.5 Derivation of Equation 3.1 Using Substrate Inhibition Mechanism

Mechanism:

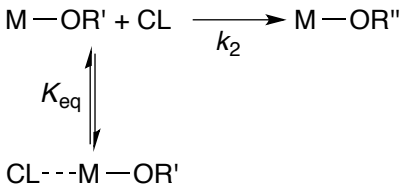

Definitions:

$$\frac{d[M-OR'']}{dt} = v = k_2[M-OR'][CL] \quad K_{eq} = \frac{[CL-M-OR']}{[M-OR'][CL]}$$

$$[M-OR']_{tot} = [M-OR'] + [CL-M-OR']$$

Divide rate equation v by [M-OR']$_{tot}$:

$$\frac{v}{[M-OR']_{tot}} = \frac{k_2[M-OR'][CL]}{[M-OR'] + [CL-M-OR']}$$

Apply definition for K_{eq}:

$$\frac{v}{[M-OR']_{tot}} = \frac{k_2[M-OR'][CL]}{[M-OR'] + K_{eq}[M-OR'][CL]}$$

Cancel [M-OR'] from numerator and denominator:

$$\frac{v}{[M-OR']_{tot}} = \frac{k_2[CL]}{1 + K_{eq}[CL]}$$

Rearrange:

$$v = \frac{k_2[M-OR']_{tot}[CL]}{1/K_{eq} + [CL]}$$

3.5.6 Experimental Details for X-ray Structure of 2 (R = OMe)

A crystal (approximate dimensions 0.30 x 0.25 x 0.15 mm^3) was placed onto the tip of a 0.1 mm diameter glass capillary and mounted on a Bruker APEX-II CCD

diffractometer for a data collection at 173(2) K.[123] A preliminary set of cell constants was calculated from reflections harvested from three sets of 20 frames. These initial sets of frames were oriented such that orthogonal wedges of reciprocal space were surveyed. This produced initial orientation matrices determined from 89 reflections. The data collection was carried out using MoKα radiation (graphite monochromator) with a frame time of 40 seconds and a detector distance of 6 cm. A randomly oriented region of reciprocal space was surveyed to the extent of one sphere and to a resolution of 0.77 Å. Four major sections of frames were collected with 0.30º steps in ω at four different φ settings and a detector position of -28º in 2θ. The intensity data were corrected for absorption and decay (SADABS).[124] Final cell constants were calculated from the xyz centroids of 9997 strong reflections from the actual data collection after integration (SAINT).[125] The structure was solved using SHELXS-97 (Sheldrick, 1990)[126] and refined using SHELXL-97 (Sheldrick, 1997).[126] The space group $P2_1/c$ was determined based on systematic absences and intensity statistics. A direct-methods solution was calculated which provided most non-hydrogen atoms from the E-map. Full-matrix least squares / difference Fourier cycles were performed which located the remaining non-hydrogen atoms. All non-hydrogen atoms were refined with anisotropic displacement parameters. All hydrogen atoms were placed in ideal positions and refined as riding atoms with relative isotropic displacement parameters. The final full matrix least squares refinement converged to $R1 = 0.0470$ and $wR2 = 0.1319$ (F^2, all data).

3.6 Acknowledgments

This work was supported by the Center for Sustainable Polymers at the University of Minnesota, a National Science Foundation (NSF) supported Center for Chemical Innovation (CHE-1136607), and by NSF grants to D. J. M. and C. J. C. (CHE-0952054), an NSF graduate research fellowship to M. O. M. (grant no. 00006595), and UM Lando and Heisig grants in support of undergraduate student research (Y. D. and M. A. J.).

4 Catalytic Decarbonylation of Biomass-Derived Carboxylic Acids as an Efficient Route to Commodity Monomers

In part from:

Maria O. Miranda, Agostino Pietrangelo, Marc A. Hillmyer, and William B. Tolman. *Green Chemistry*, **2012**, *14*, 490-494.

4.1 Overview

The palladium-catalyzed decarbonylation of bio-derived carboxylic acids to alkyl acrylates, styrene, and acrylonitrile is reported. The olefins were isolated by continuous distillation in yields up to 87% by heating a neat, equimolar mixture of pivalic anhydride with the appropriate carboxylic acid to 190 °C in the presence of a Pd-phosphine catalyst.

4.2 Introduction

As described in Chapter 1, escalating demands for resources derived from diminishing fossil fuel reserves have made the quest for sustainable alternatives of paramount importance. With an annual global production of billions of metric tons per year,[72] biomass (in the form of carbohydrates, oils, lignins, and terpenes) has emerged as a sustainable platform from which the generation of commodity chemicals, fuel, and energy can be realized.[71,163,164] As an example, the production of olefins via transition-metal-catalyzed decarbonylation is of considerable interest given the availability, low toxicity, and structural diversity of bio-derived carboxylic acids. Miller and coworkers were among the first to prepare terminal alkenes from long chain fatty acids by heating

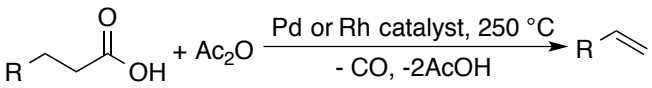

Figure 4.1. Decarbonylation of long-chain fatty acids using Pd or Rh catalysts first demonstrated by Miller.

the latter to 250 °C (Figure 4.1) neat with one equivalent of acetic anhydride, (Ac_2O), triphenylphosphine (PPh_3, 0.5 mol%), and 0.01 mol% of a Pd- or Rh-based catalyst.[81] During this transformation, a mixed anhydride (generated *in situ*) is postulated to undergo oxidative addition to a transition-metal species to yield an acyl complex (Scheme 4.1).[80] Subsequent decarbonylation followed by β-hydride elimination affords the corresponding olefin along with an equivalent of carbon monoxide and two equivalents of acetic acid. In principle, both the CO and acetic acid can be recycled to make syngas and acetic anhydride, respectively. Subsequent work by Gooβen[87] and Scott[90] showed that lower temperatures (*ca*. 110 °C) can be employed at the expense of using a solvent and higher palladium (*ca*. 3 mol%) and ligand (*ca.* 9 mol%) loadings; Ryu and coworkers have recently reported similar results using Ir-based catalysts in lieu of Pd.[165] After our work

was published, alternative procedures were reported by Stoltz and coworkers using Pd(II), phosphine ligands and a biphenol protic additive. However, despite utilizing low loadings of Pd (0.05 mol%) and ligand (0.06 mol%) and moderately lower temperatures (132 °C), the method requires portion-wise addition of the low boiling acetic anhydride, and only results in moderate yields (less than 60%) of the desired terminal olefin.[82]

Herein, we report a simple and facile method that converts bio-sourced mono-alkyl succinates into alkyl acrylates, monomers used extensively in the paint, coatings, adhesive, and textile industries.[166] Moreover, we have extended the scope of this method to include the production of styrene and acrylonitrile from bio-derived hydrocinnamic acid and 3-cyanopropanoic acid, respectively. Clostridia enzymatically produce hydrocinnamic acid from *l*-phenylalanine[167] and hydrocinnamic acid can also be prepared from cinnamaldehyde, a renewable resource.[168] 3-Cyanopropanoic acid can be prepared

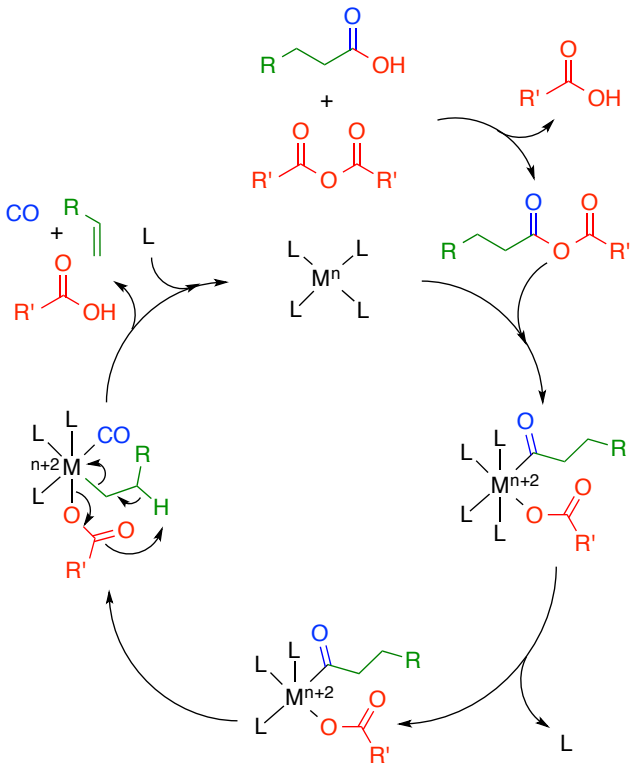

Scheme 4.1. Proposed decarbonylation mechanism.

from glutamic acid, another biorenewable resource.[169] As is the case with alkyl acrylates, both styrene and acrylonitrile are high volume petrochemically derived commodity chemicals that are used in the production of many consumer items (*i.e.*, toys, housings, computer components, furniture, disposable tableware),[170] fibers in the textile industry and molded components in the automobile and appliance industries.[171]

In addition to the novel substrates studied and practical application of the products, we also use lower catalyst and ligand loadings (ligands studied presented in Figure 4.2) and shorter reaction times than reported by Gooβen and Scott,[87,90] as well as a solvent-free reaction and simple distillation procedure that avoids aqueous workup. In contrast to the method of Miller,[81] we have chosen a high-boiling exogenous anhydride that avoids continuous addition to the reaction. Finally, we demonstrate the robustness of the reaction to air, water, and increased scale.

4.3 Results and Discussion

4.3.1 Mono-Alkyl Succinates

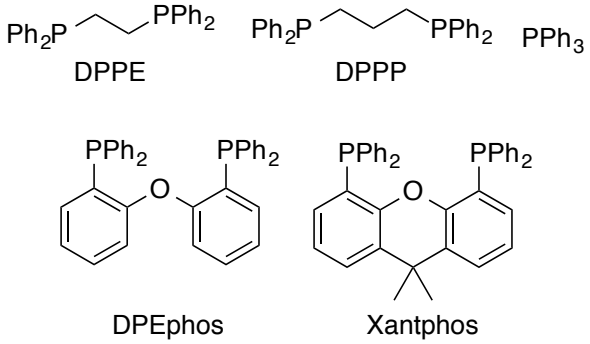

Figure 4.2. Ligands used in this chapter to study catalytic decarbonylation of carboxylic acids.

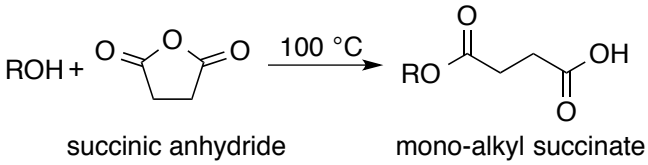

Figure 4.3. Preparation of mono-alkyl succinates from succinic acid and alcohols.

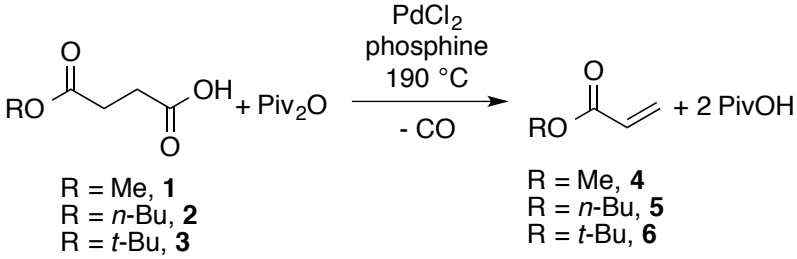

Figure 4.4. Decarbonylation of mono-alkyl succinates to alkyl acrylates.

Mono-alkyl succinates were readily prepared according to Figure 4.3 by heating an alcohol (R = Me, *t*-Bu, *n*-Bu) with succinic anhydride, the dehydration product of succinic acid, a biorenewable resource produced from the fermentation of sugars.[71,172–174] In our variation of Miller's procedure,[81] one equivalent of pivalic anhydride (Piv_2O, b.p. = 193 °C) was used in lieu of Ac_2O (b.p. = 140 °C) at a reduced temperature of 190 °C to

avoid continuous addition of anhydride during each experiment. To both compensate for the lower temperature and possibly increase reaction rates, palladium (*i.e.*, $PdCl_2$) and ligand loadings were initially increased to 0.25 mol% and 2.2 mol%, respectively, as compared to Miller's protocol. Using a standard short-path distillation head under a moderate flow of N_2 (or Ar), a clear solution was isolated by continuous distillation after 2 hours of heating dry mono-succinate ester (**1**, **2** or **3**), Piv_2O, $PdCl_2$, and ligand (Figure 4.4).

Table 4.1. Yields (%) for the catalytic decarbonylation of mono-alkyl succinates.[a]

Entry	Ligand	R	Acrylate[b]	PivOR[b]	PivOH[c]
1	PPh_3	Me	50	3	71
2	DPEphos	Me	64	12	49
3	PPh_3	*n*-Bu	62	8	62
4	DPEphos	*n*-Bu	45	21	60
5	PPh_3	*t*-Bu	31	11	79
6	DPEphos	*t*-Bu	18	10	90

[a] All experiments were carried out using dry reagents under an N_2 or Ar atmosphere unless otherwise noted. $PdCl_2$ loading: 0.25 mol%, ligand loading: 2.2 mol%, calculated based on succinic ester substrate. T ≅ 190 °C. All results calculated from GC-MS data. [b] Yields based on succinic ester substrate. [c] Yields based on stoichiometry of Figure 4.4 (2 moles PivOH per mole Piv_2O).

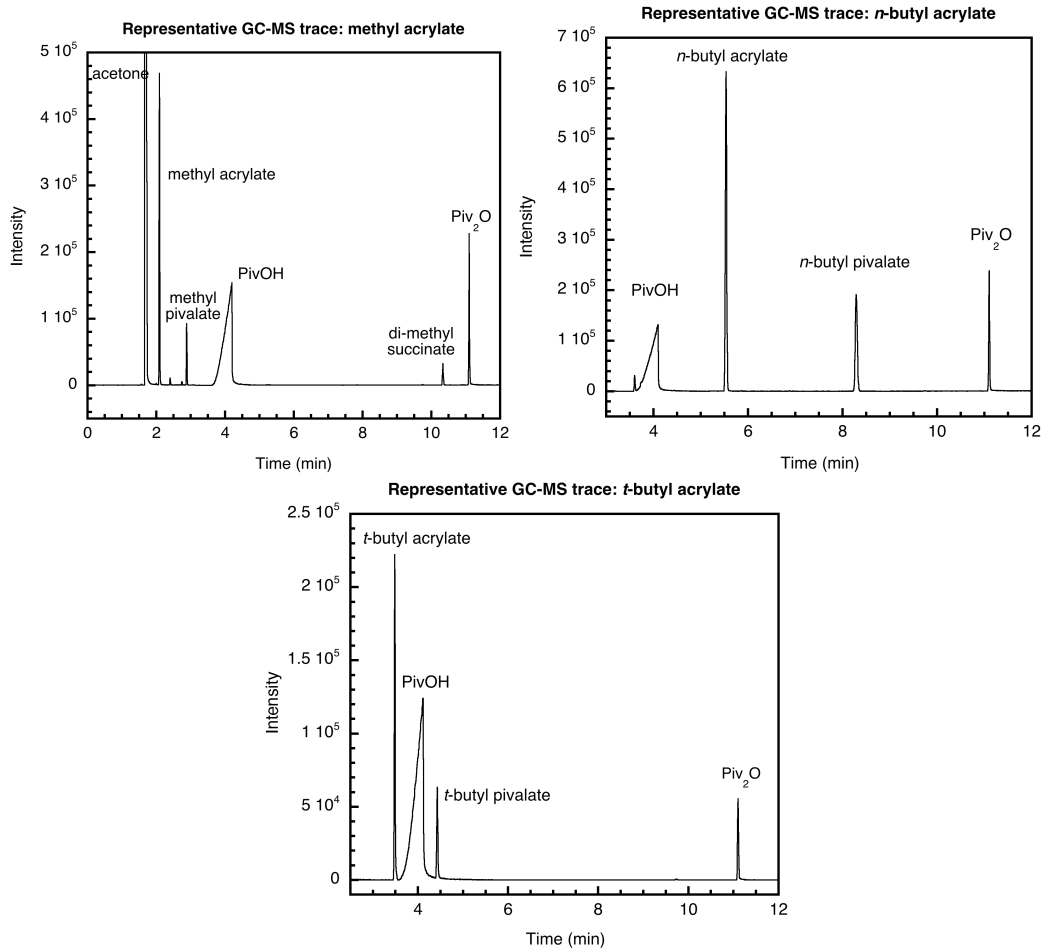

Figure 4.5. Representative GC-MS traces of distillate mixtures from decarbonylation of the mono-alkyl succinates **1**, **2**, and **3**, and PPh_3 as the ligand for **1** and DPEphos as the ligand for **2** and **3**.

Analysis of the distillate by both gas chromatography-mass spectrometry (GC-MS) and ^{1}H NMR spectroscopy confirmed the presence of the desired alkyl acrylate. Methyl acrylate (**4**) was prepared in 50% and 64% yield when using PPh_3 and bis[(2-diphenylphosphino)phenyl] ether (DPEPhos) as the ligands, respectively (entries 1 and 2, Table 4.1). Results for the production of *n*-butyl acrylate (**5**) were comparable, but the yields of *t*-butyl acrylate (**6**) from mono-*t*-butyl succinate (**3**) were lower, 31% when using PPh_3 and 18% when using DPEphos (entries 5 and 6, Table 4.1). Interestingly,

minor amounts of alkyl pivalates (PivOR) were also produced during the course of these experiments, suggesting the presence of a competitive reaction. Indeed, in a control experiment, Piv_2O and **1** (or **3**) were heated in an equimolar ratio to 190 °C for two hours. GC-MS analysis of the crude mixture (Figure 4.6) detected succinic anhydride, PivOH, and methyl pivalate (or *t*-butyl-pivalate). We hypothesize that the mono-alkyl succinates undergo an intramolecular cyclization to reform succinic anhydride and alcohol, with the latter reacting with Piv_2O to form PivOH and PivOR (Figure 4.7).

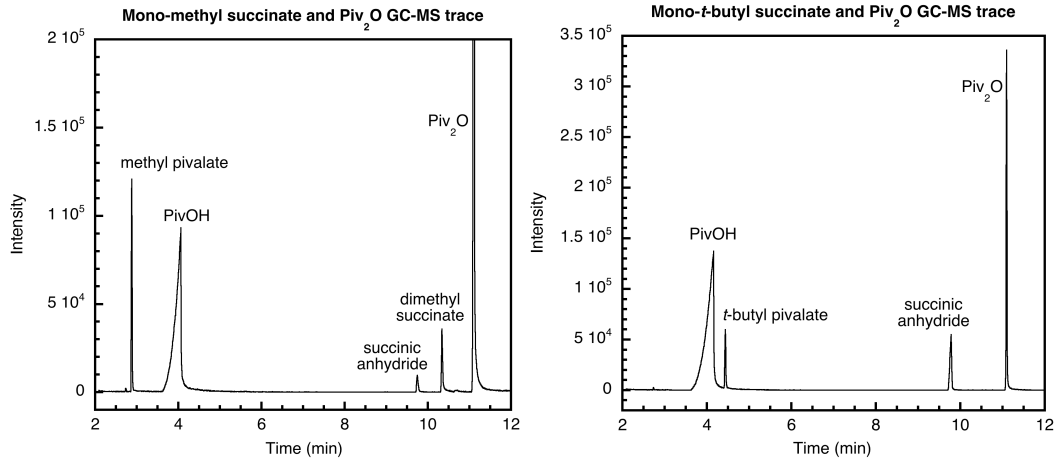

Figure 4.6. GC-MS traces of the sealed reaction between **1** (left) and **3** (right) and pivalic anhydride at 190 °C for 2 hours.

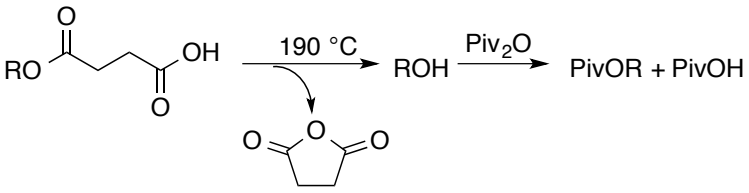

Figure 4.7. Competitive reaction with decarbonylation that produces alkyl pivalates.

4.3.2 Hydrocinnamic Acid

In an expansion of the scope to other bio-derived carboxylic acids, we examined the production of styrene from hydrocinnamic acid (Figure 4.8). Both GC-MS and ^1H NMR analyses of the distillate (isolated under the aforementioned reaction conditions

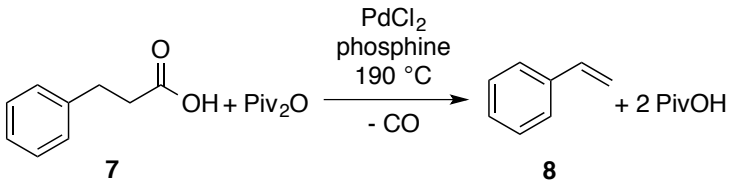

Figure 4.8. Decarbonylation of hydrocinnamic acid to styrene.

using PPh_3 as the ligand) revealed the formation of styrene in 74% (GC-MS) yield (entry 1, Table 4.2). Distillation began after approximately 30 minutes at 180–190 °C, and the reaction was allowed to continue for 2 h. Isolation of pure styrene was achieved by washing the diluted distillate with aqueous NaOH to remove the pivalic acid, followed by a short silica column to remove remaining pivalic anhydride. Pivalic anhydride can also be removed by stirring with concentrated aqueous *para*-toluenesulfonic acid (*p*-TsOH). The separation of styrene from pivalic acid and pivalic anhydride through fractional distillation was unsuccessful due to co-distillation of styrene and pivalic acid and polymerization of styrene. In the previous study by Gooβen, low yields (27%) were reported when PPh_3 was used as the ligand under their procedures.[87]

Table 4.2. Yields (%) of decarbonylation using hydrocinnamic acid.[a]

Entry	Ligand	Ligand mol %[b]	Styrene[c]	PivOH[c]
1	PPh_3	2.2	74 (73)	65 (66)
2	DPPE	2.2	0 (0)	0 (0)
3	DPPP	2.2	55 (52)	52 (54)
4	DPEphos	2.2	81 (82)	83 (81)
5	Xantphos	2.2	80 (84)	85 (84)
6	PPh_3	4.4	65 (70)	81 (82)
7	DPPE	4.4	0 (0)	0 (0)
8	DPPP	4.4	48 (40)	60 (60)
9	DPEphos	4.4	84 (87)	85 (81)
10	Xantphos	4.4	87 (92)	86 (83)
11[d]	DPEphos	0.5	68 (74)	88 (85)

12[e]	DPEphos	2.2	72 (75)	73 (78)
13[f]	DPEphos	2.2	78 (72)	84 (90)
14[f]	PPh_3	2.2	71 (61)	66 (75)
15[d,f]	PPh_3	0.5	57 (50)	60 (64)
16[g]	DPEphos	0.25	54 (58)	70 (69)

[a] All experiments were carried out using dry reagents under an N_2 or Ar atmosphere unless otherwise noted. $PdCl_2$ loading: 0.25 mol% and 1 g scale of hydrocinnamic acid unless otherwise noted. T ≅ 190 °C [b] Calculated based on hydrocinnamic acid substrate. [c] Percent yield in distillate calculated from GC-MS (NMR) data. A representative GC-MS trace can be found in Figure 4.9. [d] $PdCl_2$ loading: 0.01 mol% and 25 g scale of hydrocinnamic acid. [e] Air was used as carrier gas. [f] Air was used as carrier gas. Reagents were left open to atmosphere for at least 24 h. [g] $PdCl_2$ loading: 0.005 mol% and 50 g scale of hydrocinnamic acid. Allowed to react for 31 h.

The nature of the ligand and its effect on the product yield were investigated by examining a number of bidentate phosphine ligands (Table 4.2). Styrene formation was inhibited when 1,2-bis(diphenylphosphino)ethane (DPPE) was used in lieu of PPh_3 (entries 2 and 7, Table 4.2). In these cases, analysis of the crude reaction mixture by ^1H NMR spectroscopy revealed only the presence of the mixed anhydride formed from hydrocinnamic acid and pivalic anhydride. In addition, palladium black formed instantly upon heating to 160 °C suggesting that the DPPE-palladium catalyst is not stable under these conditions. Using 1,3-bis(diphenylphosphino)propane (DPPP) as the ligand afforded styrene, although lower yields and longer times for the onset of distillation (30−45 min) were observed (entries 3 and 8, Table 4.2). DPEphos (known to be successful, *vida supra*) and 4,5-bis(diphenylphosphino)-9,9-dimethylxanthene (Xantphos), also were considered since both are strongly coordinating phosphine ligands that have been shown to improve product yields for hydrocyanation [175] and hydrocarbonylation[176] of styrene and the decarbonylation of phenylbutanoic acid to 3-phenylpropene.[87] Consistent with trends reported by Gooβen and coworkers,[87] Xantphos

and DPEphos were determined to be the most effective phosphines in promoting decarbonylation, generating styrene in *ca*. 80% yield (entries 4,5,9-13,16, Table 4.2). Unlike the more sluggish PPh_3 and DPPP systems, the onset of distillation proceeded quickly (*ca*. 5 min.), and rapid evolution of CO was observed once the reaction flask reached 190 °C. Increasing the ligand loading to 4.4 mol% (entries 6-10,Table 4.2) and/or adding the stabilizer *t*-butyl catechol (data not shown) had a negligible effect on product yield. In contrast to the stark difference in yields reported by Gooβen for the decarbonylation of phenylbutyric acid (27% for PPh_3 vs. 83-81% DPEphos),[87] the improvements in yields for the more expensive chelating phosphines DPEphos and Xantphos relative to PPh_3 were negligible in our system. Scaling up the decarbonylation of hydrocinnamic acid was successful; using much lower $PdCl_2$ (0.01 mol%) and DPEphos (0.5 mol%) loadings on a *ca.* 25 g scale afforded styrene in ~ 70% yield (entry 11, Table 4.2).

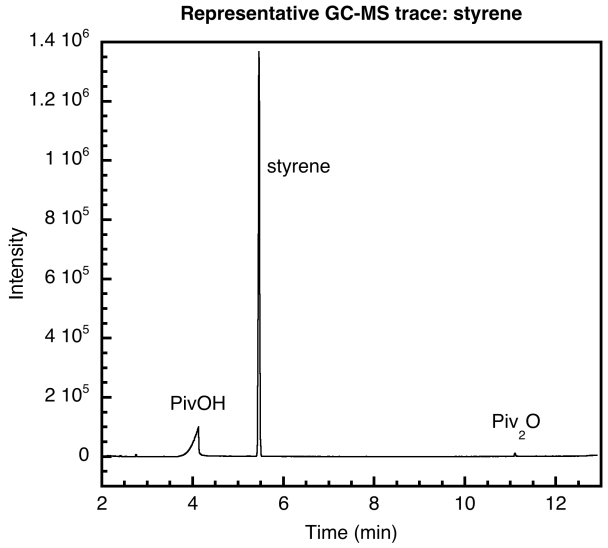

Figure 4.9. Representative GC-MS trace of distillate mixture using hydrocinnamic acid (**7**) as the substrate and DPEphos as the ligand.

To test the robustness of the decarbonylation reaction, a series of experiments were performed using a combination of wet or dry reagents and air instead of N_2 or Ar as the carrier gas. Performing the reactions using dry reagents (i.e., $PdCl_2$, Piv_2O, DPEphos) and reagent-grade hydrocinnamic acid under a moderate flow of air afforded styrene in ~72% yield (entry 12, Table 4.2), only *ca.* 9% less when compared to using N_2 as a carrier gas and recrystallized, sublimed and dried hydrocinnamic acid (entry 4, Table 4.2). Heating wet reagents ($PdCl_2$, Piv_2O, and ligands were left open to atmosphere for at least 24 hours and hydrocinnamic acid was used as received without purification and left open to atmosphere for ~ 4 months) under a moderate flow of air (otherwise identical conditions) resulted in the formation of styrene in comparable yields to using dry reagents under air (entry 13, Table 4.2). Using PPh_3 in lieu of DPEphos as a ligand gave rise to styrene in similar yields (entry 14, Table 4.2). Reducing the wet $PdCl_2$ and PPh_3 loadings to 0.01 mol% and 0.5 mol%, respectively, on a *ca.* 25 g scale of reagent-grade hydrocinnamic acid afforded styrene in ~57% (GC-MS) yield (entry 15, Table 4.2). Thus, in contrast to previous studies that reported decarbonylation reactions using dried reagents and under a flow of inert gas, we have demonstrated that this reaction is robust to both air and water; rigorously dried reagents and a flow of inert gas do not markedly improve yields or reduce reaction times. This finding renders the overall transformation less energy, solvent and time intensive.

In an effort to further improve the reaction efficiency for the production of styrene, the Pd and ligand loadings were reduced to 0.005 mol% and 0.025 mol%, respectively (entry 16, Table 4.2). The yield for this reaction is comparable to yields with higher loadings. However, the reaction is slower, requiring 31 h to complete the distillation, whereas reactions with double the Pd and ligand loadings (0.01 mol% Pd, 0.5 mol% ligand) required a maximum 3 h to complete the distillation.

Finally, we were able to scale up our procedure to synthesize 100 g of bio-based styrene in a project supported by Bridgestone Corporation. In order to ensure that the styrene product was entirely bio-based, we synthesized hydrocinnamic acid from naturally sourced cinnamaldehyde.[168] The starting cinnamaldehyde (purchased from Sigma Aldrich) was determined to be 99 ± 3% bio-based by the standard analytical testing procedure ASTM-D6866-12, performed by Beta Analytic Inc. This procedure is similar to radiocarbon dating in that it compares the naturally occurring ^{14}C isotope in an unknown sample to that of a known standard (see section 4.5.4 for the results provided by the testing agency Beta Analytic Inc.). Hydrogenation of cinnamaldehyde followed by nitric acid oxidation yielded the bio-based hydrocinnamic acid starting material in 67% yield; subsequent decarbonylation of the purified (but not dried) hydrocinnamic acid in small (10-15 g) batches was achieved using the aforementioned $PdCl_2$ (0.25 mol%) and DPEphos (2.2 mol%) system with isolated yields of approximately 65% (comparable to smaller scale yields in Table 4.2). Unreacted Piv_2O in the distillate was removed by vigorous stirring of the diluted distillate with concentrated aqueous *p*-TsOH, and then washing the organic fraction with aqueous sodium hydroxide to remove pivalic acid. Testing of the isolated styrene using the same ASTM-D6866-12 standard determined the styrene to have a bio-based content of 97 ± 3%.

4.3.3 3-Cyanopropanoic Acid

Finally, we have applied our methodology to the synthesis of acrylonitrile from 3-cyanopropanoic acid. Using rather mild reagents (NaOCl, NaBr, water), 3-cyanopropanoic acid can be synthesized by the oxidative decarboxylation of glutamic acid, a biorenewable resource.[169] Subsequent decarbonylation of 3-cyanopropanoic acid using our procedure ($PdCl_2$ 0.25 mol%, PPh_3 2.2 mol%) resulted in isolation of distillate that contained acrylonitrile in 23% yield by GC-MS (Figure 4.10). The distillate also

contained PivOH and Piv_2O. The low yields are explained by the presence of polyacrylonitrile in the reaction mixture, as observed by ^1H NMR spectroscopy. Addition of *t*-butyl catechol to the reaction mixture as an inhibitor did not improve the yield of isolated acrylonitrile. Recently, similar results were obtained by Scott and coworkers[169] using a modified version of Gooβen's procedure.

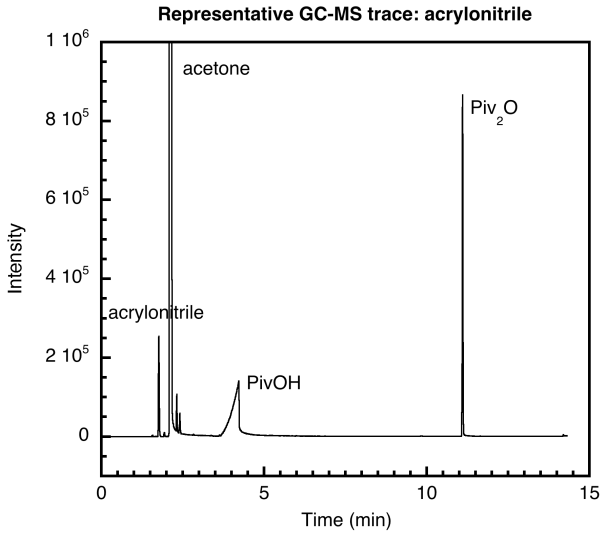

Figure 4.10. Representative GC-MS trace of distillate mixture using 3-cyanopropanoic acid as the substrate and PPh_3 as the ligand.

4.4 Summary and Conclusions

Using palladium-catalyzed decarbonylation of bio-derived carboxylic acids we prepared alkyl acrylates, styrene, and acrylonitrile in good yields. The developed procedure is applicable to a diverse set of carboxylic acid substrates, and involves continuous distillation of the desired products from the reaction mixture. In addition, catalyst loadings can be lowered to 0.005 mol% and the reaction scale increased to 50 grams with only a small reduction in product yield. We also performed a careful ligand screening using a variety of chelating phosphines, highlighting the importance of the ligand on reaction efficacy. Interestingly, PPh_3 was nearly as good a ligand at promoting the decarbonylation reaction as the strongly coordinating diphosphines DPEphos and Xantphos, demonstrating that a simple and inexpensive system can be realized for the decarbonylation of bio-derived carboxylic acids. Finally, we illustrated the robustness of this system. Using reagent-grade and wet starting materials under an air purge gives comparable yields to reactions using purified and dried reagents and an inert (N_2 or Ar) gas purge. Additionally we were able to synthesize 100 g of bio-based styrene using our procedure starting from naturally derived cinnamaldehyde. Extending this chemistry to utilize first-row transition metals as catalysts with hopes to achieve lower temperatures (to prevent *in situ* polymerization of the product and deleterious side-reactions) and minimize cost is described in Chapter 5.

4.5 Experimental Section

4.5.1 General Considerations

All experiments were carried out in an inert atmosphere unless otherwise noted. All organic reagents were purchased from Sigma Aldrich and used without further purification unless otherwise noted. Mono-methyl succinate[177] and 3-cyanopropanoic acid[169] were prepared according to literature procedures. While purchased from Sigma Aldrich, mono-*tert*-butyl succinate can be prepared by reacting succinic anhydride with *tert*-butanol.[178] Palladium (II) chloride was purchased from Strem Chemicals and dried under vacuum for 24 h at 90 °C. Pivalic anhydride was dried over molecular sieves. Hydrocinnamic acid was recrystallized from dry pentane and sublimed prior to use. All phosphine ligands were dried under vacuum for 24 h at 90 °C. PPh_3, DPPP, and DPPE were recrystallized from ethanol prior to drying under vacuum. 4-*tert*-butyl catechol was recrystallized from pentanes and dried under vacuum for 24 h at 120 °C. Triethylamine was allowed to stir over CaH_2 overnight prior to use. Cinnamaldehyde (natural, >93%) was purchased from Aldrich and purified by vacuum distillation before use. Ether and dichloromethane were passed through a purification column (Glass Contour, Laguna, CA) prior to use. All ^1H NMR spectra were collected on either a Varian VXR-500 or Varian VI-300 spectrometer and calibrated to the residual protonated solvent at δ 7.24 for deuterated chloroform ($CDCl_3$). All GC-MS experiments were conducted on an Agilent Technologies 7890A GC system and 5975C VL MSD. The GC column was a HP-5 ms with dimensions 30 m x 0.25 mm. The standard method used for all runs involved an initial oven temperature of 50 °C (held for 2 min) followed by a 20 °C/min ramp to 70 °C (held for 6 min), followed by a final 20 °C/min ramp to 230 °C (held for 3 min).

4.5.2 Synthetic Procedures

Mono-*n*-Butyl Succinate. In a modified version of a reported procedure,[179] to a 250-mL oven dried round bottom flask succinic anhydride (49.6 g, 49.2 mol) and *n*-butanol (44 mL, 48.1 mol) were added and a reflux condensor was attached. The mixture was heated to 120 °C and allowed to reflux for 3 h. After cooling overnight to room temperature, a white precipitate was observed. The unreacted succinic anhydride was removed by filtration, leaving crude mono-*n*-butyl succinate. A portion of the crude material (9.4 g) was chromatographed (column diameter = 7.6 cm, column height = 56 cm) on silica using dichloromethane as the eluent until the di-butyl succinate ester eluted. Ethyl acetate was then added to the column to remove the desired product, mono-*n*-butyl succinate. The product was dissolved in 50 mL of dry ether and dried over $MgSO_4$, which was removed by filtration. The solvent was removed from the filtrate *in vacuo* to afford the product as a yellow oil (5.04 g, 54%). ^{1}H NMR (300 MHz, $CDCl_3$) δ 11.49 (1H, s, O*H*), 4.07 (2H, t, *J* = 6.6 Hz, $OCH_2CH_2CH_2CH_3$), 2.62 (4H, m, $COCH_2CH_2CO$), 1.58 (2H, quintet, *J* = 7.3 Hz, $OCH_2CH_2CH_2CH_3$), 1.34 (2H, dq, *J* = 15.1, 7.5 Hz, $OCH_2CH_2CH_2CH_3$), 0.892 (3H, t, *J* = 7.3 Hz, $OCH_2CH_2CH_2CH_3$) ppm.

Standard Decarbonylation Reaction Protocol. In a dinitrogen atmosphere glovebox, hydrocinnamic acid (1 g, 6.7 mmol), palladium(II) chloride (3 mg, 0.25 mol%), pivalic anhydride (1.35 mL, 6.7 mmol), and phosphine ligand (2.2 mol% or 4.4 mol%) were loaded into an oven-dried 15 mL round-bottom flask equipped with a Teflon stir bar. Not all of the reagents were soluble at room temperature, resulting in a heterogeneous mixture. The round-bottom flask was attached to an oven-dried short-path distillation apparatus, removed from the glovebox and placed under an atmosphere of dinitrogen or argon gas. The reaction flask was lowered into a 160 to 170 °C oil bath and allowed to continue to heat until the oil bath reached 190 °C. In most cases, the reaction mixture became homogenous and yellow after heating. Once the reaction mixture reached

about 185 °C, it began to bubble vigorously, indicating loss of carbon monoxide. The reaction was allowed to proceed for two hours, during which time a distillate was collected. After 2 h, heating was ceased and the reaction was exposed to air. Both the colorless distillate and yellow residual reaction mixture were analyzed using ^{1}H NMR spectroscopy, and the distillate was also analyzed using GC-MS. For GC-MS yield determinations, a solution containing a known mass of the isolated distillate was injected on the GC-MS instrument. Each trace was analyzed using the Agilent GC/MSD ChemStation software package and the area under each peak of interest was determined. Previously generated calibration curves were used to determine the concentration and mass ratio of each component in the mixture from the peak areas. The percent yield was calculated from averages of multiple (3-5) GC-MS runs.

Styrene Separation Protocol. A mixture comprised of styrene (3.13 g, 30.0 mmol), pivalic acid (6.35 g, 62.1 mmol), and pivalic anhydride (0.63 g, 3.4 mmol) was diluted with 35 mL of pentanes and washed with a 1.7 M aqueous NaOH solution (3 x 50 mL). The organic phase was diluted with an additional 15 mL of pentanes and dried over $MgSO_4$. After filtration, solvent was removed to afford a mixture of styrene and pivalic anhydride (as characterized by ^{1}H NMR spectroscopy) that was then chromatographed (column diameter = 5 cm, column height = 25 cm) on silica using pentane as the eluent to yield styrene (2.03 g, 65 %). The column can be avoided if before the basic workup, the pentane solution is stirred with a concentrated aqueous solution of *p*-TsOH overnight. The pentane solution can be checked for presence of Piv_2O by GC-MS, and allowed to stir longer if necessary. After washing with 1.7 M or 3.4 M aqueous NaOH (3 x 50 mL), removal of the aqueous layer, drying over $MgSO_4$, and careful concentration of the pentane yields styrene in similar yields.

***N*-Butyl Pivalate Ester.**[180] Butanol (6.2 mL, 67.8 mmol), pivaloyl chloride (10.1 mL, 82.1 mmol), 4-dimethylaminopyridine (0.4196 g, 3.4 mmol) and dry dichloromethane (140 mL) were added to an oven dried 250-mL round bottom flask equipped with a stir bar. To this, triethylamine was added (11.5 mL, 82.5 mmol). After an exothermic reaction, a white precipitate formed. The reaction was allowed to stir overnight, then 100 mL of dichloromethane was added. The organic layer was washed with 250 mL water twice, 250 mL of 1M HCl once, 250 mL of saturated aqueous Na_2CO_3 once, and 250 mL saturated aqueous NaCl once. The organic layer was dried over $MgSO_4$, filtered, and the dichloromethane was removed from the filtrate *in vacuo*. A portion of the crude product (2.44 g) was chromatographed (column diameter = 5 cm, column height = 25 cm) using dichloromethane as the eluent (2.09 g, 86%). The ^{1}H NMR spectrum of the product matched data reported previously.[181]

Hydrocinnamaldehyde. A 250 mL stainless steel hydrogenator was loaded with 10% Pd/C catalyst (800 mg, 0.75 mmol Pd) and filled with nitrogen. The catalyst was activated by heating the hydrogenator at 80 °C for 2 hours under vacuum. Cinnamaldehyde (130 g, 0.86 mol) was transferred into the hydrogenator, which was then purged with hydrogen gas three times and eventually filled with with hydrogen to a final pressure of 400 psi. The temperature on the hydrogenator was then slowly raised to 80 °C, was allowed to react between 2 and 3 days. The hydrogen was refilled approximately to 500 psi every 8-12 hours, ensuring continued consumption of hydrogen. The pressure in the reactor will decrease very rapidly in the first 12 hours and should be repressurized with hydrogen whenever the pressure reads below 100 psi. After the first 12-18 hours, the reaction proceeds more slowly, and can be repressurized less frequently. Completion of the reaction can be identified by stabilization of or even a slow increase in the pressure of the reactor. After the reaction was completed, the Pd/C catalyst was filtered away,

discarded and the neat hydrocinnamaldehyde was used without purification in the next reaction.

Hydrocinnamic acid. To a 1 L round bottom flask cooled in an ice bath, nitric acid (400 mL, 63 wt%) and sodium nitrite (3.2 g) were added and allowed to stir for 15 minutes. Hydrocinnamaldehyde (130 g) in toluene (130 mL) was added to the vigorously stirred solution dropwise at 0 °C. The temperature was maintained at 0 °C until addition of the hydrocinnamaldehyde solution was complete. The dark yellow mixture was allowed to warm to room temperature and stirred vigorously for two to three days, upon which time the color lightened to a light yellow solution. It is critical that the reaction stir vigorously over the entire reaction time. After two to three days, the lower acid layer was drained away, and the upper organic layer was washed with distilled water (3 x 100 mL) and saturated aqueous sodium chloride (3 x 100 mL), followed by removal of toluene *in vacuo*. The remaining yellow oil was vacuum distilled under reduced pressure twice at 110°C to give a pale yellow liquid that solidified upon exposure to air. The doubly distilled product was then recrystallized from warm pentane, cooled to room temperature then to 0 °C yielding white crystals that were washed with cold pentane (85 g, 67%).

4.5.3 Large Scale Decarbonylation Reactions

General Considerations. It is very important that not only the reaction flask and contents be between 180-185 °C, but also the short path distillation head be kept warm as well to ensure efficient distillation of styrene. While never used in any reactions to date, the distillation head may be wrapped with heating tape if reaction scale is so large that the residual heat from the oil bath is unable to consistently keep the glass of the distillation head above approximately 140 °C. The distillation head should be wrapped in glass wool and the reaction flask was secured to the distillation head through the copper necklace and rubber bands to ensure no leakage of distillate. It is likely that the heat of the oil bath

will snap some rubber bands and spares should be kept on hand in case. This reaction should be checked on periodically (about every 30 minutes) due to this issue. It is crucial that the contents of the flask take up no more than 50% of the volume of the flask, as the reaction is quite vigorous and is very prone to bumping the solution into the receiving flask and the yield decreases. The maximum recommended scale for a 100 mL reaction flask is 10 g (larger reaction scales are possible without sacrificing yield if reaction flask is of appropriate size and distillation head is kept above approximately 140 °C). The isolated distillate from the decarbonylation reaction is a mixture of styrene, pivalic acid and pivalic anhydride. Removing the pivalic anhydride is troublesome due to its extremely low rate of hydrolysis, but we found that stirring a pentane-diluted solution over concentrated aqueous *p*-TsOH overnight was adequate to remove any remaining pivalic anhydride. It is critical that the *p*-TsOH solution is as concentrated as possible, otherwise hydrolysis of pivalic anhydride is very slow.

Procedure. An oven-dried 100 mL round bottom flask with a copper wire necklace was brought into the glove box, loaded with $PdCl_2$ (29.5 mg, 0.25 mol%) and DPEphos (795 mg, 2.2 mol%) and capped with a septum. The round bottom was removed from the glove box and hydrocinnamic acid (10 g, 66.59 mmol) and pivalic anhydride (13.5 mL, 66.59 mmol) were added to the flask containing the Pd and phosphine, and quickly attached to a short-path distillation head with a 50 mL pear-shaped receiving flask under a flow of argon gas. The condenser on the short-path distillation head was cooled with water. The reaction flask was submerged about 2/3 of the way into an oil bath at 170 °C and wrapped with aluminum foil and glass wool and allowed to heat to between 180 °C and 185 °C. After the reaction has completed (no more distillation observed, approximately 3 hours), the distillate was diluted with pentane (1:1) and stirred vigorously overnight with 50 mL of *p*-TsOH. The pentane layer can be

checked by GC-MS to ensure removal of pivalic anhydride. After hydrolysis is complete, the pentane layer was washed 4 times with 100 mL of 3.4 M aqueous sodium hydroxide. In the same manner as before, the pentane layer can be checked by GC-MS to ensure removal of the pivalic acid. After the pivalic acid has been removed, the pentane was removed on the rotovap with gentle heating (30 °C), and pure styrene remained (4.4 g, 64%). The styrene was inhibited with 50 ppm 4-*tert*-butylcatechol and stored in the freezer. According to the bio-based determination using ASTM-D6866-12 by Beta Analytic Inc., the bio-content of styrene synthesized from natural cinnamaldehyde in this manner was 97% ± 3%.

4.5.4 ASTM-D6866-12 Standard Test Results

4.5.4.1 Cinnamaldehyde

ISO-17025 Accredited Testing Laboratory

PJLA ISO/IEC 17025:2005 Testing Accreditation# 59423

Beta Analytic Inc.
4985 SW 74 Court
Miami, Florida 33155 USA
Tel: 305-667-5167
Fax: 305-663-0964
info@betalabservices.com
www.betalabservices.com

Summary of Results : Biobased Determination using ASTM-D6866-12

Submitter:	Dr. Keying Ding	**Date Received**	March 27, 2013
Company:	University of Minnesota	**Date Reported**	April 01, 2013

Laboratory Number	Submitter Label	Material	Method of Analysis	Biobased Result
Beta-345539	cinnamaldehyde	Biobased Material	D6866-12/Method-B	99 %

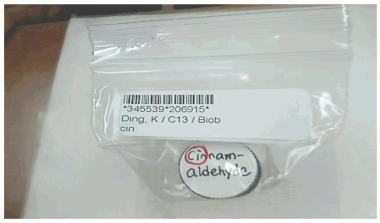

Package received -labeling COC

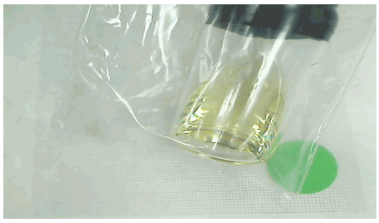

View of content (1mm x 1mm scale)

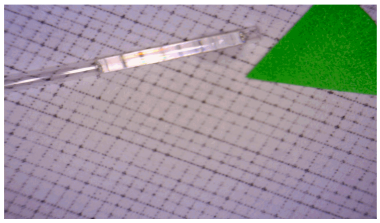

Reresentative Sample analyzed (1mm x 1mm scale)

* ASTM-D6866 cites precision on The Mean Biobased Result as +/- 3% (absolute). This is the most conservative estimate of error in the measurement of complex biobased containing solids and liquids based on empirical results. Real precision for readily combustible and homogenous materials (e.g. gasoline) and especially samples recieved as CO_2 (e.g. flue gas or CEMS exhaust) can be as low as +/- 0.5-2%. The result only applies to the analyzed material. Fluctuations in carbon content within a batch of product, gasoline or flue gas must be determined separately (e.g. averaged measurements of multiple solids or liquids, and single measurement of the combination of gas aliquots collected over time). The accuracy of the result as it applies to the analyzed product, fuel, or flue gas relies upon all the carbon in the analyzed material originating from either recently respired atmospheric carbon dioxide (within the last decade) or fossil carbon (more than 50,000 years old). "Percent biobased" specifically relates % renewable (or fossil) carbon to total carbon, not to total mass or molecular weight. Mean Biobased estimates greater than 100% are assigned a value of 100% for simplification.

ISO-17025 Accredited Testing Laboratory

PJLA ISO/IEC 17025:2005 Testing Accreditation# 59423

Beta Analytic Inc.
4985 SW 74 Court
Miami, Florida 33155 USA
Tel: 305-667-5167
Fax: 305-663-0964
info@betalabservices.com
www.betalabservices.com

Analytical Measure : Biobased Determination using ASTM-D6866-12

Submitter: Dr. Keying Ding

Company: University of Minnesota

Date received March 27, 2013

Date reported April 01, 2013

Submitter label	Material	Laboratory Number	Percent modern carbon (pmc)	Atmospheric correction factor
cinnamaldehyde	Biobased Material	Beta-345539	104.7 +/- 0.3 pMC	x 0.95

Note: % biobased = pMC x 0.95

* ASTM-D6866 cites precision on The Mean Biobased Result as +/- 3% (absolute). This is the most conservative estimate of error in the measurement of complex biobased containing solids and liquids based on empirical results. Real precision for readily combustible and homogenous materials (e.g. gasoline) and especially samples recieved as CO_2 (e.g. flue gas or CEMS exhaust) can be as low as +/- 0.5-2%. The result only applies to the analyzed material. Fluctuations in carbon content within a batch of product, gasoline or flue gas must be determined separately (e.g. averaged measurements of multiple solids or liquids, and single measurement of the combination of gas aliquots collected over time). The accuracy of the result as it applies to the analyzed product, fuel, or flue gas relies upon all the carbon in the analyzed material originating from either recently respired atmospheric carbon dioxide (within the last decade) or fossil carbon (more than 50,000 years old). "Percent biobased" specifically relates % renewable (or fossil) carbon to total carbon, not to total mass or molecular weight. Mean Biobased estimates greater than 100% are assigned a value of 100% for simplification.

ISO-17025 Accredited Testing Laboratory

PJLA ISO/IEC 17025:2005 Testing Accreditation# 59423

Beta Analytic Inc.
4985 SW 74 Court
Miami, Florida 33155 USA
Tel: 305-667-5167
Fax: 305-663-0964
info@betalabservices.com
www.betalabservices.com

Report of Biobased Content Analysis using ASTM-D6866-12

Submitter: University of Minnesota
Submitter Label: cinnamaldehyde

Laboratory Number: Beta-345539
Material: Biobased Material
Date Received: March 27, 2013
Date Reported: April 01, 2013

Mean Biobased Result : 99 % *

Proportions Biobased vs. Fossil Based indicated by 14C content

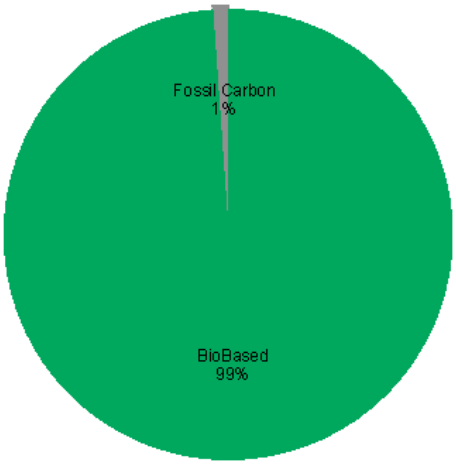

* ASTM-D6866 cites precision on The Mean Biobased Result as +/- 3% (absolute). This is the most conservative estimate of error in the measurement of complex biobased containing solids and liquids based on empirical results. Real precision for readily combustible and homogenous materials (e.g. gasoline) and especially samples recieved as CO_2 (e.g. flue gas or CEMS exhaust) can be as low as +/- 0.5-2%. The result only applies to the analyzed material. Fluctuations in carbon content within a batch of product, gasoline or flue gas must be determined separately (e.g. averaged measurements of multiple solids or liquids, and single measurement of the combination of gas aliquots collected over time). The accuracy of the result as it applies to the analyzed product, fuel, or flue gas relies upon all the carbon in the analyzed material originating from either recently respired atmospheric carbon dioxide (within the last decade) or fossil carbon (more than 50,000 years old). "Percent biobased" specifically relates % renewable (or fossil) carbon to total carbon, not to total mass or molecular weight. Mean Biobased estimates greater than 100% are assigned a value of 100% for simplification.

ISO-17025 Accredited Testing Laboratory

PJLA ISO/IEC 17025:2005 Testing Accreditation# 59423

Beta Analytic Inc.
4985 SW 74 Court
Miami, Florida 33155 USA
Tel: 305-667-5167
Fax: 305-663-0964
info@betalabservices.com
www.betalabservices.com

Explanation of Results

Biobased Analysis using ASTM-D6866-12, May 2012

The application of ASTM-D6866 to derive a "Biobased content" is built on the same concepts as radiocarbon dating, but without use of the age equations. It is done by deriving a ratio of the amount of radiocarbon (14C) in an unknown sample to that of a modern reference standard. This ratio is calculated as a percentage with the units "pMC" (percent modern carbon). If the material being analyzed is a mixture of present day radiocarbon and fossil carbon (containing no radiocarbon), then the pMC value obtained correlates directly to the amount of biomass derived carbon in the sample.

The modern reference standard used in radiocarbon dating is a NIST (National Institute of Standards and Technology) standard with a known radiocarbon content equivalent approximately to the year AD 1950. AD 1950 was chosen since it represented a time prior to thermo-nuclear weapons testing which introduced large amounts of excess radiocarbon into the atmosphere with each explosion (termed "bomb carbon"). This was a logical point in time to use as a reference for archaeologists and geologists. For an archaeologist or geologist using radiocarbon dates, AD 1950 equals "zero years old". It also represents 100 pMC.

"Bomb carbon" in the atmosphere reached almost twice normal levels in 1963 at the peak of testing and prior to the treaty halting the testing. Its distribution within the atmosphere has been approximated since its appearance, showing values that are greater than 100 pMC for plants and animals living since AD 1950. It has gradually decreased over time with today's value being near 105 pMC. This means that a fresh biomass material such as corn, sugar cane or soybeans would give a radiocarbon signature near 105 pMC.

Combining fossil carbon with present day carbon into a material will result in a dilution of the present day pMC content. By presuming ~105 pMC represents present day biomass materials and 0 pMC represents petroleum derivatives, the measured pMC value for that material will reflect the proportions of the two component types. For example, a material derived 100% from present day soybeans would give a radiocarbon signature near 105 pMC. But if it was diluted with 50% petroleum carbon, it would give a radiocarbon signature near 53 pMC.

The "biobased content" of a material is reported as a percent value relating total renewable organic carbon to total organic carbon. The final result is calculated by multiplying the pMC value measured for the material by 0.95 (to adjust for bomb carbon effect). The final value is cited as the MEAN BIOBASED RESULT and assumes all the components within the analyzed material were either present day living (within the last decade) or fossil in origin.

The results provided in this report are uniquely applicable to the analyzed material and are reported using the designated labeling provided with the sample. Although analytical precision is typically 0.1 to 0.5 pMC, empirical data has demonstrated that indeterminant errors can introduce uncertainty to 2 to 3 pMC. As such, ASTM-D6866 cites an uncertainty of +/- 3 % (absolute) on each result. Remember the results only relate carbon source, not mass source. A reported percentage does not represent to the total mass of fossil vs. renewable components present. Only the amount of renewable carbon vs fossil carbon present is indicated.

4.5.4.2 Styrene

ISO-17025 Accredited Testing Laboratory

PJLA ISO/IEC 17025:2005 Testing Accreditation# 59423

Beta Analytic Inc.
4985 SW 74 Court
Miami, Florida 33155 USA
Tel: 305-667-5167
Fax: 305-663-0964
info@betalabservices.com
www.betalabservices.com

Summary of Results : Biobased Determination using ASTM-D6866-12

Submitter:	Dr. Keying Ding	**Date Received**	May 23, 2013
Company:	University of Minnesota	**Date Reported**	May 29, 2013

Laboratory Number	Submitter Label	Material	Method of Analysis	Biobased Result
Beta-349734	Styrene	Biobased Material	D6866-12/Method-B	97 %

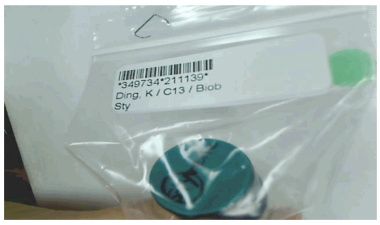

Package received -labeling COC

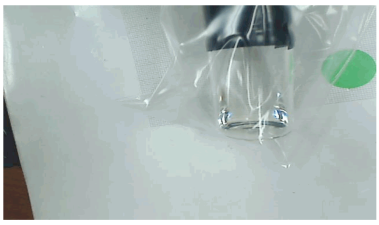

View of content (1mm x 1mm scale)

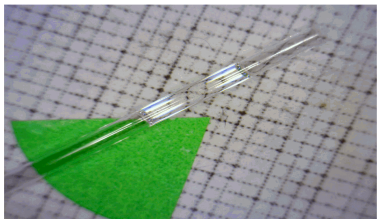

Representative Sample Analyzed (1mm x 1mm scale)

* ASTM-D6866 cites precision on The Mean Biobased Result as +/- 3% (absolute). This is the most conservative estimate of error in the measurement of complex biobased containing solids and liquids based on empirical results. Real precision for readily combustible and homogenous materials (e.g. gasoline) and especially samples recieved as CO_2 (e.g. flue gas or CEMS exhaust) can be as low as +/- 0.5-2%. The result only applies to the analyzed material. Fluctuations in carbon content within a batch of product, gasoline or flue gas must be determined separately (e.g. averaged measurements of multiple solids or liquids, and single measurement of the combination of gas aliquots collected over time). The accuracy of the result as it applies to the analyzed product, fuel, or flue gas relies upon all the carbon in the analyzed material originating from either recently respired atmospheric carbon dioxide (within the last decade) or fossil carbon (more than 50,000 years old). "Percent biobased" specifically relates % renewable (or fossil) carbon to total carbon, not to total mass or molecular weight. Mean Biobased estimates greater than 100% are assigned a value of 100% for simplification.

ISO-17025 Accredited Testing Laboratory

PJLA ISO/IEC 17025:2005 Testing Accreditation# 59423

Beta Analytic Inc.
4985 SW 74 Court
Miami, Florida 33155 USA
Tel: 305-667-5167
Fax: 305-663-0964
info@betalabservices.com
www.betalabservices.com

Analytical Measure : Biobased Determination using ASTM-D6866-12

Submitter: Dr. Keying Ding

Company: University of Minnesota

Date received May 23, 2013

Date reported May 29, 2013

Submitter label	Material	Laboratory Number	Percent modern carbon (pmc)	Atmospheric correction factor
Styrene	Biobased Material	Beta-349734	102.5 +/- 0.3 pMC	x 0.95

Note: % biobased = pMC x 0.95

* ASTM-D6866 cites precision on The Mean Biobased Result as +/- 3% (absolute). This is the most conservative estimate of error in the measurement of complex biobased containing solids and liquids based on empirical results. Real precision for readily combustible and homogenous materials (e.g. gasoline) and especially samples recieved as CO_2 (e.g. flue gas or CEMS exhaust) can be as low as +/- 0.5-2%. The result only applies to the analyzed material. Fluctuations in carbon content within a batch of product, gasoline or flue gas must be determined separately (e.g. averaged measurements of multiple solids or liquids, and single measurement of the combination of gas aliquots collected over time). The accuracy of the result as it applies to the analyzed product, fuel, or flue gas relies upon all the carbon in the analyzed material originating from either recently respired atmospheric carbon dioxide (within the last decade) or fossil carbon (more than 50,000 years old). "Percent biobased" specifically relates % renewable (or fossil) carbon to total carbon, not to total mass or molecular weight. Mean Biobased estimates greater than 100% are assigned a value of 100% for simplification.

ISO-17025 Accredited Testing Laboratory

PJLA ISO/IEC 17025:2005 Testing Accreditation# 59423

Beta Analytic Inc.
4985 SW 74 Court
Miami, Florida 33155 USA
Tel: 305-667-5167
Fax: 305-663-0964
info@betalabservices.com
www.betalabservices.com

Report of Biobased Content Analysis using ASTM-D6866-12

Submitter: University of Minnesota
Submitter Label: Styrene

Laboratory Number: Beta-349734
Material: Biobased Material
Date Received: May 23, 2013
Date Reported: May 29, 2013

Mean Biobased Result : 97 % *

Proportions Biobased vs. Fossil Based indicated by 14C content

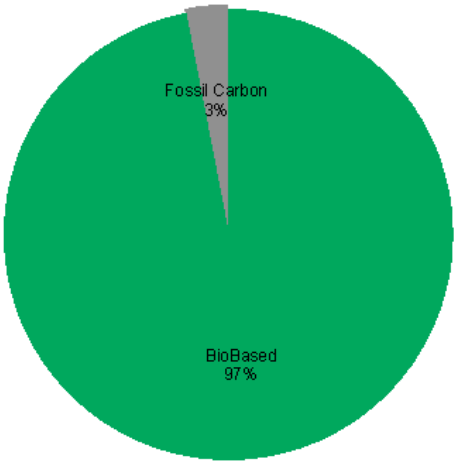

* ASTM-D6866 cites precision on The Mean Biobased Result as +/- 3% (absolute). This is the most conservative estimate of error in the measurement of complex biobased containing solids and liquids based on empirical results. Real precision for readily combustible and homogenous materials (e.g. gasoline) and especially samples recieved as CO_2 (e.g. flue gas or CEMS exhaust) can be as low as +/- 0.5-2%. The result only applies to the analyzed material. Fluctuations in carbon content within a batch of product, gasoline or flue gas must be determined separately (e.g. averaged measurements of multiple solids or liquids, and single measurement of the combination of gas aliquots collected over time). The accuracy of the result as it applies to the analyzed product, fuel, or flue gas relies upon all the carbon in the analyzed material originating from either recently respired atmospheric carbon dioxide (within the last decade) or fossil carbon (more than 50,000 years old). "Percent biobased" specifically relates % renewable (or fossil) carbon to total carbon, not to total mass or molecular weight. Mean Biobased estimates greater than 100% are assigned a value of 100% for simplification.

ISO-17025 Accredited Testing Laboratory

PJLA ISO/IEC 17025:2005 Testing Accreditation# 59423

Beta Analytic Inc.
4985 SW 74 Court
Miami, Florida 33155 USA
Tel: 305-667-5167
Fax: 305-663-0964
info@betalabservices.com
www.betalabservices.com

Explanation of Results

Biobased Analysis using ASTM-D6866-12, May 2012

The application of ASTM-D6866 to derive a "Biobased content" is built on the same concepts as radiocarbon dating, but without use of the age equations. It is done by deriving a ratio of the amount of radiocarbon (14C) in an unknown sample to that of a modern reference standard. This ratio is calculated as a percentage with the units "pMC" (percent modern carbon). If the material being analyzed is a mixture of present day radiocarbon and fossil carbon (containing no radiocarbon), then the pMC value obtained correlates directly to the amount of biomass derived carbon in the sample.

The modern reference standard used in radiocarbon dating is a NIST (National Institute of Standards and Technology) standard with a known radiocarbon content equivalent approximately to the year AD 1950. AD 1950 was chosen since it represented a time prior to thermo-nuclear weapons testing which introduced large amounts of excess radiocarbon into the atmosphere with each explosion (termed "bomb carbon"). This was a logical point in time to use as a reference for archaeologists and geologists. For an archaeologist or geologist using radiocarbon dates, AD 1950 equals "zero years old". It also represents 100 pMC.

"Bomb carbon" in the atmosphere reached almost twice normal levels in 1963 at the peak of testing and prior to the treaty halting the testing. Its distribution within the atmosphere has been approximated since its appearance, showing values that are greater than 100 pMC for plants and animals living since AD 1950. It has gradually decreased over time with today's value being near 105 pMC. This means that a fresh biomass material such as corn, sugar cane or soybeans would give a radiocarbon signature near 105 pMC.

Combining fossil carbon with present day carbon into a material will result in a dilution of the present day pMC content. By presuming ~105 pMC represents present day biomass materials and 0 pMC represents petroleum derivatives, the measured pMC value for that material will reflect the proportions of the two component types. For example, a material derived 100% from present day soybeans would give a radiocarbon signature near 105 pMC. But if it was diluted with 50% petroleum carbon, it would give a radiocarbon signature near 53 pMC.

The "biobased content" of a material is reported as a percent value relating total renewable organic carbon to total organic carbon. The final result is calculated by multiplying the pMC value measured for the material by 0.95 (to adjust for bomb carbon effect). The final value is cited as the MEAN BIOBASED RESULT and assumes all the components within the analyzed material were either present day living (within the last decade) or fossil in origin.

The results provided in this report are uniquely applicable to the analyzed material and are reported using the designated labeling provided with the sample. Although analytical precision is typically 0.1 to 0.5 pMC, empirical data has demonstrated that indeterminant errors can introduce uncertainty to 2 to 3 pMC. As such, ASTM-D6866 cites an uncertainty of +/- 3 % (absolute) on each result. Remember the results only relate carbon source, not mass source. A reported percentage does not represent to the total mass of fossil vs. renewable components present. Only the amount of renewable carbon vs fossil carbon present is indicated.

4.6 Acknowledgments

We especially thank Dr. Keying Ding for her collaboration in preparation of the bio-based styrene. Additionally, we would like to thank the National Science Foundation (grant CHE-0842654 to W.B.T and M.A.H and a Graduate Research Fellowship under Grant No. 00006595 to M.O.M.) and the Center for Sustainable Polymers, a National Science Foundation supported Center for Chemical Innovation (CHE-1136607) and Bridgestone Corporation for financial support of this research.

5 Earth-Abundant Metal Catalysts for the Decarbonylation of Hydrocinnamic Acid to Styrene

5.1 Overview

Combining high-throughput experimentation with conventional experiments expedited discovery of new first-row transition metal catalysts for the decarbonylation of the bio-derived substrate hydrocinnamic acid to produce bio-derived styrene. Conventional experiments using a continuous distillation process (180 °C) revealed that Ni(II) and Ni(0) precursors (NiI_2, $Ni(PPh_3)_4$) with simple aryl phosphine ligands were most successful, achieving high conversions but moderate yields due to formation of side-products.

5.2 Introduction

Synthetic polymers are ubiquitous in modern life. However, nearly all commercial monomers are derived from petroleum, a limited resource with volatile prices. For this reason, developing alternative methods to synthesize high-volume and high-value monomers from renewable resources is a burgeoning area of research.[164,182,183] In view of the prevalence of carboxylic acid functional groups in biomass-derived feedstocks, catalytic decarbonylation to yield olefins is an appealing approach for the synthesis of bioderived monomers (Scheme 5.1). Building upon previous work using precious metals such as palladium,[80,81,87,90] rhodium,[81] and iridium,[165] the catalytic decarbonylation of the renewable substrates hydrocinnamic acid (from cinnamaldehyde[167,168]), mono-alkyl succinates (from bio-based succinic acid), and 3-cyanopropanoic acid (from the amino acid glutamic acid[169]) to styrene, alkyl acrylates and acrylonitrile, respectively, in high yields (> 80%) using a palladium-phosphine based catalyst system with pivalic anhydride as an additive was achieved and described in Chapter 4 (Scheme 5.2).[184] A variety of palladium/phosphine combinations were screened, and triphenylphosphine was found to be as effective as chelating phosphines like DPEphos and Xantphos.

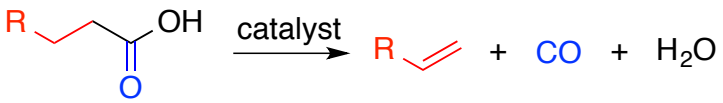

Scheme 5.1. Catalytic decarbonylation of carboxylic acids to alkenes.

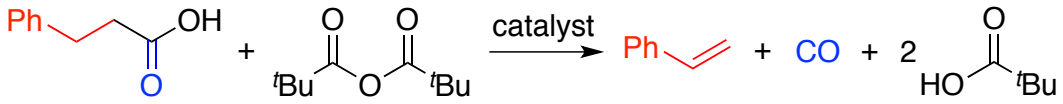

Scheme 5.2. Catalytic decarbonylation of hydrocinnamic acid to styrene using pivalic anhydride as an additive.

Although precious metals are effective catalysts, they are also expensive and rare. The use of inexpensive and readily available first-row transition metals is desirable, but there have been few reports of their use for the decarbonylation of carboxylic acids. Recently, an iron-based catalyst was reported for the decarbonylation of long chain fatty acids to terminal olefins.[84] Using 10 mol% $FeCl_2$, 20–40 mol% of an added phosphine ligand, 100 mol% of the additives KI and acetic anhydride, and 20 psi of CO, high yields of terminal olefin products were obtained. In a non-catalytic route, alkenes were prepared in yields up to 56% from cyclic anhydrides and thioanhydrides using stoichiometric amounts of $(PPh_3)_2Ni(CO)_2$, $Fe_2(CO)_9$ or $(PPh_3)_3RhCl$; however, side reactions were observed for anhydrides containing abstractable hydrogens.[86,185] In addition, a low valent nickel species generated in situ from $NiCl_2$ and zinc dust was shown to be effective for the decarbonylation of 2-pyridyl thioates.[186] The decarbonylation of thioesters under similar conditions generated thioethers from unsaturated or aromatic substrates and alkenes from aliphatic substrates.[187] A disadvantage of these approaches is that 2-pyridyl thioates and thioesters must be prepared from the carboxylic acid in a first step prior to decarbonylation. In the patent literature, nickel, cobalt and iron precursors were reported to be effective decarbonylation catalysts for carboxylic acids in the presence of KI or by using an iodide precursor, although conversions are lower than those observed with palladium or rhodium precursors.[188,189]

Inspired by literature precedent that suggested that the first row metals could catalyze decarbonylation reactions, we were interested in screening a broad range of first-row transition metal-ligand combinations for the decarbonylation of bio-derived carboxylic acids. The conversion of hydrocinnamic acid to styrene was selected as a convenient and illustrative test case (Scheme 5.2). Herein we report the results of these studies, using a combination of high-throughput experimentation (HTE) and conventional

batch catalyst assessment. HTE was used to expedite the initial discovery process, and conventional catalyst screening was used to explore active systems in more detail. As a result of these studies, several new types of catalysts were identified and mechanistic insights were obtained that will guide future catalyst development.

5.3 Results and Discussion

5.3.1 Primary High-Throughput Experimentation Screen

In the first round of primary screening, Ni, Co, Mn, Fe, Cu, and Zn complexes, as well as a Pd control, were screened in combination with an array of ligands for the decarbonylation of hydrocinnamic acid. All reagents were dispensed robotically. Metal-ligand combinations were screened in parallel in 96 x 1 mL arrays and thin-layer chromatography (TLC) with UV light detection was used as a rapid, qualitative measure of reactivity because of its sensitivity to detect styrene (< 1 mg). Metal precursors and ligands screened in the first set of experiments are shown in Figure 5.1.

Validation of the high throughput workflow as a suitable primary screen came from the observation of styrene using the previously described[184] Pd/PPh_3 control systems. A large number of metal-ligand combinations were identified as active catalysts

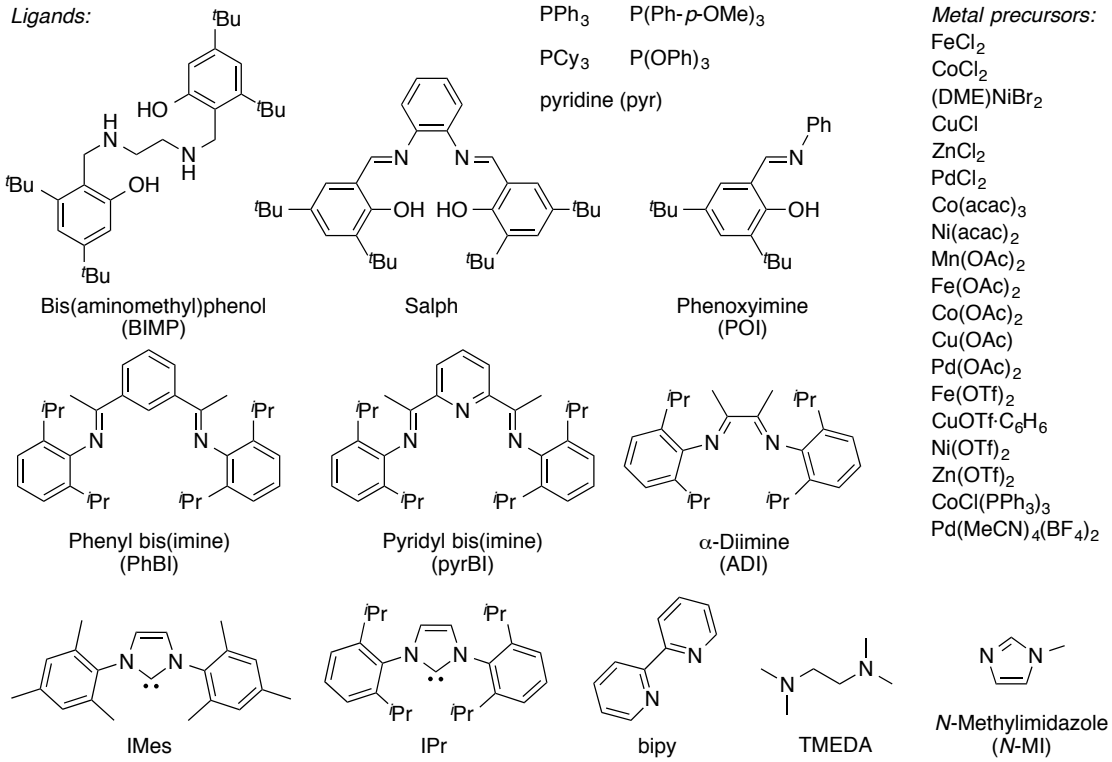

Figure 5.1. Ligands and metal precursors used in primary high-throughput screening reactions.

in the primary screening experiments (illustrative data presented in Table 5.1; complete data provided in section 5.5.2, Table 5.5, Table 5.6, Table 5.7, and Table 5.8), with the most successful metal precursors being Co(III), Fe(II), Cu(I), and Ni(II) (as well as the Pd(II) controls) in combination with the aryl phosphine ligands PPh_3 and $P(p\text{-}OMePh)_3$. Multidentate N,O ligands such as bis(aminomethyl)phenol, salph or diimine-based chelates provided no apparent advantage over simple monodentate ligands. Improved activity was observed qualitatively with increased metal loadings (2 mol% vs. 1 mol%), and halide-containing (Cl, Br) precursors were generally more effective than their acetate, triflate or acetylacetonate counterparts.

Table 5.1. Representative results of HTE primary screen reactions of hydrocinnamic acid to yield styrene.[a]

	$Pd(OAc)_2$	$Pd(MeCN)_4(BF_4)_2$	$CoCl_2$	$Co(PPh_3)_3Cl$	$FeCl_2$	$Fe(OTf)_2$	$(DME)NiBr_2$	$Ni(OTf)_2$	CuCl	$Cu(OTf)\bullet C_6H_6$	$ZnCl_2$	$Zn(OTf)_2$	$Ni(acac)_2$	Cu(OAc)	$Fe(OAc)_2$	$Co(acac)_3$	$Mn(OAc)_2$
PPh_3	✔	✔	✔	✔	✔		✔		✔								
PCy_3	✔	✔														✔	
P(Ph-*p*-OMe)	✔	✔	✔		✔		✔										
bipy	✔																
TMEDA	✔	✔	✔														
N-MI	✔																
IMes	✔	✔															
IPr	✔	✔															
pyr	✔												✔	✔		✔	
No ligand	✔													✔		✔	✔
POI	✔																
Salph																	
BIMP	✔																
ADI	✔																
pyrBI	✔																✔
PhBI																	

[a] Metal loading: 1 mol%. Ligand loading: 10 mol%, except pyr: 20 mol%. Temperature: 180 °C. Time: 30-40 min. Check marks indicate styrene observed by TLC.

5.3.2 Secondary High-Throughput Experimentation Screen

A second round of HTE was performed on the most promising precursors, Fe(II) and Ni(II), to study the effects of metal loading, ligand loading, ligand to metal ratio and addition of KI on styrene yield. Despite showing promise in the primary HTE screen, when conventional experiments with Cu and Co and a variety of ligands were conducted, very low yields of styrene (less than 5%) were present in the distillate, with most showing no activity. However, Ni and Fe precursors were much more successful, which is why we chose to pursue those in another round of HTE. In this secondary screen we used $FeCl_2$, FeI_2, $NiCl_2$ and NiI_2 as metal precursors (5 mol%), PPh_3 as the ligand (0–20 mol%) and 10 mol% KI. The ligand to metal ratio (from 0:1 to 4:1) and the reaction time (1–2 hrs) were also varied; all reactions were performed at 180 °C, and yields were determined via GC (heat map of data shown in Figure 5.2; full data listed in section 5.5.2, Table 5.9 and Table 5.10). Overall, yields for styrene were low (<10%), reflecting the fact that the reaction vessels were sealed, so the product gas, CO, could not escape (potentially inhibiting the reaction; vide infra), and styrene was not removed from the reaction as it proceeded, enabling it to undergo secondary reactions. Nonetheless, significant differences in yields were seen that enabled general trends to be noted. Longer reaction times (2 h) were more successful overall, and as metal to ligand loading increased so did styrene yield, up to a point where higher ligand/metal ratios (>2:1 L/M) caused a decrease in the yield (Figure 5.2). Also, higher yields were observed for the Ni(II) precursors than their Fe(II) counterparts and iodide salts were more effective than chlorides (Table 5.9 and Table 5.10). Careful inspection of the GC data resulted in the identification of a co-product, ethylbenzene. In most cases, the [styrene]/[ethylbenzene] ratio ranged from 1:1 to 4:1, with a few cases having higher (6:1, 5 mol% NiI_2 and 2.5 mol% PPh_3) and lower (0.8:1, 5 mol% NiI_2 and 15-20 mol% PPh_3) ratios (Figure 5.2, Table 5.9 and Table 5.10).

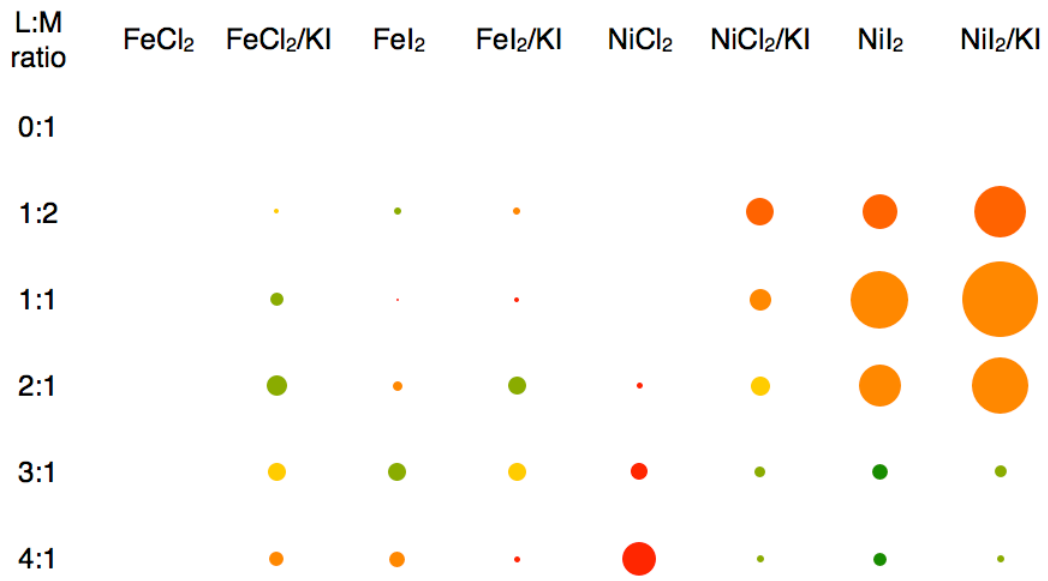

Figure 5.2. Heat map illustrating the effect of L/M ratio on styrene yield and [styrene]/[ethylbenzene] ratio. M = 5 mol%, L = PPh_3, KI = 10 mol%, 2 hr, 180 °C. Data adapted from **Table 5.10**. The size of the circle is proportional to the styrene yield in that well. Colors correspond to [styrene]/[ethylbenzene] ratio: 0.8–1 green; 1–1.8 yellow-green; 1.8–2.5 yellow; 2.5–5 orange; 5–7 red orange, >7 red.

To determine how the metal precursor impacts decarbonylation, another HTE screen of zero-valent metal precursors (2 mol% metal loading) was performed, with and without added KI (10 mol%). An array of common phosphine ligands and nitrogen donor ligands (Figure 5.3) were examined (heat map of data in Figure 5.4).[190] Nearly all Ni/phosphine combinations screened showed activity, but no styrene formation was observed with any of the phosphine/iron combinations or any of the wells containing phenanthroline. Interestingly, both Ni(0)-based precursors $Ni(COD)_2$ and $Ni(PPh_3)_4$ showed considerable activity for the decarbonylation reaction, and in certain cases appeared to inhibit the formation of ethylbenzene. With DPPB, DPPF, and Davephos, comparatively high yields of styrene were observed, and no ethylbenzene was detected via GC for DPPB and DPPF. With Davephos, [styrene]/[ethylbenzene] ranged from 6:1 to 60:1 depending on conditions (Figure 5.4, Table 5.11).

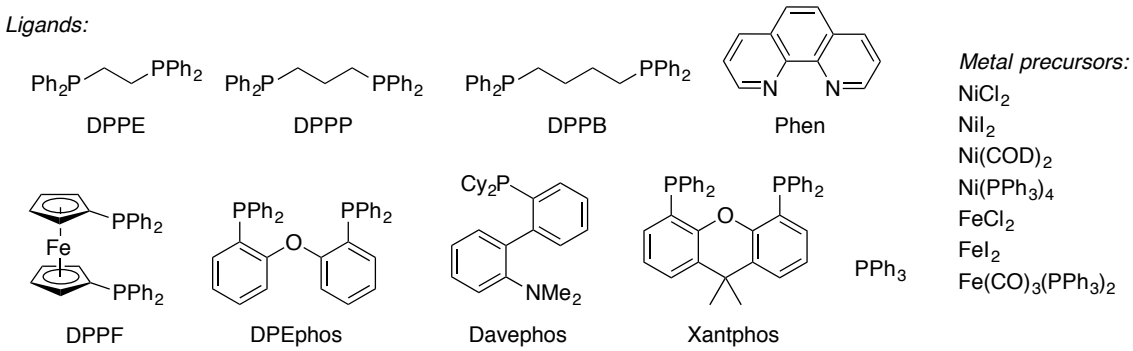

Figure 5.3. Ligands and metal precursors used in the second set of high-throughput screening reactions.

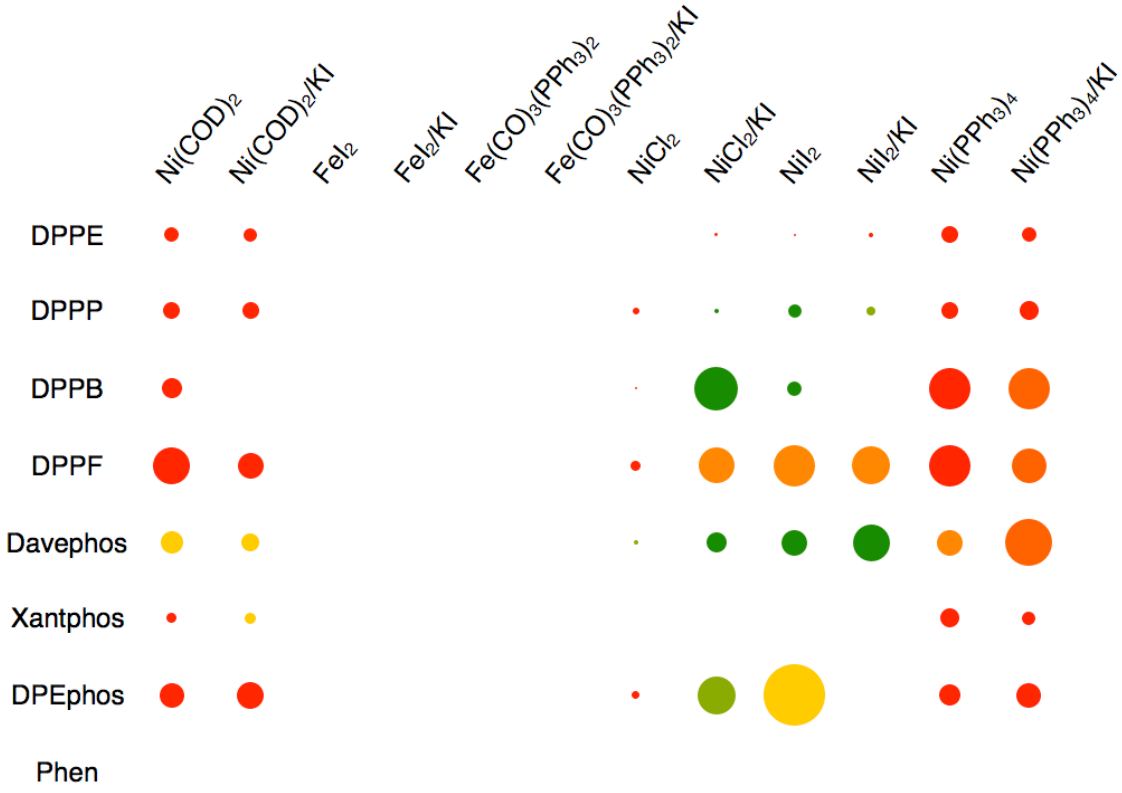

Figure 5.4. Heat map illustrating styrene yields from the HTE screen of reactions with Ni(0), Ni(II), Fe(0), and Fe(II) precursors and phosphine ligands. M = 2 mol%, L = 10 mol%, KI =10 mol%, 2 hr, 180 °C. Data adapted from **Table 5.11**. The size of a circle is proportional to the styrene yield in that well. Colors correspond to [styrene]/[ethylbeznene] ratio: 1–2 green; 2–4 yellow-green; 4–8 yellow; 8–27 orange; 27–74 red orange, >74 red.

To explore the effect of gas pressure on the decarbonylation reaction, one 96-well

reaction was screened in a pressurized reactor vessel[191] at 100 psi CO and 180 °C for 2 h (Table 5.12). It was clear from the results that CO is an inhibitor for the reaction; styrene yields overall were much lower and activity was only seen for Ni(0) precursors. Similar results were observed when the reaction of $Ni(PPh_3)_4$ (5 mol%) and PPh_3 (10 mol%) with hydrocinnamic acid was scaled up (0.5-1.0 g hydrocinnamic acid) under 80 psi of either CO, CO_2 (CO_2 was reported to enhance the decarbonylation yield of aldehydes using iridium catalysts[192]), or an ambient pressure of N_2 (Table 5.2). Under CO, styrene yield is diminished (Table 5.2, Entry 1) compared to the reaction run under N_2 (Table 5.2, Entry 3). Interestingly, CO_2 appeared to enhance the yield of ethylbenzene (Table 5.2, Entry 2).

Table 5.2. Effect of CO, CO_2, and N_2 on decarbonylation of hydrocinnamic acid.[a]

Entry	Gas identity (psi)	Styrene yield (%)	Ethylbenzene yield (%)	[styrene]/[ethylbenzene]
1	CO (80)	7.7	2.3	3.3
2	CO_2 (80)	7.5	6.0	1.3
3	N_2 (ambient)	11.7	3.8	3.1

[a] Conditions: 1 gram (CO, CO_2) or 0.5 gram (N_2) hydrocinnamic acid, 1 equiv Piv_2O, 5 mol% $Ni(PPh_3)_4$, 10 mol% PPh_3, 180 °C, 1.5 hours. Yields determined using GC.

5.3.3 Conventional Experimentation

In order to determine whether the general trends observed under high throughput conditions were replicated under conventional batch conditions on a larger scale, reactions using the most promising Ni(II) and Ni(0) precursors, NiI_2 and $Ni(PPh_3)_4$, and PPh_3 were run using the traditional experimental setup and scale. In agreement with the HTE results, the optimal ligand-to-metal ratio was 2:1 for both Ni(II) and Ni(0) precursors, as seen in Table 5.3 (Entries 3 and 8). Using NiI_2 as the metal precursor, the highest yield for styrene was found with 10 mol% NiI_2 and 20 mol% PPh_3 (23%, Table 5.3, Entry 3). Reactions using NiI_2 precursors generally required higher loadings, with an

optimal loading of 10 mol%. An optimal loading of 5 mol% was determined for $Ni(PPh_3)_4$; higher styrene yields were not observed at 10 mol% $Ni(PPh_3)_4$ (Table 5.3, Entries 8 and 11). Addition of KI enhances styrene yield slightly for $Ni(PPh_3)_4$ (Table 5.3, Entries 10 and 11), and has minimal effect on the yield for NiI_2 (Table 5.3, Entries 3-6). Despite relatively low styrene yields, high yields of PivOH (70-80%) are observed for the catalyst conditions that generate the highest yields of styrene (Table 5.3, Entries 3, 4, 8, 10, 11), suggesting that decarbonylation is proceeding in high yield. We propose that styrene undergoes side reactions under the decarbonylation conditions (vide infra).

Table 5.3. Effect of nickel precursor, KI and PPh_3/Ni ratio on decarbonylation of hydrocinnamic acid.[a]

Entry	Ni precursor (mol%)	PPh_3 (mol%)	KI (mol%)	Styrene yield (%)	Ethylbenzene yield (%)	PivOH yield (%)
1	NiI_2 (5)	10	0	13	2.6	43
2	NiI_2 (5)	20	0	13	2.9	45
3	NiI_2 (10)	20	0	23	4.7	80
4	NiI_2 (10)	20	100	19	5.2	81
5	NiI_2 (10)	40	0	19	2.9	48
6	NiI_2 (10)	40	100	13	2.6	45
7	$Ni(PPh_3)_4$ (2)	8	100	7.0	0.4	7.4
8	$Ni(PPh_3)_4$ (5)	10	100	29	2.6	71
9	$Ni(PPh_3)_4$ (5)	20	100	13	1.1	25
10	$Ni(PPh_3)_4$ (10)	20	0	27	4.1	80
11	$Ni(PPh_3)_4$ (10)	20	100	30	3.2	81

[a] Temperature: 180 °C. Under flow of N_2 or Ar using distillation method. Reaction time: 2 hours. Styrene, ethylbenzene, PivOH yields determined by GC-MS.

Using the optimized ligand-to-metal ratios and metal precursor loadings, the effect of ligand identity on the decarbonylation efficiency and styrene yield was then explored (Table 5.4). Using NiI_2, the highest yields were obtained with DPPB (Table 5.4, Entry 3), with conversion reaching 81% and styrene yield of 34%, although higher yields

of ethylbenzene were also observed (8%). Allowing the reaction to proceed for 24 h did not afford an increase in styrene yield (Table 5.4, Entry 5). Although the bidentate phosphine DPPB gave the highest conversions, reactions with other bidentate phosphines did not show improved performance relative to PPh_3. Davephos (Table 5.4, Entry 1) and DPEphos (Table 5.4, Entry 2) resulted in comparable yields of styrene and PivOH to those observed with PPh_3, and DPPF (Table 5.4, Entry 4) had the lowest performance of the ligands tested with Ni(II).

Table 5.4. Optimiziation of Ni-catalyzed decarbonylation of hydrocinnamic acid.[a]

Entry	Ni precursor (mol%)	Ligand (mol%)	Styrene yield (%)	Ethylbenzene yield (%)	PivOH yield (%)
1	NiI_2 (10)	Davephos (20)	20	4.2	71
2	NiI_2 (10)	DPEphos (10)	21	2.5	61
3	NiI_2 (10)	DPPB (10)	34	8	81
4	NiI_2 (10)	DPPF (10)	15	2.7	58
5[b]	NiI_2 (10)	DPPB (20)	28	6.9	83
6	$Ni(PPh_3)_4$ (5)	Davephos (10)	27	2.7	85
7	$Ni(PPh_3)_4$ (5)	DPEphos (5)	34	3.0	90
8	$Ni(PPh_3)_4$ (5)	DPPB (5)	23	2.4	60
9	$Ni(PPh_3)_4$ (5)	DPPF (5)	30	2.6	78
10[d]	$Ni(PPh_3)_4$ (5)	DPPB (5)	24	4.5	44
11[c,d]	$Ni(PPh_3)_4$ (5)	DPPB (5)	28	2.6	75

[a] Temperature: 180 °C. Time: 2 hr, unless otherwise noted. KI loading: 100 mol%, unless otherwise noted. Under flow of N_2 or Ar using distillation method. Styrene, ethylbenzene, PivOH yields determined by GC-MS. [b] Time: 24 hr. [c] Time: 18 hr. [d] KI loading: 0 mol%

In general, $Ni(PPh_3)_4$ was more efficacious than NiI_2 with the ligands tested; DPEphos had very high conversions (90%) and yield of styrene (34%, Table 5.4, Entry 7). Davephos (Table 5.4, Entry 6) and DPPF were also high yielding and resulted in styrene yields comparable to reactions with PPh_3 as the ligand, while DPPB was least

successful with Ni(0) precursors. Addition of KI was found to enhance conversion and reduce ethylbenzene formation, although styrene yield was nearly unchanged (Table 5.4, Entries 8 and 10). Extending the reaction time to 18 h also resulted in increased decarbonylation conversion, but only with a modest increase in styrene yield (Table 5.4, Entries 10 and 11).

5.3.4 Mechanistic Implications

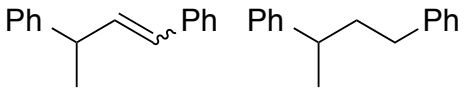

Figure 5.5. Styrene dimers isolated from reaction mixture.

From the data in Table 5.3 and Table 5.4, a discrepancy between decarbonylation conversion and styrene yield is evident; high conversions were observed, but low yields of styrene were obtained in the distillate. These findings can be explained by the presence of styrene dimers and/or oligomers (including the species shown in Figure 5.5) observed by GC-MS and NMR spectroscopy after the reaction had been worked up (see section 5.5.2 and Figure 5.7, Figure 5.8, Figure 5.9, Figure 5.10, and Figure 5.11). Metal hydride (M = Ni,[193–196] Pd,[197–200] Ir,[201] Ru[202]) species are known to facilitate the dimerization of styrene (and other alkenes) to give alkene- and alkane-containing dimers via a variety of mechanisms; typically, pathways analogous to those for olefin polymerization are invoked, although alternatives have been proposed.[197,201,202] A proposed mechanism for the decarbonylation is shown in Scheme 5.3. According to this hypothesis, initial reaction of hydrocinnamic acid with pivalic anhydride results in a mixed anhydride **1**, which after oxidative-addition to a Ni(0) center, results in an acyl-carboxylate species, **2**. This species can undergo ligand loss followed by decarbonylation to generate an alkyl-carboxylate species similar to **3**. Dissociation of CO (**4**) followed by *β*-hydride elimination results in **5**, a nickel-hydride-carboxylate species, and styrene. Persistence of this Ni-H under the

reaction conditions (i.e., slow reductive elimination of PivOH) could allow for reinsertion of styrene and dimerization (from **6**, Figure 5.6, equations 1 and 2). Alternatively, reductive elimination of a di-alkyl species could also be imagined as a potential source for styrene coupling (Figure 5.6, equations 1 and 2).[203] Ethylbenzene may be formed if Ni alkyl intermediates such as **3** or **4** are protonated by pivalic acid (Figure 5.6, equation 3).

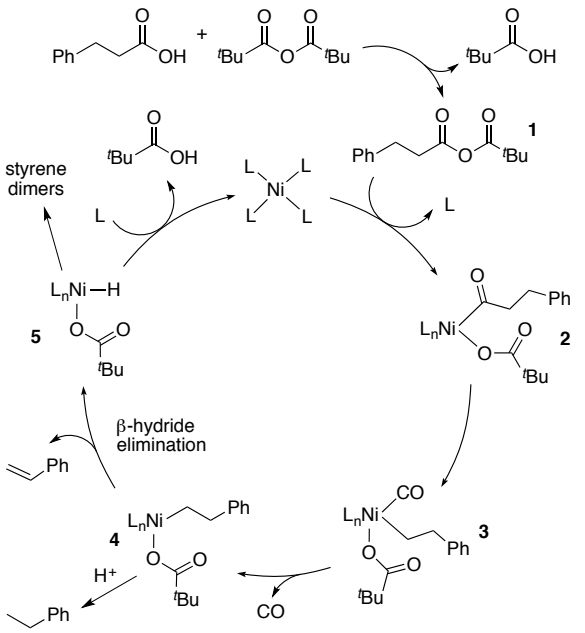

Scheme 5.3. Proposed mechanism of Ni-catalyzed decarbonylation.

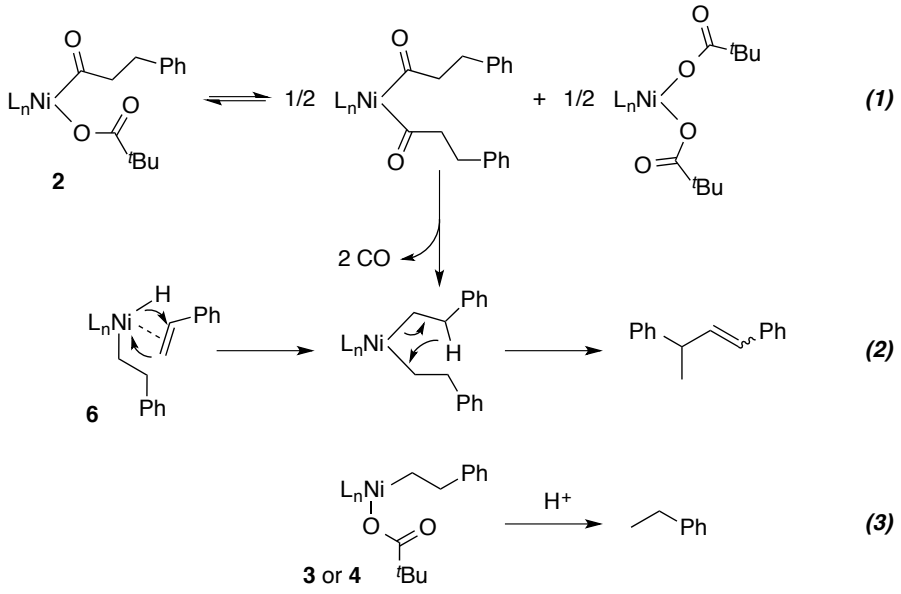

Figure 5.6. Potential side reactions to produce styrene dimers and ethylbenzene.

5.4 Summary and Conclusions

Using a combination of high throughput and conventional experiments, we determined that a combination of Ni and arylphosphines catalyze the decarbonylation of hydrocinnamic acid to form styrene. Optimal ligand-to-metal ratios were determined to be 2:1, with a decrease in ligand-to-metal ratio resulting in a decreased yield of PivOH and styrene. The reaction is inhibited by CO. A variety of phosphines were studied, and simple bidentate phosphines like DPPB and DPEphos were found to increase the styrene yield, although they were only modestly better than PPh_3. Despite high conversions of decarbonylation, low isolated styrene yields were observed and are proposed to result from persistent Ni-H intermediates, which may cause side reactions yielding styrene dimers and ethylbenzene. These side reactions are not observed in the Pd-catalyzed reactions. Future work on developing these Ni-based catalysts should focus on understanding the mechanistic details for the system. Ideally, having a more fundamental understanding of the mechanism would allow optimization of the system through judicious use of ligands and additives to minimize side products, decrease reaction temperatures, and expand the substrate scope.

5.5 Experimental Section

5.5.1 General Considerations

All experiments were carried out in an inert atmosphere unless otherwise noted. Metal precursors were purchased from Strem Chemicals or Sigma Aldrich and used without further purification. $Ni(PPh_3)_4$ was synthesized according to literature procedures.[204] Pivalic anhydride was dried over molecular sieves. Hydrocinnamic acid was recrystallized from dry pentane and sublimed prior to use. KI was crushed in a mortar and pestle then dried in an oven at 120 °C for 3 days prior to use. PPh_3 was recrystallized from ethanol prior to drying under vacuum. Bipy was recrystallized from hexane prior to drying under vacuum. TMEDA and *N*-methylimidazole were dried over CaH_2 and vacuum distilled prior to used. IMes[205], IPr[205], phenyl bis(imine)[206], pyridyl bis(imine)[207], α-diimine[208], and bis(aminomethylphenol)[209] were synthesized according to literature procedures. Phenoxy-imine and salph ligands were prepared by condensation of one or two equivalents of 3,5-di-*tert*-butylsalicylaldehyde, respectively, and aniline (for phenoxy imine) or *o*-phenylenediamine (for salph) in ethanol. All other organic compounds were purchased from Sigma Aldrich or Strem and used as received. All GC-MS and GC experiments were conducted on an Agilent Technologies 7890A GC system with a 5975C VL MSD and a HP-5 ms silica column (30 m x 0.25 mm) or a Hewlett-Packard 6890 series gas chromatograph using a flame ionization detector, and a Supelco 2-4304 beta-Dex 120 fused silica capillary column (30 m x 0.25 mm ID, 0.25 μm film thickness). The standard method (with He as carrier gas) used for all runs involved an initial oven temperature of 50 °C (held for 2 min) followed by a 20 °C min^{-1} ramp to 70 °C (held for 6 min), followed by a final 20 °C min^{-1} ramp to 230 °C (held for 3 min).

5.5.2 High-throughput Screening

General Procedures. All high throughput experiments were performed using a Freeslate Core Module 3TM (CM3) under a N2 atmosphere in an MBraun glovebox. Experiments were designed and executed using Library StudioTM and Automation StudioTM software. Reactions were performed in an Al rack containing 96 x 1 mL or 48 x 2 mL glass vials. Ligands were dispensed as stock solutions in tetrahydrofuran (THF), and metal precursors were dispensed as solids or as solutions or slurries in THF (10-20 mg/mL). The reaction mixtures were allowed to complex for 1 hour at room temperature and then solvent was removed *in vacuo* using a ThermoSavant Speedvac vacuum centrifuge. Equimolar amounts of hydrocinnamic acid and Piv_2O were added robotically. KI was added via automated solid addition. The plates were sealed and heated to either 100 °C or 180 °C and allowed to react for between 30 and 120 minutes, depending on the plate. At the end of the experiment, the arrays were removed from the glove box, cooled and analyzed for the presence of styrene using TLC (silica on glass as stationary phase, hexanes as mobile phase, imaged using UV light) or GC. TLC visualized with UV light is a very sensitive qualitative detection method for styrene; even very low amounts of styrene (>1 mg) can be detected.

Preparation of Primary Screen Experiments. The experiment was set up as described above. All reagents were added robotically using the CM3. The metal precursors were slurried or dissolved in THF with rapid stirring at 40-50 °C. Each metal precursor solution had a concentration of 10 or 20 mg/mL, and was used on the plate in a 1-2 mol% loading. The ligands were either dissolved in THF with a concentration ranging from 0.5 M to 1 M, or in the case of the liquid ligands, were added neat to the reaction wells. The ligand loading ranged from 10-20 mol%. Figure 5.1 contains selected ligand structures. Each plate was prepared by first addition of the metal precursors, then addition of the ligand solutions. The plate was then placed into the vacuum centrifuge to

remove the THF. After the THF had been removed, the neat ligands were added. Finally, the hydrocinnamic acid was melted using an 80 °C hot plate, and was dispensed to each well neat. Pivalic anhydride was the last component added, and was also added neat to each well.

After completing the addition of the metal precursors, ligands, hydrocinnamic acid and pivalic anhydride to the entire plate, the plate was covered with a Teflon liner, a silicone gasket, a butyl rubber gasket, and a metal plate. The plate assembly was then sealed, placed on a heated stirrer on the CM3, (100 or 180 °C), and allowed to react for the desired amount of time (0.5–2 hours). After the reaction had finished, the reaction block was removed from the heat, transferred out of the glove box and cooled rapidly on ice. When the reaction block had reached room temperature, the cover plate and gaskets were removed. Each well was analyzed by TLC (silica on glass, hexanes as mobile phase, imaged using UV light) and the first plate was analyzed by pooled GC experiments. To obtain the pooled GCs, 50 μL of each well was pooled together by columns and rows (column 1 rows 1-8, column 2 rows 1-8… row 1 columns 1–12, etc). After the columns and rows were pooled, each sample was passed through a plug of silica gel and acetone was used to wash the products from the silica. The filtered samples were injected on a Hewlett-Packard 6890 series gas chromatograph using a flame ionization detector, and a Supelco 2-4304 beta-Dex 120 fused silica capillary column (30 m x 0.25 mm ID, 0.25 μm film thickness). The method used was an initial oven temperature of 50 °C held for 2 minutes, followed by a 20 °C/min ramp to 70 °C which was held for 6 minutes. A final 20 °C/min ramp to 230 °C was carried out and held at 230 °C for 3 minutes. Using this method, styrene eluted at 11 minutes. GC was only run on the samples from the first plate, as it corroborated the TLC data. The makeup of the plates is described in Table 5.5,

Table 5.6, Table 5.7, and Table 5.8. Wells that were determined to contain styrene with TLC are marked in green.

Table 5.5. HTE primary screen, plate 1. Reaction temperature: 180 °C. Reaction time: 30 min. Metal loading: 1 mol%. Ligand loading: 10 mol%.

	$Pd(OAc)_2$	$Pd(MeCN)_4(BF_4)_2$	$CoCl_2$	$Co(PPh_3)_3Cl$	$FeCl_2$	$Fe(OTf)_2$	$(DME)NiBr_2$	$Ni(OTf)_2$	CuCl	$Cu(OTf).C_6H_6$	$ZnCl_2$	$Zn(OTf)_2$
PPh_3												
PCy_3												
$P(Ph\text{-}p\text{-}OMe)_3$												
Bipy												
TMEDA												
N-MeImid												
IMes												
IPr												

Table 5.6. HTE primary screen, plate 2. Reaction temperature 100 °C. Reaction time: 60 min. Metal loading: 1 mol%. Ligand loading: 10 mol%.

	$Pd(OAc)_2$	$Pd(MeCN)_4(BF_4)_2$	$CoCl_2$	$Co(PPh_3)_3Cl$	$FeCl_2$	$Fe(OTf)_2$	$(DME)NiBr_2$	$Ni(OTf)_2$	CuCl	$Cu(OTf).C_6H_6$	$ZnCl_2$	$Zn(OTf)_2$
PPh_3												
PCy_3												
$P(Ph\text{-}p\text{-}OMe)_3$												

Bipy												
TMEDA												
N-MeImid												
IMes												
IPr												

Table 5.7. HTE primary screen, plate 3. Reaction temperature 180 °C. Reaction time: 40 min. Metal loading: 1 mol%. Ligand loading: 10 mol%, except pyridine (20 mol%). Ligands on left-hand side of bolded line were loaded with the first six metal precursors, and ligands on the right-hand side of the bolded line were loaded with the final six precursors.

	$Ni(acac)_2$	$Cu(OAc)$	$Fe(OAc)_2$	$Co(OAc)_2$	$Co(acac)_3$	$Mn(OAc)_2$	$Pd(OAc)_2$	$(DME)NiBr_2$	$Fe(OTf)_2$	$CoCl_2$	$CuCl$	$Mn(OAc)_2$	
PPh_3							■						POI
PCy_3					■								Salph
$P(Ph\text{-}p\text{-}OMe)_3$							■						BIMP
Bipy							■						ADI
TMEDA							■					■	pyrBI
$P(OPh)_3$													PhBI
Pyridine	■	■			■		■						Pyridine
No ligand		■			■		■					■	No ligand

Table 5.8. HTE primary screen, plate 4. Reaction temperature: 180 °C. Reaction time: 30 min. Metal loading: 1 mol% (first six columns), 2 mol% (final six columns). Ligand loading: 10 mol%, except pyridine (20 mol%). Green denotes strong signal for styrene when visualized under UV light, orange denotes a weaker signal (qualitative).

	$Co(acac)_3$	$CoCl_2$	$Co(PPh_3)_3Cl$	$(DME)NiBr_2$	CuCl	$FeCl_2$	$Co(acac)_3$	$CoCl_2$	$Co(PPh_3)_3Cl$	$(DME)NiBr_2$	CuCl	$FeCl_2$
PPh_3												
PCy_3												
$P(Ph\text{-}p\text{-}OMe)_3$												
Bipy												
TMEDA												
$P(OPh)_3$												
Pyridine												
IPr												

Preparation of Secondary Screen Experiments and Experiments with Zero-valent and Divalent Metal Precursors. Robot additions, concentrations, experimental procedures were as described above. The reaction was performed in a 48-member array of 2 mL GC vials (Table 5.9 and Table 5.10) or a 96-member array of 1 mL vials (Table 5.11 and Table 5.12). Each well was visualized both by previously described TLC and GC methods (Hewlett-Packard 6890 series gas chromatograph using a flame ionization detector, and a Supelco 2-4304 beta-Dex 120 fused silica capillary column (30 m x 0.25 mm ID, 0.25 μm film thickness). For quantitative GC, 0.8-1 mL of hexane was added to each well of each plate along with a small amount of silica gel. After slurrying sample with silica in hexanes, the silica was filtered away and 120, 150 or 200 μL of the sample was taken into a GC vial. To each GC vial, 1.60 or 1.35 mL of mesitylene stock solution with a known concentration (16.7–22.5 mM) was added and GC was run on the

instrument and method described previously. Concentrations and yields were calculated from a known calibration relative to the mesitylene standard. The makeup of the plates and yields obtained from GC are described in Table 5.9, Table 5.10, Table 5.11, and Table 5.12.

Table 5.9. HTE secondary screen to determine styrene yields based on metal precursor and L/M ratio. Reaction temperature: 180 °C. Reaction time: 1 hr. Under N_2 atmosphere (ambient pressure).

Entry	Metal precursor (5 mol%)	KI loading (mol%)	PPh_3 loading (mol%)	Styrene yield (%)	[styrene]/ [ethylbenzene]
1	$FeCl_2$	0	0	0	
2	$FeCl_2$	0	2.5	0	
3	$FeCl_2$	0	5	0	
4	$FeCl_2$	0	10	0	
5	$FeCl_2$	0	15	0	
6	$FeCl_2$	0	20	0	
7	$FeCl_2$	10	0	0	
8	$FeCl_2$	10	2.5	0.2	>90
9	$FeCl_2$	10	5	1.5	3.8
10	$FeCl_2$	10	10	1.1	>90
11	$FeCl_2$	10	15	0.9	>90
12	$FeCl_2$	10	20	0.8	>90
13	FeI_2	0	0	0	
14	FeI_2	0	2.5	0.3	>90
15	FeI_2	0	5	0.5	>90
16	FeI_2	0	10	1.4	5.1
17	FeI_2	0	15	2.1	5.8
18	FeI_2	0	20	1.2	>90
19	FeI_2	10	0	0	
20	FeI_2	10	2.5	0.3	>90
21	FeI_2	10	5	0.6	>90
22	FeI_2	10	10	1.0	>90

23	FeI_2	10	15	1.1	>90
24	FeI_2	10	20	1.8	6.5
25	$NiCl_2$	0	0	0	
26	$NiCl_2$	0	2.5	0	
27	$NiCl_2$	0	5	0.3	>90
28	$NiCl_2$	0	10	0.5	>90
29	$NiCl_2$	0	15	0.9	>90
30	$NiCl_2$	0	20	2.3	>90
31	$NiCl_2$	10	0	0	
32	$NiCl_2$	10	2.5	0.3	>90
33	$NiCl_2$	10	5	1.6	4.3
34	$NiCl_2$	10	10	0.5	>90
35	$NiCl_2$	10	15	0.4	>90
36	$NiCl_2$	10	20	0.3	>90
37	NiI_2	0	0	0	
38	NiI_2	0	2.5	1.3	6.5
39	NiI_2	0	5	1.5	5.6
40	NiI_2	0	10	1.0	>90
41	NiI_2	0	15	0.3	>90
42	NiI_2	0	20	0.2	>90
43	NiI_2	10	0	0	
44	NiI_2	10	2.5	1.7	5.9
45	NiI_2	10	5	0.8	>90
46	NiI_2	10	10	1.0	>90
47	NiI_2	10	15	0.1	>90
48	NiI_2	10	20	0.3	>90

Table 5.10. HTE secondary screen to determine styrene yields based on metal precursor and L/M ratio. Reaction temperature: 180 °C. Reaction time: 2 hr. Under N_2 atmosphere (ambient pressure).

Entry	Metal precursor (5 mol%)	KI loading (mol%)	PPh_3 loading (mol%)	Styrene yield (%)	[styrene]/ [ethylbenzene]
1	$FeCl_2$	0	0	0	
2	$FeCl_2$	0	2.5	0	

3	$FeCl_2$	0	5	0	
4	$FeCl_2$	0	10	0	
5	$FeCl_2$	0	15	0	
6	$FeCl_2$	0	20	0	
7	$FeCl_2$	10	0	0	
8	$FeCl_2$	10	2.5	0.5	2.1
9	$FeCl_2$	10	5	1.3	1.2
10	$FeCl_2$	10	10	1.9	1.6
11	$FeCl_2$	10	15	1.7	2.1
12	$FeCl_2$	10	20	1.4	2.9
13	FeI_2	0	0	0	
14	FeI_2	0	2.5	0.7	1.5
15	FeI_2	0	5	0.3	>90
16	FeI_2	0	10	0.9	2.6
17	FeI_2	0	15	1.7	1.6
18	FeI_2	0	20	1.5	2.5
19	FeI_2	10	0	0	
20	FeI_2	10	2.5	0.6	2.5
21	FeI_2	10	5	0.4	>90
22	FeI_2	10	10	1.7	1.2
23	FeI_2	10	15	1.7	2.0
24	FeI_2	10	20	0.6	>90
25	$NiCl_2$	0	0	0	
26	$NiCl_2$	0	2.5	0	
27	$NiCl_2$	0	5	0	
28	$NiCl_2$	0	10	0.6	>90
29	$NiCl_2$	0	15	1.6	>90
30	$NiCl_2$	0	20	3.1	>90
31	$NiCl_2$	10	0	0	
32	$NiCl_2$	10	2.5	2.6	5.7
33	$NiCl_2$	10	5	2.1	3.3
34	$NiCl_2$	10	10	1.8	2.3
35	$NiCl_2$	10	15	1.0	1.2
36	$NiCl_2$	10	20	0.7	1.3

37	NiI_2	0	0	0	
38	NiI_2	0	2.5	3.3	6.2
39	NiI_2	0	5	5.5	4.4
40	NiI_2	0	10	4.0	2.5
41	NiI_2	0	15	1.5	0.8
42	NiI_2	0	20	1.2	0.8
43	NiI_2	10	0	0	
44	NiI_2	10	2.5	4.8	6.4
45	NiI_2	10	5	7.1	4.8
46	NiI_2	10	10	5.3	2.8
47	NiI_2	10	15	1.2	1.3
48	NiI_2	10	20	0.7	1.3

Table 5.11. HTE primary screen to determine styrene yields with zero valent and divalent Ni and Fe precursors and phosphine ligands. Reaction temperature: 180 °C. Reaction time: 2 hr. Under N_2 atmosphere (ambient pressure).

Entry	Metal precursor (2 mol%)	KI loading (mol%)	Ligand (10 mol%)	Styrene yield (%)	[styrene]/ [ethylbenzene]
1	$Ni(COD)_2$	0	DPPE	1.7	>90
2	$Ni(COD)_2$	0	DPPP	1.9	>90
3	$Ni(COD)_2$	0	DPPB	2.3	>90
4	$Ni(COD)_2$	0	DPPF	4.3	>90
5	$Ni(COD)_2$	0	DavePhos	2.5	8.1
6	$Ni(COD)_2$	0	Xantphos	1.1	>90
7	$Ni(COD)_2$	0	DPEphos	2.8	>90
8	$Ni(COD)_2$	0	Phen	0	
9	$Ni(COD)_2$	10	DPPE	1.6	>90
10	$Ni(COD)_2$	10	DPPP	1.9	>90
11	$Ni(COD)_2$	10	DPPB	0	
12	$Ni(COD)_2$	10	DPPF	3.0	>90
13	$Ni(COD)_2$	10	DavePhos	2.0	6.3
14	$Ni(COD)_2$	10	Xantphos	1.3	6.9
15	$Ni(COD)_2$	10	DPEphos	3.0	>90
16	$Ni(COD)_2$	10	Phen	0	

17	FeI_2	0	DPPE	0	
18	FeI_2	0	DPPP	0	
19	FeI_2	0	DPPB	0	
20	FeI_2	0	DPPF	0	
21	FeI_2	0	DavePhos	0	
22	FeI_2	0	Xantphos	0	
23	FeI_2	0	DPEphos	0	
24	FeI_2	0	Phen	0	
25	FeI_2	10	DPPE	0	
26	FeI_2	10	DPPP	0	
27	FeI_2	10	DPPB	0	
28	FeI_2	10	DPPF	0	
29	FeI_2	10	DavePhos	0	
30	FeI_2	10	Xantphos	0	
31	FeI_2	10	DPEphos	0	
32	FeI_2	10	Phen	0	
33	$Fe(CO)_3(PPh_3)_2$	0	DPPE	0	
34	$Fe(CO)_3(PPh_3)_2$	0	DPPP	0	
35	$Fe(CO)_3(PPh_3)_2$	0	DPPB	0	
36	$Fe(CO)_3(PPh_3)_2$	0	DPPF	0	
37	$Fe(CO)_3(PPh_3)_2$	0	DavePhos	0	
38	$Fe(CO)_3(PPh_3)_2$	0	Xantphos	0	
39	$Fe(CO)_3(PPh_3)_2$	0	DPEphos	0	
40	$Fe(CO)_3(PPh_3)_2$	0	Phen	0	
41	$Fe(CO)_3(PPh_3)_2$	10	DPPE	0	
42	$Fe(CO)_3(PPh_3)_2$	10	DPPP	0	
43	$Fe(CO)_3(PPh_3)_2$	10	DPPB	0	
44	$Fe(CO)_3(PPh_3)_2$	10	DPPF	0	
45	$Fe(CO)_3(PPh_3)_2$	10	DavePhos	0	
46	$Fe(CO)_3(PPh_3)_2$	10	Xantphos	0	
47	$Fe(CO)_3(PPh_3)_2$	10	DPEphos	0	
48	$Fe(CO)_3(PPh_3)_2$	10	Phen	0	
49	$NiCl_2$	0	DPPE	0	
50	$NiCl_2$	0	DPPP	0.8	>90

51	$NiCl_2$	0	DPPB	0.2	>90
52	$NiCl_2$	0	DPPF	1.1	>90
53	$NiCl_2$	0	DavePhos	0.5	2.8
54	$NiCl_2$	0	Xantphos	0	
55	$NiCl_2$	0	DPEphos	0.9	>90
56	$NiCl_2$	0	Phen	0	
57	$NiCl_2$	10	DPPE	0.4	>90
58	$NiCl_2$	10	DPPP	0.5	1.8
59	$NiCl_2$	10	DPPB	5.0	1.5
60	$NiCl_2$	10	DPPF	4.1	24
61	$NiCl_2$	10	DavePhos	2.3	1.5
62	$NiCl_2$	10	Xantphos	0	
63	$NiCl_2$	10	DPEphos	4.4	3.6
64	$NiCl_2$	10	Phen	0	
65	NiI_2	0	DPPE	0.3	>90
66	NiI_2	0	DPPP	1.6	1.6
67	NiI_2	0	DPPB	1.6	2.0
68	NiI_2	0	DPPF	4.7	20
69	NiI_2	0	DavePhos	3.0	1.8
70	NiI_2	0	Xantphos	0	
71	NiI_2	0	DPEphos	7.0	5.3
72	NiI_2	0	Phen	0	
73	NiI_2	10	DPPE	0.5	>90
74	NiI_2	10	DPPP	1.1	2.1
75	NiI_2	10	DPPB	0	
76	NiI_2	10	DPPF	4.4	27
77	NiI_2	10	DavePhos	4.3	1.8
78	NiI_2	10	Xantphos	0	
79	NiI_2	10	DPEphos	0	
80	NiI_2	10	Phen	0	
81	$Ni(PPh_3)_4$	0	DPPE	1.9	>90
82	$Ni(PPh_3)_4$	0	DPPP	2.0	>90
83	$Ni(PPh_3)_4$	0	DPPB	4.7	>90
84	$Ni(PPh_3)_4$	0	DPPF	4.7	>90

85	$Ni(PPh_3)_4$	0	DavePhos	2.9	19
86	$Ni(PPh_3)_4$	0	Xantphos	2.2	>90
87	$Ni(PPh_3)_4$	0	DPEphos	2.4	>90
88	$Ni(PPh_3)_4$	0	Phen	0	
89	$Ni(PPh_3)_4$	10	DPPE	1.7	>90
90	$Ni(PPh_3)_4$	10	DPPP	2.2	>90
91	$Ni(PPh_3)_4$	10	DPPB	4.7	74
92	$Ni(PPh_3)_4$	10	DPPF	3.9	70
93	$Ni(PPh_3)_4$	10	DavePhos	5.4	63
94	$Ni(PPh_3)_4$	10	Xantphos	1.5	>90
95	$Ni(PPh_3)_4$	10	DPEphos	2.8	>90
96	$Ni(PPh_3)_4$	10	Phen	0	

Table 5.12. HTE primary screen to determine styrene yields with zero-valent and divalent Ni and Fe precursors and phosphine ligands. Reaction temperature: 180 °C. Reaction time: 2 hr. Under CO atmosphere (100 psi).

Entry	Metal precursor (2 mol%)	KI loading (mol%)	Ligand (10 mol%)	Styrene yield (%)	[styrene]/ [ethylbenzene]
1	$Ni(COD)_2$	0	DPPE	0	
2	$Ni(COD)_2$	0	PPh_3	1.6	14
3	$Ni(COD)_2$	0	DPPB	1.3	>90
4	$Ni(COD)_2$	0	DPPF	0.9	>90
5	$Ni(COD)_2$	0	DavePhos	1.3	3.4
6	$Ni(COD)_2$	0	Xantphos	0.6	>90
7	$Ni(COD)_2$	0	DPEphos	0.5	>90
8	$Ni(COD)_2$	0	Phen	0	
9	$Ni(COD)_2$	10	DPPE	0	
10	$Ni(COD)_2$	10	PPh_3	2.0	21
11	$Ni(COD)_2$	10	DPPB	0	
12	$Ni(COD)_2$	10	DPPF	0.8	>90
13	$Ni(COD)_2$	10	DavePhos	0.9	3.5
14	$Ni(COD)_2$	10	Xantphos	0.5	>90
15	$Ni(COD)_2$	10	DPEphos	0.3	>90
16	$Ni(COD)_2$	10	Phen	0	

17	FeI_2	0	DPPE	0
18	FeI_2	0	PPh_3	0
19	FeI_2	0	DPPB	0
20	FeI_2	0	DPPF	0
21	FeI_2	0	DavePhos	0
22	FeI_2	0	Xantphos	0
23	FeI_2	0	DPEphos	0
24	FeI_2	0	Phen	0
25	FeI_2	10	DPPE	0
26	FeI_2	10	PPh_3	0
27	FeI_2	10	DPPB	0
28	FeI_2	10	DPPF	0
29	FeI_2	10	DavePhos	0
30	FeI_2	10	Xantphos	0
31	FeI_2	10	DPEphos	0
32	FeI_2	10	Phen	0
33	$Fe(CO)_3(PPh_3)_2$	0	DPPE	0
34	$Fe(CO)_3(PPh_3)_2$	0	PPh_3	0
35	$Fe(CO)_3(PPh_3)_2$	0	DPPB	0
36	$Fe(CO)_3(PPh_3)_2$	0	DPPF	0
37	$Fe(CO)_3(PPh_3)_2$	0	DavePhos	0
38	$Fe(CO)_3(PPh_3)_2$	0	Xantphos	0
39	$Fe(CO)_3(PPh_3)_2$	0	DPEphos	0
40	$Fe(CO)_3(PPh_3)_2$	0	Phen	0
41	$Fe(CO)_3(PPh_3)_2$	10	DPPE	0
42	$Fe(CO)_3(PPh_3)_2$	10	PPh_3	0
43	$Fe(CO)_3(PPh_3)_2$	10	DPPB	0
44	$Fe(CO)_3(PPh_3)_2$	10	DPPF	0
45	$Fe(CO)_3(PPh_3)_2$	10	DavePhos	0
46	$Fe(CO)_3(PPh_3)_2$	10	Xantphos	0
47	$Fe(CO)_3(PPh_3)_2$	10	DPEphos	0
48	$Fe(CO)_3(PPh_3)_2$	10	Phen	0
49	$NiCl_2$	0	DPPE	0
50	$NiCl_2$	0	PPh_3	0

51	$NiCl_2$	0	DPPB	0	
52	$NiCl_2$	0	DPPF	0	
53	$NiCl_2$	0	DavePhos	0	
54	$NiCl_2$	0	Xantphos	0	
55	$NiCl_2$	0	DPEphos	0	
56	$NiCl_2$	0	Phen	0	
57	$NiCl_2$	10	DPPE	0	
58	$NiCl_2$	10	PPh_3	0	
59	$NiCl_2$	10	DPPB	0	
60	$NiCl_2$	10	DPPF	0	
61	$NiCl_2$	10	DavePhos	0	
62	$NiCl_2$	10	Xantphos	0	
63	$NiCl_2$	10	DPEphos	0	
64	$NiCl_2$	10	Phen	0	
65	NiI_2	0	DPPE	0	
66	NiI_2	0	PPh_3	0	
67	NiI_2	0	DPPB	0	
68	NiI_2	0	DPPF	0	
69	NiI_2	0	DavePhos	0.1	>90
70	NiI_2	0	Xantphos	0	
71	NiI_2	0	DPEphos	0	
72	NiI_2	0	Phen	0	
73	NiI_2	10	DPPE	0	
74	NiI_2	10	PPh_3	0	
75	NiI_2	10	DPPB	0	
76	NiI_2	10	DPPF	0	
77	NiI_2	10	DavePhos	0	
78	NiI_2	10	Xantphos	0	
79	NiI_2	10	DPEphos	0	
80	NiI_2	10	Phen	0	
81	$Ni(PPh_3)_4$	0	DPPE	0.1	>90
82	$Ni(PPh_3)_4$	0	PPh_3	0	
83	$Ni(PPh_3)_4$	0	DPPB	1.0	>90
84	$Ni(PPh_3)_4$	0	DPPF	1.6	>90

85	$Ni(PPh_3)_4$	0	DavePhos	2.0	11
86	$Ni(PPh_3)_4$	0	Xantphos	1.0	7.1
87	$Ni(PPh_3)_4$	0	DPEphos	1.4	8.2
88	$Ni(PPh_3)_4$	0	Phen	0	
89	$Ni(PPh_3)_4$	10	DPPE	0.1	>90
90	$Ni(PPh_3)_4$	10	PPh_3	0	
91	$Ni(PPh_3)_4$	10	DPPB	1.9	>90
92	$Ni(PPh_3)_4$	10	DPPF	2.0	>90
93	$Ni(PPh_3)_4$	10	DavePhos	1.8	5.6
94	$Ni(PPh_3)_4$	10	Xantphos	1.3	8.4
95	$Ni(PPh_3)_4$	10	DPEphos	1.1	>90
96	$Ni(PPh_3)_4$	10	Phen	0	

5.5.3 Large Scale Decarbonylation Reactions

Reactions Under $CO/CO_2/N_2$ pressure. In an inert atmosphere glove box, hydrocinnamic acid (1.0 g, 6.6 mmol or 0.50 g, 3.3 mmol), Piv_2O (1.35 mL, 6.66 mmol or 0.68 mL, 3.3 mmol), $Ni(PPh_3)_4$ (368 mg, 0.333 mmol or 154 mg, 0.139 mmol), PPh_3 (175 mg, 0.666 mmol or 77 mg, 2.9 mmol) were added to a Fischer-porter bottle, sealed and removed from the glove box. The reactor was pressurized to 80 psi of CO or CO_2 gas or left at ambient pressure under N_2. The reaction was heated to 180 °C and allowed to react for 1.5 hours. After the reaction time had finished, the reaction was cooled and diluted with 10 mL of hexanes. A 200 μL aliquot was taken for GC analysis, and diluted to 1.5 mL using a solution of mesitylene in hexanes (201.2 mg in 100 mL hexanes). Yields were determined from a calibration curve using mesitylene as an internal standard and are reported in Table 5.2.

Conventional Decarbonylation Reactions. In a nitrogen-filled glovebox, hydrocinnamic acid (1.0 g, 6.7 mmol), Ni precursor (2–10 mol%), pivalic anhydride (1.35 mL, 6.66 mmol), KI (0–100 mol%) and phosphine ligand (5–20 mol%) were loaded into an oven-dried 10 mL round-bottom flask equipped with a Teflon stir bar. Not all of

the reagents were soluble at room temperature, resulting in a heterogeneous mixture. The round-bottom flask was capped with a rubber septum, removed from the glovebox and quickly attached to an oven-dried short-path distillation apparatus under a flow of argon gas. The reaction flask was lowered into a 160 to 170 °C oil bath and allowed to continue

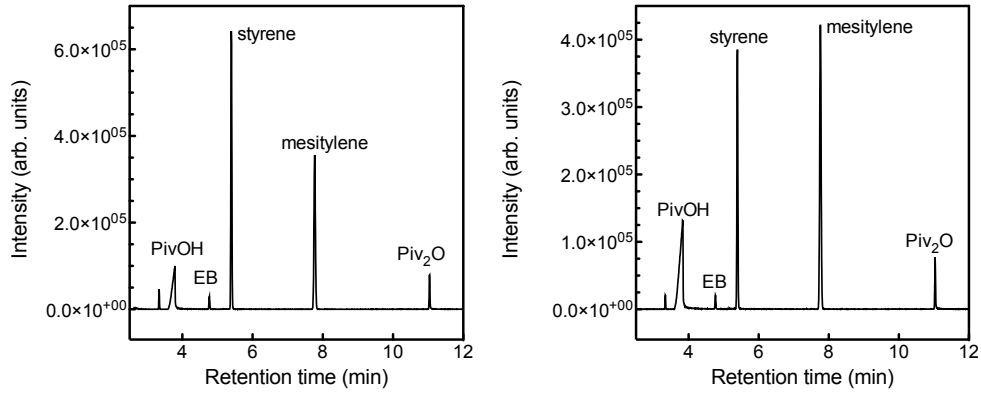

Figure 5.7. Representative GC-MS chromatograms of distillate isolated from reaction in **Table 5.4**, Entry 7 (left) and **Table 5.4**, Entry 8 (right).

to heat until the oil bath reached 180 °C. Once the reaction mixture reached about 175 °C it began to bubble, indicating loss of carbon monoxide. The reaction was allowed to proceed for the indicated time, during which time a distillate was collected. After 2 h, heating was ceased and the reaction was exposed to air. The distillate was analyzed using GC-MS, using mesitylene as an internal standard (representative GC-MS chromatograms in Figure 5.7).

Workup of Reaction Flask to Isolate Styrene Dimers. To the reaction with conditions in Table 4, Entry 5, 200 mL of hexane was added to the reaction flask after it had cooled to room temperature to dissolve any hexane soluble species. After stirring for 30 min, the hexane was separated from the hexane-insoluble components by filtration and the hexane was removed *in vacuo*. The residual material was analyzed by GC-MS (Figure 5.8 and Figure 5.9). To the hexane-insoluble material, 125 mL of $CHCl_3$ was added with 100 mL of deionized water, and was allowed to stir for 30 min until everything dissolved

in the chloroform/water phases. The layers were allowed to separate, and the yellow chloroform layer was washed once with 100 mL of NaOH (0.23 M) yielding a colorless solution, then once with 1 M aq. HCl (20 mL). The chloroform was removed *in vacuo* to yield a yellow solid, which was also subjected to GC-MS analysis (Figure 5.10 and Figure 5.11). Both the hexane soluble and hexane insoluble GC-MS traces had styrene dimers as the majority components present.

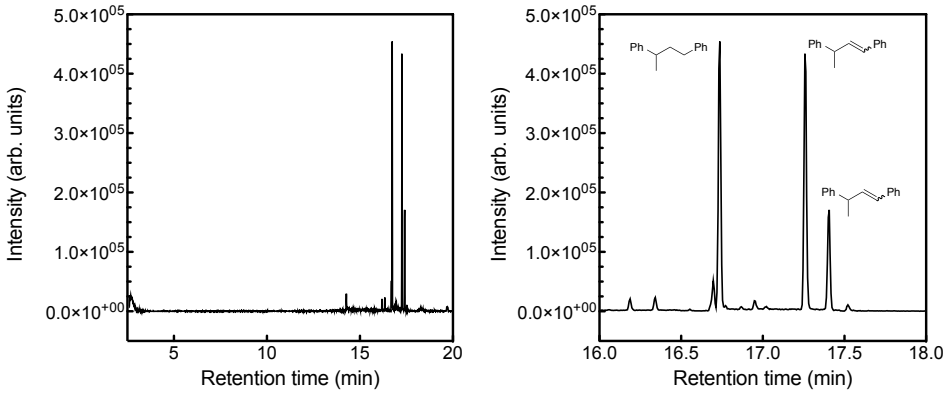

Figure 5.8. GC-MS chromatogram (full, left; zoom of region from 16 to 18 min, right) of reaction flask after reaction had been terminated, diluted with hexanes, and filtered. The solvent was removed *in vacuo* and reside was taken up in a small amount of hexanes for GC-MS analysis.

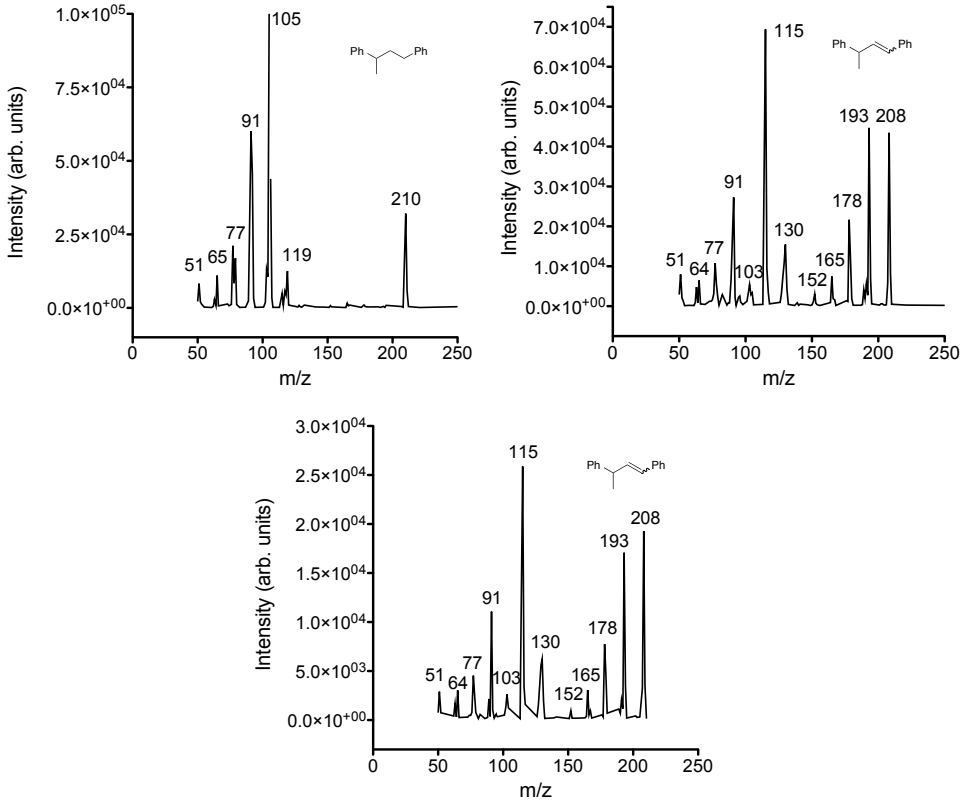

Figure 5.9. Mass spectrum of peaks with retention times 16.73 min (top left), 17.26 min (top right), and 17.41 min (bottom) from chromatograms in **Figure 5.8**.

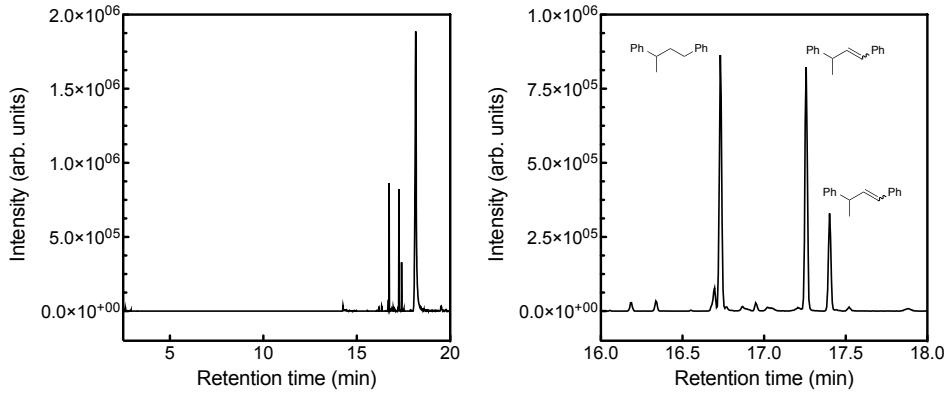

Figure 5.10. GC-MS chromatogram (full, left; zoom of region from 16 to 18 min, right) of solid residue left in the reaction flask after reaction had been terminated, diluted with hexanes, and filtered to obtain the insoluble products. The insoluble products were then dissolved in $CHCl_3$, stirred with deionized water, and then washed with NaOH and HCl. The $CHCl_3$ was removed *in vacuo* and this is the GC-MS of the resulting solid.

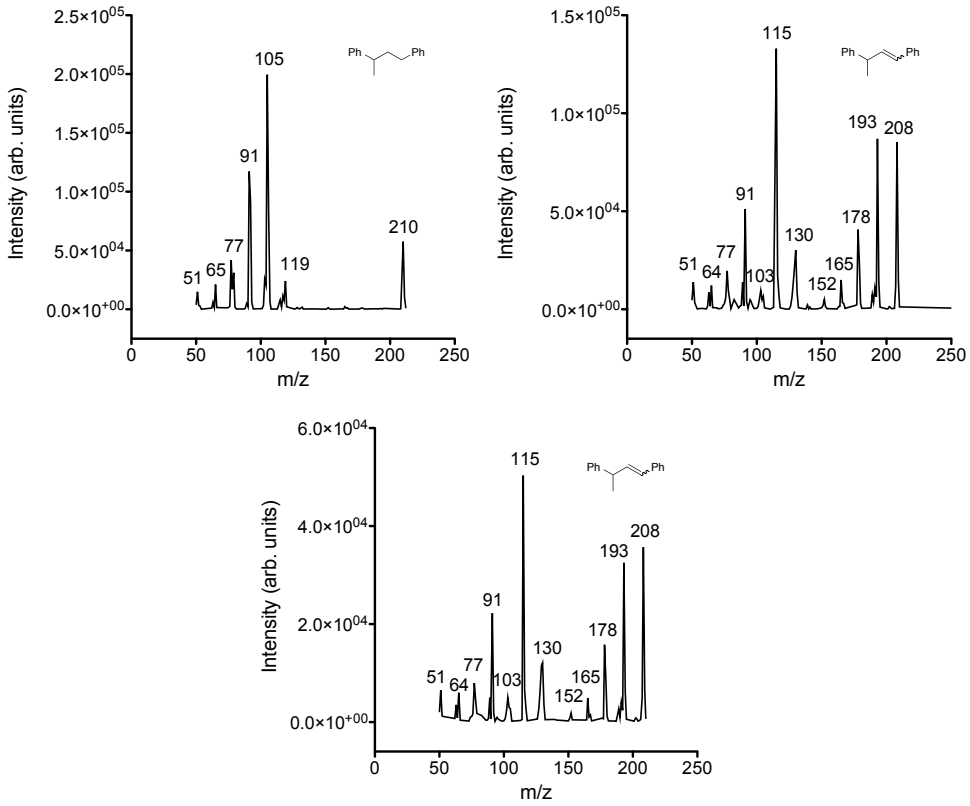

Figure 5.11. Mass spectrum of peaks with retention times 16.73 min (top left), 17.26 min (top right), and 17.41 min (bottom) from chromatograms in **Figure 5.10**.

5.6 Acknowledgments

We especially thank Dr. Keying Ding, Dr. Anne M. LaPointe, and Prof. Geoffrey Coates for their input and collaboration on this project. Additionally, we would like to thank the National Science Foundation (a Graduate Research Fellowship under Grant No. 00006595 to M.O.M.) and the Center for Sustainable Polymers, a National Science Foundation supported Center for Chemical Innovation (CHE-1136607), the Department of Energy (DE-FG02-05ER15687) for financial support of this research.

6 Bibliography

1. U.S. Environmental Protection Agency. Plastics Common Wastes & Materials http://www.epa.gov/osw/conserve/materials/plastics.htm (accessed Apr 9, 2014).
2. Gandini, A. The Irruption of Polymers From Renewable Resources on the Scene of Macromolecular Science and Technology. *Green Chem.* **2011**, *13*, 1061.
3. Report of the World Commission on Environment and Development: Our Common Future; United Nations General Assembly, 1987; pp. 1–300.
4. Freinkel, S. *Plastic: A Toxic Love Story*; Houghton Mifflin Harcourt: Boston, 2011.
5. Gross, R. A.; Kalra, B. Biodegradable Polymers for the Environment. *Science* **2002**, *297*, 803–807.
6. Vennestrøm, P. N. R.; Osmundsen, C. M.; Christensen, C. H.; Taarning, E. Beyond Petrochemicals: the Renewable Chemicals Industry. *Angew. Chem. Int. Ed.* **2011**, *50*, 10502–10509.
7. Vink, E. T. H.; Rabago, K. R.; Glassner, D. A.; Springs, B.; O'Connor, R. P.; Kolstad, J.; Gruber, P. R. The Sustainability of NatureWorks(TM) Polylactide Polymers and Ingeo(TM) Polylactide Fibers: an Update of the Future. *Macromol. Biosci.* **2004**, *4*, 551–564.
8. Auras, R.; Harte, B.; Selke, S. An Overview of Polylactides as Packaging Materials. *Macromol. Biosci.* **2004**, *4*, 835–864.
9. Drumright, R. E.; Gruber, P. R.; Henton, D. E. Polylactic Acid Technology. *Adv. Mater.* **2000**, *12*, 1841–1846.
10. Bogaert, J.-C.; Coszach, P. Poly(Lactic Acids): a Potential Solution to Plastic Waste Dilemma. *Macromol. Symp.* **2000**, *153*, 287–303.
11. Sinclair, R. G. The Case for Polylactic Acid as a Commodity Packaging Plastic. *J. Macromol. Sci., Pure Appl. Chem.* **1996**, *A33*, 585–597.
12. Langer, R.; Vacanti, J. P. Tissue Engineering. *Science* **1993**, *260*, 920–926.
13. Langer, R. S. Drug Delivery and Targeting. *Nature* **1998**, *392*, 5–10.
14. Uhrich, K. E.; Cannizzaro, S. M.; Langer, R. S.; Shakesheff, K. M. Polymeric Systems for Controlled Drug Release. *Chem. Rev.* **1999**, *99*, 3181–3198.
15. O'Keefe, B.; Hillmyer, M.; Tolman, W. Polymerization of Lactide and Related Cyclic Esters by Discrete Metal Complexes. *J. Chem. Soc., Dalton Trans.* **2001**, 2215–2224.

16 . Kamber, N. E.; Jeong, W.; Pratt, R. C.; Lohmeijer, B. G. G.; Waymouth, R. M.; Hedrick, J. L. Organocatalytic Ring-Opening Polymerization. *Chem. Rev.* **2007**, *107*, 5813–5840.

17. Buntara, T.; Noel, S.; Phua, P. H.; Melian-Cabrera, I.; Vries, J. G. de; Heeres, H. J. Caprolactam From Renewable Resources: Catalytic Conversion of 5‐Hydroxymethylfurfural Into Caprolactone. *Angew. Chem. Int. Ed.* **2011**, *50*, 7083–7087.

18. Zhang, D.; Hillmyer, M. A.; Tolman, W. B. Catalytic Polymerization of a Cyclic Ester Derived From a "Cool" Natural Precursor. *Biomacromolecules* **2005**, *6*, 2091–2095.

19. Wanamaker, C. L.; O'Leary, L. E.; Lynd, N. A.; Hillmyer, M. A.; Tolman, W. B. Renewable-Resource Thermoplastic Elastomers Based on Polylactide and Polymenthide. *Biomacromolecules* **2007**, *8*, 3634–3640.

20. Wanamaker, C. L.; Bluemle, M. J.; Pitet, L. M.; O'Leary, L. E.; Tolman, W. B.; Hillmyer, M. A. Consequences of Polylactide Stereochemistry on the Properties of Polylactide-Polymenthide-Polylactide Thermoplastic Elastomers. *Biomacromolecules* **2009**, *10*, 2904–2911.

21. Lowe, J. R.; Tolman, W. B.; Hillmyer, M. A. Oxidized Dihydrocarvone as a Renewable Multifunctional Monomer for the Synthesis of Shape Memory Polyesters. *Biomacromolecules* **2009**, *10*, 2003–2008.

22. Knight, S. C.; Schaller, C. P.; Tolman, W. B.; Hillmyer, M. A. Renewable Carvone-Based Polyols for Use in Polyurethane Thermosets. *RSC Adv.* **2013**, *3*, 20399–20404.

23. Dechy-Cabaret, O.; Martin-Vaca, B.; Bourissou, D. Controlled Ring-Opening Polymerization of Lactide and Glycolide. *Chem. Rev.* **2004**, *104*, 6147–6176.

24. Müller, H.-M.; Seebach, D. Poly(Hydroxyalkanoates): a Fifth Class of Physiologically Important Organic Biopolymers? *Angew. Chem. Int. Ed.* **1993**, *32*, 477–502.

25. Thomas, C. M. Stereocontrolled Ring-Opening Polymerization of Cyclic Esters: Synthesis of New Polyester Microstructures. *Chem. Soc. Rev.* **2010**, *39*, 165–173.

26. Bero, M.; Dobrzynski, P.; Kasperczyk, J. E. Synthesis of Disyndiotactic Polylactide. *J. Polym. Sci., Part A: Polym. Chem.* **1999**, *37*, 4038–4042.

27. Kasperczyk, J. E. Microstructure Analysis of Poly(Lactic Acid) Obtained by Lithium Tert-Butoxide as Initiator. *Macromolecules* **1995**, *28*, 3937–3939.

28. Kricheldorf, H. R.; Kreiser-Saunders, I. Polylactones, 19. Anionic Polymerization of L-Lactide in Solution. *D. Makromol. Chem.* **1990**, *191*, 1057–1066.

29. Jedlinski, Z.; Walach, W.; Kurcok, P.; Adamus, G. Polymerization of Lactones, 12. Polymerization of L-Dilactide and L,D-Dilactide in the Presence of Potassium Methoxide. *D. Makromol. Chem.* **1991**, *192*, 2051–2057.

30. Kricheldorf, H. R.; Dunsing, R. Polylactones, 8. Mechanism of the Cationic Polymerization of L,L-Dilactide. *D. Makromol. Chem.* **1986**, *187*, 1611–1625.

31. Kricheldorf, H. R.; Kreiser, I. Polylactones, 11. Cationic Copolymerization of Glycolide with L,L-Dilactide. *D. Makromol. Chem.* **1987**, *188*, 1861–1873.

32. Bourissou, D.; Martin-Vaca, B.; Dumitrescu, A.; Graullier, M.; Lacombe, F. Controlled Cationic Polymerization of Lactide. *Macromolecules* **2005**, *38*, 9993–9998.

33. Nederberg, F.; Connor, E. F.; Möller, M.; Glauser, T.; Hedrick, J. New Paradigms for Organic Catalysts: the First Organocatalytic Living Polymerization. *Angew. Chem. Int. Ed.* **2001**, *40*, 2712–2715.

34. Myers, M.; Connor, E. F.; Glauser, T.; Möck, A.; Nyce, G.; Hedrick, J. Phosphines: Nucleophilic Organic Catalysts for the Controlled Ring-Opening Polymerization of Lactides. *J. Polym. Sci., Part A: Polym. Chem.* **2002**, *40*, 844–851.

35. Nyce, G. W.; Glauser, T.; Connor, E. F.; Mock, A.; Waymouth, R. M.; Hedrick, J. L. In Situ Generation of Carbenes: a General and Versatile Platform for Organocatalytic Living Polymerization. *J. Am. Chem. Soc.* **2003**, *125*, 3046–3056.

36. Dove, A. P.; Li, H.; Pratt, R. C.; Lohmeijer, B. G. G.; Culkin, D. A.; Waymouth, R. M.; Hedrick, J. L. Stereoselective Polymerization of *rac*-and *meso*-Lactide Catalyzed by Sterically Encumbered *N*-Heterocyclic Carbenes. *Chem. Commun.* **2006**, 2881–2883.

37. Jensen, T. R.; Breyfogle, L. E.; Hillmyer, M. A.; Tolman, W. B. Stereoelective Polymerization of D,L-Lactide Using *N*-Heterocyclic Carbene Based Compounds. *Chem. Commun.* **2004**, 2504–2505.

38. Stanford, M. J.; Dove, A. P. Stereocontrolled Ring-Opening Polymerisation of Lactide. *Chem. Soc. Rev.* **2010**, *39*, 486.

39. Kiesewetter, M. K.; Shin, E. J.; Hedrick, J. L.; Waymouth, R. M. Organocatalysis: Opportunities and Challenges for Polymer Synthesis. *Macromolecules* **2010**, *43*, 2093–2107.

40. Kricheldorf, H. R. Syntheses of Biodegradable and Biocompatible Polymers by Means of Bismuth Catalysts. *Chem. Rev.* **2009**, *109*, 5579–5594.

41. Dijkstra, P.; Du, H.; Feijen, J. Single Site Catalysts for Stereoselective Ring-Opening Polymerization of Lactides. *Polym. Chem.* **2011**, *2*, 520–527.

42. Hiemenz, P. C.; Lodge, T. P. Polymer Chemistry; 2nd ed.; CRC Press: Boca Raton, FL, 2007; pp. 119–126.

43. Kowalski, A.; Duda, A.; Penczek, S. Polymerization of L,L-Lactide Initiated by Aluminum Isopropoxide Trimer or Tetramer. *Macromolecules* **1998**, *31*, 2114–2122.

44. Schwach, G.; Coudane, J.; Engel, R.; Vert, M. Ring Opening Polymerization of D,L-Lactide in the Presence of Zinc Metal and Zinc Lactate. *Polym. Int.* **1998**, *46*, 177–182.

45. Kricheldorf, H. R.; Damrau, D.-O. Polylactones, 37. Polymerizations of L-Lactide Initiated with Zn(II) L-Lactate and Other Resorbable Zn Salts. *Macromol. Chem. Phys.* **1997**, *198*, 1753–1766.

46. Spassky, N.; Simic, V.; Montaudo, M. S.; Hubert-Pfalzgraf, L. G. Inter-and Intramolecular Ester Exchange Reactions in the Ring-Opening Polymerization of (D,L)-Lactide Using Lanthanide Alkoxide Initiators. *Macromol. Chem. Phys.* **2000**, *201*, 2432–2440.

47. Stevels, W. M.; Ankone, M. J. K.; Dijkstra, P. J.; Feijen, J. Well Defined Block Copolymers of ε-Caprolactone and L-Lactide Using $Y_5(M\text{-}O)(O\textit{i}\text{-}Pr)_{13}$ as an Initiator. *Macromol. Chem. Phys.* **1995**, *196*, 1153–1161.

48. Zhong, Z.; Dijkstra, P. J.; Birg, C.; Westerhausen, M.; Feijen, J. A Novel and Versatile Calcium-Based Initiator System for the Ring-Opening Polymerization of Cyclic Esters. *Macromolecules* **2001**, *34*, 3863–3868.

49. Finne, A.; Reema; Albertsson, A.-C. Use of Germanium Initiators in Ring-Opening Polymerization of L-Lactide. *J. Polym. Sci., Part A: Polym. Chem.* **2003**, *41*, 3074–3082.

50. Kowalski, A.; Libiszowski, J.; Duda, A.; Penczek, S. Polymerization of L,L-Dilactide Initiated by Tin (II) Butoxide. *Macromolecules* **2000**, *33*, 1964–1971.

51. Chisholm, M. H.; Delbridge, E. E. A Study of the Ring-Opening Polymerization (ROP) of L-Lactide by Ph_2SnX_2 Precursors (X=NMe_2, O*i*-Pr): the Notable Influence of Initiator Group. *New J. Chem.* **2003**, *27*, 1177–1183.

52. Chisholm, M. H.; Delbridge, E. E. Ring-Opening of Lactides and Related Cyclic Monomers by Triaryltin (IV) Alkoxides and Amides. *Chem. Commun.* **2001**, 1308–1309.

53. O'Keefe, B. J.; Monnier, S. M.; Hillmyer, M. A.; Tolman, W. B. Rapid and Controlled Polymerization of Lactide by Structurally Characterized Ferric Alkoxides. *J. Am. Chem. Soc.* **2001**, *123*, 339–340.

54. Spassky, N.; Wisniewski, M.; Pluta, C.; LeBorgne, A. Highly Stereoselective Polymerization of *rac*-(D,L)-Lactide with a Chiral Schiff's Base/Aluminium Alkoxide Initiator. *Macromol. Chem. Phys.* **1996**, *197*, 2627–2637.

55. Ovitt, T. M.; Coates, G. W. Stereoselective Ring-Opening Polymerization of Rac-Lactide with a Single-Site, Racemic Aluminum Alkoxide Catalyst: Synthesis of Stereoblock Poly(Lactic Acid). *J. Polym. Sci., Part A: Polym. Chem.* **2000**, *38*, 4686–4692.

56. Radano, C. P.; Baker, G. L.; Smith, M. R. Stereoselective Polymerization of a Racemic Monomer with a Racemic Catalyst: Direct Preparation of the Polylactic Acid Stereocomplex From Racemic Lactide. *J. Am. Chem. Soc.* **2000**, *122*, 1552–1553.

57. Ovitt, T. M.; Coates, G. W. Stereochemistry of Lactide Polymerization with Chiral Catalysts: New Opportunities for Stereocontrol Using Polymer Exchange Mechanisms. *J. Am. Chem. Soc.* **2002**, *124*, 1316–1326.

58. Cheng, M.; Attygalle, A. B.; Lobkovsky, E. B.; Coates, G. W. Single-Site Catalysts for Ring-Opening Polymerization: Synthesis of Heterotactic Poly(Lactic Acid) From *rac*-Lactide. *J. Am. Chem. Soc.* **1999**, *121*, 11583–11584.

59. Chamberlain, B. M.; Cheng, M.; Moore, D. R.; Ovitt, T. M.; Lobkovsky, E. B.; Coates, G. W. Polymerization of Lactide with Zinc and Magnesium β-Diiminate Complexes: Stereocontrol and Mechanism. *J. Am. Chem. Soc.* **2001**, *123*, 3229–3238.

60. Chisholm, M. H.; Gallucci, J.; Phomphrai, K. Coordination Chemistry and Reactivity of Monomeric Alkoxides and Amides of Magnesium and Zinc Supported by the Diiminato Ligand $CH(CMeNC_6H_3\text{-}2,6\text{-}i\text{-}Pr_2)_2$. a Comparative Study. *Inorg. Chem.* **2002**, *41*, 2785–2794.

61. Chisholm, M. H.; Choojun, K.; Chow, A. S.; Fraenkel, G.; Gallucci, J. C. THF Exchange and Molecular Dynamics in the Series (BDI)MgX(THF), Where X = *n*Bu, NEt_2, and *t*OBu and BDI = 2-[(2,6-Diisopropylphenyl)Amino]-4-[(2,6-Diisopropylphenyl)Imino]Pent-2-Ene. *Inorg. Chem.* **2013**, *52*, 11302–11310.

62. Dove, A. P.; Gibson, V. C.; Marshall, E. L.; White, A. J. P.; Williams, D. J. A Well Defined Tin(II) Initiator for the Living Polymerisation of Lactide. *Chem. Commun.* **2001**, 283–284.

63. Chisholm, M. H.; Gallucci, J.; Phomphrai, K. Lactide Polymerization by Well-Defined Calcium Coordination Complexes: Comparisons with Related Magnesium and Zinc Chemistry. *Chem. Commun.* **2003**, 48–49.

64. Espenson, J. H. Chemical Kinetics and Reaction Mechanisms; McGraw-Hill: New York, 1981; pp. 153–155.

65. Christianson, M. D.; Tan, E. H. P.; Landis, C. R. Stopped-Flow NMR: Determining the Kinetics of [*rac*-(C_2H_4(1-Indenyl)$_2$)ZrMe][MeB(C_6F_5)$_3$]-Catalyzed Polymerization of 1-Hexene by Direct Observation. *J. Am. Chem. Soc.* **2010**, *132*, 11461–11463.

66. Pietrangelo, A.; Knight, S. C.; Gupta, A. K.; Yao, L. J.; Hillmyer, M. A.; Tolman, W. B. Mechanistic Study of the Stereoselective Polymerization of D,L-Lactide Using Indium(III) Halides. *J. Am. Chem. Soc.* **2010**, *132*, 11649–11657.

67. Douglas, A. F.; Patrick, B. O.; Mehrkhodavandi, P. A Highly Active Chiral Indium Catalyst for Living Lactide Polymerization. *Angew. Chem. Int. Ed.* **2008**, *47*, 2290–2293.

68. Williams, C. K.; Breyfogle, L. E.; Choi, S. K.; Nam, W.; Young, V. G.; Hillmyer, M. A.; Tolman, W. B. A Highly Active Zinc Catalyst for the Controlled Polymerization of Lactide. *J. Am. Chem. Soc.* **2003**, *125*, 11350–11359.

69. Zhong, Z.; Dijkstra, P. J.; Feijen, J. Controlled and Stereoselective Polymerization of Lactide: Kinetics, Selectivity, and Microstructures. *J. Am. Chem. Soc.* **2003**, *125*, 11291–11298.

70. Barakat, I.; Dubois, P.; Jérôme, R.; Teyssié, P. Macromolecular Engineering of Polylactones and Polylactides. X. Selective End-Functionalization of Poly(D,L)-Lactide. *J. Polym. Sci., Part A: Polym. Chem.* **1993**, *31*, 505–514.

71. Corma, A.; Iborra, S.; Velty, A. Chemical Routes for the Transformation of Biomass Into Chemicals. *Chem. Rev.* **2007**, *107*, 2411–2502.

72. Röper, H. Renewable Raw Materials in Europe-Industrial Utilisation of Starch and Sugar. *Starch-Stärke* **2002**, *54*, 89–99.

73. Werpy, T.; Petersen, G.; Aden, A.; Bozell, J.; Holladay, J.; White, J.; Manheim, A.; Elliot, D.; Lasure, L.; Jones, S.; et al. Top Value Added Chemicals From Biomass; U.S Department of Energy, 2004.

74. Semsarilar, M.; Perrier, S. “Green” Reversible Addition-Fragmentation Chain-Transfer (RAFT) Polymerization. *Nat. Chem.* **2010**, *2*, 811–820.

75. O'Connor, J.; Ma, J. Metal-Catalyzed Decarbonylation of Primary Aldehydes at Room Temperature. *J. Org. Chem* **1992**, *57*, 5075–5077.

76. Andrews, M.; Klaeren, S. Decarbonylation of Sugars of Chlorotris (Triphenylphosphine) Rhodium. *J. Chem. Soc., Chem. Commun.* **1988**, 1266–1267.

77. Tsuji, J.; Ohno, K. Decarbonylation Reactions Using Transition Metal Compounds. *Synthesis* **1969**, 157–169.

78. Fenton, D. Process for Preparation of Olefins. *U.S. Patent 3,530,198* **1970**.

79. Prince, R.; Raspin, M. Olefin Formation From Saturated Aldehydes and Acids by Reaction with Ruthenium and Rhodium Complexes. *Chem. Commun.* **1966**, *6*, 156–157.

80. Foglia, T.; Barr, P. Decarbonylation Dehydration of Fatty Acids to Alkenes in the Presence of Transition Metal Complexes. *J. Am. Oil Chem. Soc.* **1976**, *53*, 737–741.

81. Miller, J. A.; Nelson, J. A.; Byrne, M. P. A Highly Catalytic and Selective Conversion of Carboxylic Acids to 1-Alkenes of One Less Carbon Atom. *J. Org. Chem* **1993**, *58*, 18–20.

82. Liu, Y.; Kim, K. E.; Herbert, M. B.; Fedorov, A.; Grubbs, R. H.; Stoltz, B. M. Palladium-Catalyzed Decarbonylative Dehydration of Fatty Acids for the Production of Linear Alpha Olefins. *Adv. Synth. Catal.* **2014**, *356*, 130–136.

83. Stern, R.; Hillion, G. Process for Manufacturing a Linear Olefin From a Saturated Fatty Acid or Fatty Acid Ester. *U.S. Patent 4,554,397* **1985**.

84. Maetani, S.; Fukuyama, T.; Suzuki, N.; Ishihara, D.; Ryu, I. Iron-Catalyzed Decarbonylation Reaction of Aliphatic Carboxylic Acids Leading to α-Olefins. *Chem. Commun.* **2012**, *48*, 2552–2554.

85. Suzuki, N.; Tahara, H.; Ishihara, D.; Danjo, H.; Ryu, I.; Fukuyama, T. Method for Producing Olefin. *US Patent 2013/0296626 A1* **2013**.

86. Trost, B. M.; Chen, F. Transition Metal Mediated Eliminations in Anhydrides and Thioanhydrides. *Tetrahedron Lett.* **1971**, *28*, 2603–2607.

87. Gooßen, L. J.; Rodriguez, N. A Mild and Efficient Protocol for the Conversion of Carboxylic Acids to Olefins by a Catalytic Decarbonylative Elimination Reaction. *Chem. Commun.* **2004**, 724–725.

88. Damez, C.; Estrine, B.; Bessmertnykh, A.; Bouquillon, S.; Henin, F.; Muzart, J. Effects of the Reactants Concentration in the Butadiene Telomerization with D-Xylose and Parallel Influence of Triethylamine as Additive. *J. Mol. Catal. A* **2006**, *244*, 93–98.

89. Vollmuller, F.; Magerlein, W.; Klein, S.; Krause, J.; Beller, M. Palladium-Catalyzed Reactions for the Synthesis of Fine Chemicals, 16-Highly Efficient Palladium-Catalyzed Telomerization of Butadiene with Methanol. *Adv. Synth. Catal.* **2001**, *343*, 29–33.

90. Le Nôtre, J.; Scott, E. L.; Franssen, M. C. R.; Sanders, J. P. M. Selective Preparation of Terminal Alkenes From Aliphatic Carboxylic Acids by a Palladium-Catalysed Decarbonylation-Elimination Reaction. *Tetrahedron Lett.* **2010**, *51*, 3712–3715.

91. Wu, J. C.; Yu, T. L.; Chen, C. T.; Lin, C. C. Recent Developments in Main Group Metal Complexes Catalyzed/Initiated Polymerization of Lactides and Related Cyclic Esters. *Coord. Chem. Rev.* **2006**, *250*, 602-626.

92. Pounder, R. J.; Dove, A. P. Towards poly(ester) nanoparticles: recent advances in the synthesis of functional poly(ester)s by ring-opening polymerization. *Polym. Chem.* **2010**, *1*, 260-271.

93. Marshall, E. L.; Gibson, V. C.; Rzepa, H. S. A Computational Analysis of the Ring-Opening Polymerization of *rac*-Lactide Initiated by Single-Site *β*-Diketiminate Metal Complexes: Defining the Mechanistic Pathway and the Origin of Stereocontrol. *J. Am. Chem . Soc.* **2005**, *127*, 6048-6051.

94. Dove, A. P.; Gibson, V. C.; Marshall, E. L.; Rzepa, H. S.; White, A. J. P.; Williams, D. J. Synthetic, Structural, Mechanistic, and Computational Studies on Single-Site *β*-Diketiminate Tin(II) Initiators for the Polymerization of *rac*-Lactide. *J. Am. Chem. Soc.* **2006**, *128*, 9834-9843.

95. Chisholm, M. H.; Gallucci, J. C.; Quisenberry, K. T.; Zhou, Z. Complexities in the Ring-Opening Polymerization of Lactide by Chiral Salen Aluminum Initiators. *Inorg. Chem.* **2008**, *47*, 2613-2624.

96. Bhaw-Luximon, A.; Jhurry, D.; Spassky, N. Controlled polymerization of D,L-lactide using a Schiff's base Al-alkoxide initiator derived from 2-hydroxyacetphenone. *Polym. Bull.* **2000**, *44*, 31-38.

97. Tang, Z.; Gibson, V. C. *rac*-Lactide polymerization using aluminum complexes bearing tetradentate phenoxy-amine ligands. *Eur. Polym. J.* **2007**, *43*, 150-155.

98. Hormnirun, P.; Marshall, E. L.; Gibson, V. C.; White, A. J. P.; Williams, D. J. Remarkable Stereocontrol in the Polymerization of Racemic Lactide Using Aluminum Initiators Supported by Tetradentate Aminophenoxide Ligands. *J. Am. Chem. Soc.* **2004**, *126*, 2688-2689.

99. Hormnirun, P.; Marshall, E. L.; Gibson, V. C.; Pugh, R. I.; White, A. J. P. Study of ligand substituent effects on the rate and stereoselectivity of lactide polymerization using aluminum salen-type initiators. *Proc. Natl. Acad. Sci. U.S.A.* **2006**, *103*, 15343-15348.

100. Gregson, C. K. A.; Blackmore, I. J.; Gibson, V. C.; Long, N. J.; Marshall, E. L.; White, A. J. P. Titanium-salen complexes as initiators for the ring-opening polymerisation of *rac*-lactide. *Dalton Trans.* **2006**, 3134-3140.

101. Wu, J.; Chen, Y.-Z.; Hung, W.-C.; Lin, C.-C. Preparation, Characterization, and Catalytic Studies of Magnesium Phenoxides: Highly Active Initiators for Ring-Opening Polymerization of L-Lactide. *Organometallics* **2008**, *27*, 4970-4978.

102. Chisholm, M. H. Trispyrazolylborate ligands as ancillary ligands in the development of single-site metal alkoxide catalysts for ring-opening polymerization of cyclic esters. *Inorg. Chim. Acta* **2009**, *362*, 4284-4290.

103. Poirier, V.; Roisnel, T.; Carpentier, J.-F.; Sarazin, Y. Versatile catalytic systems based on complexes of zinc, magnesium and calcium supported by a bulky bis(morpholinomethyl)phenoxy ligand for the large-scale immortal ring-opening polymerisation of cyclic esters. *Dalton Trans.* **2009**, 9820-9827.

104. Börner, J.; Flörke, U.; Glöge, T.; Bannenberg, T.; Tamm, M.; Jones, M. D.; Döring, A.; Kuckling, D.; Herres-Pawlis, S. New insights into the lactide polymerisation with neutral N-donor stabilised zinc complexes: Comparison of imidazolin-2-imine vs. guanidine complexes. *J. Mol. Catal. A* **2010**, *316*, 139-145

105. Alcazar-Roman, L. M.; O'Keefe, B. J.; Hillmyer, M. A.; Tolman, W. B. Electronic influence of ligand substituents on the rate of polymerization of ε-caprolactone by single-site aluminium alkoxide catalysts. *Dalton Trans.* **2003**, 3082-3087.

106. Amgoune, A.; Thomas, C. M.; Roisnel, T.; Carpentier, J.-F. Ring-opening polymerization of lactide with group 3 metal complexes supported by dianionic alkoxy-amino-bisphenolate: Combining high activity, productivity, and selectivity. *Chem. Eur. J.* **2006**, *12*, 169-179.

107. Breyfogle, L. E. Mechanistic Studies of Cyclic Ester Polymerizations by Discrete Metal-Alkoxide Catalysts. Ph.D. Thesis, University of Minnesota, Minneapolis, MN, 2005.

108. Duda, A.; Penczek, S. Thermodynamics of L-Lactide Polymerization. Equilibrium Monomer Concentration. *Macromolecules* **1990**, *23*, 1636-1639.

109. Hoops, S.; Sahle, S.; Gauges, R.; Lee, C.; Pahle, J.; Simus, N.; Singhal, M.; Xu, L.; Mendes, P.; Kummer, U. COPASI—A COmplex PAthway SImulator. *Bioinformatics* **2006**, 22, 3067-74.

110. Colby, D.A.; Bergman, R.G.; Ellman, J.A. Synthesis of Dihydropyridines and Pyridines from Imines and Alkynes via C–H Activation. *J. Am. Chem. Soc.* **2008**, *130*, 3645-3651.

111. Blackmond, D. Reaction progress kinetic analysis: a powerful methodology for mechanistic studies of complex catalytic reactions. *Angew. Chem. Int. Ed.* **2005**, *44*, 4302-4320.

112. Mathew, J.; Klussmann, M.; Iwamura, H.; Valera, F.; Futran, A.; Emanuelsson, E.; Blackmond, D. Investigations of Pd-catalyzed ArX Coupling Reactions Informed by Reaction Progress Kinetic Analysis. *J. Org. Chem.* **2006**, *71*, 4711-4722.

113. Addison, A. W.; Rao, T. N.; Reedijk, J.; Rijn, J. v.; Verschoor, G. C. Synthesis, Structure, and Spectroscopic Properties of Copper(II) Compounds Containing Nitrogen-Sulphur Donor Ligands; the Crystal and Molecular Structure of

Aqua(1,7-bis(*N*-methylbenimidazol-2'-yl)-2,6-dithiaheptane]copper(II) Perchlorate. *J. Chem. Soc., Dalton Trans.* **1984**, 1349-1356.

114. Hansch, C.; Leo, A.; Taft, R.W. A Survey of Hammett Substituent Constants and Resonance and Field Parameters. *Chem. Rev*. **1991**, *91*, 165-195.

115. Meier, M.; Basolo, F.; Pearson, R. G. Rates of Substitution Reactions of Tetrakis(triethylphosphite)metal(0) Compounds of the Nickel Triad. *Inorg. Chem*. **1969**, *8*, 795-801.

116. Barroso, S.; Adão, P.; Madeira, F.; Duarte, M. T.; Pessoa, J. C.; Martins, A. M. Vanadium Diaminebis(phenolate) Complexes: Syntheses, Structures, and Reactivity in Sulfoxidation Catalysis. *Inorg. Chem.* **2010**, *49*, 7452-7463.

117. Labourdette, G.; Lee, D. J.; Patrick, B. O.; Ezhova, M. B.; Mehrkhodavandi, P. Unusually Stable Chiral Ethyl Zinc: Reactivity and Polymerization of Lactide. *Organometallics* **2009**, *28*, 1309-1319.

118. Sato, K.; Kawakami, K.; Tanaka, T. Barrier to the Intramolecular Rearrangement of Tetrakis (isocyano)(tetracyanoethylene)cobalt(I) and-rhodium(I) Complexes. *Inorg. Chem.* **1979**, *18*, 1532–1534.

119. Toupance, T.; Duberley, S. R.; Rees, N. H.; Tyrrell, B. R. Mountford, P. Zirconium Complexes of Diamine-Bis(phenolate) Ligands: Synthesis, Structures, and Solution Dynamics. *Organometallics*, **2002**, *21*, 1367.

120. Yann, S.; Ruth H. H.; David, L. H.; Simon, M. H.; Manfred, B. Titanium, zinc and alkaline-earth metal complexes supported by bulky *O*,*N*,*N*,*O*-multidentate ligands: syntheses, characterisation and activity in cyclic ester polymerisation. *Dalton Transactions*, **2006**, *2*, 340-350

121. Michel, F; Hamman, S.; Philouze, C.;. Del Valle, C. P; Saint-Amana, E.; Thomas, F. Galactose oxidase models: insights from ^{19}F NMR spectroscopy. *Dalton Trans.*, **2009**, 832–842.

122. Garland, C. W.; Nibler, J. W.; Shoemaker, D. P. *Experiments in Physical Chemistry*, 7th ed.; McGraw-Hill: New York, 2003; pp 42-59.

123. SMART V.5.054, Bruker Analytical X-ray Systems, Madison, WI (2001).

124. An empirical correction for absorption anisotropy, R. Blessing, *Acta Cryst.* A51,, **1995**, 33-38.

125. SAINT+ V6.45, Bruker Analytical X-Ray Systems, Madison, WI (2003).

126. SHELXTL V6.14, Bruker Analytical X-Ray Systems, Madison, WI (2000).

127. Zhao, Y.; Truhlar, D. G. A new local density functional for main-group thermochemistry, transition metal bonding, thermochemical kinetics and noncovalent interactions. *J. Chem. Phys.* **2006**, *125*, 194101.

128. Hehre, W. J.; Radom, L.; Schleyer, P. v. R.; Pople, J. A. *Ab Initio Molecular Orbital Theory*; Wiley: New York, 1986.

129. Cramer, C. J. *Essentials of Computational Chemistry: Theories and Models*; 2nd ed.; John Wiley & Sons: Chichester, 2004.

130. Zhao, Y.; Truhlar, D. G. The M06 suite of density functionals for main group thermochemistry, thermochemical kinetics, noncovalent interactions, excited states, and transition elements: two new functionals and systematic testing of four M06-class functionals and 12 other functionals. *Theor. Chem. Acc.* **2008**, *120*, 215-241.

131. Zhao, Y.; Truhlar, D. G. Density Functionals with Broad Applicability in Chemistry. *Acc. Chem. Res.* **2008**, *41*, 157-167.

132. Zhao, Y.; Truhlar, D. G. Benchmark Energetic Data in a Model System for Grubbs II Metathesis Catalysis and Their Use for Assessment and Validation of Electronic Structure Methods. *J. Chem. Theory Comput.* **2009**, *5*, 324-333.

133. Marenich, A. V.; Cramer, C. J.; Truhlar, D. G. Universal solvation model based on solute electron density and on a continuum model of the solvent defined by the bulk dielectric constant and atomic surface tensions. *J. Phys. Chem. B* **2009**, *113*, 6378-6396.

134. Frisch, M. J.; Trucks, G. W.; Schlegel, H. B.; Scuseria, G. E.; Robb, M. A.; Cheeseman, J. R.; Scalmani, G.; Barone, V.; Mennucci, B.; Petersson, G. A.; Nakatsuji, H.; Caricato, M.; Li, X.; Hratchian, H. P.; Izmaylov, A. F.; Bloino, J.; Zheng, G.; Sonnenberg, J. L.; Hada, M.; Ehara, M.; Toyota, K.; Fukuda, R.; Hasegawa, J.; Ishida, M.; Nakajima, T.; Honda, Y.; Kitao, O.; Nakai, H.; Vreven, T.; Montgomery, J. A.; Peralta, J. E.; Ogliaro, F.; Bearpark, M.; Heyd, J. J.; Brothers, E.; Kudin, K. N.; Staroverov, V. N.; Kobayashi, R.; Normand, J.; Raghavachari, K.; Rendell, A.; Burant, J. C.; Iyengar, S. S.; Tomasi, J.; Cossi, M.; Rega, N.; Millam, J. M.; Klene, M.; Knox, J. E.; Cross, J. B.; Bakken, V.; Adamo, C.; Jaramillo, J.; Gomperts, R.; Stratmann, R. E.; Yazyev, O.; Austin, A. J.; Cammi, R.; Pomelli, C.; Ochterski, J. W.; Martin, R. L.; Morokuma, K.; Zakrzewski, V. G.; Voth, G. A.; Salvador, P.; Dannenberg, J. J.; Dapprich, S.; Daniels, A. D.; Farkas, Ö.; Foresman, J. B.; Ortiz, J. V.; Cioslowski, J.; Fox, D. J. *Gaussian 09, Revision A.02*; Gaussian, Inc.: Wallingford, CT, 2010.

135. Gandini, A. Polymers from Renewable Resources: A Challenge for the Future of Macromolecular Materials. *Macromolecules* **2008**, *41*, 9491-9504.

136. *Renewable Polymers: Synthesis, Processing, and Technology*; Mittal, V., Ed.; John Wiley & Sons and Scrivener Publishing: Hoboken, New Jersey, and Salem, Massachusetts, 2012.

137. Nomura, N.; Ishii, R.; Yamamoto, Y.; Kondo, T. Stereoselective Ring-Opening Polymerization of a Racemic Lactide by Using Achiral Salen- and Homosalen-Aluminum Complexes. *Chem.-Eur. J.* **2007**, *13*, 4433–4451.

138. Wang, Y.; Ma, H. Exploitation of dinuclear salan aluminum complexes for versatile copolymeriation of ε-caprolactone and L-lactide. *Chem. Commun.* **2012**, *48*, 6729–6731.

139. Ding, K.; Miranda, M. O.; Moscato-Goodpaster, B.; Ajellal, N.; Breyfogle, L. E.; Hermes, E. D.; Schaller, C. P.; Roe, S. E.; Cramer, C. J.; Hillmyer, M. A.; Tolman, W. B. Roles of Monomer Binding and Alkoxide Nucleophilicity in Aluminum-Catalyzed Polymerization of ε-Caprolactone. *Macromolecules* **2012**, *45*, 5387–5396.

140. Cozzi, P. G. Metal-Salen Schiff base complexes in catalysis: practical aspects. *Chem. Soc. Rev.* **2004**, *33*, 410-421.

141. Che, C.-M.; Huang, J.-S. Metal complexes of chiral binaphthyl Schiff-base ligands and their application in stereoselective organic transformations. *Coord. Chem. Rev.* **2003**, *242*, 97-113.

142. Ovitt, T. M.; Coates, G. W. Stereoselective Ring-Opening Polymerization of *meso*-Lactide: Synthesis of Syndiotactic Poly(lactic acid). *J. Am. Chem. Soc.* **1999**, *121*, 4072-4073.

143. Majerska, K.; Duda, A. Stereocontrolled Polymerization of Racemic Lactide with Chiral Initiator: Combining Stereoelection and Chiral Ligand-Exchange Mechanism. *J. Am. Chem . Soc.* **2004**, *126*, 1026-1027.

144. Breteler, M. R. T.; Zhong, Z.; Dijkstra, P. J.; Palmans, A. R. A.; Peeters, J.; Feijen, J. Ring-Opening Polymerization of Substituted ε-Caprolactones with a Chiral (Salen) Al*O*i*P*r Complex. *J. Polym. Sci. A Polym. Chem.* **2007**, *45*, 429-436.

145. Yang, J.; Yu, Y.; Li, Q.; Li, Y.; Cao, A. Chemical Synthesis of Biodegradable Aliphatic Polyesters and Polycarbonates Catalyzed by Novel Versatile Aluminum Metal Complexes Bearing Salen Ligands. *J. Polym. Sci. A Polym. Chem.* **2005**, *43*, 373-384.

146. Chisholm, M. H.; Patmore, N. J.; Zhou, Z. Concering the relative importance of enantiomorphic site vs. chain end control in the stereoselective polymerization of lactides: reactions or (*R*,*R*-salen)- and (*S*,*S*)-salen-aluminum alkoxides LAlOCH_2R complexes (R = CH_3 and *S*-CHMeCl). *Chem. Commun.* **2005**, 127-129.

147. van der Meulen, I.; Gubbels, E.; Huijser, S.; Sablong, R. l.; Koning, C. E.; Heise, A.; Duchateau, R. Catalytic Ring-Opening Polymerization of Renewable Macrolactones to High Molecular Weight Polyethylene-like Polymers. *Macromolecules* **2011**, *44*, 4301-4305.

148. Pepels, M. P. F.; Bouyahyi, M.; Heise, A.; Duchateau, R. Kinetic Investigation on the Catalytic Ring-Opening (Co)Polymerization of (Macro)Lactones Using Aluminum Salen Complexes. *Macromolecules* **2013**, *46*, 4324-4334.

149. Cross, E. D.; Allan, L. E. N.; Decken, A.; Shaver, M. P. Aluminum Salen and Salan Complexes in the Ring-Opening Polymerization of Cyclic Esters: Controlled Immortal and Copolymerization of *rac*-β-Butyrolactone and *rac*-Lactide. *J. Polym. Sci. Part A-Polym. Chem.* **2012**, *51*, 1137-1146.

150. Du, H.; Pang, X.; Yu, H.; Zhuang, X.; Chen, X.; Cui, D.; Wang, X.; Jing, X. Polymerization of *rac*-Lactide Using Schiff Base Aluminum Catalysts: Structure, Activity, and Stereoselectivity. *Macromolecules* **2007**, *40*, 1904–1913.

151. Atwood, D. A.; Harvey, M. J. Group 13 Compounds Incorporating Salen Ligands. *Chem. Rev.* **2001**, *101*, 37-52.

152. Chen, P.; Chisholm, M. H.; Gallucci, J. C.; Zhang, X.; Zhou, Z. Binding of Propylene Oxide to Porphyrin- and Salen-M(III) Cations, Where M = Al, Ga, Cr, and Co. *Inorg. Chem.* **2005**, *44*, 2588–2595.

153. Muñoz-Hernández, M.-A.; Keizer, T. S.; Parkin, S.; Zhang, Y.; Atwood, D. A. Chelated Aluminum Alkoxides. *J. Chem. Crystallogr.* **2000**, *30*, 219–222.

154. Talarico, G.; Barone, V.; Joubert, L.; Adamo, C. General Computational Strategy to Study Polymerization Reactions at Aluminum-Based Catalysts. *Int. J. Quant. Chem.* **2003**, *91*, 474-482.

155. Marenich, A. V.; Jerome, S. V.; Cramer, C. J.; Truhlar, D. G. Charge Model 5: An Extension of Hirshfeld Population Analysis for the Accurate Description of Molecular Interactions in Gaseous and Condensed Phases. *J. Chem. Theor. Comput.* **2012**, *8*, 527-541.

156. Jegier, J. A.; Muñoz-Hernández, M.-Á.; Atwood, D. A. Six-coordinate aluminium cations: synthesis, characterization and catalysis. *J. Chem. Soc., Dalton Trans.* **1999**, 2583-2588.

157. Muñoz-Hernández, M.-Á.; McKee, M. L.; Keizer, T. S.; Yearwood, B. C.; Atwood, D. A. Six-coordinate aluminium cations: characterization, catalysis, and theory. *J. Chem. Soc., Dalton Trans.* **2002**, 410-414.

158. Getzler, Y. D.; Mahadevan, V.; Lobkovsky, E. B.; Coates, G. W. Stereochemistry of epoxide carbonylation using bimetallic Lewis acid/metal carbonyl complexes. *Pure Appl. Chem.* **2004**, *76*, 557-564.

159. Kurahashi, T.; Fujii, H. One-Electron Oxidation of Electronically Diverse Manganese(III) and Nickel(II) Salen Complexes: Transition from Localized to Declocalized Mixed-Valence Ligand Radicals. *J. Am. Chem. Soc.* **2011**, *133*, 8307-8316.

160. Cavazzini, M.; Manfredi, A.; Montanari, F.; Quici, S.; Pozzi, G. Asymmetric Epoxidation of Alkenes in Fluorinated Media, Catalyzed by Second-Generation Fluorous Chiral (Salen)manganese Complexes. *Eur. J. Org. Chem.* **2001**, 4639-4649

161. Braun, M.; Fleischer, R.; Mai, B.; Schneider, M.-A.; Lachenicht, S. The Regioisomeric Triphenylaminoethanols – Comparison of their Efficiency in Enantioselective Catalysis. *Adv. Synth. Catal.* **2004**, *346*, 474–482.

162. Ribeiro, R. F.; Marenich, A. V.; Cramer, C. J.; Truhlar, D. G. Use of Solution-Phase Vibrational Frequencies in Continuum Models for the Free Energy of Solvation. *J. Phys. Chem. B* **2011**, *115*, 14556-14562.

163. Zakzeski, J.; Bruijnincx, P. C. A.; Jongerius, A. L.; Weckhuysen, B. M. The Catalytic Valorization of Lignin for the Production of Renewable Chemicals. *Chem. Rev.* **2010**, *110*, 3552–3599.

164. Huber, G. W.; Iborra, S.; Corma, A. Synthesis of Transportation Fuels From Biomass: Chemistry, Catalysts, and Engineering. *Chem. Rev.* **2006**, *106*, 4044–4098.

165. Maetani, S.; Fukuyama, T.; Suzuki, N.; Ishihara, D.; Ryu, I. Efficient Iridium-Catalyzed Decarbonylation Reaction of Aliphatic Carboxylic Acids Leading to Internal or Terminal Alkenes. *Organometallics* **2011**, *30*, 1389–1394.

166. Penzel, E. Polyacrylates. In *Ullmann's Encyclopedia of Industrial Chemistry*; Wiley-VCH Verlag GmbH & Co. KGaA: Weinheim, Germany, 2000; Vol. 28, pp. 515–536.

167. Moss, C. W.; Lambert, M. A.; Goldsmith, D. J. Production of Hydrocinnamic Acid by Clostridia. *Appl. Microbiol.* **1970**, *19*, 375–378.

168. Muller, A. J.; Bowers, J. S.; Eubanks, J. R. I.; Geiger, C. C.; Santobianco, J. G. Processes for Preparing Hydrocinnamic Acid. *U.S. Patent 5,939,581* **1999**.

169. Le Nôtre, J.; Scott, E.; Franssen, M. C. R.; Sanders, J. P. Biobased Synthesis of Acrylonitrile From Glutamic Acid. *Green Chem.* **2011**, *13*, 807.

170. Maul, J.; Frushour, B. G.; Kontoff, J. R.; Eichenauer, H.; Ott, K.-H.; Schade, C. Polystyrene and Styrene Copolymers. In *Ullmann's Encyclopedia of Industrial Chemistry*; Wiley-VCH Verlag GmbH & Co. KGaA: Weinheim, Germany, 2007; Vol. 29, pp. 475–522.

171. Brazdil, J. F. Acrylonitrile. In *Ullmann's Encyclopedia of Industrial Chemistry*; Wiley-VCH Verlag GmbH & Co. KGaA: Weinheim, Germany, 2000.

172. Beauprez, J. J.; Mey, M. D.; Soetaert, W. K. Microbial Succinic Acid Production: Natural Versus Metabolic Engineered Producers. *Process Biochem.* **2010**, *45*, 1103–1114.

173. Gokarn, R. R.; Eiteman, M. A.; Sridhar, J. Production of Succinate by Anaerobic Microorganisms. *ACS Symp. Ser.* **1997**, *666*, 237–263.

174. Nghiem, N. P.; Davison, B. H.; Suttle, B. E.; Richardson, G. R. Production of Succinic Acid by Anaerobiospirillum Succiniciproducens. *Appl. Biochem. Biotechnol.* **1997**, *63-65*, 565–576.

175. Kranenburg, M.; Kamer, P. C. J.; Leeuwen, P. W. V.; Vogt, D.; Keim, W. Effect of the Bite Angle of Diphosphine Ligands on Activity and Selectivity in the Nickel-Catalysed Hydrocyanation of Styrene. *J. Chem. Soc., Chem. Commun.* **1995**, 2177–2178.

176. Rio, I. D.; Ruiz, N.; Claver, C.; Veen, L. A. V. D.; Leeuwen, P. W. V. Hydroxycarbonylation of Styrene with Palladium Catalysts: the Influence of the Mono-and Bidentate Phosphorus Ligand. *J. Mol. Catal. A: Chem.* **2000**, *161*, 39–48.

177. Cason, J. β-Carbomethoxypropionyl Chloride. *Organic Syntheses*; Wiley & Sons: New York, 1955, III, 169–171.

178. Srinivasan, R.; Uttamchandani, M.; Yao, S. Q. Rapid Assembly and in situ Screening of Bidentate Inhibitors of Protein Tyrosine Phosphatases. *Org. Lett.* **2006**, *8*, 713–716.

179. Yerino, L. V.; Osborn, M. E.; Mariano, P. S. The Hydroazocine Route to Highly Functionalized Pyrrolizidines. *Tetrahedron* **1982**, *38*, 1579–1591.

180. Simmons, E. M.; Hartwig, J. F. Iridium-Catalyzed Arene Ortho-Silylation by Formal Hydroxyl-Directed C− H Activation. *J. Am. Chem. Soc.* **2010**, *132*, 17092–17095.

181. Guo, Q.; Miyaji, T.; Hara, R.; Shen, B.; Takahashi, T. Group 5 and Group 6 Metal Halides as Very Efficient Catalysts for Acylative Cleavage of Ethers. *Tetrahedron* **2002**, *58*, 7327–7334.

182. Dapsens, P. Y.; Mondelli, C.; Pérez-Ramírez, J. Biobased Chemicals From Conception Toward Industrial Reality: Lessons Learned and to Be Learned. *ACS Catal.* **2012**, *2*, 1487–1499.

183. Ragauskas, A. J.; Williams, C. K.; Davison, B. H.; Britovsek, G.; Cairney, J.; Eckert, C. A.; Frederick, W. J.; Hallett, J. P.; Leak, D. J.; Liotta, C. L.; et al. The Path Forward for Biofuels and Biomaterials. *Science* **2006**, *311*, 484–489.

184. Miranda, M. O.; Pietrangelo, A.; Hillmyer, M. A.; Tolman, W. B. Catalytic Decarbonylation of Biomass-Derived Carboxylic Acids as an Efficient Route to Commodity Monomers. *Green Chem.* **2012**, *14*, 490–494.

185. Dauben, W. G.; Rivers, G. T.; Twieg, R. J.; Zimmerman, W. T. Efficient Syntheses of Barrelene and Nenitzescu's Hydrocarbon. *J. Org. Chem* **1976**, *41*, 887–889.

186. Goto, T.; Onaka, M.; Mukaiyama, T. Synthesis of Olefins by Nickel-Catalyzed Decarbonylation of S-(2-Pyridyl) Thioates. *Chem. Lett.* **1980**, 709–712.

187. Wenkert, E.; Chianelli, D. Nickel-Catalysed Decarbonylation of Thioesters. *J. Chem. Soc., Chem. Commun.* **1991**, 627–628.

188. Suzuki, N.; Tahara, H.; Ishihara, D.; Danjo, H.; Mimura, T.; Ryu, I.; Fukuyama, T. Process for Production of Olefin. *US Patent 2011/0190564A1* **2011**.

189. Suzuki, N.; Tahara, H.; Ishihara, D.; Danjo, H.; Ryu, I.; Fukuyama, T. Method for Producing Olefin. *US Patent 2013/0296626 A1* **2013**, 1–9.

190. Li, C.; Li, P.; Yang, J.; Wang, L. Palladium-Catalyzed Deamidative Arylation of Azoles with Arylamides Through a Tandem Decarbonylation-C-H Functionalization. *Chem. Commun.* **2012**, *48*, 4214–4216.

191. Freeslate Core Module 96 x 1 mL HiP Reactor

192. Geilen, F. M. A.; Stein, vom, T.; Engendahl, B.; Winterle, S.; Liauw, M. A.; Klankermayer, J.; Leitner, W. Highly Selective Decarbonylation of 5-(Hydroxymethyl)Furfural in the Presence of Compressed Carbon Dioxide. *Angew. Chem. Int. Ed.* **2011**, *50*, 6831–6834.

193. Kron, T. E.; Lopatina, V. S.; Morozova, L. N.; Lebedev, S. A.; Isaeva, L. S.; Kravtsov, D. N.; Petrov, S. Catalytic Activity of Nickel Complexes in Vinyl Hydrogen Substitution Reactions and Styrene Dimerization. *Russ. Chem. Bull.* **1989**, *38*, 703–707.

194. Yi, C.; Hua, R.; Zeng, H. Efficient and Selective Nickel(II)-Catalyzed Tail-to-Head Dimerization of Styrenes Affording 1,3-Diaryl-1-Butenes. *Catalysis Communications* **2008**, *9*, 85–88.

195. Faissner, R.; Huttner, G. Nickel(II) Compounds Derived From Tripod Ligands: Efficient Catalysts for the Stereoselective Heterodimerization of Styrene and Propene. *Eur. J. Inorg. Chem.* **2003**, *2003*, 2239–2244.

196. Jin, J.; RajanBabu, T. V. Heterodimerization of Propylene and Vinylarenes: Functional Group Compatibility in a Highly Efficient Ni-Catalyzed Carbon–Carbon Bond-Forming Reaction. *Tetrahedron* **2000**, *56*, 2145–2151.

197. Peng, J.; Li, J.; Qiu, H.; Jiang, J.; Jiang, K.; Mao, J.; Lai, G. Dimerization of Styrene to 1,3-Diphenyl-1-Butene Catalyzed by Palladium–Lewis Acid in Ionic Liquid. *J. Mol. Catal. A: Chem.* **2006**, *255*, 16–18.

198. Myagmarsuren, G.; Tkach, V. S.; Shmidt, F. K.; Mohamad, M.; Suslov, D. S. Selective Dimerization of Styrene to 1,3-Diphenyl-1-Butene with Bis(B-

Diketonato)Palladium/Boron Trifluoride Etherate Catalyst System. *J. Mol. Catal. A: Chem.* **2005**, *235*, 154–160.

199. Bedford, R. B.; Betham, M.; Blake, M. E.; Garcés, A.; Millar, S. L.; Prashar, S. Asymmetric Styrene Dimerisation Using Mixed Palladium–Indium Catalysts. *Tetrahedron* **2005**, *61*, 9799–9807.

200. Fanfoni, L.; Meduri, A.; Zangrando, E.; Castillon, S.; Felluga, F.; Milani, B. New Chiral P-N Ligands for the Regio- and Stereoselective Pd-Catalyzed Dimerization of Styrene. *Molecules* **2011**, *16*, 1804–1824.

201. Bhalla, G.; Oxgaard, J.; Goddard, W. A.; Periana, R. A. Hydrovinylation of Olefins Catalyzed by an Iridium Complex via CH Activation. *Organometallics* **2005**, *24*, 5499–5502.

202. Lee, D. W.; Yi, C. S. Chain- and Regioselective Ethylene and Styrene Dimerization Reactions Catalyzed by a Well-Defined Cationic Ruthenium-Hydride Complex: New Insights on the Styrene Dimerization Mechanism. *Organometallics* **2010**, *29*, 3413–3417.

203. Uhlig, E.; Nestler, B. Oxydative Addition Von Carbonsäureanhydriden an Nickel(0)-Komplexe. *Z. Chem.* **1981**, *21*, 451–452.

204. Ittel, S. D.; Berke, H.; Dietrich, H.; Lambrecht, J.; Hrter, P.; Opitz, J.; Springer, W. Complexes of Nickel(0). *Inorg. Synth.* **1990**, *28*, 98–104.

205. Bantreil, X.; Nolan, S. P. Synthesis of N-Heterocyclic Carbene Ligands and Derived Ruthenium Olefin Metathesis Catalysts. *Nat. Protoc.* **2011**, *6*, 69–77.

206. Nückel, S.; Burger, P. Transition Metal Complexes with Sterically Demanding Ligands. 2. Meisenheimer Complex Formation and Deprotonation Reactions of a Sterically Demanding Aromatic Diimine. *Organometallics* **2000**, *19*, 3305–3311.

207. Small, B. L.; Brookhart, M.; Bennett, A. M. A. Highly Active Iron and Cobalt Catalysts for the Polymerization of Ethylene. *J. Am. Chem. Soc.* **1998**, *120*, 4049–4050.

208. Johnson, L. K.; Killian, C. M.; Brookhart, M. New Pd(II)-and Ni(II)-Based Catalysts for Polymerization of Ethylene and α-Olefins. *J. Am. Chem. Soc.* **1995**, *117*, 6414–6415.

209. Tshuva, E. Y.; Gendeziuk, N.; Kol, M. Single-Step Synthesis of Salans and Substituted Salans by Mannich Condensation. *Tetrahedron Lett.* **2001**, *42*, 6405–6407.

A Kinetics of Cyclic Ester Polymerization Initiators Using Stopped-Flow 1H NMR Spectroscopy

In collaboration with Hanna Macaranas from the University of Minnesota and Anna Dunn and Prof. Clark Landis from the University of Wisconsin, Madison.

A.1 Overview

This appendix describes the preliminary data and data analysis obtained in collaboration with Prof. Clark Landis and his student, Anna Dunn, to monitor polymerization kinetics using the stopped-flow ^{1}H NMR spectroscopy technique developed in the Landis group on a set of very rapid ROP initiators.

A.2 Background

Previously, we studied the kinetics of the ring-opening polymerization (ROP) ε-caprolactone (CL) using aluminum alkoxide complexes at high concentrations of CL ([CL] ≥ 2 M) in order to see saturation, or Michaelis-Menten kinetics to understand the origin of the differences in rate between two sets of electronically-varied aluminum alkoxide complexes (Chapters 2 and 3). While we were able to see saturation kinetics and glean interesting mechanistic information about the ROP of CL by these aluminum alkoxide complexes, these initiators are rather slow, often taking many hours at elevated temperature to reach full conversion of monomer. Additionally, we found, in the case of the aluminum salen alkoxides (Chapter 3), that the saturation behavior was due to an inhibition mechanism, not a pre-equilibrium of monomer binding to catalyst followed by an irreversible alkoxide insertion step. Instead, theoretical calculations revealed that monomer binding and alkoxide insertion appeared to happen in a single step. We surmised that it is possible that very rapid ROP catalysts could operate by a similar mechanism, but do not suffer from an inhibition pathway that would reduce the overall observed rate. Thus, we wanted to study the kinetic behavior of some very rapid catalysts at high concentrations of monomer.

However, since the initiators are very rapid, monitoring monomer consumption can be very challenging. Stopped-flow techniques have been used widely with a variety of other spectroscopic methods (e.g., UV-visible spectroscopy), but have recently been used in conjunction with ^{1}H NMR spectroscopy by Prof. Clark Landis' group to study polymerization of 1-hexene by a zirconium metallocene-based catalyst.[65] ^{1}H NMR spectroscopy usually is poorly suited to monitor very rapid reactions, due to the time required to input a traditional sample into the magnet and begin to acquire spectra. However, when coupled with a stopped-flow setup, ^{1}H NMR spectroscopy is able to monitor reactions with very rapid reaction rates.

We chose to study three well-studied and well-characterized initiators, shown in Figure A.1. Their rates are either well-studied, in the case of the two zinc complexes for the ROP of LA, or in the case of the magnesium complex, only preliminarily. They are all rapid for the ROP of LA at room temperature, reaching full conversion in under approximately 5 minutes for [(NNO)ZnOEt][68] and [(BDI)MgO*i*-Pr]$_2$[59] and approximately 20 minutes for [(BDI)ZnO*i*-Pr]$_2$[65]. However, the kinetics for these initiators were all studied at low concentrations of LA (under 0.5 M), as is usually done. The catalysts were synthesized according to literature procedures in each case, except (NNO)ZnOEt (updated procedure detailed in section A.4.2), and purity was verified by ^{1}H NMR spectroscopy and elemental analysis.

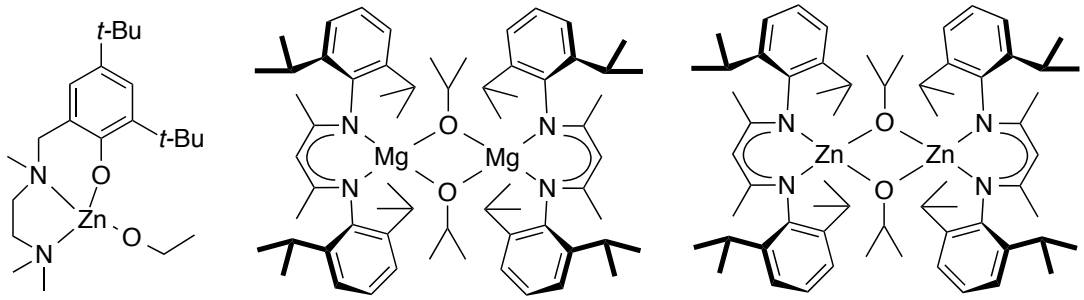

(NNO)ZnOEt [(BDI)MgO*i*-Pr]$_2$ [(BDI)ZnO*i*-Pr]$_2$

Figure A.1. Initiators studied using stopped-flow ^{1}H NMR spectroscopy for the ROP of CL.

A.3 Stopped-Flow ^{1}H NMR Spectroscopy Experiments

As is the case with stopped-flow ^{1}H NMR spectroscopy, reactions were run in protio-dichloromethane, and stock solutions of catalyst and monomer were prepared such that when they mix under the experimental conditions their concentrations would be accurate (e.g. the CL stock was prepared at a 4 M concentration, so upon mixing with a equal volume of an initiator stock solution the concentration would be diluted to the target $[CL]_0 = 2$ M). Addition of an internal standard, bis-*para*-trimethylsilylbenzene was used to verify concentrations. Arrayed spectra in sets of 34 were obtained using a single scan with a known delay time (d1), which was varied to obtain time points that represent the entire polymerization to full conversion.

Unfortunately, much of the data obtained from the stopped-flow experiments is difficult treat quantitatively. Because we are using high concentrations of monomer and low catalyst loadings, polymer molecular weights become rather high, and the solution becomes viscous while in the spectrometer. As a result, after the first set of arrayed spectra, the resulting polymer does not get fully "rinsed" away, leaving a polymer solution to coat the glass inside of the spectrometer. In every subsequent spectra obtained, polymer (and catalyst and remaining internal standard) are still present in unknown quantities, obscuring accurate measurements of concentration for every shot until the solution is rinsed through. Due to experimental setup, rinsing of the glass lines with pure solvent between each set of spectra is not possible. Silyating the glass inside the spectrometer did not facilitate removal of the polymer after the initial injection of monomer and initiator. Despite these complicating factors, we were able to obtain some preliminary data for the ROP of CL by the initiators (NNO)ZnOEt and $[(BDI)MgO\textit{i}\text{-}Pr]_2$.

For each data set that was analyzed, the arrayed set of ^{1}H NMR spectra were phased, baseline corrected, and integrated using Mestrenova software. Integrals were exported into a spreadsheet where they were converted into concentrations using either

the internal standard or from conversion (based on $[CL]_0$ = 2 M). Time was calculated using the specific experimental d1, the calibrated 30 ° pulse width, the acquisition time, and the spooler delay. Concentration *vs*. time data was input into COPASI (version 4.10 build 55) and modeled using the parameter estimation model with either a first order rate equation or the Michaelis-Menten rate equation, using similar starting values and protocols as described in Chapter 2 and 3.

A.3.1 [(BDI)MgO*i*-Pr]$_2$ Initiator

Looking first at the [(BDI)MgO*i*-Pr]$_2$ initiator, only a single set of data was amenable to quantitative analysis ($[[(BDI)MgO\textit{i}\text{-Pr}]_2]_{tot}$ = 2.5 mM). However, the results are quite interesting. Based on the raw [CL] *vs*. time data in Figure A.2, there is a very clear induction period before the onset of polymerization. Interestingly, when the induction period is removed and the onset of polymerization is treated as t = 0 and the data is fit to a Michaelis-Menten or a first order fit, it is clear that the Michaelis-Menten rate equation fit is improved compared to that of the first order reaction fit (Figure A.3). Attempts to fit the induction period and the polymerization behavior with more complicated models were unsuccessful.

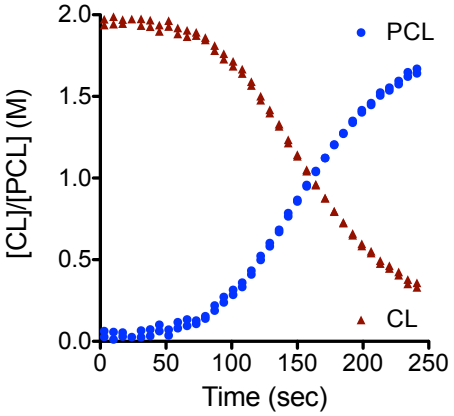

Figure A.2. Concentration *vs*. time profile for ROP of CL initiated by [(BDI)MgO*i*-Pr]$_2$.

Based on the fits in Figure A.3, saturation kinetics are observed using [(BDI)MgO*i*-Pr]$_2$ for the ROP of CL. However, looking at the raw ^{1}H NMR spectra (Figure A.10) that were used to generate the plots in Figure A.2 and Figure A.3, shifting of the ^{1}H NMR resonances associated with equilibrium for a monomer bound and unbound initiator species is not observed. In the literature associated with the [(BDI)MgO*i*-Pr]$_2$ initiator, extensive speciation studies were conducted in the presence of lactide and a coordinating solvent or a non-coordinating solvent. In the case of a non-coordinating solvent like dichloromethane, the resting state of the catalyst was determined to be a dimeric species based on ^{1}H NMR studies, indicating that the possible pre-equilibrium that would explain the saturation kinetics is a monomer-dimer catalyst equilibrium, followed by a single step for monomer association and alkoxide attack (Figure A.4).[60]

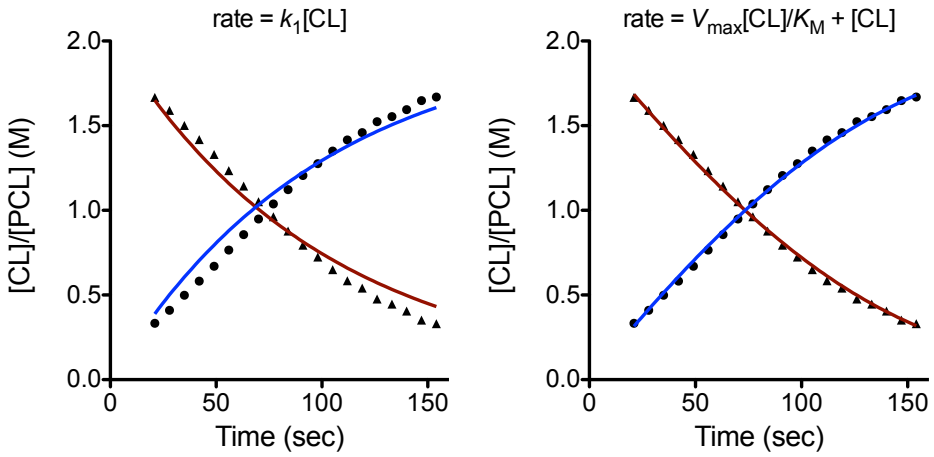

Figure A.3. Fits of concentration *vs*. time for ROP of CL initiated by [(BDI)MgO*i*-Pr]$_2$ for first order rate equation (left) and Michaelis-Menten rate equation (right). Fit parameters for first order fit: k_1 = 0.0101(1) s^{-1}. Fit parameters for Michaelis-Menten fit: V_{max} = 0.024(8) M/s, k_2 = 9.6(3) s^{-1}, K_M = 1.09(8) M, K_{eq} = 0.92(7) M^{-1}.

Additionally, the induction period could be explained by similar monomer-dimer equilibrium to prevent rapid initiation of the polymerization, as the initiator exists as a

dimer in the solid as well as solution state in non-coordinating solvents like dichloromethane or toluene. It is possible that the dimeric complex either has very sluggish rates of initiation on its own, or must break apart to monomeric units before initiation can occur. This is not unprecendented, as high dispersity values for the complex ($Đ$ = 1.56) and higher than expected molecular weights (nearly twice the expected molecular weight based on monomer to initiator ratio) were obtained in the absence of exogenous *iso*-propanol. However, in the presence of 1 equiv. of *iso*-propanol, both molecular weights and dispersities decreased to expected values ($Đ$ < 1.35), implying the ability of a coordinating element to affect initiation efficiency.[59]

Obviously, further control studies by traditional ^{1}H NMR spectroscopy could provide more evidence for this type of monomer-dimer equilibrium being responsible for the observed saturation kinetics for this initiator system. The resting state of the catalyst could also be a five-coordinate monomeric species with CL monomers or polymer chains in both axial positions and one equatorial position of a trigonal bipyramidal geometry around the Mg. A similar species has recently been observed in the presence of high concentrations of THF, but it is unclear whether that species is implicated during conditions relevant to polymerization (i.e., in the presence of monomer in a non-coordinating solvent).[61]

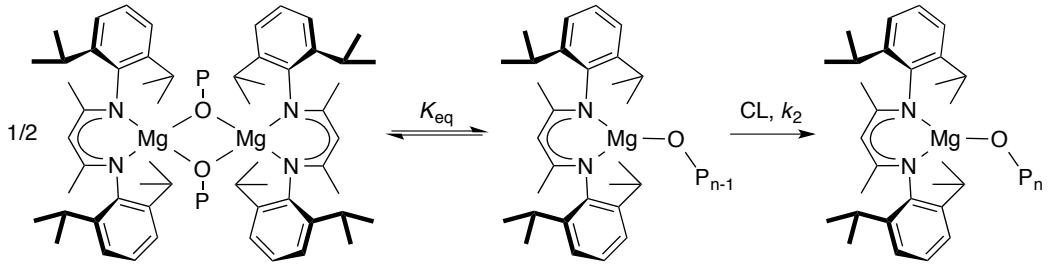

Figure A.4. Potential monomer-dimer catalyst equilibrium to explain observed saturation kinetics for the ROP of CL by [(BDI)MgO*i*-Pr]$_2$.

A.3.2 (NNO)ZnOEt Initiator

Moving to the (NNO)ZnOEt initiator, a different situation arises. No induction period is observed, and again, very little shifting of the monomer peaks in ^{1}H NMR spectra is observed (Figure A.11 and Figure A.12). When $[(NNO)ZnOEt]_{tot}$ = 2.5 mM, the data is fit to a first order rate equation and a Michaelis-Menten rate equation, differences between the two fits are very difficult to ascertain by eye (Figure A.5). In fact, when the fits are overlayed as in Figure A.5, bottom, they are nearly indistinguishable from one other.

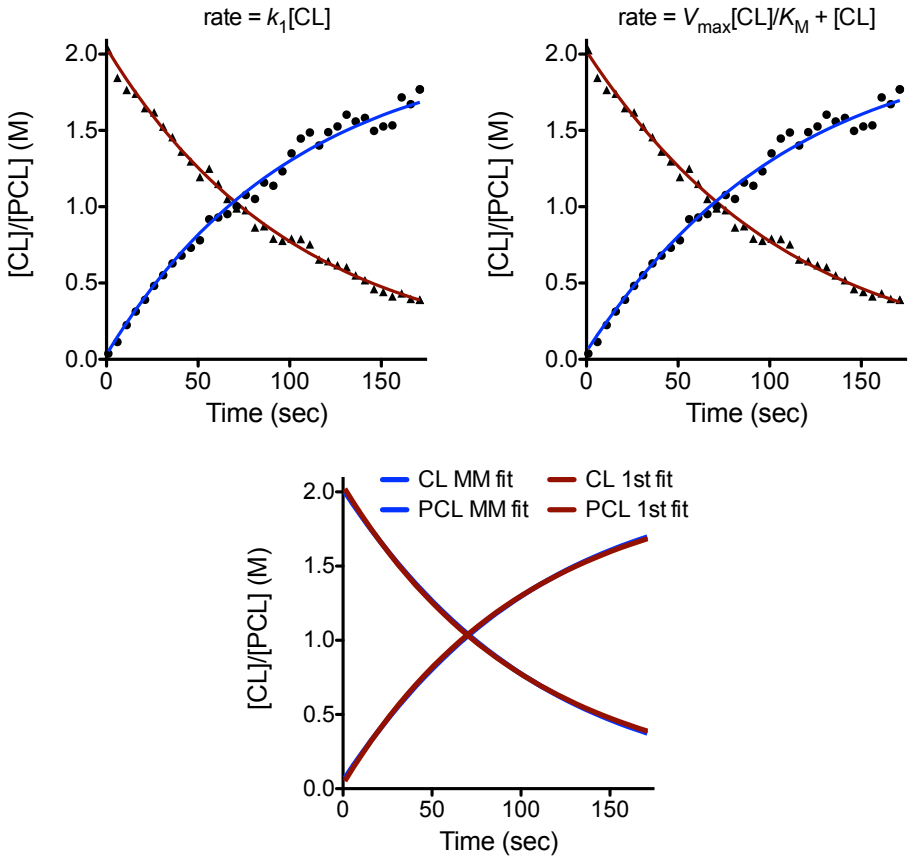

Figure A.5. Fits of concentration *vs*. time for ROP of CL initiated by (NNO)ZnOEt for first order rate equation (top, left), Michaelis-Menten rate equation (top, right) and overlay of fits from both rate equations (bottom). Fit parameters for first order fit: k_1 = 0.00970(6) s^{-1}. Fit parameters for Michaelis-Menten fit: V_{max} = 0.12(4) M/s, k_2 = 48 ± 16 s^{-1}, K_M = 11 ± 4 M, K_{eq} = 0.09(3) M^{-1}. [(NNO)ZnOEt] = 2.5 mM.

Another set of data using a higher concentration of (NNO)ZnOEt initiator ($[(NNO)ZnOEt]_{tot}$ = 7 mM) was able to be analyzed in a similar fashion (Figure A.6). Again, fits to a first order rate equation and the Michaelis-Menten equation are nearly indistinguishable (from Figure A.6, bottom). A summary of the rate constants obtained is in Table A.1.

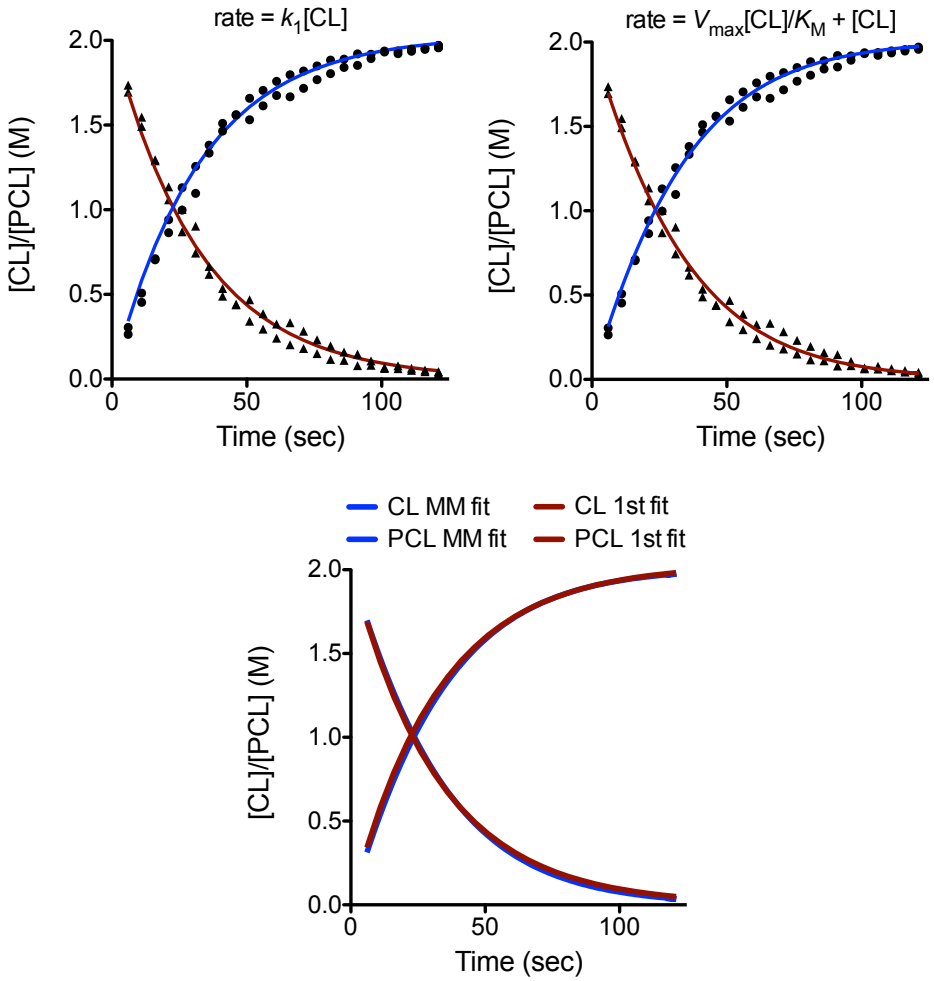

Figure A.6. Fits of concentration *vs*. time for ROP of CL initiated by (NNO)ZnOEt for first order rate equation (top, left), Michaelis-Menten rate equation (top, right) and overlay of fits from both rate equations (bottom). Fit parameters for first order fit: k_1 = 0.0307(2) s^{-1}. Fit parameters for Michaelis-Menten fit: V_{max} = 0.25(7) M/s, k_2 = 36 ± 10 s^{-1}, K_M = 7 ± 2 M, K_{eq} = 0.14(4) M^{-1}. $[(NNO)ZnOEt]_{tot}$ = 7 mM.

Table A.1 Summary of the kinetic parameters obtained from stopped-flow ^{1}H NMR spectroscopy.

Initiator	$[I]_0$ (mM)	k_1 (s^{-1}) (x10^3)	$t_{1/2}$ (s)	V_{max} (M/s)	k_2 (s^{-1})	K_M (M)	K_{eq} (M^{-1})
[(BDI)MgO*i*-Pr]$_2$	2.5	10.1(1)	68.6(7)	0.024(8)	9.6(3)	1.09(8)	0.92(7)
(NNO)ZnOEt	2.5	9.70(6)	71.5(4)	0.12(4)	48(16)	11(4)	0.09(3)
(NNO)ZnOEt	7	30.7(2)	22.6(1)	0.25(7)	36(10)	7(2)	0.14(4)

From the data in Table A.1 and the qualities of the fits from Figure A.5 and Figure A.6, it is hard to definitively say that we are observing saturation kinetics for the (NNO)ZnOEt complex. The small differences between the first order fit and the Michaelis-Menten fit, combined with the high error bars on the Michaelis-Menten fits, indicate that the Michaelis-Menten fit is likely an overfit of the data.

Encouragingly, the first order fits are in line with previous data for the ROP of LA, where the reported $t_{1/2}$ for LA polymerization with $[(NNO)ZnOEt]_{tot}$ = 2.2 mM is approximately 150 seconds.[68] We find that at a similar concentration ($[(NNO)ZnOEt]_{tot}$ = 2.5 mM) the $t_{1/2} \approx 72$ seconds, which is in line with a slightly elevated initiator concentration and that a different monomer was studied in each case. Additionally, the obtained k_1 does incrementally increase with concentration, with the obvious caveat that there are only two data points to compare.

Because it is unlikely (or at best unclear) that saturation kinetics are observed for the (NNO)ZnOEt complex, two scenarios can be imagined. It is possible that the coordination and insertion events occur in a concerted fashion, explaining the observed first order dependence on [CL]. Another possibility is that K_M for these systems is very large, in which case we may not be in the saturation regime even with $[CL]_0$ = 2 M. The fit parameters indicate that K_M could be larger than in previous systems, but not large enough to move entirely outside the saturation regime. Initial rate studies with larger $[CL]_0$ could help pinpoint whether $[CL]_0$ = 2 M is on the edge of a saturation regime.

Additionally, because the reactions are so rapid, the pre-equilibrium approximation may in fact not be applicable to these systems, and instead a steady state approximation could be considered. That is, K_M is no longer equal to $1/K_{eq}$, and instead takes on a more complicated form: $K_M = (k_{-1} + k_2)/k_1$, where k_{-1} and k_1 are related to the equilibrium for formation (k_1) and collapse (k_{-1}) of a monomer-initiator steady state bound complex. Studies with stoichiometric and sub-stoichiometric amounts of a non-polymerizable monomer like γ-butyrolactone to try and ascertain the resting state of the catalyst under conditions relevant to polymerization (as well as potentially determining a rate constant for k_1 or k_{-1}) would be extremely helpful to determine whether we reach a steady state during polymerization or not. Although it is possible that K_M could be high, it seems counterintuitive that very rapid ROP initiators have a lower affinity for the monomer substrate (K_M is inversely proportional to substrate affinity), but this very well may be the case and has quite interesting implications for initiator development and design.

Obviously this data is preliminary, but it illustrates the utility of stopped-flow ^{1}H NMR spectroscopy to study very rapid catalysts at high concentrations of monomer. It obviously raised a number of questions about the resting states of these rapid initiators, which are markedly different than those studied previously using high monomer concentrations. Understanding nuances about the resting state of these catalysts, as well as more detailed kinetic studies will help clarify why they are so rapid compared to other initiators, potentially opening avenues for development of new initiators.

A.4 Experimental Section

A.4.1 General Considerations

All reactions were carried out under an inert atmosphere using standard Schlenk and drybox techniques, unless otherwise indicated. Reagents were obtained from commercial suppliers and used as received unless otherwise indicated. CL was purified by distillation from CaH_2 and stored under N_2. Deuterated solvents were dried over CaH_2 or sodium, distilled under vacuum and stored under N_2. Protiated solvents were degassed and passed through a solvent purification system (Glass Contour, Laguna CA) prior to use. ^1H and ^{13}C NMR spectra were recorded on a Varian VI-300 NMR spectrometer or a Bruker Avance III 500 MHz spectrometer equipped with a BBFO SmartProbe and their chemical shifts (δ) for ^1H NMR spectra are referenced to residual protium in the deuterated solvent (for ^1H). Stopped-flow 1H NMR spectra were obtained using the reported setup.[65] Elemental analyses were performed by Roberston Microlit Laboratories, Inc, Ledgewood, NJ.

A.4.2 Updated Synthesis of (NNO)ZnOEt

The reported[68] and altered (improved) synthesis of the catalyst is summarized in Figure A.7.

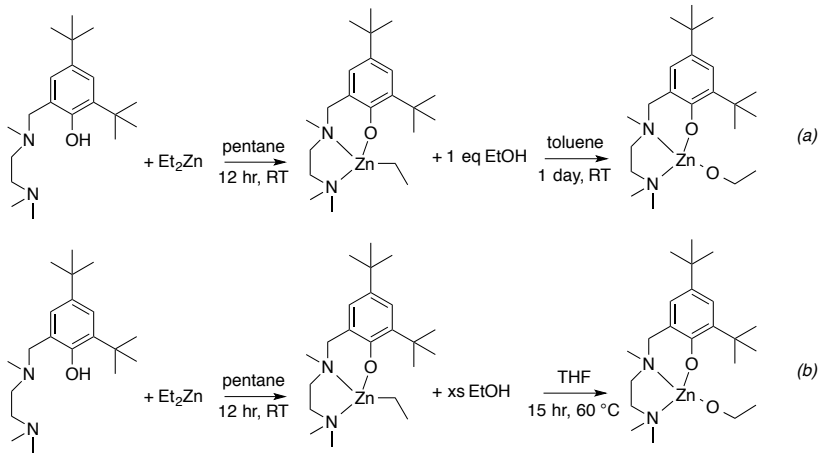

Figure A.7. (a) Reported synthetic route to (NNO)ZnOEt. (b) Altered and succcessful synthetic route to same product.

The reported route to the (NNO)ZnEt compound is unchanged in the improved route. I will not detail the experimental procedures here because they are identical to what is reported. When the reported procedure for the synthesis of the (NNO)ZnOEt compound is followed (to the letter, except for scale – instead of a 1 g scale based on (NNO)ZnEt, 0.5 g was used), the conversion to the (NNO)ZnOEt is about 75%, with the remaining material being unreacted starting material. No demetallation or side reactions are observed. The EtOH was dried overnight under Ar with CaH_2, then degassed, vacuum transferred and stored over a small amount of CaH_2 in a nitrogen-filled glove box. The EtOH was filtered before use to remove any CaH_2. Figure A.8 is an overlay of the spectra of each compound.

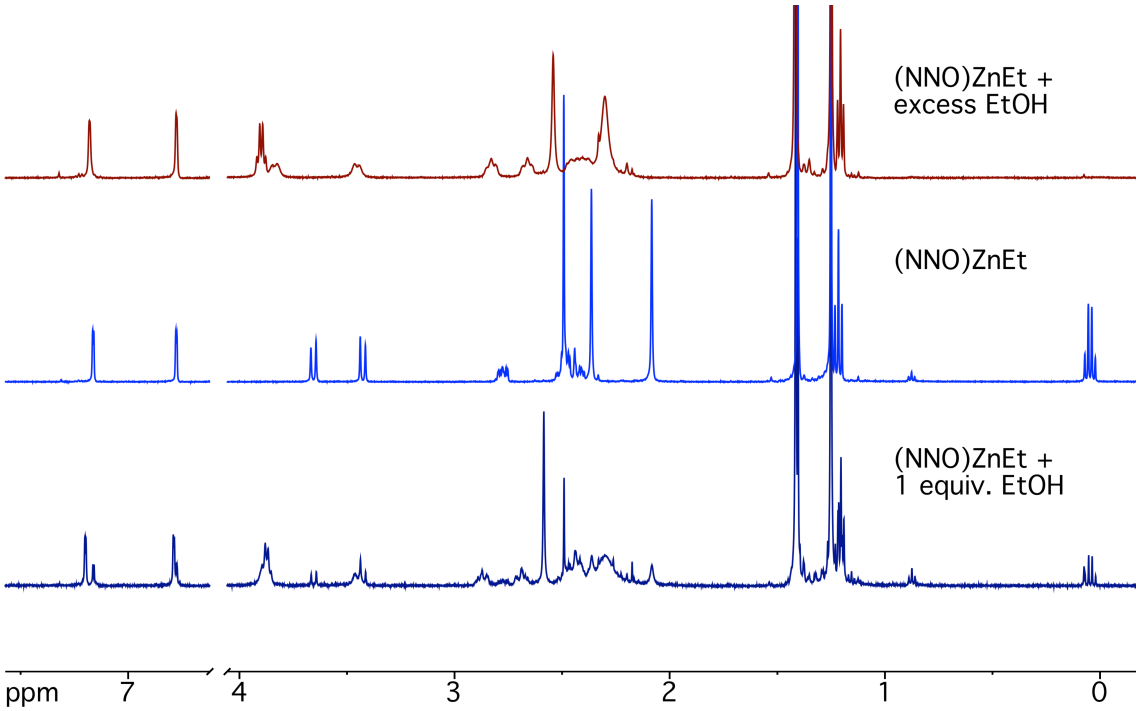

Figure A.8. Overlay of the ^{1}H NMR spectra of the clean reaction product between (NNO)ZnEt and excess EtOH (top, red), (NNO)ZnEt alone (middle, light blue), and the crude reaction product between (NNO)ZnEt and 1 equiv. EtOH (bottom, dark blue).

In order to push the reaction to completion, excess EtOH is required (approx.10-fold) and heating in THF. In an oven-dried 15 mL thick-walled screw cap vessel, (NNO)ZnEt (0.5 g 1.21 mmol) was dissolved in 3 mL of THF (dried over Na/benzophenone ketyl radical, degassed, vacuum transferred and stored over activated 3 Å molecular sieves in glove box) and EtOH was added (0.6 mL, 10.3 mmol). A stir bar was added, the bomb was sealed and removed from the glove box and heated to 60 °C for 15 hours. After 15 hours, a solid had deposited on the sides of the vessel, and the vessel was cooled and returned to the glove box. The THF and unreacted EtOH were removed *in vacuo*, and the resulting white solid was triturated three times with 5 mL pentane each time. A white powder remained. The crude material was recrystallized from toluene/pentane at -40 °C, yielding white crystals, which were crushed and dried overnight (0.212 g, 41%). The same spectrum on the top of Figure A.8 is repeated in Figure A.9 with assignments. This spectrum is nearly identical to the ^{1}H NMR spectrum reported. Anal. Calcd for $C_{22}H_{40}N_2O_2Zn$ C, 61.46%; H, 9.38%; N, 6.52%. Found C, 60.89%; H, 8.89%; N, 6.50%.

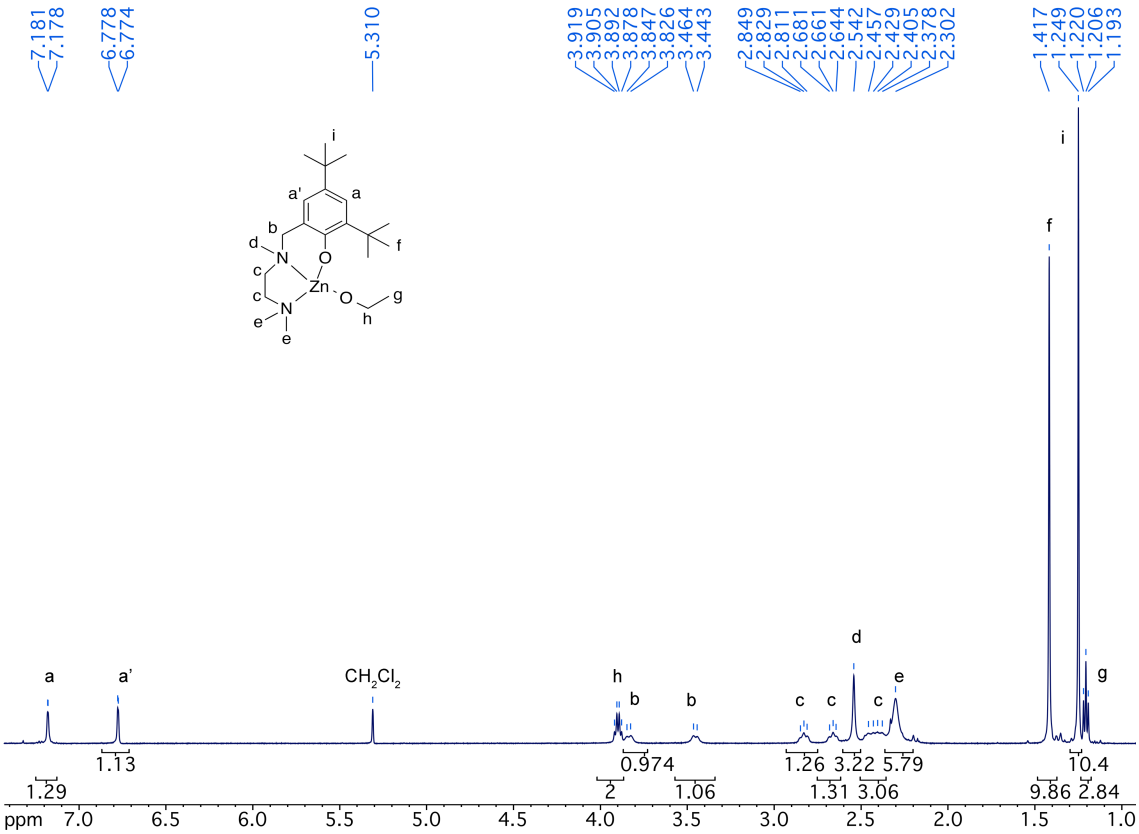

Figure A.9. ^{1}H NMR spectrum of the isolated (NNO)ZnOEt after reaction with excess EtOH and heating in THF.

A.4.3 Stopped-Flow Stacked ^{1}H NMR Spectra

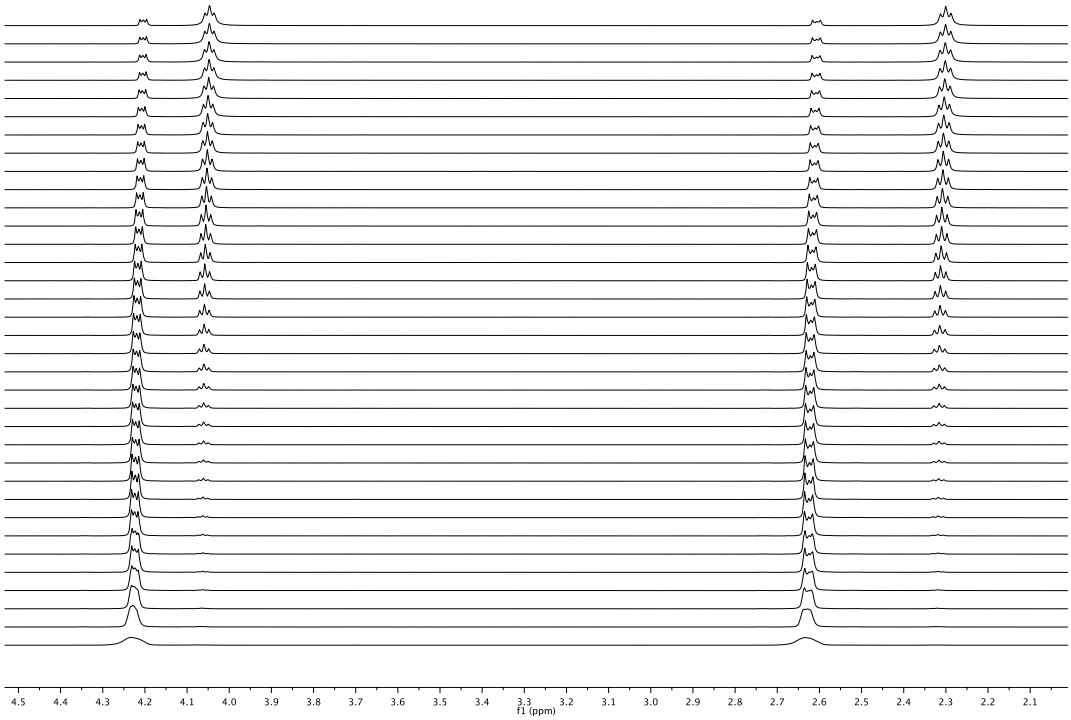

Figure A.10. Stacked ^{1}H NMR spectra obtained from stopped-flow experiment using $[[(BDI)MgO\textit{i}\text{-}Pr]_2]_0$ = 2.5 mM. First spectrum (bottom) was obtained 3 seconds after mechanical stop, and every subsequent spectra was obtained every 7 seconds.

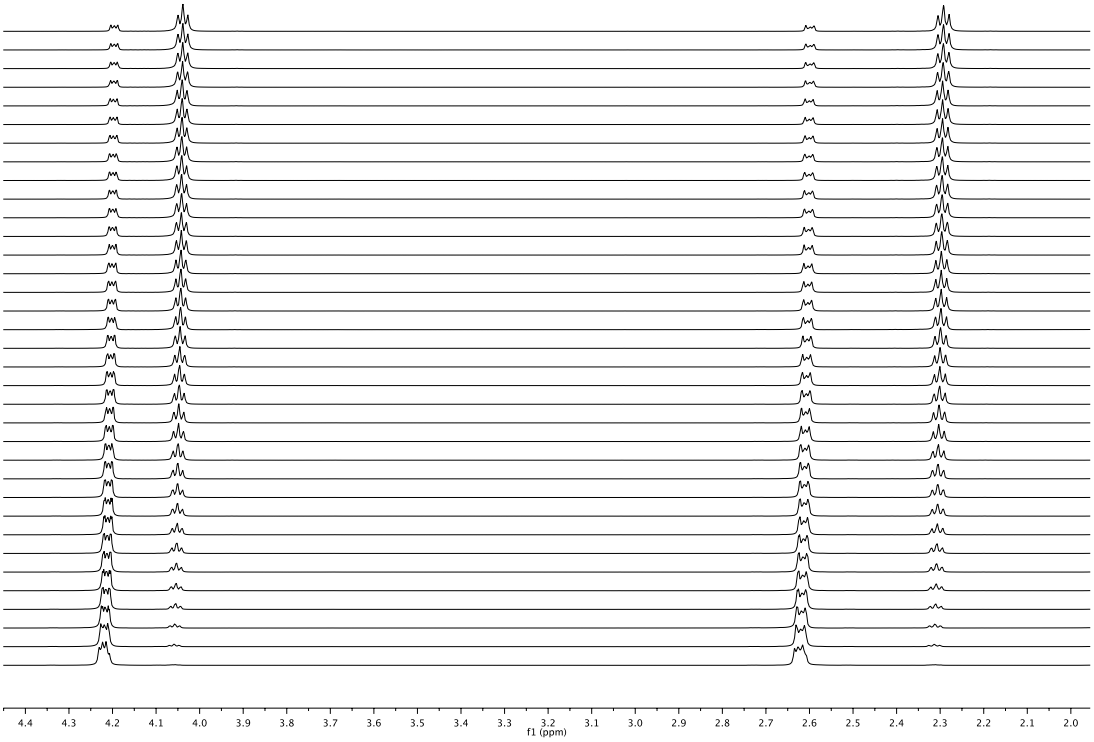

Figure A.11. Stacked ^{1}H NMR spectra obtained from stopped-flow experiment using $[(NNO)ZnOEt]_0$ = 2.5 mM. First spectrum (bottom) obtained 1 second after mechanical stop, and every subsequent spectra was obtained every 5 seconds.

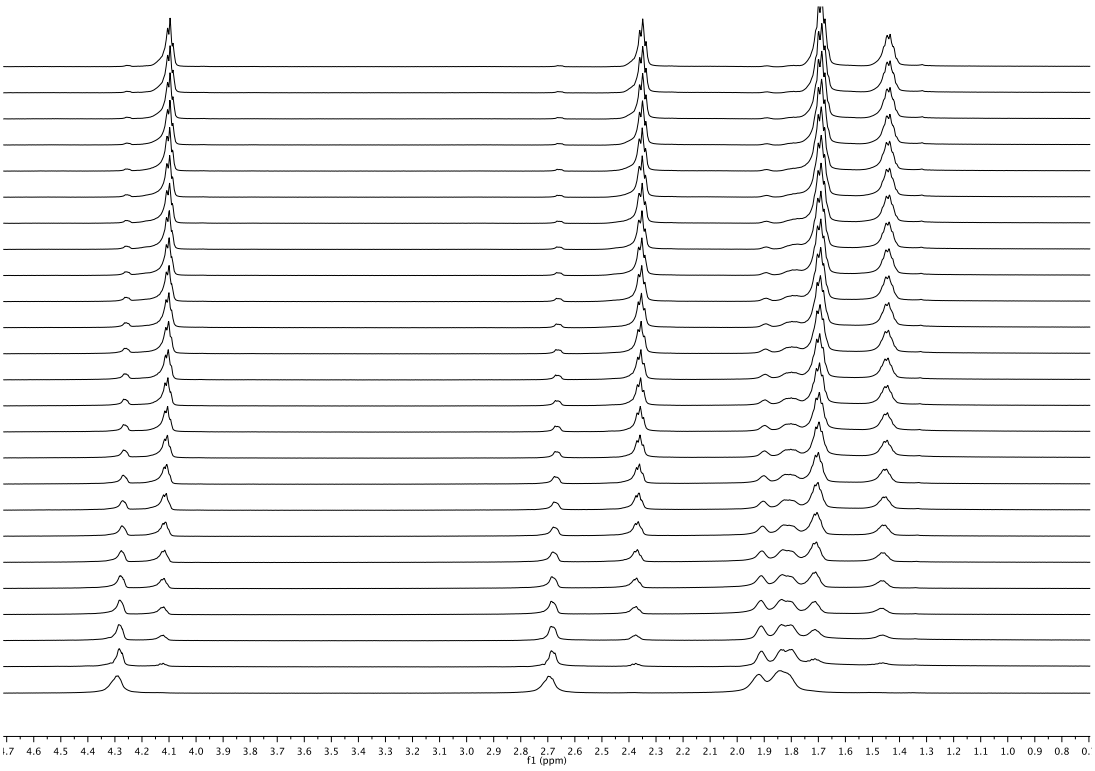

Figure A.12. Stacked ^{1}H NMR spectra obtained from stopped-flow experiment using [(NNO)ZnOEt] = 7 mM. First spectrum (bottom) obtained 1 second after mechanical stop, and every subsequent spectra obtained every 5 seconds.